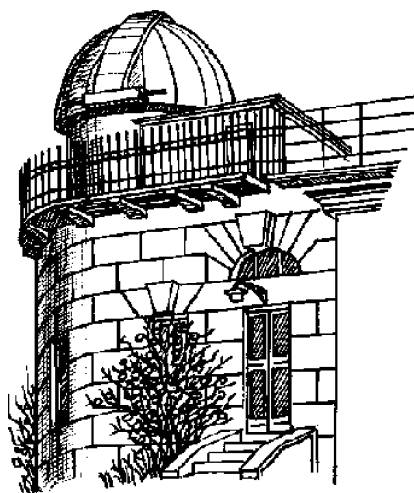


ODESSA ASTRONOMICAL PUBLICATIONS

**Volume 33
(2020)**



Astronomical Observatory
of I. I. Mechnikov Odessa National University

**ODESSA ASTRONOMICAL
PUBLICATIONS**

Volume 33
(2020)

Editorial Board:

- Editor-in-Chief* – Andrievsky S.M., Prof., RI "Astronomical Observatory"
Odessa I.I.Mechnikov National University
- Executive Secretary* – Kovtyukh V.V., ScD, RI "Astronomical Observatory"
Odessa I.I.Mechnikov National University
- Technical editing* – PhD Dragunova A.V., Strakhova S.L.

Advisory Editors:

Andronov I.L., ScD (Ukraine); Bagrov A.V., ScD (Russia); Bazey A.A., PhD (Ukraine); Eglitis I., PhD (Latvia); Ismailov N., PhD (Azerbaijan); Kim Y., ScD (Republic Korea); Koshkin N.I., PhD (Ukraine); Kucinskas A., PhD (Lithuania); Kudzej I., PhD (Slovakia); Lozitskiy V.G., ScD (Ukraine); Mishenina T.V., ScD (Ukraine); Novosyadlyj B.S., ScD (Ukraine); Panko E.A., ScD (Ukraine); Picazzio E., PhD (Brasil); Pilyugin L.S., ScD (Ukraine); Turner D., PhD (Canada); Udovichenko S.N., PhD (Ukraine); Ulyanov O.M., PhD (Ukraine); Vavilova I.B., PhD (Ukraine); Yushchenko A., PhD (Republic Korea); Zhuk A.I., ScD (Ukraine).

Address:

Astronomical Observatory, Odessa National University, E-mail: astronomical_observatory@onu.edu.ua
T. G. Shevchenko Park, Odessa, 65014, UKRAINE <http://www.astro-observ-odessa0.1gb.ua>
Tel.: + 38 048 722-84-42

The electronic version of the journal is on the web page: <http://oap.onu.edu.ua>

Одеські Астрономічні Публікації
Видається з 1946 року (видання відновлено в 1993 р., №6)

Свідоцтво про державну реєстрацію друкованого засобу масової інформації:

серія КВ № 14722-3693Р від 30.10.2008 р.

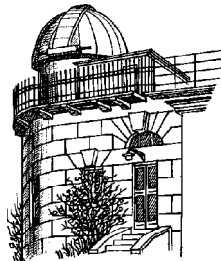
Журнал включено до списку МОН України наказом МОНУ № 1643 від 28.12.2019 р.

Друкується за рішенням Вченої ради НДІ "Астрономічна обсерваторія" Одеського національного університету імені І.І.Мечникова від 17 вересня 2020 р., протокол №6

Printed in UKRAINE
"PROMART" PUBLISHING COMPANY

ODESSA ASTRONOMICAL PUBLICATIONS

Volume 33
(2020)



CONTENTS

Balyshev M., Vavilova I. TO THE PERSONALITIES OF THE UKRAINIAN ASTRONOMY: SCIENTIFIC WORK OF KOSTYANTYN SAVCHENKO	5
--	---

Cosmology, gravitation, astroparticle physics, high energy physics

Khokhlov D.L. THE HOT DARK MATTER MODEL: FURTHER INVESTIGATION	11
Tsvilev A.P. ON THE QUESTION OF THE HELIUM ABUNDANCE IN ORION A MEASURED BY RADIO RECOMBINATION LINES. AND THE PRIMORDIAL HELIUM ABUNDANCE.	18
Tugay A.V., Zadorozhna L.V., Shevchenko S.Yu. DISCRETE X-RAY SOURCES IN GALAXY CLUSTERS	22

Astrophysics

Butkovskaya V.V., Plachinda S.I. PROBE OF THE MAGNETIC FIELD IN THE HOT SUPERGIANT ζ Per	25
Doikov D.N. INDUCING INTRINSIC γ -RAY EMISSION OF THE INTERSTELLAR MEDIUM BY INTENSE FLUXES OF PROTONS AND α -PARTICLES IN ACTIVE GALACTIC NUCLEI	28
Kudashkina L.S. MULTI-COMPONENT VARIABILITY OF PULSATING VARIABLE STARS OF RV TAURI TYPE	34
Mishenina T., Usenko I., Kniazev A., Kovtyukh V. HD 121135: FEATURES OF ITS CHEMICAL COMPOSITION	40
Nazarenko V.V. THE ON- AND OFF-STATE GENERATIONS IN CLASSICAL MICROQUASARS. 3-D NUMERICAL HYDRODYNAMICAL SIMULATIONS ON HIGH RESOLUTION GRID IN THE CASE OF INTERMEDIATE MASS TRANSFER RATE IN ACCRETION DISK OF MICROQUASAR CYG X-1	45
Plachinda S.I., Butkovskaya V.V. DETECTION OF EMERGENCE OF MAGNETIC FLUX TUBES IN THE PHOTOSPHERES OF DWARF 61 Cyg A, SUBGIANT β Aql AND GIANT β Gem	48
Udovichenko S.N., Keir L.E. PHOTOMETRY AND THE BLAZHKO EFFECT IN THE RR Lyr VARIABLE STAR Y Vul	53
Usenko I.A., Kniazev A.Yu., Katkov I.Yu., Kovtyukh V.V., Mishenina T.V., Miroshnichenko A.S., Turner D.G. SPECTROSCOPIC INVESTIGATIONS OF GALACTIC CLUSTERS WITH ASSOCIATED CEPHEID VARIABLES. IV. COLLINDER 220 AND UW CAR	58
Usenko I.A., Miroshnichenko A.S., Danford S., Kovtyukh V.V., Turner D.G. SPECTROSCOPIC INVESTIGATIONS OF THE POLARIS (α UMi) SYSTEM: RADIAL VELOCITY MEASUREMENTS, NEW ORBIT, AND COMPANION INFLUENCE FOR THE CEPHEID POLARIS Aa PULSATION ACTIVITY	65

Radioastronomy

Lytvynenko O.A., Panishko S.K. DISTRIBUTION OF THE OCCURRENCE OF THE INTENSIVE IONOSPHERE SCINTILLATIONS ON THE OBSERVATIONS OF THE COSMIC RADIO SOURCES AT THE DECAMETER WAVE RANGE	72
---	----

Sun, solar activity and astrobiology

Chornogor S.N., Kondrashova N.N. FEATURES OF THE DEVELOPMENT OF A CIRCULAR SOLAR FLARE	75
---	----

Isaeva E.A. RELATIONSHIP OF SCR, CME AND CORONAL SHOCK WAVES WITH THE PARAMETERS OF TYPE IV AND II SOLAR RADIO BURSTS	79
Krivodubskij V.N. THE ROLE OF MACROSCOPIC TURBULENT DIAMAGNETISM IN ENSURING LONG-TERM STABILITY OF SUNSPOTS	85
Lozitsky V.G., Osipov S.M., Stodilka M.I. ANOMALOUS WIDENING OF 5434.5 LINE IN SUNSPOTS: SUPER-STRONG MAGNETIC FIELDS?	89
Yakovkin I.I., Lozitsky V.G. ON THE POSSIBLE EXISTENCE OF SUPERSTRONG MAGNETIC FIELDS IN A LIMB SOLAR FLARE	93

Solar system

<u>Fashchevsky N.N.</u> , Podlesnyak S.V., Bondarenko Yu.N., Andrievsky S.M., Romanyuk Ya.O. A NEW WIDE-FIELD TELESCOPE WITH A MIRROR DIAMETER OF 600 MM FOR THE TELESCOPE NETWORK OF THE ODESSA OBSERVATORY	97
Gorbanev Yu.M., Konovalova N.A., Davruqov N.Kh. GROUPS OF METEORITE-PRODUCING METEORIODS AND METEORITES IN ASTEROIDAL ORBITS AND THEIR SOURCES	101
Kleshchonok V.V., Kashuba S.G., Andrievsky S.M., Gorbanev Yu.M. SPECIFIC FEATURES OF STRUCTURES IN THE INNER COMA OF COMET C/2017 T2 (PANSTARRS) AS OBSERVED WITH THE OMT-800 TELESCOPE OF THE ODESSA OBSERVATORY TELESCOPE NETWORK.....	105
Kolomiyets S.V., Kolomiets K.A., Kyrychenko I.Yu., Prymachov Yu.D. CENTENARY OF THE BIRTH OF THE FAMOUS UKRAINIAN RESEARCHER OF RADIOMETEORS PROF. B.L.KASHCHEYEV (1920-2004), HIS HERITAGE AND TRAJECTORY MEASUREMENTS TODAY.....	109
Kosaka N., Itoh Y., Saito T., Tozuka M., Endo T., Ando T. IMAGING POLARIMETRY OF GEOSTATIONARY SATELLITE EXPRESS-AM5	115
Koshkin N., Shakun L., Melikyants S., Korobeynikova E., Strakhova S., Bilinsky A., Vovchik Ye., Kudak V., Motrunich I., Neubauer I., Kozhukhov O., Romanyuk Ya., Ryabov A., Terpan S., Dragomiretsky V., Golubovskaya T. SIMULTANEOUS MULTI-SITE PHOTOMETRY OF LEO SATELLITES TO CHARACTERISE THEIR ROTATION STATES	119
Kulichenko M.O., Kaliuzhnyi M.P., Bushuev F.I., Shulga O.V., Malynovskiy Ye.V., Savchuk S.G., Yankiv-Vitkovska L.M., Hrudynin B.O. UKRAINIAN RADIO METEOR NETWORK — DEVELOPMENT AND FIRST RESULTS	125
Kulichenko M.O., Maigurova N.V., Shulga O.V. INVESTIGATION OF THE PHOTOMETRIC SYSTEM OF THE METEOR TV CCD CAMERAS	129
Kuznyetsova Y., Pavlenko Ya., Kulyk I., Zakhzhay O., Korsun P., Borysenko S., Krushevska V., Shubina O., Andreev M. SIGNATURES OF EXOCOMET ACTIVITY AROUND STARS AT DIFFERENT EVOLUTIONARY STAGES ...	133
Sukhov P.P., Sukhov K.P. DEGRADATION OF THE REFLECTANCE PROPERTIES OF SOME GSS IN SPACE, PRELIMINARY RESULTS ..	138

Astroinformatics

Khokhlov S.A., Miroshnichenko A.S., Zharikov S.V., Manset N., Zakhzhay O.V., Bilinsky I.O., Grankin K.N., Kusakin A.V., Omarov C.T., Kokumbaeva R.I., Reva I.V., Korčáková D., Usenko I.A., Kuratova A.K. THE EMISSION-LINE DUSTY OBJECT IRAS 07080+0605, A LESS-EVOLVED EXAMPLE OF THE RED RECTANGLE	141
Protsyuk Yu.I., Maigurova N.V. RE-REDUCTION OF THE OLD PHOTOGRAPHIC OBSERVATIONS OF INTERAMNIA (704) BASED ON GAIA DR2 REFERENCE CATALOGUE	147
Protsyuk Yu.I., Maigurova N.V. SOFTWARE FOR SEARCH AND MEASURING OF WDS CATALOG DOUBLE AND MULTIPLE STARS FROM DATABASE OF RESULTS OF CCD OBSERVATION	150
Shatokhina S.V., Relke H., Mullo-Abdolv A.Sh., Yizhakevych O.M., Yuldoshev Q.X., Protsyuk Yu.I., Andruk V.M. ASTEROID POSITIONS BASED ON THE DUSHANBE PART OF THE FON PROJECT OBSERVATIONS	154
Zolotukhina A.V., Pakuliak L.K., Vavilova I.B., Kaminsky B.M. UKRVO SPECTRAL PHOTOGRAPHIC ARCHIVE OF VARIABLE STARS	158

DOI: <http://dx.doi.org/10.18524/1810-4215.2020.33.216290>

UDK 929:521+521.35+523-52

TO THE PERSONALITIES OF THE UKRAINIAN ASTRONOMY: SCIENTIFIC WORK OF KOSTYANTYN SAVCHENKO

Marat Balyshev¹, Iryna Vavilova²

¹ Central State Scientific and Technical Archives of Ukraine, Kharkiv, Ukraine
m.a.balyshev@gmail.com

² Main Astronomical Observatory, National Academy of Science, Kyiv, Ukraine
irivav@mao.kiev.ua

ABSTRACT. The research is devoted to the study of the life and work of the outstanding Ukrainian astronomer-theoretician Kostyantyn Savchenko (1910–1956), who worked in the field of celestial mechanics and dynamic cosmogony at the Kharkiv and Odesa astronomical observatories in 1930–1950 years. As a result of historiographic analysis, we found that till now there is no comprehensive study of his scientific biography besides several publications related to certain facts of his life and activity, mostly in the Odesa period, including the reminiscences by Prof. V.K.Abalakin. Despite this, the vast majority of aspects of the scientist's life, including his scientific and teaching activity in the Kharkiv period in 1930s, remains unexplored.

The astronomer's scientific work was devoted to the study of the motion and rotation of celestial bodies with variable masses, the exploration of the perturbations of the planets by geometry methods, research of the physical nature of gravity, and the development of cosmogonic theories.

We consistently describe the life and activity of Prof. K.N.Savchenko at the Kharkiv and Odesa astronomical observatories, the scientific and teaching work at the Kharkiv State University, the Kherson State Pedagogical Institute, and the Odesa State University, analyzing the archive documents and his scientific publications.

Keywords: dynamic astronomy, minor planets, celestial mechanics, cosmogony, Kharkiv Astronomical Observatory, Odessa Astronomical Observatory.

АНОТАЦІЯ. У роботі оприлюднено основні віхи життя та творчості видатного українського астронома-теоретика К.М. Савченка, який працював у галузі небесної механіки та динамічної космогонії. На основі архівних документів наведено факти з біографії та проаналізовано основні етапи наукової роботи астронома, присвяченої дослідженню руху та обертання небесних тіл зі змінною масою, збурень планет методами геометрії, фізичної природи тяжіння, розробці космогонічних теорій про походження Сонячної системи.

Документально підтверджена наукова діяльність проф. К.М.Савченка в Харківській та Одеській астрономічних обсерваторіях, викладацька робота в Харківському державному університеті ім. О.М.Горького, Херсонському державному педагогічному інституті та Одеському державному університеті ім. І.І.Мечникова, проаналізовано його наукові публікації.

Ключові слова: динамічна астрономія, малі планети, небесна механіка, космогонія Сонячної системи, Харківська астрономічна обсерваторія, Одеська астрономічна обсерваторія.

1. Introduction

The personality of Professor Kostyantyn Savchenko (27.12.1910 Kherson – 29.11.1956 Odesa), who was a well-known astronomer-theoretician in celestial mechanics and dynamical cosmogony, still remains out of the scientific community. His scientific and lecturing activity is mostly related to the period of 1930s in Kharkiv and in 1944–1956 years in Odesa. The astronomer's scientific work was devoted to the study of the motion and rotation of celestial bodies with variable masses, the exploration of the perturbations of the planets by geometry methods, the calculation and correction of the elements of the orbits of asteroids of the main belt of the Solar system, the research of the physical nature of gravity, and the development of cosmogonic theories about the origin of the Solar system. He was deeply interested in the development of theoretical foundations for substantiating the Kant's cosmogonic hypothesis by the methods of celestial mechanics. Kostyantyn Savchenko had been dealing with this problem all his life, but he never published his manuscript.

We conducted historiographical analysis and testified to the absence of a comprehensive study aimed at reproducing the scientific biography of the astronomer. Some facts from the life and work of Prof. Savchenko can be found in a few biographical and memorial publications, in particular, by Abalakin (1975, 1995), Alexandrov et al. (2002), Zakhozhay (2002), Karetnikov (2005), Sharomova (2007), Vavilova et al. (2012), Bakhchynvanzhy (2015), Omelchuk (2017), Hrushytska (2017), Ivanchenko (2018) as well as in the monograph “200 years of astronomy at Kharkiv University” edited by Shkuratov (2008).

In view of the abovementioned, the aim of our work is to consistently describe the life and activity of Professor K.N. Savchenko (Figure 1) at the Kharkiv and Odesa astronomical observatories, the scientific and teaching work at the Kharkiv State University, the Kherson State Pedagogical Institute, and the Odesa State University analyzing the archive documents and various publications.



Figure 1: Professor K.N. Savchenko (1910–1956), theoretician in celestial mechanics and dynamic cosmogony

2. The life and scientific activity of Prof. K.N.Savchenko (Kherson and Kharkiv period of life)

Kostyantyn N. Savchenko was born on December 27, 1910 in Kherson in the family of the worker Nikolay I. Savchenko. In 1917, he entered the Kherson city elementary school for seven years; after graduating (1926) he studied at the Construction Department of the Industrial Vocational School.

In 1927, K. Savchenko entered the Faculty of Physics and Mathematics of the Kherson Institute of Public Education named after N.K. Krupskaya (KIPE). Being at the second grade of education, he began also to teach mathematics (at the Courses for Preparation for Higher Education providing by the City Committee of the Komsomol) and physics (at the Cooperative and Veterinary Vocational Schools) as well as to work as an Assistant Professor in physics at the KIPE (Archive of the V.N. Karazin Kharkiv National University (1936–1939), p. 2).

In 1931, after completing a full course of higher education at the KIPE, Savchenko K. became the post-graduate student of the Department of Celestial Mechanics of the Kharkiv Astronomical Observatory (KhAO), Kharkiv State University (KhSU). His scientific supervisor was Prof. Aleksey I. Razdolsky (1877–1942), the outstanding astronomer-theoretician (Shkuratov, 2008; Balyshev 2020c). He chose the topic of his dissertation under the influence of the well-known works by Prof. I.V. Meshchersky (1859–1935) on the gravitational dynamics of bodies with variable masses.

In 1934, Savchenko was appointed a Researcher at the KhAO. He also began teaching at KhSU as an Associate Professor of astronomy, in particular, he lectured theoretical astronomy and celestial mechanics at the Astronomical Department of the Faculty of Physics and Mathematics. Since the autumn semester of 1934, Savchenko annually went also to the Kherson and Poltava pedagogical institutes, where he lectured these courses as an Associate Professor (Archive of the Odessa I.I. Mechnikov National University, Personnel File of Savchenko K.N., p. 2).

At the Kharkiv Astronomical Observatory, Savchenko has concentrated his attention and skills on a number of topics and problems. Among them we note as follows: correction of the elements of the orbit of asteroids (89) Julia, (1115) Sabaud, and (1203) Nanna using the method by P. Hansen, as well as (1137) Raisa with taking into account perturbations by the method of mechanical conjugation; study of the series convergence for the decomposition of the perturbation function proposed by M.F. Subbotin (1922); study of the motion of bodies with variable masses; development of cosmogonic theories and other research (for example, Savchenko, 1935). In 1935, Kostyantyn Savchenko defended his dissertation “On the motion of celestial bodies, the mass of which changes over time”. The list of his publications to the dissertation is stored in the Archive of the Institute of Astronomy of the V.N. Karazin Kharkiv National University.

At that time, Kostyantyn Savchenko focuses his attention to elucidating the cosmogony problems, namely the main ways of scattering the substance of the gas-dust cloud, which did not enter the protoplanetary disks during their formation, filling the gaps between the orbits of these disks and their satellites. And he came to the conclusion that this substance plays a significant role in bringing the system to a stable form, but in the future – it’s dissipated by the same system just like “... as exhaust gas by the engine”. Savchenko believes that comets, from this point of view, are streams of matter that previously belonged to the gas-dust cloud, and arose due to the perturbed action of protoplanetary disks and they were pushed out of the Solar system. One of his first cosmogonic works, “On the question of the origin of the Solar system” (Savchenko, 1936) received a good response (Barabashov, 1936; Abalakin, 1975).

In the second half of the 1930s, his theoretical activity was aimed to solve problems on perturbed elements of planetary orbits by the geometrical method, theory of epicyclic motion, problem of two bodies, development of field theory by the geometric method (State Archive of the Kharkiv Region, p.10). The Figures 2 and 3 represent a collective of the Kharkiv astronomers (Shkuratov, 2008) with whom Savchenko has collaborated at those times.

During 1938–1939 years, Savchenko lectured on celestial mechanics and mathematical processing of observations for students of the Astronomical Department of the Physics and Mathematics Faculty of KhSU. Altogether with his wife, astronomer L.I. Krysenko (1907–1997), they traveled between Kharkiv and Kherson for a whole year, where they lectured for students at the KhSPI as part-time Associate Professors. On September 1, 1939, the Kharkiv period of life of Prof. Savchenko was over.

Savchenko began to work at the KhSPI, Kherson, as his main place of work, teaching courses in general astronomy and mathematical physics, and his wife in geophysics and physics. But till June, 1940, he continued to work as a Senior Researcher at the Kharkiv Astronomical Observatory. On July 5, 1940 Savchenko K.N. received a degree of Cand. Sci. and diploma of Associate Professor at the Mathematical Analysis Department (Archive of the Odessa I.I. Mechnikov National University, Personnel File of Savchenko K.N.). He followed study on theory of rotational motion of a solid body (Savchenko, 1939).



Figure 2: Astronomers of the Kharkiv observatory, early 1930s. From left to right, 1st row – Krysenko L.I., Razdolsky A.I., Evdokimov N.N., Barabashov N.P., Ostaschenko-Kudryavtsev B.P. and his daughter Zoya, Gerasimovich B.P., Parkhomenko P.G.; 2nd row – Zinkovsky K.N., Semeykin B.E. (?), Shyngarev L.I., Fadeyev Yu.N., Efimenko E.D., Sawron M.S., Mikhaylov V.A., Savchenko K.N., Inyakhin D.E., Salygin A.S.



Figure 3: Astronomers of the Kharkiv observatory, late 1930s. From left to right, 1st row – Ostaschenko-Kudryavtsev B.P., Razdolsky A.I., Evdokimov N.N., Slastenov A.I., Krysenko L.I.; 2nd row – Salygin A.S., Semeykin B.E. (?), Pluzhnikov V.H., Furdylo V.D., Savchenko K.N., Efimenko E.D., Fadeyev Yu.N., Parkhomenko P.G.

The war separated the astronomical Savchenko-Krysenko family. In particular, yet in January, 1941, she came back to Kharkiv because of the deterioration of her mother's health. The last letter from the husband, Savchenko K.N., she received on July, 1941, from whom she learned that he had been drafted into the Red Army. From the memoirs by K.N. Savchenko about the events of the war period: *"In July 1941, a group of teachers from the Kherson institute, who did not serve in the army and had no military training, was sent to organize dig trenches around Mykolaiv. Coming back to Kherson after this work (August 17, 1941), we were detained by the German troops but released after a two-day stay in the camp. During the German occupation of Kherson, I worked as a watchmaker in the artel of the Kustprom. On November 3, 1943, the German command ordered all the men to gather at the P.O.W. camp (Kherson city prison) that meant the general evacuation of all the men to Germany. Trying to avoid it, I fled to Odessa, where I got a job as a watchmaker in one of the private workshops, and worked there until the liberation of the city by the Red Army"* (Archive of the Odesa I.I. Mechnikov National University, Personnel File of Savchenko K.N.).

3. The life and scientific activity of Prof. K.N.Savchenko (Odessa period of life)

Prof. K.D. Pokrovsky (1868–1944), at that time the Director of the Odessa Astronomical Observatory (OAO) of the Odessa State University (OSU), helped K.N. Savchenko to settle in occupied Odessa (watch workshop was placed on the territory of the observatory). At the suggestion of Pokrovsky, Savchenko began working at the OAO since April, 1944, as a Senior Researcher. A statement by K.N. Savchenko, dated April 15, 1944, from his Personnel File: *"From 1934 to 1941, I worked as an astronomer at the Kharkiv Astronomical Observatory and Associate Professor at Kharkiv University, lecturing on celestial mechanics and mathematical processing of observations. During this time I also lectured at the Kherson Pedagogical Institute, where taught general astronomy and theoretical mechanics"*. According to this Personnel File, the fact of his work at KhSU was confirmed by two former lecturers I.G. Wittenzon (1902–1969) and G.M. Mirakyan (1907–1964), who found themselves in post-war Odessa as employees of the re-evacuated Hydrometeorological Institute. It should be noted that these colleagues were not only well acquainted with Konstantin Nikolaevich in teaching at the university (in the 1920s – active members of the Kharkiv Astronomical Club), but also had common scientific interests. For example, Wittenzon also dealt with the problems of dynamics of bodies of variable masses.

In May 1944, Prof. K.D. Pokrovsky was arrested by the NKVD under Art. 54–1 (parricide). Six months after he died in an NKVD prison (Archive of the Office of the Security Service of Ukraine in the Odessa region (1944)).

So, having found himself in Odessa after severe wartime hardships, in April, 1944, Savchenko K.N. began to work at the Odessa Astronomical Observatory as a Senior Researcher, later on as a Head of the Department of Theoretical Astronomy (Karetnikov, 2005). In October 1, 1944, Savchenko was appointed an Associate Professor of Astronomy at the OSU (Archive of the Odesa I.I. Mechnikov

National University, K. M. Savchenko, 1956, p. 34).

In 1945, Savchenko K.N. took part in the Jubilee Astronomical Conference dedicated to the 100th anniversary of the Astronomical Observatory of the Kyiv University. Circumstances of wartime did not prevent well-known astronomers, representatives of many observatories, to go to Kyiv. Scientific reports at the conference from Odessa were made by Prof. V.P. Tsesevich (1907–1983) and K.M. Savchenko. He presented a report "On the nature of gravity", the main postulate of which was a critique of Einstein's General Relativity Theory. In his opinion, for the theory of relativity, gravity remains a hidden property of matter, which it directs to the geometric properties of space. Based on these assumptions, Savchenko considered the gravitational interaction from other positions, focusing on the comparison of certain positions of the wave-mechanical hypothesis of the Gravity Law and the General Relativity. The full text of presentation was later published in the "Vedomosti of the Odessa Astronomical Observatory" (Savchenko, 1949).

In 1946–1947, in order to prepare his doctoral dissertation, K.N. Savchenko continued to develop the theoretical research on the cause of gravity (scientific and theoretical problem of philosophy). He prepared a manuscript of a monograph on "The Nature of Gravity" (not published), which covered in detail the history of the issue. In this work, Savchenko abandoned the critique of A. Einstein's theory, proposing his own wave hypothesis of gravity "Interference of de Broglie waves" and predicted its astronomical consequences. Note that the main positions of the new hypothesis were presented by the author at many scientific events.

In February 1948, Savchenko K.N. defended his doctoral dissertation "The experience of qualitative substantiation of Kant's cosmogony hypothesis"; a year later, in October 1949, by the decision of the Higher Attestation Commission he was approved in the academic title of Doctor of Physical and Mathematical Sciences, and in 1952 was awarded in the title of Professor (Archive of the Odesa I.I. Mechnikov National University of Odessa (1944–1956), p. 15–18).

After Savchenko's defense, two astronomical departments were established at the Faculty of Physics and Mathematics: the Department of Astrophysics (headed by Prof. V.P. Tsesevich, who was the Dean of the Faculty) focused on cooperation with the Department of Physics, and the Department of Astronomy focused on cooperation with the Department of Mathematics. In 1949, Savchenko was approved as a Head of the Department of Astronomy (since 1950 on a permanent basis) and in 1953 he headed the joint Department of Astronomy and Theoretical Mechanics in this university (ibid, p. 31–32). He lectured many different courses, led a student research group, and was a supervisor of post-graduate student's works. Among the courses Savchenko K.N. taught as follows: "Spherical and Theoretical Astronomy", "Celestial Mechanics", "Mathematical Theory of Planetary Figures", "Higher Geodesy", "Theory of Tides", "Dynamic Cosmogony", and "History of Astronomy". Later on he began to give lectures on theoretical mechanics on a part-time basis at the Odessa Higher Maritime Academy (ibid, p. 41–44).

In 1954, K.N. became an Editor-in-Chief of the "Vedomosti of the Astronomical Observatory of Odessa State University" (now – "Odessa Astronomical Publications").

Among the scientific works by K.N. Savchenko during

the Odesa period of life it is necessary to note the following: “Kepler’s problem”, “On the motion of the centers of copulation of new stars”, “On the origin of the satellites of the planets by gravitational capturing”, “On the stability of local dust clusters in nebulae”, “On some questions of non-classical celestial mechanics and cosmogony”; monograph “Essays on celestial mechanics” and the textbook for students “The beginning of the mechanics of the Solar system (Course of Celestial Mechanics)” (Duboshin, 1968).

In 1954, Savchenko K.N. completed a generalized work, the monograph “Kant’s cosmogony and the problem of the origin of minor bodies of the Solar system” (Savchenko, 1975), in which he proposed his own cosmogonic concept. But this book as well as the most of Savchenko’s scientific works remained in manuscripts and were not published, as the astronomer died suddenly on November 29, 1956, after a heart attack.

One of his post-graduate students, later on an outstanding world-well-known astronomer in field of celestial mechanics, Prof. Viktor K. Abalakin wrote: “... *From numerous, rather frank, conversations with K.N. Savchenko, his personality was emerged as the talented, original, and versatile scientist, the intellectual-nugget type of a-self-made-man, who went through arduous and difficult life path in Soviet times*” (Abalakin, 1995). The monograph “Kant’s cosmogony and the problem of the origin of minor bodies of the Solar system” was issued only in 1975 due to the efforts of Prof. V.K. Abalakin.

4. Conclusion

Professor K.M. Savchenko successfully worked in the field of dynamic astronomy and cosmogony, focusing on the problems of non-classical celestial mechanics. He conducted research at the top level of those times at the Kharkiv and Odesa astronomical observatories as well as lectured at the universities in Kharkiv, Odesa, Kherson. The main field of Savchenko’s scientific interest was a cosmogony. Investigation of his publications related to the origin of minor bodies of the Solar system requires a deeper analysis and will allow us to understand a worldwide of this outstanding Ukrainian astronomer of the first half of the XX century (Balyshv, 2021).

We assume that the materials of historical and biographical research of the life and work of Prof. Savchenko could be used among others personalities when studying the history of astronomy in Ukraine. Among such papers we note essays about Orlov A.Ya. (Yatskiv et al., 2005a, 2012; Volianskaia et al., 2005), Fedorov E.P. (Korsun’, 1989) and Braude S.Ya. (Vavilova et al., 2007), dynasties by Knorre (Pinigin, 2009) and Struve (Krisciunas, 1988; Artemenko et al., 2009), scientists who worked in field of the General Relativity (Yatskiv et al., 2005, p. 194–237; 2017), recent publications dedicated to Tsesevich V.P. (Andronov, 2017; Vavilova, 2017) as well as series of papers about the Kharkiv astronomers as Otto Struve (monograph by Balyshv, 2008; Balyshv, 2007), P. Parkhomenko (Balyshv, 2018a), B. Semeykin (Balyshv, 2018b, 2018c), M. Sawron (Balyshv, 2020a), A. Razdolsky (Balyshv, 2020b) etc. Among the works of a general overview related to the “Astronomers – Ukraine” we note biographical encyclopedia by Kolchinskij et al. (1986) and Vavilova &

Plachinda (2003), series of books about the Odesa astronomers edited by Karetnikov (1994) (see, also, Korpun & Tsesevich (1956), Mykolaiv astronomers edited by Pinigin (1998), Kyiv astronomers by Kazantseva & Kislyuk (2006), Crimean astronomers by Polosukhina (2011), L’viv astronomers edited by Novosyadlyj (2011), and fundamental monograph “200 years of astronomy at Kharkiv University” edited by Shkuratov (2008) where numerous papers are collected about scientific school by Prof. N.P. Barabashov (see, also, Yatskiv & Vavilova, 2011).

The most of biographies of the Ukrainian astronomers are available at the web-site of the Ukrainian Virtual Observatory: <http://ukr-vo.org/personalities/index.php?b&6> (Vavilova et al., 2014) as well as some of well-known personalities are included into the biographical encyclopedias of astronomers (for example, Lankford, 1996; Krisciunas, 2004; Hockey, 2007, 2013).

References

- Archive of the Institute of Astronomy V. N. Karazin Kharkiv National University (1931–1939). [in Ukrainian].
- Archive of the Odessa I.I. Mechnikov National University (1944–1956). Inv. of D.E.T. in 1956. Personnel File by Savchenko K. M., 48 p. [in Russian].
- Archive of the Odesa I.I. Mechnikov National University; K. M. Savchenko. For scientific cadres. 1956. No 37. December 5, 4 [in Ukrainian].
- Archive of the Office of the Security Service of Ukraine in the Odesa region (1944). Archive-criminal File № 26277-p on Pokrovsky K.D. (1868-1944). Vol. 1. P. 48–320.
- Archive of the V.N. Karazin Kharkiv National University (1936–1939). Inv. of D.E.T. in 1933–1941, Case File No. 278, 4 p. [in Ukrainian].
- Let’s not forget, we remember: employees of Odesa I.I. Mechnikov National University during the Second World War (2015). Eds. A.P. Bakhchivanzhy, A.S. Lozheshnik. Odesa, 437 p.
- Nikolaev Astronomical Observatory. Stellar Way in 175 years: 1821-1996 (1998). Ed. G.I. Pinigin. Nikolaev.
- Pages of History of Astronomy in Odessa (1994). Part I, Ed. V. G. Karetnikov. Odessa. [in Russian].
- State Archive of the Kharkiv Region (1938). F. r-5875. In. 1. C. 16. P. 10. [in Russian].
- The History of the Astronomical Observatory of Ivan Franko National University of L’viv (2011). Ed. B. Novosyadlyj. LNU, L’viv.
- The Names of Ukraine in Space (2003). Eds. I. B. Vavilova and V. P. Plachinda. K., VAITE (see, also, Vavilova I.B. (2006): *Innovation in Teaching/Learning Astronomy Methods*, IAU Special Session, 2.
- Abalakin, V. K. (1975): Konstantin Nikolaevich Savchenko. In: The problems of the origin of the bodies of the Solar system, pp. 3–6. M.–L.: AS USSR [in Russian].
- Abalakin, V. K. (1995): Professor K. N. Savchenko. In: V.G. Karetnikov (Ed.) Pages of the history of astronomy in Odessa. Part 2, pp. 33–39. Odessa [in Russian].
- Alexandrov Yu.V., Dudinov V.N., Zakhzhay V.A. (2002): *Astronomical School’s Report*, 3, 2, 5. DOI: 10.18372/2411-6602.03.2005.
- Andronov, I. L. (2017): *Odessa Astron. Publ.*, 30, 252. DOI: 10.18524/1810-4215.2017.30.118686

- Artemenko, T. G., Balyshev, M. A., Vavilova, I. B. (2009): *Kinemat. Phys. Celest. Bodies*, **25**, 3, 153. DOI: 10.3103/S0884591309030040
- Balyshev, M. A. (2007): *Istoriko-Astronomicheskie Issledovaniya*, **32**, 138.
- Balyshev, M.A. (2008): Otto Ludwigovich Struve, 1987–1963. Moscow, Nauka.
- Balyshev, M. A. (2018a): *Science and Science of Science*, **1**, 114. DOI: 10.15407/sofs2018.01.114.
- Balyshev, M. A. (2018b): *Kinemat. Phys. Celest. Bodies*, **34**, 2, 98. DOI: 10.3103/S0884591318020022
- Balyshev, M. A. (2018c): *Istoriko-Astronomicheskie Issledovaniya*, **40**, 127.
- Balyshev, M. A. (2020a): *Science and Science of Science*, **2**, 96. DOI: 10.15407/sofs2020.02.096.
- Balyshev, M. A. (2020b): *Studies in History and Philosophy of Science and Technology*, **29**, 1, 44. DOI: 10.15421/272006.
- Balyshev, M. A. (2020c): *Science and Science of Science*, **3**, 92. DOI: 10.15407/sofs2020.03.092
- Balyshev M.A. (2021): *Kinemat. Phys. Celest. Bodies*, **37**, 2 (accepted)
- Barabashov, M. P. (1936): *Astron. Zh.*, **13**, 282 [in Russian].
- Duboshin, G.N. (1968): Celestial Mechanics. Mechanics in the USSR for 50 years. Vol. 1 “General and Applied Mechanics”. Moscow, Nauka, 416 p.
- Ivanchenko, A. V. (Ed.). (2018): The scientists of the universities of Odessa: a bibliography. Issue 2 Natural Science. Part 4 (1946–2017). Physicists. Astronomers. Odessa, ONSL, 256 p. [in Ukrainian].
- Hockey, T., Trimble, V., Williams, Th. R. et al. (2007). The Biographical Encyclopedia of Astronomers, Set of 2 volumes, A-L and M-Z. New York, Springer.
- Hockey, T., Trimble, V., Williams, Th. R. et al. (2013): The Biographical Encyclopedia of Astronomers, Set of 2 volumes, A-L and M-Z. New York, Springer.
- Hrushytska, I.B. (2017): Odesa Astronomical Observatory in postwar years. *Sci. papers of the Historical Faculty of Zaporizhzhya National University*, **49**, 268. DOI: 10.26661/swfh-2017-49-051 [in Ukrainian].
- Karetnikov, V. G. (2005): Savchenko Konstantin Nikolaevich. Astronomer. In: Professors of Odessa (Novorossiysk) University: biographical dictionary. Vol. 4: «R–Ya», pp. 52–53. Odessa: Astroprint [in Ukrainian].
- Kazantseva L.V., Kislyuk V. S. (2006): Kyiv Window into Space: the History of Kyiv Astronomical Observatory in the Context of the History of Progress of National and World Science. Kyiv, Nash chas [in Ukrainian].
- Kolchinskij, I. G., Korsun', A. A., Rodrigues, M.G. (1986): Astronomers. Biographical Handbook. Second supplemented and revised edition. Kiev, Naukova Dumka, 512 pp. [in Russian].
- Korpun Ya. Yu. & Tsevevich, V. P. (1956): *Istoriko-Astronomicheskie Issledovaniya*, **2**, 289.
- Korsun', A. A. (1989): *Istor.-Astron. Issled.*, **21**, 327.
- Krisciunas, K. (2004): Name Index to *Sky and Telescope*, vol. 1, no. 1 (Nov. 1941) to vol. 108, no. 6 (Dec. 2004).
- Lankford, J. (1996): History of Astronomy: An Encyclopedia (Garland Encyclopedias in the History of Science, vol. 1. New York, Garland.
- Omelchuk, S.A., Samsakova, I.V. (2017): *Tavriysky visnyk osvity*, **2**, 5 [in Ukrainian].
- Pavlenko, Ya. V., Vavilova, I. B., Kostiuk, T. (2006): Astronomy in Ukraine. In: Organizations and Strategies in Astronomy, Vol. 7. Ed. A. Heck. Springer, Dordrecht, the Netherlands, p. 71. DOI: 10.1007/978-1-4020-5301-6_4.
- Pinigin, G. (2009): *Astron. Nach.*, **330**, 6, 578. DOI: 10.1002/asna.200911220
- Polosykhina, N. S. (2011): Crimean Astrophysical Observatory. Foundation, Development, Prosperity. Simferopol, Business-Inform.
- Savchenko, K. M. (1935): *Bull. of the Astron. Observatory of Kharkiv State University*, **3**, 2 [in Ukrainian].
- Savchenko, K. M. (1936): *Ucheni zapysky Kharkiv derzhavnogo universytetu*, **6–7**, 25.
- Savchenko K.M. (1939): Theory of rotational motion of a solid body of variable masses. In: “Scientific notes of the Kherson State Pedagogical Institute”.
- Savchenko K.N. (1949): *Vedomosti of the Odessa Astronomical Observatory*.
- Savchenko, K. N. (1975): Kant’s cosmogony and the problem of origin of minor bodies of the Solar system. *Probl. proiskhozhhd. tel soln. sist.*, p. 8 – 243.
- Sharomova, V. (2007): Savchenko K.M. In: Ukrainian Physicists and Astronomers: textbook. Ternopil, p. 212.
- Shkuratov, Y. G. (Ed.). (2008): 200 years of astronomy at Kharkiv University. Kharkiv: Kharkiv V.N. Karazin National University, 632 p. [in Russian].
- Subbotin, M. (1922): *MNRAS*, **82**, 383. DOI: 10.1093/mnras/82.6.383
- Vavilova, I. B.; Konovalenko, A. A.; Megn, A. V. (2007): *Astron. Nach.*, **328**, 5, 420 DOI: 10.1002/asna.200710762
- Vavilova, I. B., Artemenko, T. G., Pakuliak, L. K. (2012): *Kinemat. Phys. Celest. Bodies*, **30**, 1, 46. DOI: 10.3103/S0884591314010073
- Vavilova, I. B. (2017): *Odessa Astron. Publ.*, **30**, 256. DOI: 10.18524/1810-4215.2017.30.118718
- Volianskaia, M. Yu., Karetnikov, V. G., Mandel, O. E. (2005): *Odessa Astron. Publ.*, **18**, 138.
- Zakhochay, V.A. (2002): *Astronomical School's Report*, **3**, 26. DOI: 10.18372/2411-6602.03.2026.
- Yatskiv, Ya. S., Korsun', A. A., Vavilova, I. B. (2005a): *Kinemat. Fiz. Neb. Tel*, **21**, 6, 403.
- Yatskiv, Ya. S., Alexandrov, A. N., Vavilova, I. B. et al. (2005b). General Relativity theory: tests through time. Kyiv, MAO NAS of Ukraine, 288 p. ISBN 966-02-3728-6
- Yatskiv, Ya., Vavilova, I.B. (2011): IAU Symposium, **260**, 696. DOI: 10.1017/S1743921311003048
- Yatskiv, Ya. S., Vavilova, I. B., Korsun', A. A. (2012): *Odessa Astron. Publ.*, **25**, 74.
- Yatskiv, Ya. S., Vavilova, I. B., Romanets, O. A., Savchuk, V.S. (2017): *Space Sci. & Tech.*, **23**, 3, 64. DOI: 10.15407/knit2017.03.064.

COSMOLOGY, GRAVITATION, ASTROPARTICLE PHYSICS, HIGH ENERGY PHYSICS

DOI:<http://dx.doi.org/10.18524/1810-4215.2020.33.216299>THE HOT DARK MATTER MODEL:
FURTHER INVESTIGATION

D.L. Khokhlov

Sumy State University (Retired),
Ukraine, dlkhokhl@rambler.ru

ABSTRACT. In a recent paper, the model of the galaxy with hot dark matter was considered. The galaxy is divided into the inner region with the dominant baryonic matter (the elliptic orbit of the test particle) and the outer region with the dominant hot dark matter (the parabolic orbit of the test particle). It was assumed that the hot dark matter consists of hypothetical Planck neutrinos arising in the decay of the protons at the Planck scale. Galaxies formed from the baryonic matter, and the hot dark matter appears in the galaxies later. The rotation curves of the galaxies were studied in the model, including Milky Way, M33, NGC 2366 and IC 2574. In the present paper, the hot dark matter model is further investigated, with the application to M31, the system of M31 and the Milky Way, the globular clusters NGC 2419 and MGC1, the dwarf spheroidal galaxy Sculptor, ultra-massive quiescent galaxies from the COSMOS and UDS fields. The baryonic matter mass of M31 was estimated from the rotation curves, with the average value $1.6 \times 10^{11} m_{\odot}$. The gravitational interaction of the Milky Way and M31 is considered. In the hot dark matter model, the dynamical masses of the Milky Way and M31 are twice their baryonic matter masses that gives the radial velocity of M31 toward the Milky Way, 106 km s^{-1} . The hot dark matter mass in the globular clusters NGC 2419 and MGC1 is estimated. The value is small compared to the stellar mass in both the clusters. The hot dark matter mass within the half-light radius of the dwarf spheroidal galaxy Sculptor is estimated, $0.5 \times 10^6 m_{\odot}$. The sum of the stellar and hot dark matter mass within the half-light radius is consistent with the dynamical mass within the half-light radius of the Sculptor derived from the kinematics of the metal rich stars. The instability of the baryonic matter due to the influence of the hot dark matter and some perturbations flattens the velocity profile of the metal poor stars which is unsuitable to derive the dynamical mass. The evolution of ultra-massive quiescent galaxies from the COSMOS and UDS fields is considered. The dynamical to stellar mass relation is doubling during the evolution from $z = 2$ to 0 that

can be explained by the absence of dark matter at $z = 2$ and the presence of the hot dark matter at $z = 0$.

Keywords: dark matter; galaxies: kinematics and dynamics; galaxies: dwarf; globular clusters: general.

АНОТАЦІЯ. В недавній статті нами розглядалася модель галактики з гарячою темною матерією. Галактика розділена на внутрішню область з переважно баріонної матерії (еліптична орбіта пробної частинки) і зовнішню область з переважно гарячою темною матерією (параболічна орбіта пробної частинки). Припускається, що гаряча темна матерія складається з гіпотетичних Планківських нейтрино, що виникають у розпаді протонів на Планковській шкалі. Галактики формуються з баріонної матерії, а гаряча темна матерія з'являється в галактиках пізніше. Криві обертання галактик вивчалися в рамках моделі, в тому числі Чумацький Шлях, M33, NGC 2366 і IC 2574. У даній статті продовжено вивчення моделі з гарячою темною матерією стосовно M31, системи M31 і Чумацького Шляху, кулястих скупчень NGC 2419 та MGC1, карликової сфероїдальної галактиці Скульптор, ультрамасивних пасивних галактик з полів COSMOS та UDS. Маса баріонної матерії у M31 була оцінена з кривих обертання, середня величина $1.6 \times 10^{11} m_{\odot}$. Розглядалася гравітаційна взаємодія Чумацького Шляху та M31. У моделі з гарячою темною матерією динамічні маси Чумацького Шляху і M31 у два рази більше маси баріонної матерії, що дає радіальну швидкість M31 у напрямку Чумацького Шляху, 106 км с^{-1} . Була оцінена маса гарячої темної матерії в кулястих скупченнях NGC 2419 та MGC1. Її величина невелика у порівнянні із зоряною масою в обох скупченнях. Маса гарячої темної матерії всередині ефективного радіуса карликової сфероїдальної галактики Скульптор була оцінена як $0.5 \times 10^6 m_{\odot}$. Сума зоряної маси і маси гарячої темної матерії всередині ефективного радіуса узгоджується з динамічною масою всередині ефективного радіуса галактики

Скульптор, отриманої з кінематики зірок з високим вмістом металів. Нестабільність баріонної матерії, яка викликана гарячою темною матерією і деякими збуреннями, призводить до плоского профілю швидкостей зірок з низьким вмістом металів, який не підходить для отримання динамічної маси. Розглядалася еволюція ультрамасивних пасивних галактик з полів COSMOS та UDS. Відношення динамічної і зоряної мас подвоюється протягом еволюції від $z = 2$ до 0, що можна пояснити відсутністю темної матерії при $z = 2$ і наявністю гарячої темної матерії при $z = 0$.

Ключові слова: темна матерія; галактики: кінематика і динаміка; галактики: карликові; кулясті скупчення: загальне.

Introduction

The flat rotation curves of spiral galaxies can be explained by the presence of dark matter (DM), e.g. (Battaner & Florido, 2000) and references therein. The modified Newtonian gravity (MOND) (Famaey & McGuagh, 2012) gives another explanation. DM is a main component ($\sim 85\%$) in the universe (Ade et al., 2016). The nature of DM is thought to be non-baryonic (Trimble, 1987). There is a belief that DM was present in the early universe and took part in the structure formation (Trimble, 1987). Observational constraints on the structure formation give support to the models with cold dark matter (CDM) and disfavour those with hot dark matter (HDM). All the known particle species are not suitable for the CDM candidates. Among the proposed CDM candidates, the most popular are weakly interacting massive particles (WIMPs) (Bertone & Tait, 2018). Attempts to detect WIMPs in several experiments have failed (Marrodán Undagoitia & Rauch, 2016; Liu et al., 2017).

The rotation curves of massive star-forming galaxies at $0.6 \leq z \leq 2.6$ from the KMOS^{3D} and SINS/zC-SINF surveys show a fall-off beyond the turnover (Lang et al., 2017). The discs of these galaxies are strongly baryon dominated (Genzel et al., 2017). This is in contrast to the flat rotation curves of local spiral galaxies of similar masses. Several studies of observed high redshift galaxies (Tanaka et al., 2019; Casey et al., 2019; Stockmann et al., 2020) found the dynamical to stellar mass relation, $m_{dyn}/m_* \sim 1$. The EDGES collaboration reported the detection of 21 cm absorption at $z \approx 17$ (Bowman et al., 2018). The observed signal is about twice the value predicted in the Λ CDM model. The EDGES result can be explained in a universe devoid of DM, with the baryon fraction 100% (McGaugh, 2018).

The foregoing data imply the absence of DM in the universe at high redshifts above $z \sim 2$. In this case, the galaxies formed from the baryonic matter (BM),

and the DM come there later. As such, there is no restrictions on the models with HDM from the structure formation.

DM may emerge in the decay of the protons (Khokhlov, 2015). The mode of the decay of proton at the Planck scale into positron and hypothetical Planck neutrinos, $p \rightarrow e^+ 4\nu_{Pl}$, was suggested in Khokhlov (2011c). The process was studied for the protons falling onto the gravastar, by giving an example of Sgr A* while interpreting Sgr A* as a gravastar (Khokhlov, 2014, 2017). Planck neutrino can be classified as a HDM candidate.

The standard cosmology is considered within the framework of the Λ CDM model (Ostriker & Steinhardt, 1995). It complies with the observations on large scales (Reyes et al., 2010), see however (López-Corredoira, 2017) and references therein. Also, observational constraints from the density perturbations in the range $10^6 - 10^{15} m_\odot$ give the preference to the model with the dominant HDM fraction rather than the Λ CDM model (Demiański & Doroshkevich, 2017). The standard cosmology is in contrast to the electrodynamics in the laboratory frame (Khokhlov, 2013). An alternative model of the universe was developed in Khokhlov (2011a,b). Testing the Λ CDM model on galaxy scales reveals several problems, e.g. (Weinberg et al., 2015; Kroupa, 2012, 2015) and references therein.

In a recent paper (Khokhlov, 2018), the model of the galaxy with HDM was considered. The HDM was treated as a gas of hypothetical Planck neutrinos, arising from the decaying BM. It was assumed that only BM took part in the galaxy formation, and the HDM appears in the galaxies later. The proposed model was successfully tested on the galaxies: Milky Way, M33, NGC 2366 and IC 2574. In the present paper, we shall further investigate the HDM model, with the application to M31 (Andromeda galaxy), the system of M31 and the Milky Way, the globular clusters NGC 2419 and MGC1, the dwarf spheroidal galaxy Sculptor. Also, we shall consider the evolution of ultra-massive quiescent galaxies from $z = 2$ to 0.

1. The HDM model of the galaxy

We shall review the HDM model of the galaxy presented in Khokhlov (2018). Assume that the HDM consists of hypothetical Planck neutrinos arising in the decay of the protons at the Planck scale, $p \rightarrow e^+ 4\nu_{Pl}$ (Khokhlov, 2011c). Planck neutrino is specified as a massless particle propagating with the speed of light (Khokhlov, 2011c). Therefore, Planck neutrinos do not form a condensed structure. Assume that the galaxy is formed from the BM, and the HDM comes there later.

Consider the BM of the galaxy embedded into the HDM. The circular velocity of the test particle at the

radius r is defined by the BM mass and the HDM mass (energy) within the radius r as

$$v_c^2 = \frac{G(m_b(< r) + m_{hdm}(< r))}{r} \quad (1)$$

where G is the Newton constant, $m_b(< r)$ is the BM mass within the radius r , $m_{hdm}(< r)$ is the HDM mass within the radius r . The radial velocity of the test particle at the radius r is defined by the HDM pressure

$$v_r^2 = \frac{2Gm_{hdm}(< r)}{r}. \quad (2)$$

The energy of the test particle of the unity mass is given by

$$E = \frac{1}{2}v_r^2 + \frac{1}{2}v_c^2 - \frac{G(m_b(< r) + m_{hdm}(< r))}{r}. \quad (3)$$

The energy eq. (3) defines the motion of the test particle in the galaxy with HDM.

The distribution of the HDM is supposed to be homogeneous, with the HDM $\rho_{hdm} = const$ and the HDM mass $m_{hdm}(< r) \propto r^3$. The galaxy is divided into the inner region with the dominant BM and the outer region with the dominant HDM. The border between the regions at some radius r_0 is defined by the equality of the HDM and BM mass, $m_{hdm}(< r_0) = m_b(< r_0)$. In the inner region $r < r_0$, the energy of the test particle is negative, $E < 0$, that defines the elliptic orbit of the test particle (Landau & Lifshitz, 1960). In the outer region $r \geq r_0$, the energy of the test particle is equal zero, $E = 0$, that defines the parabolic orbit of the test particle (Landau & Lifshitz, 1960). The stability of the structure of the galaxy implies that the HDM perturbation does not exceed the BM gravitational potential. Hence, the enclosed dynamical mass is limited by the double baryonic mass enclosed. In the outer region $r \geq r_0$, the enclosed dynamical mass is the double baryonic mass enclosed, $m_{dyn}(< r) = 2m_b(< r)$.

2. Observational constraints on the model of M31

The rotation curve of M31 was under study in several works (Geehan et al., 2006; Seigar et al., 2008; Chemin et al., 2009; Corbelli et al., 2010; Tamm et al., 2012). From ~ 10 kpc to ~ 30 kpc, it is approximately flat, decreasing from ~ 250 km s $^{-1}$ to ~ 220 km s $^{-1}$. Above ~ 30 kpc, the rotation curve is decreasing (Tamm et al., 2012). The models of the rotation curve include the mass components: the bulge, the stellar disc and the DM halo. Besides, the mass of the gas is added in Chemin et al. (2009); Corbelli et al. (2010).

Consider the HDM model of M31. We need to define the radius r_0 of the border between the inner and outer

regions in M31. In Khokhlov (2018) the radius r_0 was determined through the features in the anisotropy profile in the Milky Way, in the curve of the position angle in M33, NGC 2366, in the curve of the inclination in IC 2574. Two warps of the disc in M31 can be seen from the curves of inclination and position angle (Chemin et al., 2009). The location of the second warp have been reported by several authors, using the HI data: $r > 18$ kpc (Henderson, 1979; Brinks & Burton, 1984), $r > 25$ kpc (Corbelli et al., 2010), $r > 27$ kpc (Chemin et al., 2009), $r > 28.5$ kpc (Newton & Emerson, 1977), and the optical data: $r > 20.5$ kpc (Walterbos & Kennicutt, 1988), the values are rescaled to the distance to M31, 785 kpc (McConnachie et al., 2005). Assume that the second warp of the disc in M31 exhibits the transition to the outer region. Adopt the radius of the border between the inner and outer regions in M31, $r_0 = 19$ kpc. The BM and HDM masses are equal at $r_0 = 19$ kpc.

Estimate the BM mass of M31 from the circular velocity at $r_0 = 19$ kpc. The rotation curve in Corbelli et al. (2010) gives the circular velocity, $v(r_0) = 238$ km s $^{-1}$. From this, the BM circular velocity is estimated to be $v_{bm}(r_0) = v(r_0)/\sqrt{2} = 168$ km s $^{-1}$, and the BM mass, $m_b(< r_0) = 1.25 \times 10^{11} m_\odot$. Beyond ~ 20 kpc, the fraction of the luminous mass in M31 is estimated to be $\sim 10\%$ (Ibata et al., 2005). Then, the total BM mass of M31 can be estimated as $m_b = 1.4 \times 10^{11} m_\odot$. The rotation curve in Chemin et al. (2009) gives the circular velocity, $v(r_0) = 252$ km s $^{-1}$. From this, the BM circular velocity is estimated to be $v_{bm}(r_0) = v(r_0)/\sqrt{2} = 178$ km s $^{-1}$, and the BM mass, $m_b(< r_0) = 1.4 \times 10^{11} m_\odot$. By adding $\sim 10\%$, the total BM mass of M31 is $m_b = 1.5 \times 10^{11} m_\odot$.

At $r_0 = 19$ kpc, the radial velocity is equal to the circular velocity. The radial velocity can be calculated through the radial velocity dispersion as $v_r = 2\sigma_r$. Chapman et al. (2006) reported the radial velocities of the red giant branch stars in M31 in the range 10 – 70 kpc. The radial velocity dispersion at 19 kpc is $\sigma_r = 135$ km s $^{-1}$ (Chapman et al., 2006) that gives the radial velocity, $v_r = 270$ km s $^{-1}$. Adopt the same circular velocity, $v_c = 270$ km s $^{-1}$. The BM circular velocity is estimated to be $v_{bm}(r_0) = 191$ km s $^{-1}$. This gives the BM mass, $m_b(< r_0) = 1.6 \times 10^{11} m_\odot$. By adding $\sim 10\%$, the total BM mass of M31 is $m_b = 1.8 \times 10^{11} m_\odot$. Taking the average, the BM mass within the radius $r_0 = 19$ kpc is $m_b(< 19 \text{ kpc}) = 1.45 \times 10^{11} m_\odot$, and the total BM mass of M31 is $m_b = 1.6 \times 10^{11} m_\odot$.

The observational circular velocities in the outer region of M31, $r \geq 19$ kpc, correspond to the elliptic orbit of the test particle. Hence, they are not suitable to test the HDM model wherein the test particle moves along the parabolic orbit in the outer region. The enclosed dynamical mass in the far outer region, $r \gg r_0$, can be calculated through the radial velocity. Veljanoski et al. (2014) reported the

radial velocities of the globular clusters in M31 in the range 30 – 140 kpc. The radial velocity dispersion at 80 kpc is $\sigma_r = 83 \text{ km s}^{-1}$ (Veljanoski et al., 2014) that gives the radial velocity, $v_r = 166 \text{ km s}^{-1}$. The enclosed dynamical mass can be estimated as $m_{dyn}(< 80 \text{ kpc}) \approx v_r^2 r / 2G = 2.6 \times 10^{11} m_\odot$, and the enclosed BM mass, $m_b(< 80 \text{ kpc}) \approx 1.3 \times 10^{11} m_\odot$. The radial velocity dispersion at 100 kpc is $\sigma_r = 75 \text{ km s}^{-1}$ (Veljanoski et al., 2014) that gives the radial velocity, $v_r = 150 \text{ km s}^{-1}$. The enclosed dynamical mass can be estimated as $m_{dyn}(< 100 \text{ kpc}) \approx v_r^2 r / 2G = 2.6 \times 10^{11} m_\odot$, and the enclosed BM mass, $m_b(< 100 \text{ kpc}) \approx 1.3 \times 10^{11} m_\odot$. The radial velocity dispersion at 120 kpc is $\sigma_r = 69 \text{ km s}^{-1}$ (Veljanoski et al., 2014) that gives the radial velocity, $v_r = 138 \text{ km s}^{-1}$. The enclosed dynamical mass can be estimated as $m_{dyn}(< 120 \text{ kpc}) \approx v_r^2 r / 2G = 2.65 \times 10^{11} m_\odot$, and the enclosed BM mass, $m_b(< 120 \text{ kpc}) \approx 1.3 \times 10^{11} m_\odot$.

The mass models estimate the BM mass of M31 to be $m_b = 1.04 \times 10^{11} m_\odot$ (Geehan et al., 2006), $m_b = 0.93 \times 10^{11} m_\odot$ (Seigar et al., 2008), $m_b = 0.99 \times 10^{11} m_\odot$ (Chemin et al., 2009), $m_b = 1.4 \times 10^{11} m_\odot$ (Corbelli et al., 2010), $m_b = 1.01 \times 10^{11} m_\odot$ (Tamm et al., 2012). The BM mass consists of the bulge+disc+gas mass in Chemin et al. (2009); Corbelli et al. (2010), and of the bulge+disc mass in the other works. Tamm et al. (2012) note the uncertainties in the bulge mass, $(4.4 - 6.6) \times 10^{10} m_\odot$, and in the disc mass, $(5.7 - 8.6) \times 10^{10} m_\odot$. Thus, the BM mass of M31 estimated in the HDM model is consistent with the literature data.

Estimate the HDM density from the HDM mass at $r_0 = 19 \text{ kpc}$. The HDM mass is equal to the BM mass at $r_0 = 19 \text{ kpc}$. Hence, $m_{hdm}(< 19 \text{ kpc}) = 1.45 \times 10^{11} m_\odot$ that gives the HDM density $\rho_{hdm} = 3.4 \times 10^{-25} \text{ g cm}^{-3} = 5.05 \times 10^{-3} m_\odot \text{ pc}^{-3}$. This is consistent with the value in the Milky Way, $\rho_{hdm} = 3.1 \times 10^{-25} \text{ g cm}^{-3} = 4.6 \times 10^{-3} m_\odot \text{ pc}^{-3}$ (Khokhlov, 2018) and with the local DM density at the solar position, $\rho_{dm}(R_\odot) = 0.005 - 0.01 m_\odot \text{ pc}^{-3}$ (Weber & de Boer, 2010), $\rho_{dm}(R_\odot) = 0.005 - 0.015 m_\odot \text{ pc}^{-3}$ (Read, 2014). The similar values were obtained for M33, NGC 2366, IC 2574 (Khokhlov, 2018).

3. Radial velocity of M31 toward the Milky Way

Consider the system of the Milky Way and M31 in the HDM model. We shall treat the Milky Way and M31 as points of the BM mass, $m_{b,MW} = 1.0 \times 10^{11} m_\odot$ (Khokhlov, 2018) and $m_{b,M31} = 1.6 \times 10^{11} m_\odot$, respectively. The gravitational interaction of the Milky Way and M31 is defined by the dynamical masses of the Milky Way and M31 which are twice the BM masses of the Milky Way and M31. The radial velocity of M31

toward the Milky Way is given by

$$v = \left(\frac{4Gm_{b,MW}}{R} \right)^{1/2} + \left(\frac{4Gm_{b,M31}}{R} \right)^{1/2} \quad (4)$$

where R is the distance between the Milky Way and M31. For $R = 785 \text{ kpc}$ (McConnachie et al., 2005), the radial velocity of M31 toward the Milky Way is 106 km s^{-1} . The observational value is $109.3 \pm 4.4 \text{ km s}^{-1}$ (van der Marel et al., 2012), they adopt the distance between the Milky Way and M31, $R = 770 \text{ kpc}$. Thus, the radial velocity of M31 toward the Milky Way estimated in the HDM model is consistent with the observational value.

4. Dark matter in the globular clusters

Globular clusters (GCs) pose a problem for the Λ CDM model. According to the hierarchical structure formation, the GCs form within their own DM halos (Peebles, 1984). Observations show no evidence for DM halos of GCs, e.g. (Mashchenko & Sills, 2005a). It is reasonable to think that the DM halos of GCs were stripped by the tidal field of the host galaxy, e.g. (Mashchenko & Sills, 2005b). However, there exist GCs at large distances from the centre of the host galaxy where the effect of the tidal field is negligible. NGC 2419 in our Galaxy ($\sim 90 \text{ kpc}$ from the galactic center) and MGC1 in M31 ($\sim 200 \text{ kpc}$ from the galactic center) are distant GCs with negligible tidal effects. Observations show that the DM mass in these clusters is limited by the stellar mass as $m_{DM}/m_* < 1$ (Conroy et al., 2011; Ibata et al., 2013). Although the DM is admitted in the clusters, it is not needed to explain the data.

Consider NGC 2419 and MGC1 in the HDM model. Observations show the stellar mass $m_* \sim 10^6 m_\odot$ within the radius $r \sim 250 \text{ pc}$ in both the clusters. For the HDM density $\rho_{hdm} = 5 \times 10^{-3} m_\odot \text{ pc}^{-3}$, the HDM mass within the radius $\sim 250 \text{ pc}$ is $m_{hdm}(< 250 \text{ pc}) = 3 \times 10^5 m_\odot$. Thus, the HDM content within the radius $\sim 250 \text{ pc}$ is small compared to the stellar matter. This is consistent with the observational data.

5. Dark matter in the dwarf spheroidal galaxies

Dwarf spheroidal galaxies (dSphs) exhibit the flat velocity dispersion curves which cannot be explained by the baryonic mass alone, e.g. (Walker, 2013). The velocity dispersion gives the dynamical masses which substantially exceed the stellar masses within the half-light radii, and the dynamical mass-to-light ratios are increasing toward the outskirts of the galaxies. For the Local Group dSphs, the dynamical mass-to-light

ratios within the half-light radii can be found in Collins et al. (2014), with $[M/L]_{half}$ from $\sim 10 m_{\odot}/L_{\odot}$ to $\sim 1000 m_{\odot}/L_{\odot}$, except for several outliers. Typically, the discrepancy between the dynamical and stellar masses is ascribed to the DM.

Sculptor is a typical dSph at a distance of 86 kpc from the centre of our Galaxy (McConnachie, 2012). Battaglia et al. (2008) studied the kinematics in the Sculptor for two components of RGB stars, metal rich $[Fe/H] > -1.5$ and metal poor $[Fe/H] < -1.7$. The profile of the metal rich stars in the l.o.s. velocity dispersion shows a fall off from $\sigma \sim 9 \text{ km s}^{-1}$ in the centre to $\sigma \sim 2 \text{ km s}^{-1}$ at 0.7 kpc. The profile of the metal poor stars in the l.o.s. velocity dispersion is approximately flat, $\sigma \sim 11 \text{ km s}^{-1}$, from the centre to 0.5 kpc, and then is slightly declining to 1.8 kpc.

The difference of the profiles of the metal rich and metal poor stars can be interpreted as follows. Suppose that the metal rich stars are young, and the metal poor stars are old. Assume that the declining profile of the metal rich (young) stars traces the real gravitational potential of the galaxy while the flat profile of the metal poor (old) stars is a result of evolution not related to the gravity of the galaxy. When neglecting the HDM, the gravity of the BM is balanced by the acceleration due to the velocity dispersion thus holding the stable galaxy structure. Addition of the HDM leads to the instability of the BM. Under the influence of some perturbations, the unstable BM is spreading out that results in growing of the size of the dwarf galaxy with time. The velocity dispersion is defined by the value of perturbations and cannot be used to derive the dynamical mass of the galaxy. Perturbations may be caused by the tidal forces of the host galaxy. Hammer et al. (2018) showed for a bulk of dwarf galaxies in the Milky Way that the velocity dispersions of the dwarf galaxies can be explained by the tidal forces exerted by the Milky Way.

Estimate the dynamical mass within the half-light radius of the Sculptor from the velocity dispersion of the metal rich stars. The half-light radius of the Sculptor is $r_{half} = 283 \text{ pc}$ (McConnachie, 2012). The l.o.s. velocity dispersion of the metal rich stars at 283 pc is $\sigma \sim 5 \text{ km s}^{-1}$ (Battaglia et al., 2008). The calculation gives $[m_{dyn}]_{half} = \sigma^2 r_{half} / G = 1.6 \times 10^6 m_{\odot}$.

The observed stellar mass of the Sculptor is $m_* = 2.3 \times 10^6 m_{\odot}$ (McConnachie, 2012). The stellar mass within the half-light radius is $[m_*]_{half} = 1.15 \times 10^6 m_{\odot}$. For the HDM density $\rho_{hdm} = 5 \times 10^{-3} m_{\odot} \text{ pc}^{-3}$, the HDM mass within the half-light radius is $[m_{hdm}]_{half} = 0.5 \times 10^6 m_{\odot}$. The sum of the stellar and HDM mass within the half-light radius is $[m_* + m_{hdm}]_{half} = 1.65 \times 10^6 m_{\odot}$. Thus, the dynamical mass within the half-light radius of the Sculptor derived from the kinematics of the metal rich stars is consistent with the sum of the stellar and HDM mass within the half-light radius.

6. Evolution of ultra-massive quiescent galaxies

Stockmann et al. (2020) presented an analysis of 15 ultra-massive quiescent galaxies from the COSMOS and UDS fields ($\log(m_*/m_{\odot}) \sim 11.5$) at $z \gtrsim 2$. They obtained the ratio of dynamical to stellar mass of order unity, $m_{dyn}/m_* \sim 1$. This implies the absence of DM in the galaxies at $z = 2$. A sample of early-type galaxies from the MASSIVE Survey was taken as the local reference sample.

Comparison of the galaxies from the two samples allows to study the evolution of ultra-massive quiescent galaxies from $z = 2$ to 0. The analysis of the data shows that the local galaxies have grown by a factor of 2 in stellar mass, 4 in size, with no evolution in velocity dispersion. As a result, the dynamical to stellar mass relation is doubling during the evolution from $z = 2$ to 0. When assuming the absence of DM at $z = 2$, the two times increase in the dynamical mass can be ascribed to the HDM in the local galaxies ($z = 0$). This is consistent with the HDM model which predicts the dynamical mass of the local galaxy as twice its stellar mass.

Conclusion

In a recent paper (Khokhlov, 2018), the model of the galaxy with HDM had been considered. The model was successfully tested on the galaxies: Milky Way, M33, NGC 2366 and IC 2574. In the present paper, we have continued investigation of the HDM model, addressing M31, the radial velocity of M31 toward the Milky Way, the globular clusters NGC 2419 and MGC1, the dwarf spheroidal galaxy Sculptor. Also, we have considered the evolution of ultra-massive quiescent galaxies from $z = 2$ to 0.

The galaxy structure in the HDM model is divided into the inner and outer regions at some radius where the BM mass is equal to the HDM mass (energy). The radius of the border between the regions in M31 is taken $r_0 = 19 \text{ kpc}$, corresponding to the second warp of the disc in M31.

The BM mass of M31 within $r_0 = 19 \text{ kpc}$ has been estimated from the circular velocity at $r_0 = 19 \text{ kpc}$, and the value is $m_b(< r_0) = (1.25 - 1.4) \times 10^{11} m_{\odot}$. By adding $\sim 10\%$, the total BM mass of M31 is estimated to be $m_b = (1.4 - 1.5) \times 10^{11} m_{\odot}$. Also, the BM mass of M31 within $r_0 = 19 \text{ kpc}$ has been estimated from the radial velocity dispersion of the red giant branch stars at $r_0 = 19 \text{ kpc}$, and the value is $m_b(< r_0) = 1.6 \times 10^{11} m_{\odot}$. By adding $\sim 10\%$, the total BM mass of M31 is estimated to be $m_b = 1.8 \times 10^{11} m_{\odot}$.

The BM mass of M31 has been estimated from the radial velocities of the globular clusters in the range 80 – 120 kpc. The BM mass of M31 is estimated to be

$m_b = 1.3 \times 10^{11} m_\odot$. The BM mass of M31 estimated at $r_0 = 19$ kpc and at 80 – 120 kpc is consistent with the literature data for the bulge mass, $(4.4 - 6.6) \times 10^{10} m_\odot$, and the disc mass, $(5.7 - 8.6) \times 10^{10} m_\odot$ (Tamm et al., 2012).

The HDM density in M31 has been estimated. The value obtained is $\rho_{hdm} = 3.4 \times 10^{-25} \text{ g cm}^{-3} = 5.05 \times 10^{-3} m_\odot \text{ pc}^{-3}$. This is consistent with the values in the Milky Way, M33, NGC 2366, IC 2574 (Khokhlov, 2018) and with the local DM density at the solar position (Weber & de Boer, 2010; Read, 2014).

The gravitational interaction of the Milky Way and M31 has been considered in the HDM model. The radial velocity of M31 toward the Milky Way is estimated to be 106 km s^{-1} which is consistent with the observational value, $109.3 \pm 4.4 \text{ km s}^{-1}$ (van der Marel et al., 2012).

We have considered distant GCs NGC 2419 in our Galaxy and MGC1 in M31. The HDM mass within the radius ~ 250 pc is estimated to be $m_{hdm}(< 250 \text{ pc}) = 3 \times 10^5 m_\odot$ compared to the stellar mass $m_* \sim 10^6 m_\odot$ in both the clusters. The small DM content in these clusters is consistent with the observational data.

We have considered the problem of dark matter in the dwarf spheroidal galaxies in the HDM model, based on the kinematics of RGB stars in the Sculptor presented in Battaglia et al. (2008). We have assumed that the declining profile of the metal rich (young) RGB stars traces the real gravitational potential of the galaxy while the flat profile of the metal poor (old) RGB stars does not. It is a result of evolution caused by the instability of the BM due to the presence of the HDM and the influence of some perturbations. The dynamical mass within the half-light radius of the Sculptor derived from the kinematics of the metal rich RGB stars, $[m_{dyn}]_{half} = 1.6 \times 10^6 m_\odot$, is consistent with the sum of the stellar and HDM mass within the half-light radius, $[m_* + m_{hdm}]_{half} = 1.65 \times 10^6 m_\odot$.

We have considered the evolution of ultra-massive quiescent galaxies from $z = 2$ to 0, based on the analysis of the sample of 15 galaxies from the COSMOS and UDS fields presented in Stockmann et al. (2020). The dynamical to stellar mass relation evolves from $m_{dyn}/m_* \sim 1$ at $z = 2$ to $m_{dyn}/m_* \sim 2$ at $z = 0$ that is consistent with the HDM model.

References

- Ade P.A.R., Aghanim N., Arnaud M. et al.: 2016, *A&A*, **594**, A13
- Battaglia G., Helmi A., Tolstoy E., Irwin M., Hill V., Jablonka P.: 2008, *ApJ*, **681**, L13
- Battaner E., Florido E.: 2000, *Fund. Cosmic Phys.*, **21**, 1
- Bertone G., Tait T.M.P.: 2018, *Nature*, **562**, 51
- Brinks E., Burton W.B.: 1984, *A&A*, **141**, 195
- Bowman J.D., Rogers A.E.E., Monsalve R.A., Mozdzen T.J., Mahesh N.: 2018, *Nature*, **555**, 67
- Casey C.M., Zavala J.A., Araven M. et al.: 2019, *ApJ*, **887**, 55
- Chapman S.C., Ibata R., Lewis G.F. et al.: 2006, *ApJ*, **653**, 255
- Chemin L., Carignan C., Foster T.: 2009, *ApJ*, **705**, 1395
- Collins M.L.M., Chapman S.C., Rich R.M. et al.: 2014, *ApJ*, **783**, 7
- Conroy C., Loeb A., Spergel D.N.: 2011, *ApJ*, **741**, 72
- Corbelli E., Lorenzoni S., Walterbos R., Braun R., Thilker D.: 2010, *A&A*, **511**, A89
- Demiański M., Doroshkevich A.: 2017, preprint (arXiv:1701.03474)
- Famaey B., McGuagh S.: 2012, *Living Reviews in Relativity*, **15**, 10
- Geehan J.J., Fardal M.A., Babul A., Guhathakurta P.: 2006, *MNRAS*, **366**, 996
- Genzel R., Förster Schreiber N.M., Übler H. et al.: 2017, *Nature*, **543**, 397
- Hammer F., Yang Y., Arenou F. et al.: 2018, *ApJ*, **860**, 76
- Henderson A.P.: 1979, *A&A*, **75**, 311
- Ibata R., Chapman S., Ferguson A.M.N., Lewis G., Irwin M., Tanvir N.: 2005, *ApJ*, **634**, 287
- Ibata R., Nipoti C., Sollima A., Bellazzini M., Chapman S.C., Dalessandro E.: 2013, *MNRAS*, **428**, 3648
- Khokhlov D.L.: 2011a, *Ap&SS*, **333**, 209
- Khokhlov D.L.: 2011b, *Ap&SS*, **335**, 577
- Khokhlov D.L.: 2011c, *Open Astron. J.*, **4 SI 1**, 151
- Khokhlov D.L.: 2013, *Ap&SS*, **343**, 787
- Khokhlov D.L.: 2014, *Phys. Lett. B*, **729**, 1
- Khokhlov D.L.: 2015, *Ap&SS*, **360**, 27
- Khokhlov D.L.: 2017, *Int. J. Mod. Phys. Appl.*, **4**, 8
- Khokhlov D.L.: 2018, *Open Astronomy*, **27**, 294
- Kroupa P.: 2012, *PASA*, **29**, 395
- Kroupa P.: 2015, *Can. J. Phys.*, **93**, 169
- Landau L., Lifshitz Ye.: 1960, *Mechanics*, Pergamon Press, Oxford
- Lang P., Förster Schreiber N.M., Genzel R. et al.: 2017, *ApJ*, **840**, 92
- Liu J., Chen X., Ji X.: 2017, *Nat. Phys.*, **13**, 212
- López-Corredoira M.: 2017, *Found. Phys.*, **47**, 711
- McConnachie A.W., Irwin M.J., Ferguson R.A., Ibata R.A., Lewis G.F., Tanvir N.: 2005, *MNRAS*, **356**, 979
- McConnachie A.W.: 2012, *AJ*, **144**, 4
- McGaugh S.S.: 2018, *Phys. Rev. Lett.*, **121**, 081305
- Marrodán Undagoitia T., Rauch L.: 2016, *J. Phys. G: Nucl. Part. Phys.*, **43**, 013001
- Mashchenko S., Sills A.: 2005a, *ApJ*, **619**, 243
- Mashchenko S., Sills A.: 2005b, *ApJ*, **619**, 258
- Newton K., Emerson D.T.: 1977, *MNRAS*, **181**, 573
- Ostriker J.P., Steinhardt P.J.: 1995, *Nature*, **377**, 600
- Peebles P.J.E.: 1984, *ApJ*, **277**, 470
- Read J.I.: 2014, *J. Phys. G: Nucl. Part. Phys.*, **41**, 063101
- Reyes R., Mandelbaum R., Seljak U. et al.: 2010, *Nature*, **464**, 256

- Seigar M.S., Barth A.J., Bullock J.S.: 2008, *MNRAS*, **389**, 1911
- Stockmann M., Toft S., Gallazzi A. et al.: 2020, *ApJ*, **888**, 4
- Tamm A., Tempel E., Tenjes P., Tihhonova O., Tuvikene T.: 2012, *A&A*, **546**, A4
- Tanaka M., Valentino F., Toft S. et al.: 2019, *ApJL*, **885**, L34
- Trimble V.: 1987, *ARA&A*, **25**, 425
- van der Marel R.P., Fardal M., Besla G. et al.: 2012, *ApJ*, **753**, 8
- Veljanoski J., Mackey A.D., Ferguson A.M.N. et al.: 2014, *MNRAS*, **442**, 2929
- Walker M.: 2013, In: Oswalt T.D., Gilmore G. (eds) *Planets, Stars and Stellar Systems*, Springer, Dordrecht
- Walterbos R., Kennicutt R.: 1988, *A&A*, **198**, 61
- Weber M., de Boer W.: 2010, *A&A*, **509**, 25
- Weinberg D.H., Bullock J.S., Governato F., de Naray R.K., Peter A.H.G.: 2015, *Proc. Nat. Acad. Sci.*, **112**, 12249

DOI:<http://dx.doi.org/10.18524/1810-4215.2020.33.216303>

ON THE QUESTION OF THE HELIUM ABUNDANCE IN ORION A MEASURED BY RADIO RECOMBINATION LINES. AND THE PRIMORDIAL HELIUM ABUNDANCE.

A.P. Tsivilev

Pushchino Radio Astronomy Observatory of Lebedev Physical Institute RAS,
Moscow, Russia, tsivilev@prao.ru

ABSTRACT. Recombination radio lines (RRLs) of hydrogen (H), helium (He-4), and carbon (C) are a powerful tool for studying the interstellar medium (ISM) in space. The RRLs observations allow to obtain the physical parameters of regions of ionized hydrogen (HII regions) as well as of the photo-dissociation regions; and to estimate the effective temperature of stars that ionize the HII region. There is also an important cosmological task for RRL – measuring Primordial helium abundance produced at the stage of Primordial nucleosynthesis of the Universe. It turned out that the Orion A nebula is an interesting object for the latter task. At the time, the recombination radio lines observations of hydrogen, helium (H, He), and carbon (C) at a number of positions in the Orion A HII region were carry out with the RT22 radio telescope (Pushchino) at wavelengths of 8 and 13 mm. The relative helium abundance, $y^+ = n(He^+)/n(H^+)$, in these positions was obtained. The behavior of this value over the nebula showed that the helium ionization zone is smaller than the hydrogen one with different ratios for the core and halo. The location where the maximum y^+ value is expected was also determined. For the established ionization structure, it means that the actual helium abundance in Orion A, $n(He)/n(H)$, will not be less than the maximum y^+ value. This allows to estimate the limitations on the Primordial helium abundance. In this work, new H and He RRL observations were made at 13 mm in the direction of the expected maximum of y^+ . RRLs were observed in two transitions - 65α and 66α . It was found that the maximum y^+ value is in the range of 10 – 12%. Hence, we can expect that the Primordial helium abundance (Y_p , the ratio He/H by mass) lies in the range of $\approx 26.4 - 29\%$, and the number of light neutrino-type particles during Primordial nucleosynthesis may exceed the standard value. To refine the result the work will be continue.

Keywords: Cosmology; Radio astronomy, HII regions, radio recombination lines.

АНОТАЦІЯ. Рекомбінаційні радіолінії (РРЛ) водню (H), гелію (He-4) і вуглецю (C) є потужним засобом дослідження міжзоряного середовища (МЗС) у космосі. Вони дозволяють отримувати фізичні параметри областей іонізованого водню (HII областей) і областей фотодисоціації; оцінювати ефективну температуру зірок, які іонізують HII області. Є і важливе космологічне завдання для РРЛ - вимірювання первинного змісту гелію, виробленого на стадії первинного нуклеосинтезу Всесвіту. Виявилось, що для останнього завдання цікавим об'єктом є туманність Оріона А. Свого часу на радіотелескопі РТ22 (Пушчино) на хвилі 8 і 13 мм були проведено спостереження рекомбінаційних радіоліній водню, гелію (H, He) і вуглецю (C) в ряді напрямків області HII Оріон А. Було отримано відносний вміст гелію, $y^+ = n(He^+)/n(H^+)$, у цих напрямках. Поведінка цієї величини вздовж туманності показало, що зона іонізації гелію менша зони іонізації водню, з різним співвідношенням для ядра і гало. Було визначено також розташування місця, де очікується максимальне значення величини y^+ . Для встановленої іонізаційної структури знайдено, що дійсний вміст гелію в Оріоні А, $n(He)/n(H)$, буде не менше, ніж максимальне значення y^+ . Це дозволяє оцінити обмеження і на первинний вміст гелію. У даній роботі були проведені нові спостереження РРЛ H і He на 13 мм у напрямку на очікуваний максимум величини y^+ . РРЛ спостерігалися у двох переходах – 65α і 66α . Було отримано, що максимальне значення y^+ знаходиться в інтервалі 10 – 12%. Звідси можна очікувати, що первинний вміст гелію (Y_p , відношення He/H по масі) лежить в інтервалі $\approx 26.4 - 29\%$, а число легких частинок типу нейтрино під час первинного нуклеосинтезу може перевищити стандартне значення. Робота по уточненню цього результату буде продовжена.

Ключові слова: Космологія; Радіоастрономія, HII області, радіорекомбінаційні лінії.

1. Introduction

Recombination radio lines (RRLs) of hydrogen (H), helium (He-4), and carbon (C) are a powerful tool for studying the interstellar matter (ISM) (see Gordon and Sorochenko, 2003). The RRLs observations allow to obtain the physical parameters of the ionized hydrogen regions (HII regions) formed around young and hot stars as well as of the photo dissociation regions, which are intermediate layer between the HII zone and the parent molecular cloud (e.g., Sorochenko and Tsivilev, 2010); the effective temperatures of the stars ionized of HII regions could also be estimated (e.g., Polaykov and Tsivilev, 2007). There is also an important cosmological task for RRL - measurement of the Primordial helium abundance. As Hoyle and Taylor (1964) have showed at their time, about 90% of the observed amount of helium was formed at the pregalactic phase of the Universe's evolution, and most likely at the stage of Primordial nucleosynthesis. During Primordial nucleosynthesis (the first 2-3 minutes after the Big Bang), in addition to He-4, several other light elements were formed: deuterium (D), helium-3 (He-3), tritium (T), and lithium (Li-7). But if the yield of these elements depended only on the baryon density of the Universe, then the yield of helium (He-4) dependent to a greater extent on the conditions of the neutron-proton ratio (n/p) was frozen out (Klapdor-Kleingrothaus, Zuber, 2000). One of these conditions was the number of light relativistic particles at the time of this freezing out ($\sim 10 - 20$ s after the Big Bang).

Thus, if the above elements are indicators of the baryon density of the Universe, then the Primordial helium abundance is also an indicator of the presence or absence of unknown light particles. The contribution of known light particles in the framework of Standard Cosmological Model (SCM) is calculated with good accuracy (Klapdor-Kleingrothaus, Zuber, 2000). The available observations of fluctuations in the microwave background give the values of the Primordial helium abundance (Y_p) within the Standard cosmological model (SCM) with high accuracy. (For example, the He/H ratio by mass is, $Y_p = 24.84(B \pm 0.02)\%$ - Coc, Vangioni (2017)). And it would seem what the experiment can give in this situation, because it is difficult to achieve such accuracy in observations? At the moment, the SCM assumes the presence of three neutrino species. However, for example, Yang et al. (1984) showed that the presence of an additional fourth neutrino would lead to a $Y_p \geq 25.3\%$. The difference in Y_p values would be already quite noticeable and measurable. Thus, the presence of additional unknown light particles like neutrinos may indicate a deviation from the Standard Cosmological Model, which will manifest itself in the measured excess of the Primordial helium abundance from the SCM predictions. Within

the framework of this formulation of the problem (search for deviations from the SCM), the source - Orion A HII region - turned out to be interesting object. For a number of years, we have intensively investigated the well-known Orion A nebula by RRLs of H, He and C at wavelengths of 13 mm and 8 mm. It was found that the He^+ ionization zone is less than the H^+ zone. Under these conditions, the maximum of the obtained value $n(He^+)/n(H^+)$ makes it possible to refine the lower limit of the Y_p value.

2. Results and Discussion

At the indicated radio frequencies (the optically thin case and the absence of Stark broadening of lines) the relative helium abundance, $y = n(He)/n(H)$, was calculated as the ratio of integrals of the He and H RRLs, corresponding to the same transition numbers, using the following formula:

$$y = \frac{T_l(He)^- \Delta V(He)}{T_l(H)^- \Delta V(H)} \quad (1)$$

where T_l - line amplitude, ΔV - line width at half intensity level in km/s .

In reality, we measure the RRL of an ionized gas, i.e. the ratio of the ionized components of He^+ and H^+ . In the HII regions, the measured ($y^+ = n(He^+)/n(H^+)$) and the actual ($y = n(He)/n(H)$) helium abundance are related by a structural factor R:

$$y^+ = R \times y \quad (2)$$

where R is determined by the ionization structure, i.e. the ratio of the sizes and emission measures of the He^+ and H^+ zones. The relative helium abundance by mass (Y) is expressed by the following formula:

$$Y = 4y \times (1 - Z)/(1 + 4y) \quad (3)$$

where Z is the relative mass abundance of other elements heavier than helium, often called metallicity. Then it need to take into account the stars contribution to the production of helium. In the case of Orion A (Tsivilev, 2009) the Primordial helium abundance can be determined by the following formula, using the dependence of Y on Z due to the contribution of stellar evolution:

$$Y_p = Y - dY/dZ \times Z \quad (4)$$

In our previous works, it was shown that the ionization structure in Orion A has a core-halo structure, where the He^+ zone is smaller than the H^+ one, i.e. $R < 1$ as a whole for the nebula with a different value for the core and halo. Under these conditions, the maximum measured value y^+ will mean the lower limit on the actual helium content, $y = n(He)/n(H) \geq y_{max}^+$. This opens the way for estimating the lower

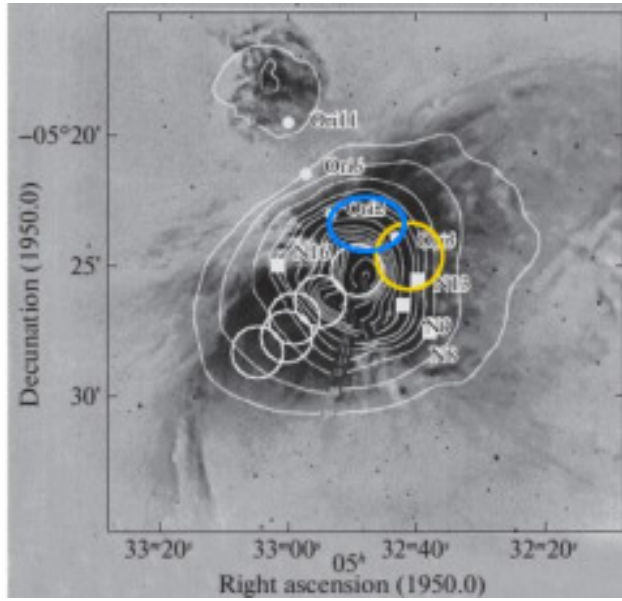


Figure 1: Positions in Orion A (see f.e. Tsivilev et al., 2019) where RRL observations with RT22 (Pushchino) were made at wavelengths of 8 mm (large and small circles) and 13 mm (squares). The yellow circle is the position where the maximum relative helium abundance was observed at 13 mm. (The size of the yellow circle corresponds to the size of the RT22 beam at 13 mm, the size of the white circle corresponds to at 8 mm one).

bound on the Primordial helium abundance (Y_p). So, the task was to find y_{max}^+ in Orion A.

In our work Poppi et al. (2007), it has been showed that y^+ increases with distance from the center with a maximum value at an angular distance of 2 – 3', and then falls. The probable area of maximum $y^+ \approx 10\%$ was indicated in the North-West of the region (see Fig. 1, marked as a blue oval) in positions Ori2 and Ori3 (Poppi et al., 2007). In subsequent works (Tsivilev et al., 2016; Tsivilev et al., 2019) a high helium abundance was also found slightly to the south, in the Ori N13 position (Fig. 1). Therefore, the highest y^+ value can be expected between the Ori3 and Ori N13 positions. In this work, we carried out the RRLs observations with RT22 (Pushchino) in this direction by the 65α transition, (large yellow circle in Fig. 1).

Indeed, we obtained a value of $y^+ \approx 12\%$ (see Fig. 2), which is higher than previously measured values. The result is stable to small variations in the spectrometer zero line. Since the result was unusually high, we made additional observations of H and He RRL in this direction for another transition - 66α . Unfortunately, the equipment in these observations worked worse; in particular, the system noise temperature was 1.5 times higher. All observations were carried out from 2017 to

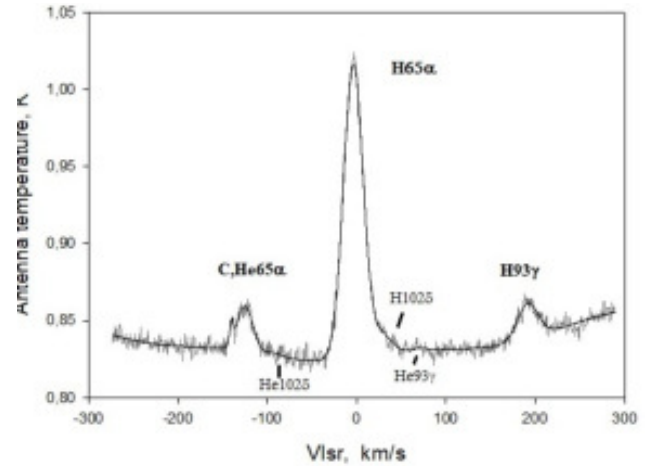


Figure 2: Obtained spectrum (transition 65α) in the direction of the y^+ maximum in Orion A at 13 mm. The vertical axis – antenna temperatures in Kelvins, on the horizontal – radial velocities in km/s. Zero corresponds to the zero velocity for RRL H. The gray line is the resulting spectrum, and the black smooth line is the fitted spectrum.

2020, the time of signal accumulation in the transition 65α – ≈ 90 hours, in the transition 66α – ≈ 60 hours. Finally, $y^+ = 11.57(\pm 0.59)\%$ was obtained for the 65α transition and $10.0(\pm 1.13)\%$ for the 66α transition. The weighted average value for the two transitions (66α and 65α) is equal to $y^+ = 11.23(\pm 0.52)\%$. The next step was to calculate the Primordial helium abundance using formulas (3) and (4) and taking $Z = 0.0112(B \pm 0.0022)$ (Baldwin et al., 1991) and $dY/dZ = 1.62(B \pm 0.29)$ (Izotov, Thuan, 2010) and assuming that $R = 1$ at the maximum y^+ position:

$$Y_p = 29.2(\pm 1.05)\%.$$

Taking minus 3σ (errors), we can estimate a formally "strong lower" constraint:

$$Y_p > 26.0\%.$$

Further, conclusions can be drawn about the limitations on the existence of unknown light particles during Primordial nucleosynthesis (Tsivilev, 2009). For example, Pagel (2000) expressed the calculated helium yield during Primordial nucleosynthesis by the analytical formula. Assuming that the free neutron lifetime closes to 887 s, and combining the first and the last (dependence on the baryon density) terms of this formula, and assuming it as the measured SCM value ($Y_{p,0}$) we obtain a dependence only on the number of light particles of the neutrino type ($N\nu$):

$$Y_p = Y_{p,0} + 0.013(N\nu - 3).$$

Taking the measured SCM value $Y_{p,o} = 24.84\%$ of Coc, Vangioni (2017), as outlined upper in the Introduction, we get:

$$N\nu = (Y_p - 24.84)\%/1.3 + 3 \quad (5)$$

Next, we derive $N\nu = 6.35$ for the main Y_p value and $N\nu > 3.9$ for the its lower limit, i.e. exceeding over the standard value $N\nu = 3$.

Is there any reason for the existence of such a high Y_p value? Some arguments are possible. For example, the presence of a "mirror world" (Okun, 2007). According to Blinnikov and Khlopov (1983), the number of all light particles that affect the expansion rate of the Universe will double. Using formulas available in the literature (for example, the Internet publication http://www.kaf07.mephi.ru/eduroom/DM/DM_L9.pdf), it can be estimated that the value of Y_p will increase by a factor ~ 1.2 , i.e. $Y_p \approx 24.84 \times 1.2 \approx 29.8\%$. It should also be noted that lately there are a lot of talk about the possible presence of fourth type neutrino (for example, Serebrov et al., 2019). It is interesting to note the recent measurements of Y_p by absorption lines in intergalactic gas towards distant quasars, which gave the $Y_p = 25.0(+3.7; -2.5)\%$ (Cooke and Fumagalli, 2018). Since the authors did not take into account the contribution of doubly ionized helium, which is abundant in the intergalactic gas, this value can be considered as some lower limit, which also allows exceeding the accepted SCM Y_p value.

3. Conclusions

So, RRL observations in Orion A derived a high helium abundance, $y_{max}^+ = 10 - 12\%$, which assumes the possibility of a "high" Primordial helium abundance (by mass), $Y_p = 26.4 - 29\%$, and the number of light particles of neutrino type can exceed the standard value. It is clear that the result requires clarification. We will continue to work in this direction and try to carry out additional RRL observations in Orion A.

Acknowledgements. The author is thankful to Dagkesamansky R.D. who has read this contribution and made useful comments.

References

- Baldwin J.A., Ferland G.J., Martin P.G. et al: 1991, *Astrophys. J.*, **374**, 580.
 Blinnikov S.I. and Khlopov M.Yu.: 1983, *Astron. Zh.*, **60**, 632.
 Coc A. and Vangioni E.: 2017, *Internat. J. Modern Phys. E*, **26**, 08.
 Cooke R.J. and Fumagalli M.: 2018, *Nature Astronomy*, **2**, 957.
 Gordon M. A. and Sorochenko R. L.: 2003, *Radio Recombination Lines: Their Physics and Astronomical Applications* (Fizmatlit, Moscow, 2003; Springer, New York, 2009).
 Hoyle F. R. S. and Teyler R. J.: 1964, *Nature*, **203**, 1108.
 Izotov Y.I. and Thuan T.X.: 2010, *Astrophys. J.*, **710**, L67.
 Klapdor-Kleingrothaus H.V. and Zuber K.: 2000, *Particle Astrophysics* (Inst. of Phys., Bristol, Philadelphia, 1997; Usp. Fiz. Nauk, Moscow, 2000).
 Okun L.B.: 2007, *Usp. Fiz. Nauk*, **177**, N4, 397.
 Pagel B.E.J.: 2000, *Phys. Rep.*, **333–334**, 433.
 Polyakov A.M. and Tsvilev A.P.: 2007, *Astron. Lett.*, **33**, 34.
 Poppi S., Tsvilev A.P., Cortiglioni S. et al: 2007, *Astron. Astrophys.*, **464**, 995.
 Serebrov A.P. et al: 2019, *JETP Letters*, **109**, 213.
 Sorochenko R.L. and Tsvilev A.P.: 2010, *Kinemat. Phys. Celestial Bodies*, **26**, 162.
 Tsvilev A.P., Krasnov V.V., Logvinenko S.V.: 2019, *Astron. Lett.*, **45**, 20.
 Tsvilev A.P., Parfenov S.Yu. Krasnov V.V.: 2016, *Odessa Astron. Publ.*, **29**, 163.
 Yang J., Turner M.S., Steigman G. et al: 1984, *Astrophys. J.*, **281**, 493.

DOI:<http://dx.doi.org/10.18524/1810-4215.2020.33.216304>

DISCRETE X-RAY SOURCES IN GALAXY CLUSTERS

A.V. Tugay¹, L.V. Zadorozhna², S.Yu. Shevchenko³

¹ Taras Shevchenko National University of Kyiv,
Kyiv, Ukraine, *e-mail: tugay.anatoliy@gmail.com*

² Taras Shevchenko National University of Kyiv,
Kyiv, Ukraine, *e-mail: zadorozhna_lida@ukr.net*

³ Schmalhausen Institute of Zoology, NASc of Ukraine,
Kyiv, Ukraine, *e-mail: astromott@gmail.com*

ABSTRACT. Current studies of extragalactic X-ray sources using data from orbital observatory XMM-Newton are at the front line of X-ray astronomy. Resolution capacity of the observatory instruments enable to detect separate X-ray sources in the close galaxies. In this study we used data from recently published 4XMM-DR9 catalog. This catalog contains 550124 unique sources covering 2,85% of the sky. The main type of extended extragalactic X-ray source is hot halo of galaxy cluster. Such objects are important for astrophysics in the tasks of revealing dark matter distribution, galaxy formation and different cosmology studies.

At the same time, some images of the galaxy clusters contain small scale pointlike X-ray sources scattered around the clusters or their halos. In many cases the nature of such objects is not clear yet and require more detailed studies. Furthermore, energy flux detection threshold of such objects is limited to a great extend not only by the instruments on board of the XMM-Newton observatory but the natural sky background radiation, which is at the level of $10^{-13} \text{Wm}^{-2} \text{sr}^{-1}$ both for XMM cameras and the sky background.

Using Hyperleda database we revealed 16 galaxy clusters among the bright XMM sources. Images of the two galaxy clusters demonstrate bright galaxy cores. These clusters are galaxy group NGC 507 and Coma cluster where nucleus of galaxy NGC 4889 was clearly detected. We also analyzed X-ray images of 14 other X-ray clusters but had not found AGNs there.

Out of the above mentioned 16 clusters in the 7 of them we have found 30 pointlike X-ray sources. These sources are presumably mainly AGNs within these clusters. From the other side, they could be also more distant X-ray objects.

Keywords: Galaxies's X-ray emission, XMM-Newton, HyperLeda, Active Galaxy Nucleus, galaxy halo, galaxy clusters.

АНОТАЦІЯ. Сучасні дослідження позагалакти-

чних джерел рентгенівського випромінювання за допомогою даних, які отримані орбітальною обсерваторією XMM-Newton знаходяться на передовій лінії рентгенівської астрономії. Роздільна здатність приладів обсерваторії дозволяє виявляти окремі джерела рентгенівських променів у близьких галактиках. У цьому дослідженні ми використовували дані нещодавно опублікованого каталогу 4XMM-DR9. Цей каталог містить 550124 унікальних джерел, що охоплюють 2,85% неба. Основним типом протяжного позагалактичного джерела рентгенівського випромінювання є гаряче гало скупчення галактик. Такі об'єкти є важливими для астрофізики в задачах виявлення розподілу темної матерії, утворення галактик та різних космологічних досліджень.

У той же час, деякі зображення скупчень галактик містять точкові рентгенівські джерела невеликого розміру, які розсіяні навколо скупчень або їх гало. У багатьох випадках природа таких об'єктів ще не ясна і вимагає більш детальних досліджень. Крім того, поріг детектування потоку енергії таких об'єктів обмежений не тільки приладами на борту обсерваторії XMM-Newton, але й природним фоном випромінювання неба в рентгенівському діапазоні, яке знаходиться на рівні $10^{-13} \text{Вт} \cdot \text{м}^{-2} \text{ср}^{-1}$ як для XMM камер, так і для фону неба.

Використовуючи базу даних Hyperleda, ми виявили 16 скупчень галактик серед яскравих джерел XMM. Зображення двох скупчень галактик демонструють яскраві ядра галактик. Ці скупчення - група галактик NGC 507 та скупчення Coma, де ядро галактики NGC 4889 було чітко виявлено. Ми також проаналізували рентгенівські зображення інших рентгенівських кластерів проте АЯГ там не було знайдено.

Серед 16 згаданих вище скупчень у 7 ми знайшли 30 точкових джерел рентгенівського випромінювання. Ці джерела, імовірно, в основному є AGN в межах цих кластерів. З іншого боку,

Table 1: Counts of discrete sources in X-ray clusters

N	BCG	Sources
1	6dFGS gJ034253.0-533753	0
2	ESO 156-8	1
3	ESO 383-76	0
4	ESO 444-46	0
5	ESO 444-76	0
6	M 87	1
7	NGC 507	9
8	NGC 708	6
9	NGC 1129	0
10	NGC 1650	2
11	NGC 3311	6
12	NGC 4696	0
13	NGC 4756	5
14	NGC 4761	0
15	NGC 4889	0
16	NGC 5044	0

такі точкові джерела можуть бути також і більш віддаленими рентгенівськими об'єктами.

Ключові слова: Рентгенівське випромінення галактик, XMM-Newton, HyperLeda, Активні ядра галактик, Галактичне гало, галактичні кластери.

1. Introduction

X-Ray observations are of a great importance for extragalactic astronomy. A number of different active objects could be currently detected only in X-ray band. During decades of X-Ray observations using orbital observatory XMM-Newton there was established a large data base which is continuously updated and accessible e.g. through Hyperleda database. Recently made available version 4XMM-DR9 (Webb et al., 2020) contains more than 500 thousand sources.

Most of X-ray emitting galaxies are more likely to have AGNs (Tugay & Vasylenko, 2011), but this statement should be verified. Galaxy clusters are another type of extragalactic X-ray sources and at the same time are important tracers of large-scale structure of the universe. Main morphology features of LSS may be characterized by filaments (Tempel, 2013; Tugay, 2014) but the clusters are much more visible especially in X-ray band. Possible correlation of X-ray clusters orientation with LSS features was considered in (Tugay et al., 2016). For complex LSS studies both optical and X-ray observations are needed as well as data on peculiar motions of the galaxies to a maximum possible sample size (Parnovsky & Tugay, 2005). In the scope of this study the aim of this paper was to analyze X-ray clusters and search for point-like sources in them. Later we are going to

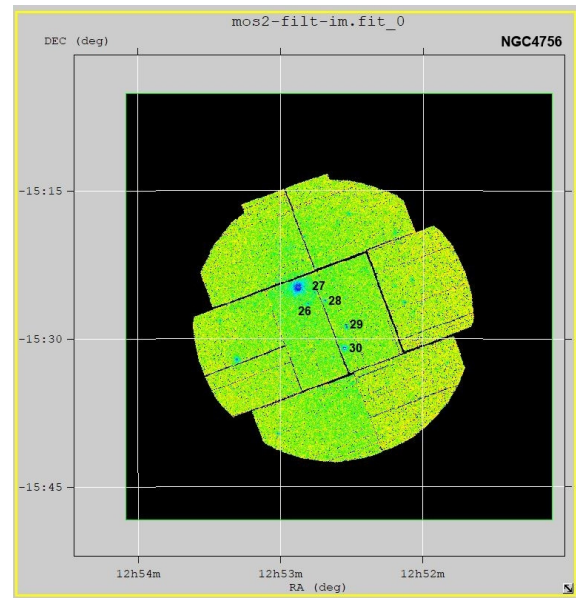


Fig. 1: NGC4756 and 5 detected point-like X-ray sources

study much more faint X-ray extragalactic sources and compare them with the sources found in this paper.

2. Methodology

XMM-Newton observatory is definitely the best facility to study large samples of X-ray sources. It holds on board three European Photon Imaging cameras (MOS1, MOS2 and PN) capable to obtain images, spectra and lightcurves of the studied objects. MOS1 and MOS2 cameras are suitably designed to build images so in this study we selected their data. Detection energy interval of MOS cameras is in the range of 0.2 keV to 12 keV. To select bright X-ray clusters we used Xgal sample of extragalactic X-ray sources (Tugay, 2014). All sources with $F_X > 10^{-13} \text{Wm}^{-2} \text{sr}^{-1}$ were identified with Simbad data base¹. 16 clusters were found with at least one X-ray galaxy inside. For data and image processing software we used fits viewer available from NASA High Energy Astrophysics Science Archive Research Center². The list of our sample is presented at Table 1. We refer to each cluster by its brightest galaxy (BCG).

3. Results

Images analysis revealed a number of the point-like sources in a relative angular proximity to the known and reliably identified X-ray sources and their X-ray environment. Such a distance in analysed sample is nearly up to the size of 10' which corresponds to radius

¹<http://simbad.u-strasbg.fr/simbad/>

²<https://heasarc.gsfc.nasa.gov/docs/software/ftools/fv/>

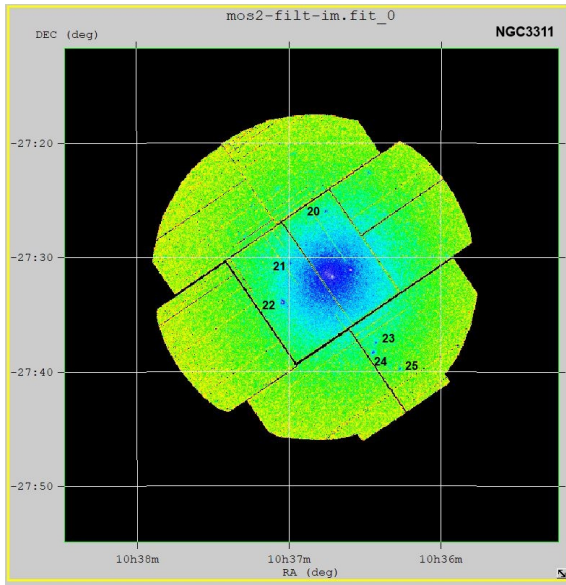


Fig. 2: NGC3311 and 6 detected point-like X-Ray sources

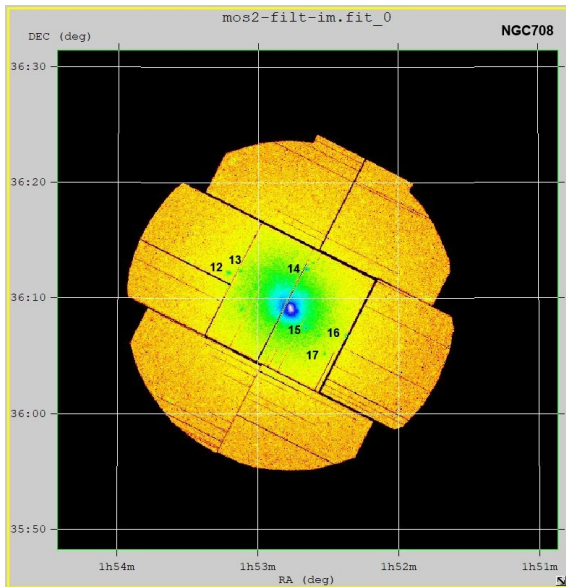


Fig. 3: NGC708 and 5 detected point-like X-ray sources

of the largest X-ray haloes. Some examples of the detected point-like sources are presented on Figs. 1 to 3. Numbers of detected sources around each BCG are given in Table 1. Detected point-like X-Ray sources coordinates are given in the Table 2.

4. Conclusion

Performed study of the currently available data enabled to reveal 30 point like X-ray objects around 7 NGC and ESO catalogue objects. Further studies of their nature and properties will be useful for models of galaxy evolution.

Table 2: Coordinates of discrete sources in X-ray clusters

N	BCG	RA	DEC
1	ESO 156-8	3h41m44.20s	-53:42:19.46
2	M 87	12h30m58.47s	12:11:21.96
3	NGC 507	1h23m11.70s	33:27:48.86
4	NGC 507	1h23m24.98s	33:25:24.82
5	NGC 507	1h23m44.86s	33:26:08.52
6	NGC 507	1h23m54.67s	33:23:39.22
7	NGC 507	1h22m58.52s	33:22:47.18
8	NGC 507	1h23m10.95s	33:19:45.88
9	NGC 507	1h23m06.30s	33:19:32.86
10	NGC 507	1h23m07.09s	33:19:23.33
11	NGC 507	1h23m10.99s	33:10:51.15
12	NGC 708	1h53m12.59s	36:12:16.36
13	NGC 708	1h53m07.63s	36:12:25.44
14	NGC 708	1h52m39.13s	36:12:31.65
15	NGC 708	1h52m39.13s	36:07:22.70
16	NGC 708	1h52m22.30s	36:06:46.64
17	NGC 708	1h52m31.96s	36:05:13.71
18	NGC 1650	4h45m11.45s	-15:46:08.04
19	NGC 1650	4h44m52.06s	-15:48:01.20
20	NGC 3311	10h36m45.29s	-27:25:54.45
21	NGC 3311	10h36m59.29s	-27:30:34.85
22	NGC 3311	10h37m02.15s	-27:33:50.38
23	NGC 3311	10h36m25.70s	-27:37:26.24
24	NGC 3311	10h36m26.57s	-27:38:21.70
25	NGC 3311	10h36m16.02s	-27:39:46.20
26	NGC 4756	12h52m48.39s	-15:26:26.79
27	NGC 4756	12h52m45.18s	-15:25:17.28
28	NGC 4756	12h52m41.13s	-15:26:06.48
29	NGC 4756	12h52m32.08s	-15:26:42.14
30	NGC 4756	12h52m33.02s	-15:30:55.24

Acknowledgements. This study was conducted using the data from recently updated XMM-Newton 4XMM-DR9 catalogue. We acknowledge the usage of the HyperLeda database (<http://leda.univ-lyon1.fr/>); SIMBAD Astronomical Database - CDS (Strasbourg) <http://simbad.u-strasbg.fr/simbad/>

References

- Makarov D., Prugniel P., Terekhova N. et al.: 2014, *A. & A.*, **570A**, 13.
- Mingo B., Watson M.G., Rosen S.R. et al.: 2016, *MNRAS*, **462**, 2631.
- Parnovsky S.L., Tugay A.V.: 2005, astro-ph/0510037.
- Tugay A.V. & Vasylenko A.A.: 2011, *Odessa Astron. Publ.*, **24**, 72.
- Tugay A.V.: 2014, *IAU Symposium*, **304**, 168.
- Tugay A.V., Dylida S.S., Panko E.A.: 2016, *Odessa Astron. Publ.*, **29**, 34.
- Webb N.A., Coriat M., Traulsen I. et al.: 2020, *A. & A.*, accepted for publication, arXiv:2007.02899.
- Watson M.G., Schröder A.C., Fyfe D. et al.: 2009, *A. & A.*, **493**, 339.

ASTROPHYSICS

DOI:<http://dx.doi.org/10.18524/1810-4215.2020.33.216281>PROBE OF THE MAGNETIC FIELD IN THE HOT
SUPERGIANT ζ PerV.V. Butkovskaya^{1,2}, S.I. Plachinda^{1,2}¹Main Astronomical Observatory of National Academy of Sciences of Ukraine,
Kyiv, Ukraine, vbutkovskaja@gmail.com²Crimean Astrophysical Observatory,
Nauchny, Crimea

ABSTRACT. At the surface of $\sim 7\%$ of single hot stars stable mainly dipolar strong magnetic fields have been detected. The main hypothesis today is that these magnetic fields are of fossil origin. In other words, these fields formed from the seed field in the molecular clouds from which the stars were formed. The recent observational and theoretical results confirm this theory: the properties of the observed fields correspond to those expected from fossil fields. Massive stars are stars whose initial mass exceeds about 8 solar masses. Massive stars play a significant role in the chemical and dynamical evolution of galaxies. However, much of their variability, particularly during their evolved supergiant stage, is poorly understood. To date magnetic field was registered only at three hot stars of I-II luminosity types: ρ Leo (B1 Ib), ζ Ori Aa (O9.2 Ib), and ϵ CMa (B1.5 II). We performed high-accuracy spectropolarimetric observation of the hot supergiant ζ Per (B1 Ib) over 26 nights from 1997 to 2012 with long-slit spectrograph mounted in the coude focus of 2.6-m reflector ZTSh at the Crimean Astrophysical Observatory. We also used circularly polarized spectra obtained during 2 nights in 2008 with echelle spectrograph ESPADONS mounted at 3.6-m CFHT. Effective magnetic field B_e (longitudinal component of the field integrated over visible hemisphere) of ζ Per was calculated in the line He I 6678.149 Å. Statistically significant longitudinal magnetic field ($B_e/\sigma_B > 3$) was registered in 14 from 199 single measurements. These significant magnetic field values are all in the range from -145 to $+148$ G with the mean error 27 G. We suppose the supergiant ζ Per can be magnetic, but its magnetic field properties is difficult to detect likely due to the insufficient precision of the used spectropolarimetric measurements compared to the expected field strength.

Key words: stars: early-type – stars: supergiants – stars: magnetic fields – stars: individual (ζ Per).

АНОТАЦІЯ. На поверхні $\sim 7\%$ поодиноких гарячих зірок виявлені стабільні, переважно дипольні магнітні поля які сягають інколи десятків кілогаус.

Головною гіпотезою сьогодні є те, що ці магнітні поля мають реліктове походження. Іншими словами, ці поля утворились із поля в молекулярних хмарах, з яких утворилися зірки. Останні спостереження та результати теоретичного моделювання підтверджують цю теорію: властивості глобальних полів що спостерігаються, відповідають тим, що мали б очікуватись у реліктових магнітних полів. Масивні зірки - це ті зірки, початкові маси яких приблизно у 8 і більше разів перевищують масу Сонця. Вони відіграють значну роль у хімічному та динамічному розвитку галактик. Однак їх змінність, особливо під час еволюційної стадії надгігантів, недостатньо вивчена. На сьогоднішній день магнітне поле було зареєстровано лише у трьох гарячих зірок I-II типів світності: ρ Leo (B1 Ib), ζ Ori Aa (O9.2 Ib) і ϵ CMa (B1.5 II). У цій роботі ми провели високоточне спектрополяриметричне дослідження гарячого надгіганта ζ Per (B1 Ib). Спостереження були виконані протягом 26 ночей з 1997 по 2012 рр. за допомогою класичного спектрографа, встановленого у фокусі куде 2,6-метрового рефлектора ЗТШ в Кримській астрофізичній обсерваторії. Ми також використали циркулярно поляризовані спектри, отримані протягом 2 ночей в 2008 році за допомогою ешел-спектрографа ESPADONS, встановленого на 3,6 м Канада-Франко-Гавайському телескопі (CFHT). Ефективне магнітне поле B_e (поздовжня складова поля, інтегрована по видимій півкулі) ζ Per було розраховано по лінії He I 6678.149 Å. Статистично значуще поздовжнє магнітне поле ($B_e/\sigma_B > 3$) було зареєстровано в 14 із 199 одиничних вимірювань. Усі ці значущі значення магнітного поля знаходяться в діапазоні від -145 до $+148$ гаусів зі середньою похибкою у 27 гаусів. На цій підставі ми припускаємо, що надгігант ζ Per має магнітне поле, але характер змінності якого по наявному матеріалу спостережень важко виявити через недостатню точність наших спектрополяриметричних вимірювань порівняно з очікуваною напруженістю поля.

Ключові слова: зірки ранніх спектральних класів, надгіганти, масивні зірки, гарячі зірки, магнітні поля зірок.

1. Introduction

At the surface of $\sim 7\%$ of single hot stars stable mainly dipolar magnetic fields have been detected. The main hypothesis today is that these magnetic fields are of fossil origin. In other words, these fields formed from the seed field in the molecular clouds from which the stars were formed. The recent observational and theoretical results confirm this theory: the properties of the observed fields correspond to those expected from fossil fields.

Massive stars are stars whose initial mass exceeds about 8 solar masses. These stars play a significant role in the chemical and dynamical evolution of galaxies. However, much of their variability, particularly during their evolved supergiant stage, is poorly understood.

To date only three hot supergiants have been found to host a magnetic field. Kholtygin et al. (2007) reported the possible detection of the magnetic field with polar strength 240 ± 50 G on ρ Leo (B1 Ib). Bouret et al. (2008) reported the detection of a weak magnetic field of 50-100 G on the supergiant ζ Ori Aa (O9.2 Ib). The result was confirmed by Blazere et al. (2015). Fossati et al. (2015) detected the magnetic field with polar strength of at least 13 G on the bright giant ϵ CMa (B1.5 II).

ζ Per (HD 24398, HR 1203, B1 Ib) is a hot supergiant, which main stellar parameters are shown in Table 1. We present here the results of magnetic field measurements on ζ Per.

Table 1: Stellar parameters of ζ Per.

Parameter	Value	Reference
Sp. Type	B1 Ib	Lesh (1968)
V	2.85	SIMBAD
T_{eff} (K)	22040	Zorec et al. (2009)
$\log g$	3.061	Huang & Gies (2008)
$v \sin i$ (km/s)	45	Simón-Díaz et al. (2017)
M/M_{\odot}	15.5	Tetzlaff et al. (2011)
R/R_{\odot}	26	P. Fracassini et al. (2001)
L/L_{\odot}	47039	Hohle et al. (2010)
t (Myr)	12.6	Tetzlaff et al. (2011)

2. Observations

Spectropolarimetric observations of ζ Per were carried out with the long-slit spectrograph and the circular polarization analyzer mounted in the coudé focus of the 2.6-m reflector ZTSh at the Crimean Astrophysical Observatory (26 nights from 1997 to 2012, spectral resolution $R \sim 30000$). We also used polarimetric

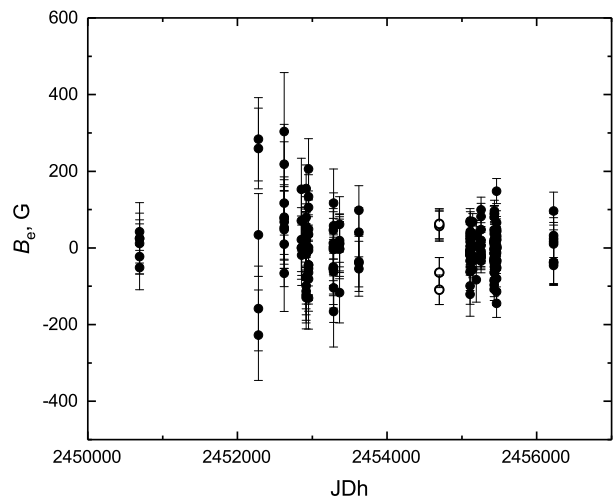


Figure 1: Magnetic field of ζ Per measured in 1997 - 2012. Filled circles indicate data obtained at ZTSh (CrAO), open circles - data obtained at ESPADONS (CFHT).

data collected during 2 nights in 2008 with the echelle spectrograph ESPADONS (spectral resolution $R \sim 65000$) mounted at the 3.6-m CFHT (Hawaii, USA). Effective magnetic field B_e (longitudinal component of the field integrated over visible hemisphere) of ζ Per was calculated in the line He I 6678.149 Å (effective Lande factor $z = 1$) with the procedure discussed in detail by Butkovskaya & Plachinda (2007).

3. Results

In Figure 1 individual magnetic field (B_e) measurements ($N = 199$) of ζ Per are presented. Statistics on the magnetic field measurement is illustrated in Figure 2. Most B_e values fall in the range from -50 to $+50$ G, and the mean value $\langle B_e \rangle = 2.6 \pm 5.2$ G. The mean error of a single measurement, $\langle \sigma_B \rangle = 52$ G, while the minimum error is 19 G. Statistically significant longitudinal magnetic field ($B_e/\sigma_B > 3$) was registered in 14 single measurements. These significant magnetic field values are all in the range from -145 to $+148$ G with mean error 27 G.

4. Conclusion

We suppose the supergiant ζ Per can be magnetic, but its magnetic field properties is difficult to detect likely due to the insufficient precision of the used spectropolarimetric measurements compared to the expected field strength.

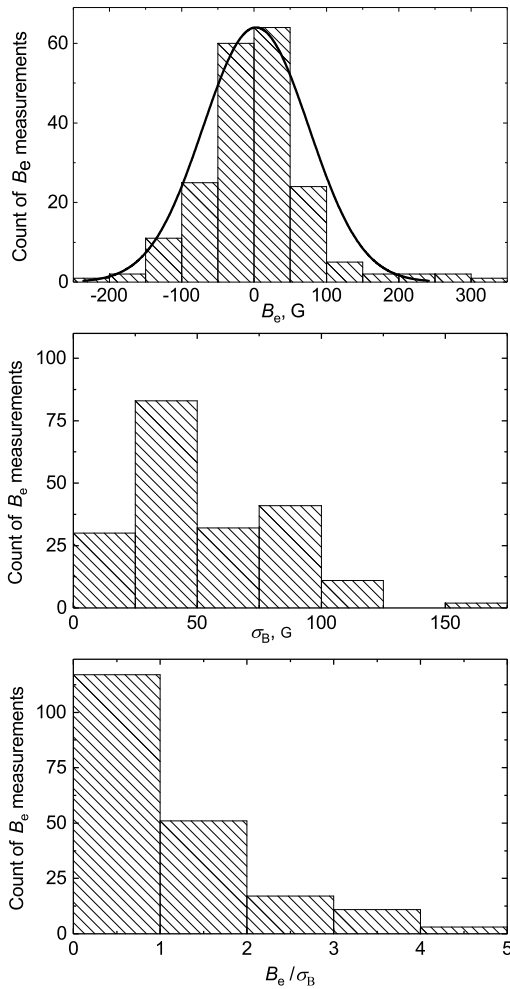


Figure 2: Distribution of the magnetic field B_e (*top panel*), its errors σ_B (*middle panel*) and signal-to-noise ratio B_e/σ_B (*bottom panel*). Normal distribution curve is shown on the top panel by the strong line.

Acknowledgements. This study particularly based on observations obtained at the Canada–France–Hawaii Telescope (CFHT). This research used the facilities of the Canadian Astronomy Data Centre operated by the National Research Council of Canada with the support of the Canadian Space Agency.

References

- Blazère, A., Neiner, C., Tkachenko, A., et al.: 2015, *Astron. Astrophys.*, **582**, A110.
- Bouret, J.-C., Donati, J.-F., Martins, F., et al.: 2008, *MNRAS*, **389**, 75.
- Butkovskaya, V. V. & Plachinda, S. I.: 2007, *Astron. Astrophys.*, **469**, 1069.
- Hohle, M. M., Neuhäuser, R., Schutz, B. F.: 2010, *Astron. Nachr.*, **331**, 349.
- Huang, W. & Gies, D.R.: 2008, *ApJ*, **683**, 1045.
- Fossati, L., Castro, N., Morel, T., et al.: 2015, *Astron. Astrophys.*, **574**, A20.
- Kholtygin A.F., Chountonov G.A., Fabrika S.N. et al.: 2007, *Physics of Magnetic Stars*, 262.
- Lesh, J.R.: 1968, *ApJSS*, No. 151, **16**, 371.
- McErlean, N.D., Lennon, D.J., Dufton, P.L.: 1999, *Astron. Astrophys.*, **349**, 553.
- Pasinetti Fracassini, L. E., Pastori, L., Covino, S., Pozzi, A.: 2001, *Astron. Astrophys.*, **367**, 521.
- Simón-Díaz, S., Godart, M., Castro, N., et al.: 2017, *Astron. Astrophys.*, **597**, A22.
- Tetzlaff, N., Neuhäuser, R., Hohle, M. M.: 2011, *MNRAS*, **410**, 190.
- Zorec, J., Cidale, L., Arias, M. L., et al., 2009, *Astron. Astrophys.*, 501, 297.

DOI:<http://dx.doi.org/10.18524/1810-4215.2020.33.216282>

INDUCING INTRINSIC γ -RAY EMISSION OF THE INTERSTELLAR MEDIUM BY INTENSE FLUXES OF PROTONS AND α -PARTICLES IN ACTIVE GALACTIC NUCLEI

D.N. Doikov

Odessa National Maritime University. Department of Natural and Technical Sciences
doikov@mail.bg

ABSTRACT. Cosmic-ray induced γ -ray emission in active galactic nuclei (AGN) has been examined in this study for the first time. Cross-sections for the formation of γ -quanta in such cosmic-ray collisions were selected in the 1-150 MeV energy range. Synthetic γ -ray spectra were computed for both interstellar gas and dust. At the same energies of particle collisions and induced emission of γ -quanta, energy intervals of diagnostic interest were determined. Specific characteristics of emission were detected in the energy ranges of 5-15 MeV and 23-30 MeV for most investigated elements. Diffuse continuous γ -ray spectra for the other energy ranges were less informative with regard to the determination of the chemical composition of interstellar gas. It has been shown that exploring cosmic-ray fluxes in the vicinity of galactic centres by employing the examined γ -ray spectra yields a pattern of their energy distribution. Diagrams of cross-sections for γ -quanta formation were computed for the α -process elements. Synthetic γ -ray spectra of interstellar gas and dust were calculated individually and collectively. It has been indicated that, under certain conditions in AGN, cross-sections for ionisation of atoms due to energy losses by cosmic-ray induced ionisation and γ -quanta emission resulting from collisions with cosmic rays are similar. It has been found that when the maximum of proton and α -particle energy distribution function falls within the investigated range of energies, it leads to the formation of the peak flux of γ -rays. This is particularly important for the interpretation of observations in the energy ranges of 5-15 MeV and 23-30 MeV. Synthetic induced γ -ray spectra of interstellar dust were computed, and methods of their observations for silicate and carbon-containing dust, which account for 80% and 20% of the interstellar-dust total mass, respectively, were determined. It has been deduced that the contribution of Compton processes to γ -quanta emission can be neglected at the investigated energies.

Keywords: Active Galactic Nuclei, Cosmic Rays, Induced γ -Ray Spectra, Diffuse Interstellar Medium.

АНОТАЦІЯ. В роботі вперше розглянуто і розраховано індуковане γ -випромінювання в активних ядрах галактик, яке виникає під дією космічних променів (далі КП). Для інтервалу енергій (1-150 MeV) підібрані перетини випромінювання γ -квантів унаслідок зазначених зіткнень. Проведено розрахунки синтетичних γ -спектрів як для міжзоряного газу, так і для міжзоряного пилу. При цих же енергіях зіткнень частинок та індукування γ -квантів визначені інтервали енергетичного

спектра, що є важливими для діагностики середовища. Визначено, що енергетичні інтервали 5-15 MeV і 23-30 MeV дають емісійні особливості для більшості розглянутих елементів. Для інших енергетичних інтервалів маємо менш інформативні для визначення хімічної структури міжзоряного газу дифузні безперервні γ -спектри. Показано, що в околицях галактичних центрів зондування потоків КП за допомогою розглянутих γ -спектрів дає структуру їх розподілу по енергіях. Обчислені діаграми перетинів утворення γ -квантів для елементів α -процесу. Синтетичні γ -спектри міжзоряного газу і пилу визначалися окремо та в сукупності. Зазначено, що за певних умов АЯГ перетину іонізації атомів в результаті іонізаційних втрат, викликаних КП та індукування γ -квантів під дією зіткнень з КП, мають близькі значення. Отримано, що якщо максимум функції розподілу по енергіях у протонів та α -частинок припадає на розглянутий нами енергетичний інтервал, то це призводить до утворення максимального потоку енергії γ -променів. Це особливо важливо для інтерпретації спостережень в інтервалах 5-15 MeV і 23-30 MeV. Обчислені синтетичні індуковані γ -спектри міжзоряного пилу та визначені способи їх спостережень для пилу зі вмістом силікатів та пилу з вмістом вуглецю за відповідним співвідношенням як 80% до 20% від загальної маси. Отримано, що при розглянутих енергіях внеском γ -квантів комптоновськими процесами можна знехтувати.

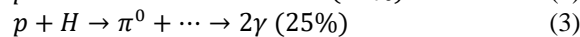
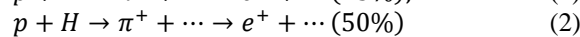
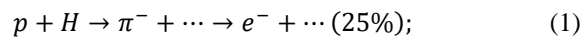
Ключові слова: активне галактичне ядро, космічні промені, індуковані спектри γ -променів, дифузне міжзоряне середовище.

1. Introduction

A distinctive feature of active galactic nuclei (AGN) is their high luminosity in all spectral bands without exception. This is why it is feasible to observe them in many diverse regions of the Universe. On such a scale, we often observe the luminosity produced just by the central region of a distant galaxy, which may extend to a radius of about 1 kpc, rather than the integrated luminosity of the entire galaxy. It has been thought up until recently that the total flux of γ - and X-rays, being initiated by a galactic central supermassive black hole (GCSMBH), originates only in the region of 1 pc, which is quite narrow on a galactic scale. Taking into account the effects of intrinsic

magnetic fields localised in accretion discs around GCSMBH, it can be deduced that it is only charged cosmic rays with energies not exceeding 3 GeV that, being deviated, return to the galactic centre through the halo (Dermer, 1986). As to the particles of higher energies, they generally leave such galaxies. In our Galaxy, a power-series semi-empirical energy distribution of protons and α -particles is observed along the disc, suggesting that maximum number of particles thus distributed have energies from 5 MeV to 150 MeV. The integrated optical and X-ray luminosity at 1 keV and γ -ray luminosity at 1 GeV is close to 10^{46} – 10^{47} erg sec⁻¹. This has been indicated in the study (Fan *et al.*, 2016), wherein observational catalogue data obtained with different space telescopes are presented and cross-correlated. In particular, they collected and processed luminosities at the afore-indicated energies from catalogues of BL Lacertae objects (BL Lac type of AGN). In this case, having observed luminosities available, it is reasonable to consider the kinetics of collisions of protons and α -particles with target atoms of the interstellar medium in AGN, resulting in induced emission of γ -rays of nuclear-reaction origin. Moreover, in this case, precise boundary conditions of the physical problem of proton and α -particle collisions are known. Astrophysical interest in such processes lies in the fact that they are quasi-elastic in the range of collision energies from 5 MeV to 150 MeV with induced γ -quanta produced in these collisions, among other products. Experimental cross-sections for such reactions have been selected and adopted by the author from the nuclear data services (Tanaka *et al.* 1994) and reported in the present paper. Even though there are some peculiarities in the induced γ -ray spectra, it will be deduced from the figures presented below that these spectra are continuous. The peculiarities per se are not narrow nuclear resonances as they cover quite a wide range of energies.

Processes of cosmic rays colliding with atoms of the interstellar medium become explicitly inelastic at energies reaching 1-3 GeV and produce pions, electrons and positrons in proportions 0.25:0.25:0.5. Positrons, in turn, produce only two γ -ray lines (at 0.511 MeV or 1.022 MeV) while the neutral pion decay generates a single γ -ray line at 67.5 MeV. Therefore, a distinctive feature of intense fluxes of cosmic rays is that they are associated with continuous, collision-induced diffuse γ -ray spectra, as well as γ -ray lines, commonly attributed to products of series of nuclear decays of Δ -resonance via the following channels (Dermer 1986):



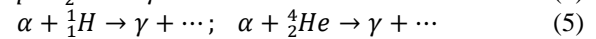
The intensities of cosmic-ray fluxes falling on a square centimetre along discs and halo of such galaxies are 10^8 – 10^{10} higher than those of similar fluxes in our Galaxy (one particle per square centimetre). Cosmic ray transport from the central to peripheral regions of AGN is described in sufficient detail in a number of papers (Lazarian & Yan, 2002; Yan & Lazarian, 2004; Yan, 2015). The takeaway of these studies is the detection of a high degree of scattering cosmic-ray fluxes directed from the AGN centres by large-scale turbulent structures of galactic discs. Thus, on a scale of up to 1 kpc,

cosmic-ray fluxes have time to become diffuse, whether it is the galactic disc or halo that they are transported through. Consequently, the induced γ -ray emission described above arises throughout the periphery of AGN.

The present paper consists of five sections, including Introduction, three main sections and Summary. Sections 2 and 3 provide the results of computing synthetic γ -ray spectra induced by interstellar gas and dust both individually and collectively. Section 4 presents the discussion and conclusions. We introduce new criteria obtained for processing observational data on the composition of cosmic rays and γ -ray spectra of AGN adopted from available catalogues of the FERMI and PAMELLA missions. Also, the physical nature of the investigated phenomena in AGN is discussed.

2. Γ -ray emission induced by interstellar atoms in AGN

As shown in the previous section, the main contribution to the processes of inducing γ -quanta emission is made by collisions of protons and α -particles with atoms in the interstellar medium. The contribution to the similar process by the leptonic component, associated with electrons and positrons, can be neglected. Thus, we obtain the most common reactions, which look as follows:



Cross-sections for the reactions responsible for producing γ -quanta have been collected from miscellaneous sources and represented graphically below. The average distribution of matter in AGN from the central to peripheral regions varies within the number density range: $n_{ism} \approx (10^8 - 10^4)$ cm⁻³. Fluxes of protons and α -particles, $I_p(R_{per})$ and $I_\alpha(R_{per})$, depending on the distance from the AGN centre, R_{per} , can be written as the following simplified relationships:

$$I_p(R_{per}) = I_{p0}(R_{per})/R_{per}^2; \quad I_\alpha(R_{per}) = I_{\alpha0}(R_{per})/R_{per}^2 \quad (6)$$

The energy spectrum of cosmic rays, $L_p(R_{per}), L_\alpha(R_{per})$, follows a power law. As compared to cosmic rays in our Galaxy, the spectra $L_p(R_{per}), L_\alpha(R_{per})$ are quite similar, having the same power, but different initial energies of particles. This is why, as an initial approximation, the powers for the afore-indicated distributions will be the same while initial distributions will be adopted from observational catalogues in similar fashion as described in the study (Fan *et al.* 2016). The final stage of determining the intensity of energy flux at a given wavelength is to establish a relationship between cross-sections for the processes of generation of secondary (induced) γ -quanta and collision energies of protons, $\sigma_\gamma(E)$, and α -particles, $\sigma_\alpha(E)$.

In the figures 1-10 we represent graphically the dependences of the target cross-sections on the energies E of the relevant collisions with interstellar atoms in AGN. The cross-sections σ_γ and σ_α , represented along the Y-axis, are expressed in millibarns (1 mbn = 10^{-24} cm²). As to the cross-sections for the yield of the target induced (secondary) γ -quanta, the energy E is expressed in MeV. The other

chemical elements in Mendeleev's periodic table exhibit rather low number densities, hence their induced spectra are only considered in some specific cases; in particular, in gas-and-dust aggregates. Carbonates and silicates comprise 20% and 80%, respectively, of interstellar dust grains. Dust grains account for 1% of the mass of the matter in between interstellar clouds. The fraction of dust inside dense clouds is several times larger due to the dust fragmentation. Therefore, it is reasonable to expect observing induced γ -ray emission, produced in interactions of dust grains with hadronic component of intense cosmic-ray fluxes. Cosmic-ray particles contain such elements as C, N, O, Si, Al, Mg, Mn, S and Fe. Optical, IR and radio spectra have served as the primary tool for studying the emission from dust grains until recently. Some interest in regard to intrinsic spectra of dust has only arisen after the Hubble Space Telescope (HST) mission discovered the soft X-ray scattering by microscopic particles (nanoparticles) produced in Novae (white dwarfs). In the present paper, hard X-ray and γ -ray emission from dust is considered to be exclusively induced. The γ -ray background produced by interstellar atoms contrasts with induced emission from dust in gas-and-dust aggregates, since the abundances of the afore-listed heavy metals in such dust grains are relatively higher. Observations of AGN performed by the FERMI and PAMELA space missions have proven the generation of intense fluxes of cosmic rays therein. In the next section, we will present cross-sections and spectra of γ -ray emission from dust, induced by collisions with such protons and α -particles.

3. Induced γ -ray emission from interstellar carbon-bearing dust in AGN

Cosmic-ray dust is comprised of a variety of chemical compounds, with the α -process elements predominating

over the others. The problem of the formation of its induced γ -ray emission comes down to the determination of induced γ -ray emissions from its components. Let us consider systematised cross-sections for induced γ -quanta from major elements comprising dust grains. With regard to graphite dust, it is sufficient to examine such cross-sections for pure carbon and its most common compounds, including simple oxides and complex compounds, such as carbonates. The mentioned cross-sections are illustrated below with the same legend as in previous figures. A specific spectroscopic feature of the CNO elements is that induced-emission peaks from all these elements are observed at energies 5-15 MeV and 23-30 MeV. In these energy ranges, induced γ -ray emission reaches its peak while there are distinctive characteristics of the emission typical for particular elements. At energies of 50-150 MeV, the diagnostic potential of the method of induced γ -ray emission decreases, making it less informative and only suitable for computations and analyses of the mean fluxes of diffuse γ -ray emission. Therefore, in the energy ranges specified above, the radiation from distant AGN originates not only from their central regions, but also throughout the periphery. It turns out that the presence of intense cosmic-ray fluxes is a prerequisite for maintaining the AGN luminosity in the γ -ray energy range.

Studying cosmic rays in our Galaxy has shown that the peak distribution of protons and α -particles falls in the investigated range of energies, which results in the induced- γ -quanta yield factor reaching its maximum. In such a case, the procedure of constructing integral induced γ -ray spectra of AGN is simplified. Prior to strict computation of the induced-emission synthetic spectra, we can estimate the probability of inducing a γ -quantum, given the boundary conditions of the physical problem.

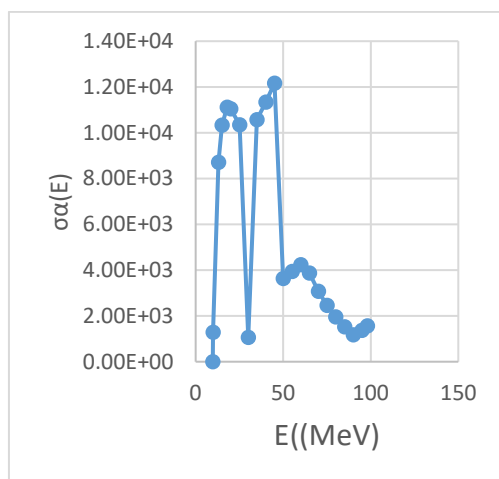


Figure 1: Reaction $\alpha + H \rightarrow \gamma + \dots$

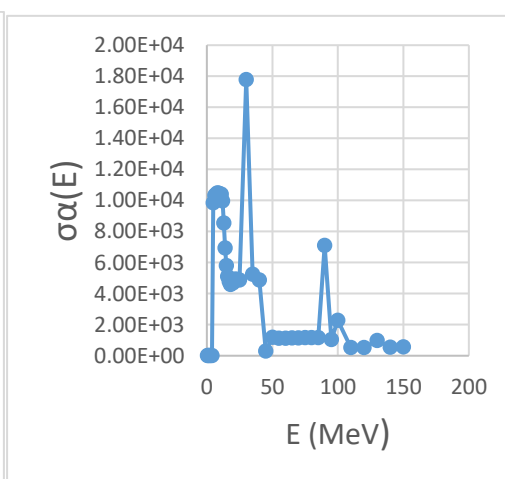


Figure 2: Reaction $\alpha + He_4 \rightarrow \gamma + \dots$

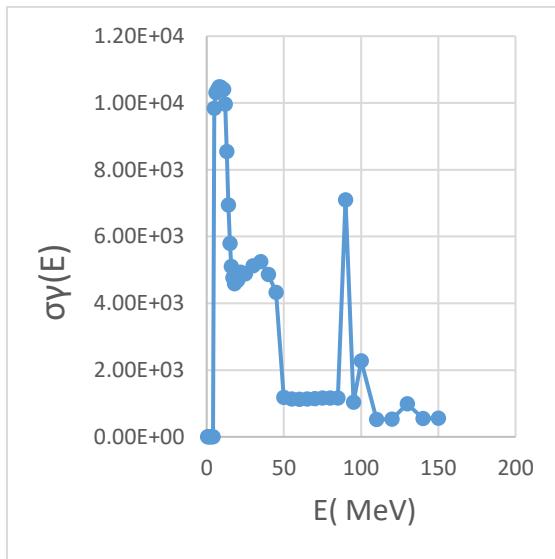


Figure 3: Reaction $p+C12 \rightarrow \gamma + \dots$

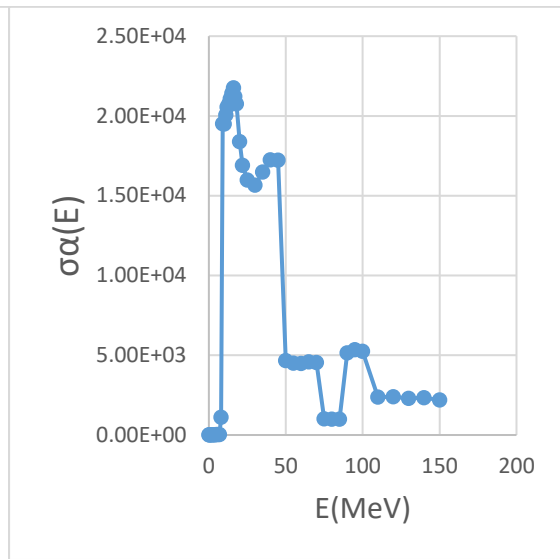


Figure 4: Reaction $\alpha+C12 \rightarrow \gamma + \dots$

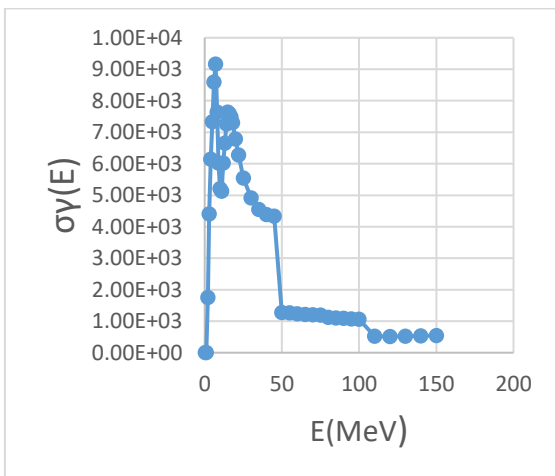


Figure 5: Reaction $p+C13 \rightarrow \gamma + \dots$

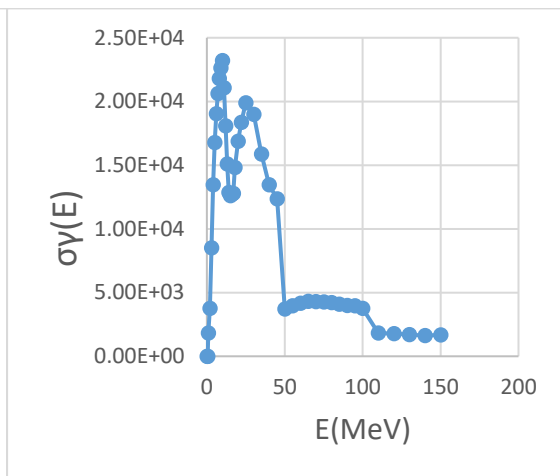


Figure 6: Reaction $\alpha+C13 \rightarrow \gamma + \dots$

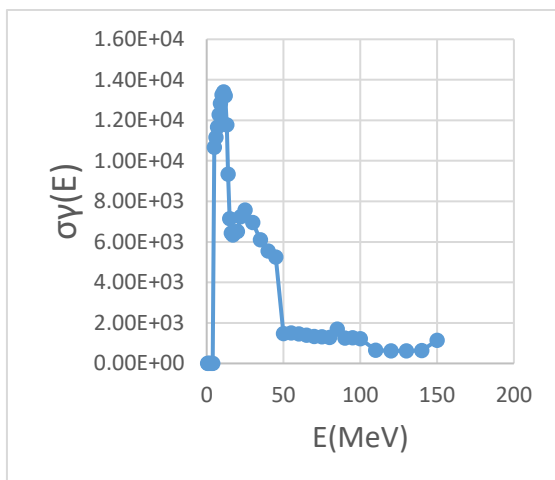


Figure 7: Reaction $p+O16 \rightarrow \gamma + \dots$

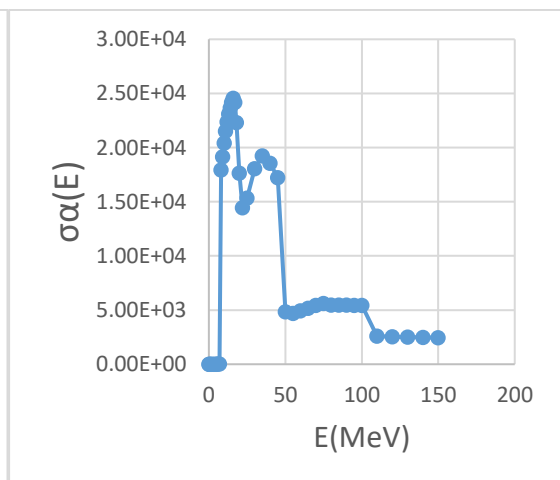
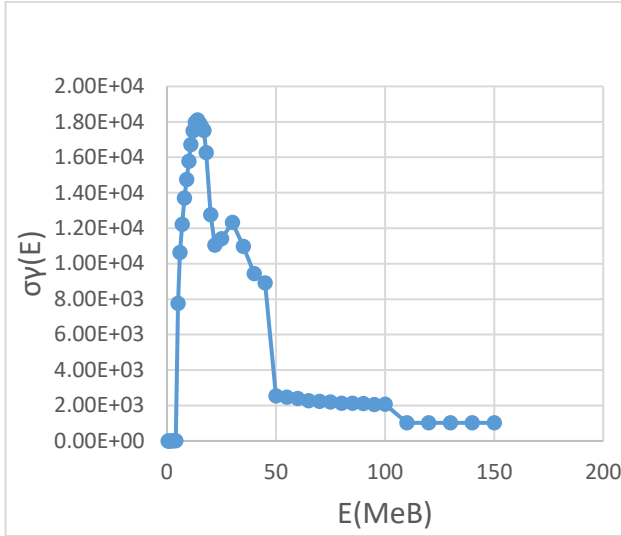
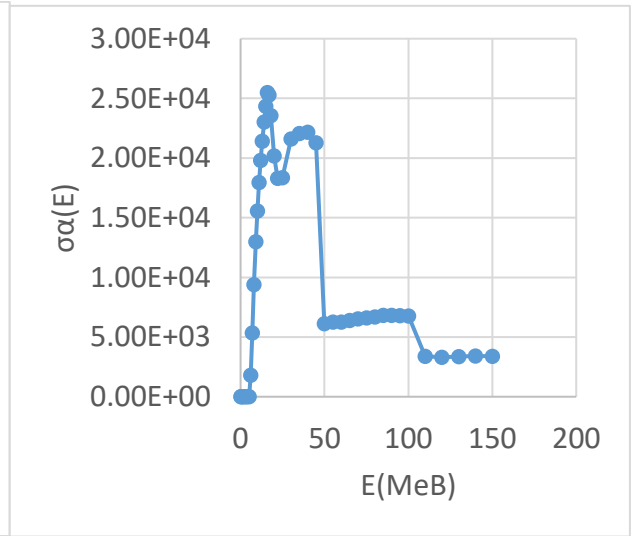


Figure 8: Reaction $\alpha+O16 \rightarrow \gamma + \dots$

Figure 9: Reaction $p + \text{Si}28 \rightarrow \gamma + \dots$ Figure 10: Reaction $\alpha + \text{Si}28 \rightarrow \gamma + \dots$

Physically, such a probability will be equal to 1 when the product $n\sigma_p L \geq 1$ or $n\sigma_\alpha L \geq 1$. The proposed conditions for interstellar gas are met on the galactic disc scale ($L \approx 10^{20}$ cm). As to gas-and-dust aggregates (interstellar clouds), such a condition, given their dimensions on a scale of $L \approx 10^{18} - 10^{19}$ cm, is fulfilled for the bulk of interstellar clouds. The concept of cosmic-ray flux in AGN is quite conventional. As mentioned in a series of works (Lazarian & Yan, 2002; Yan & Lazarian, 2004; Yan, 2015), high-energy cosmic-ray particles with $E_{Cr} \leq 3 \text{ GeV}$, being trapped by mean galactic magnetic fields, experience diffuse scattering. The whole bulk of γ -ray active medium is filled with protons and α -particles. Consequently, the appearance of such a medium will be defined by a formula similar to the Osterbrock-Lucy escape probability (OLEP) formula, modified by Városi & Dwek (Városi & Dwek, 1999). Computing the radiative transfer in diffuse medium requires preliminary calculation of cross-sections for the absorption (or respective absorption coefficients), $\sigma_{ab}(k_{ab})$, and quanta scattering, $\sigma_{sc}(\sigma_{sc})$ in the specified energy range. The cross-section σ_{ab} was adopted from the study (Kozma & Fransson, 1992). The cross-section σ_{sc} is employed from the previous paper of the author (Doikov 2019).

In the figures presented above, we can see the cross-section for γ -quanta emission, σ_{em} . Then, having computed the value ω , we can define the flux of quanta towards an observer, $F_E(R_{per})$.

$$\omega = \frac{\sigma_{em}}{\sigma_{ab} + \sigma_{sc}}; F_E(\tau) = \frac{\pi\epsilon}{\rho\kappa} \left[1 - \frac{1}{2\tau^2} + \left(\frac{1}{\tau} + \frac{1}{2\tau^2} \right) e^{-2\tau} \right] \quad (7)$$

The ratio between emissivity and absorptivity per one gram of matter, ϵ/κ , corresponds to the ratio of cross-sections for emission and absorption (per one atom). Provided that the cosmic-ray flux penetrating the galactic disc is scattered with increasing depth, the emissivity of matter for an external observer will be growing with increasing depth of the disc. Simultaneously, protons and α -particles will be losing their kinetic energies in the normal direction towards the surface proportionally to increasing depth of the disc. In contrast to problems in stellar

astrophysics, the number density of matter in galactic discs does not vary significantly in the indicated direction.

It also should be noted that, on a scale of the galactic disc depths, each proton or α -particle collides with at least one of the interstellar atoms and generates a single γ -quantum. When considering a disc as diffusively radiating, we suppose that the optical depth, τ , equals to zero on the surface of such a radiating disk. To simulate graphical representation in future papers, we reduce formula (6) to a form, which is more suitable for computations. In so doing, the cross-section σ_{sc} will be reckoned as the cross-section for Compton scattering of γ -quanta by atomic electrons. In the study (Kozma & Fransson, 1992), the following ratios have been reported: $\sigma_{ab}(\text{H}) = 0,06Z_{\text{H}}m_p \text{ cm}^2$ for hydrogen and $\sigma_{ab}(\text{He}) = 0,06Z_{\text{He}}m_p \text{ cm}^2$ for helium. For the rest of elements, the ratio is $\sigma_{ab}(i) = X_i 0,06Z_i m_p \text{ cm}^2$, where X_i, Z_i are the abundances and charge numbers of the examined chemical elements. When factoring in the contribution by interstellar dust, we adopt data obtained in the IR studies of the galactic dust, reporting that it is comprised of 20% of carbon-containing dust and 80% of silicates.

In conclusion of this chapter we presented the synthetic spectra from all AGN's disc. More specifically, the outflows energetic flux – $F_{\text{out}}(E)$ (Fig. 11) of γ -quanta created by its periphery, located outside the central zone of 1-2 parsecs. The full synthetic spectra are calculated in (0,1–150) MeV interval and consists contribution by combination of the induced γ -ray emission and photo-ionization, Compton, electron-positron scattering. In this case we used solar abundancies of the AGN's ISM. The probability of γ -quants escaping from peripheral AGN's galactic disc's a presented in a formula (7) in square brackets, are calculated and presented in Fig. 12. Number densities – $N = 10^4 \text{ cm}^{-3}$ are mean values for AGN's ISM. Galactic discs with 200 pc depths and radial sizes we propose how $R=400$ pc. The changing of this AGN's parameters leads to increasing of the energetic flows $F_{\text{out}}(E)$. The Fig. 13 presented optical dependences $\tau(E)$ for this galactic discs.

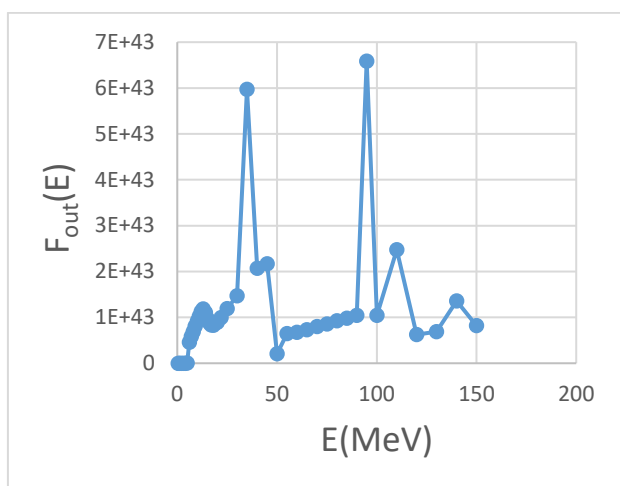


Figure 11: Synthetic spectra from AGN's ISM with Sun abundance $F_{out}(E)$

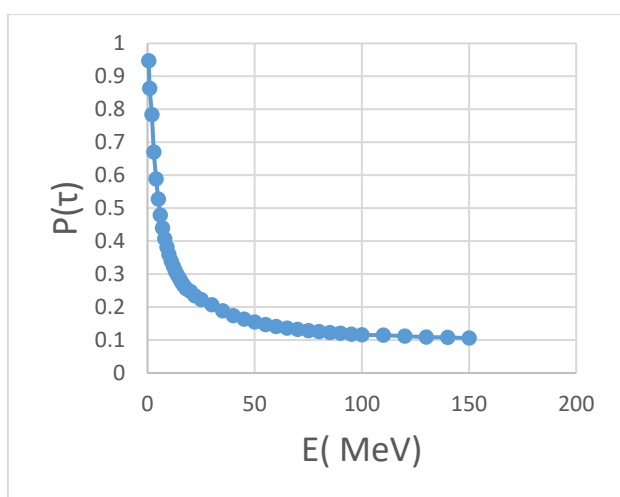


Figure 12: The γ -ray photon escape probability $P(\tau)$ from AGN's disc with sun abundances

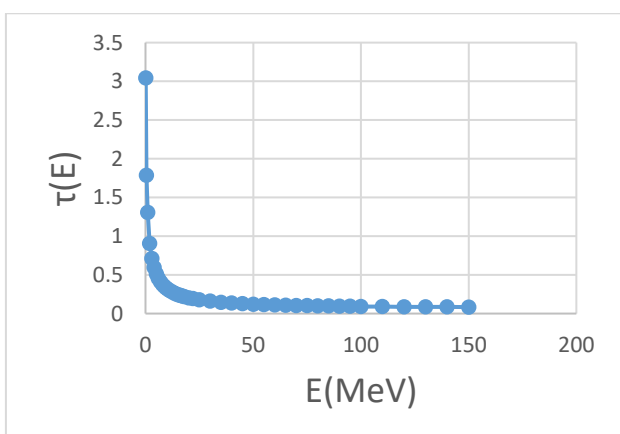


Figure 13: The AGN's ISM optical depth $\tau(E)$ with Sun abundances

4. Discussion and conclusions

Measurements of the intensities of hard γ -ray fluxes from compact sources have been of particular interest recently. In this regard, soft γ -quanta 0.511-5 MeV provide information

mainly about nuclear decays as β -transformations. Induced emissions in the 5-150 MeV energy range, examined in the present study, result from collisions between cosmic rays and interstellar atoms in AGN. Cross-sections and spectra of such processes, presented in this paper, enabled us to estimate the composition of radiation fields in the peripheral regions of AGN, located at a distance greater than 1 kpc, and also to determine its particular spectroscopic value in the region of 5-50 MeV, wherein collisions of protons and α -particles, comprising cosmic rays, with the α -process elements manifest themselves. In other words, spectra of induced γ -quanta are analogous to continuous stellar spectra. Meanwhile, the nuclear resonance lines, accompanying radiative transitions in such collisions, will be reckoned as analogous to narrow spectral γ -ray lines. Taking into account the relationship between cosmic-ray fluxes and γ -ray spectra induced by their collisions, described in the previous sections, the indicated γ -ray spectra make it possible to reconstruct a dynamic structure of both directed and scattered fluxes of cosmic rays. For distant AGN, the proposed method is the only feasible way to directly study parameters of cosmic-ray fluxes. A portion of energy transferred by the hadronic component of cosmic rays is defined by the structure of accretion discs around supermassive black holes in AGN. Implementation of the Blandford-Znajek mechanism (Blandford & Znajek, 1977), which describes the acceleration of charged particles around GCSMBH up to the cosmic-ray energies (ranging from MeV to GeV), requires the presence of strong fluctuations in magnetic fields, producing a significant potential difference in the immediate vicinity of a black hole. Integrated observations of AGN in different spectral bands enable us to draw a conclusion about existing correlation between the mass of a black hole, radiative power of the accretion disc and energy output into the surrounding medium. According to observational data, a large majority of AGN can be observed as bright sources of γ -ray emission. As it follows from the present paper, when there is a correlation between energies associated with such sources of γ -ray emission and cosmic rays, it results in expected intensities of energy fluxes of γ -quanta, induced in collisions of cosmic rays with interstellar gas and dust in the 5-150 MeV energy range.

References

- Blandford R.D. and Znajek R.L.: 1977, *MNRAS*, **179**, 433.
 Dermer C.D.: 1986, *A&A*, **157**, 223.
 Doikov D.N., Yushchenko A.V., Jeong Y.: 2019, *JASS*, Rep. Korea, **36 (1)**, 21.
 Fan J.N., Yang J.H., Liu Y. et al.: 2016, *Ap J. Suppl. Ser.*, **226**, A20, 18 pp.
 Kozma C., Fransson C.: 1992, *Ap.J.*, **390**, 602,
 Tanaka S., Yamano N., Hata K. et al.: 1994, *Proc. of 8th Int. Conf. on Rad. Shielding, Arlington*, April 24-28, **2**, 965; Am. Nucl. Soc. Inc.
 Városi F., Dwek E.: 1999, *Ap. J.*, **523**, 265.
 Yan H., Lazarian A.: 2004, *Ap. J.*, **614**, 757.
 Yan H., Lazarian A.: 2002, *Ap. J.*, **566**, L105-L108.
 Yan H.: 2015, *Ap. & Sp. Sc. Lib.*, Springer-Verlag Berlin Heidelberg, **407**, 253.
 Weingartner J.C., Draine B.T., Barr D.K.: 2006, *Astrophys. J.*, **645**, 1188.

DOI:<http://dx.doi.org/10.18524/1810-4215.2020.33.216283>

MULTI-COMPONENT VARIABILITY OF PULSATING VARIABLE STARS OF RV TAURI TYPE

L.S. Kudashkina

Department of Mathematics, Physics and Astronomy, Odessa National Maritime University, Ukraine, kuda2003@ukr.net

ABSTRACT. For the group of pulsating variable stars with multi-component variability – which are currently classified as the RV Tau-type stars – the classification based on complexity of the periodograms is discussed. Periodograms were computed using the least approximation of the data with a sinusoid. The periodograms previously classified by their shape into three groups according to the presence or absence of certain structures: two peaks in a 2:1 ratio, (biharmonic signal with two waves during a main period, or the phase curve is significantly asymmetric), the presence of satellites of these peaks at the periodogram indicating the result of modulation of characteristics of oscillations. Group I includes objects showing the periodogram typical for the RV-type stars, and the ratio of the periods of the two main peaks is indicated. These oscillations appear to be relatively stable during the observations. The Group II includes objects, the periodograms of which contain signs of multi-periodicity or, vice-versa, only one clear peak, instead of two. The presence of multiple peaks may be due to multiple periods, or due to variability of the main period. The Group III includes objects, the periodograms of which are highly noisy, mainly due to a small number of observations or they do not show typical structures of RV-type stars. Such stars may be classified in the catalogue wrongly, so, additional study is needed. For periodogram analysis, the photometric observations from the international databases of AFOEV, AAVSO and ASAS were used. A least squares method is used for the analysis, to compare the variance in the deviations from the smoothed function with the variance in the initial observations. The mean light curves and the phase plane diagrams " $dx_c(\phi)/d\phi$ " vs " $x_c(\phi)$ " was compiled and analyzed for the values of the periods corresponding to the peaks in the periodograms.

Keywords: pulsating variable stars, periodogram analysis, phase plane diagrams

АНОТАЦІЯ. Для групи пульсуючих змінних зір із багатокомпонентною змінністю – зір, що наразі віднесені до зір типу RV Тау - обговорюється класифікація на основі складності періодограм. Періодограми були обчислені із використанням апроксимації сигналу синусоїдою методом найменших квадратів Вони попередньо були класифіковані за своєю формою у три групи за наявністю або відсутністю певних структур: два піки у співвідношенні 2:1 (бігармонійний сигнал із двома хвилями за основний період, або фазова крива блиску

суттєво асиметрична), наявність “супутників” цих піків на періодограмі, що вказує на результат модуляції характеристик коливань із довшим періодом. Група I включає об’єкти, що показують періодограму, характерну для зір типу RV, і вказано співвідношення періодів двох основних піків, які є порівняно стабільними протягом спостережень. Група II включає об’єкти, періодограми яких містять ознаки багатоперіодичності або, навпаки, лише один чіткий пік, замість двох. Наявність кількох піків може бути пояснена не лише наявністю кількох різних періодів, а й змінами основного періоду із часом. До III групи належать об’єкти, періодограми яких сильно зашумлені, головним чином, завдяки невеликій кількості спостережень, або вони не демонструють типових структур зір типу RV. Такі об’єкти можуть бути класифіковані у каталозі хибно, й потрібні додаткові дослідження. Для періодограмного аналізу використовували фотометричні спостереження з міжнародних баз даних AFOEV, AAVSO та ASAS. Для аналізу використовується метод найменших квадратів для порівняння дисперсії відхилень від згладжуючої (синусоїдальної) функції з дисперсією початкових спостережень. Середні криві блиску та фазові діаграми " $dx_c(\phi)/d\phi$ " від " $x_c(\phi)$ " були складені та проаналізовані для значень періодів, що відповідають пікам у періодограмах.

1. Introduction

The multi-component variability of pulsating variable stars of the type of RV Tauri (RV-type) was studied by method of the mathematical modeling of signals. For periodogram analysis, the observations from the databases of AFOEV (<ftp://cdsarc.u-strasbg.fr/pub/aftev>), AAVSO (<http://aavso.org>) and ASAS (<http://www.astrouw.edu.pl/asas>) were used (Andronov et al., 1992; Andronov et al., 2013; Kudashkina, 2003). A description of working with these databases can be found, for example, in the articles (Andronov and Marsakova, 2006; Marsakova and Andronov, 2006; Marsakova and Andronov, 2007). The methods for determination of the characteristics of individual extrema are reviewed in the articles (Kudashkina and Rudnitskij, 1988; Andronov, 2005; Andronov et al., 2016; Andrych et al., 2017; Andrych and Andronov, 2019; Andrych, Andronov, Chinarova, 2020; Andrych et al., 2020).

2. Periodogram analysis of RV Tau-type stars

A least squares method is used for the analysis, to compare the variance in the deviations from the smoothed function with the variance in the initial observations. The statistic

$$S(f) = \frac{\sigma_c^2}{\sigma_o^2} = 1 - \frac{\sigma_{o-c}^2}{\sigma_o^2}, \quad (1)$$

is used as a test-function, where O is the mean square deviation of the “observations” O from the mean. C corresponds to the “calculated” values and $O-C$, to the deviations of the “observed” values from the “calculated” ones (Andronov, 1994; Kudashkina, 2019; Andronov, 2020; Andronov et al. 2020).

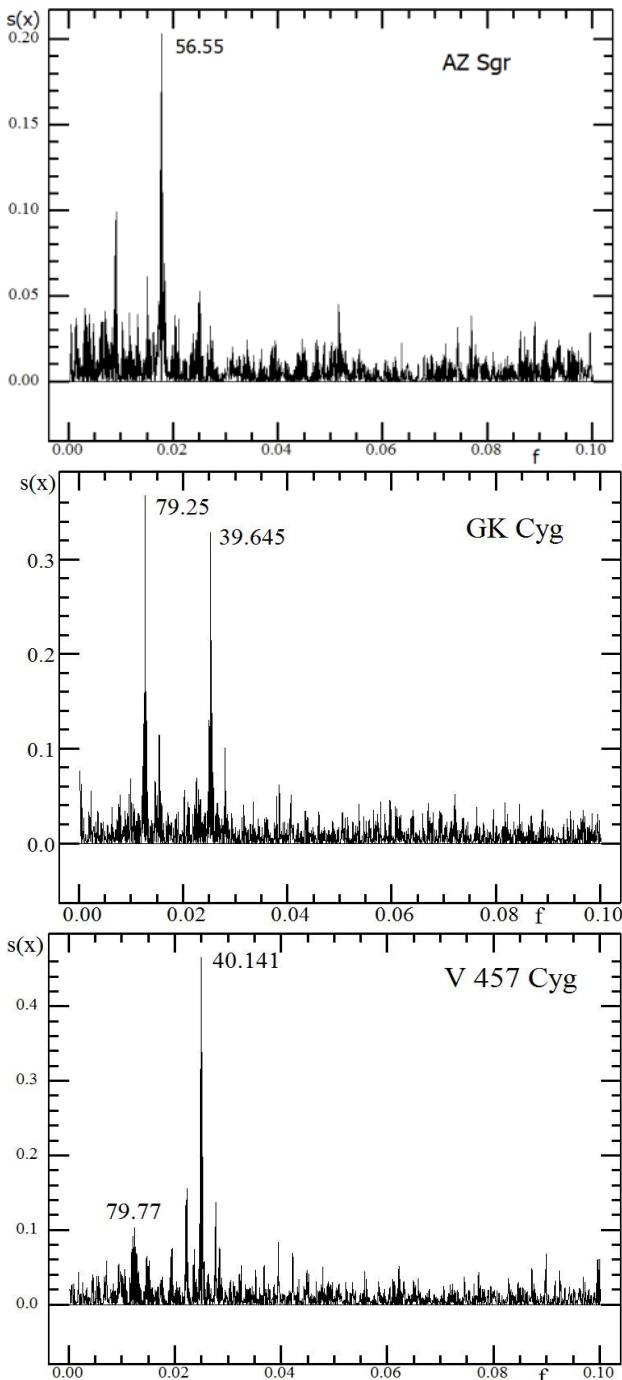


Figure 1: The periodograms for the RV Tau-type stars (from left to right) AZ Sgr, GK Cyg, and R Sge. All this stars are assigned to group I.

Figure 1, 2 show examples of the periodograms. The trial frequency $f=1/P$ is shown at the horizontal axis, and the value of the test function $S(f)$ is shown at the vertical axis.

Periodograms are previously classified by their shape into three groups according to the presence or absence of certain structures: two peaks in a 2:1 ratio, the presence of satellites at these peaks indicating the result of beats (Kudashkina, 2020).

Group I includes objects showing the periodogram typical for the RV-type stars, and the ratio of the periods of the two main peaks is indicated. The Group II includes objects, the periodograms of which contain signs of multi-periodicity (Multi-p) or, vice-versa, only one clear peak (Single-p), instead of two. The Group III includes objects, the periodograms of which are highly noisy, mainly due to a small number of observations or they do not show typical structures of RV-type stars (figures 1-3).

Sometimes, semi-regular variables show two very different periods. This phenomenologically resembles intermediate polars, in which the two very distinct periods are seen, although they have different nature (Breus et al., 2012; Breus et al., 2013).

The mean light curves with the statistically best period, the approximations are computed using the program MCV (Andronov and Baklanov, 2004; Kudashkina and Andronov, 2010). These light curves are shown in the figure 4. The characteristics of the mean light curves were calculated with the program FDCN (Andronov, 1994). These light curves are shown in the figure 5 (top). Further, phase portraits (Kudashkina and Andronov, 2017ab) were constructed: the magnitude are on the horizontal axis and its phase derivatives are on the vertical axis (figure 5 (bottom)).

It can also be assumed that in group 3 there are RV-type stars (or other types, for example, SR) that undergo a turbulent (stochastic) stage of self-oscillations before or after chaos.

Let some quantity R be the ratio of two parameters:

$$R = \mu/\gamma, \quad (2)$$

where μ is responsible for the buildup of oscillations, and γ for linear damping. With an increase in R , chaos occurs at a value of R_2 , which is greater than the value of R_1 , at which chaos disappears. A hysteresis region arises $R_1 < R < R_2$, in which either a regime with equidistant spectra or turbulence is established (depending on the initial conditions) (Rabinovich, 1978).

Taking into account the studies of different authors, such objects can be attributed, for example, DF Cyg (Plachy, Bódi and Kolláth, 2018), R Sct (Veldhuizen and Percy, 1990), U Mon (Kudashkina, 2019), S Per (SRc) (Kudashkina, 1999; Kudashkina, 2012; Kudashkina and Rudnitskij, 1994), Y CVn (Kudashkina and Andronov, 2010), RX Boo (Andronov and Kudashkina, 1988).

In this regard, I would also like to draw attention to the star IW Car (Kudashkina, 2020) for which it was not possible to reliably identify a quasi-period typical for RV-type stars, perhaps, from the scarce data available for it. Actually, several values of the periods have been determined, however, the mean light curve can be calculated only according to the largest of them.

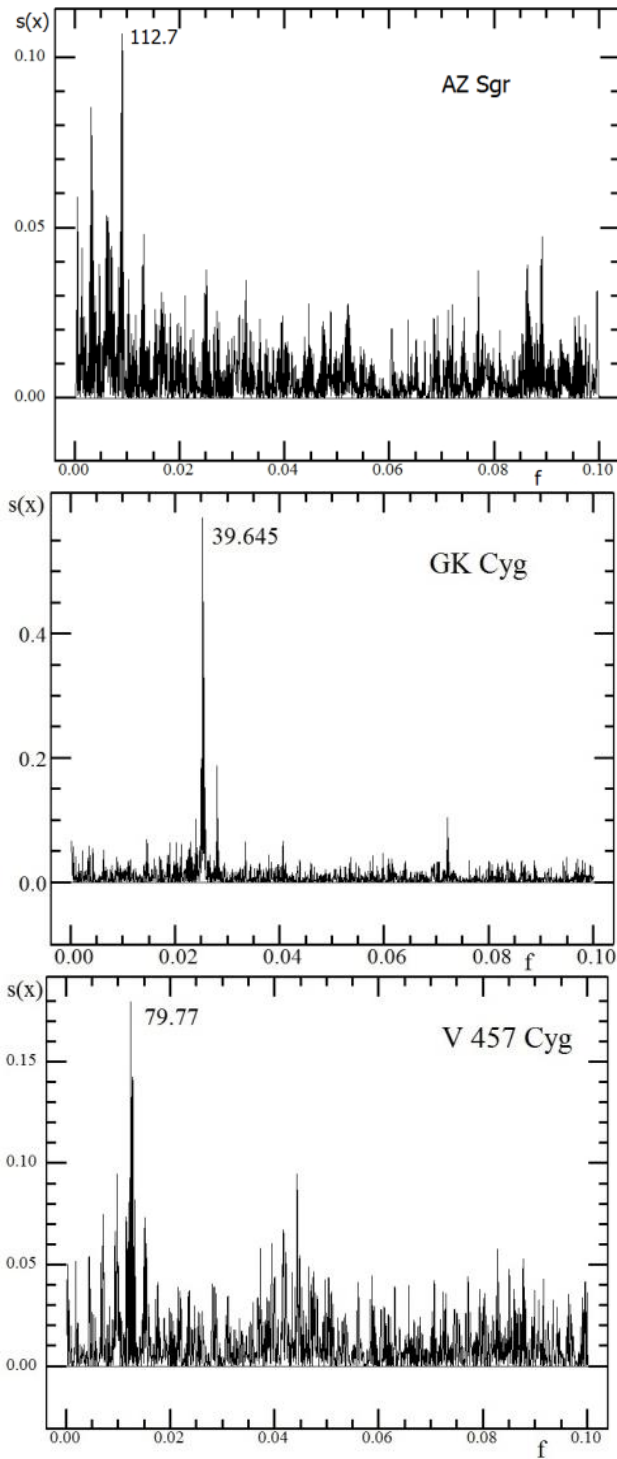


Figure 2: In these periodograms we have “prewhitened” the data by subtracting the contribution with a period corresponding to the highest peak in the figure 1.

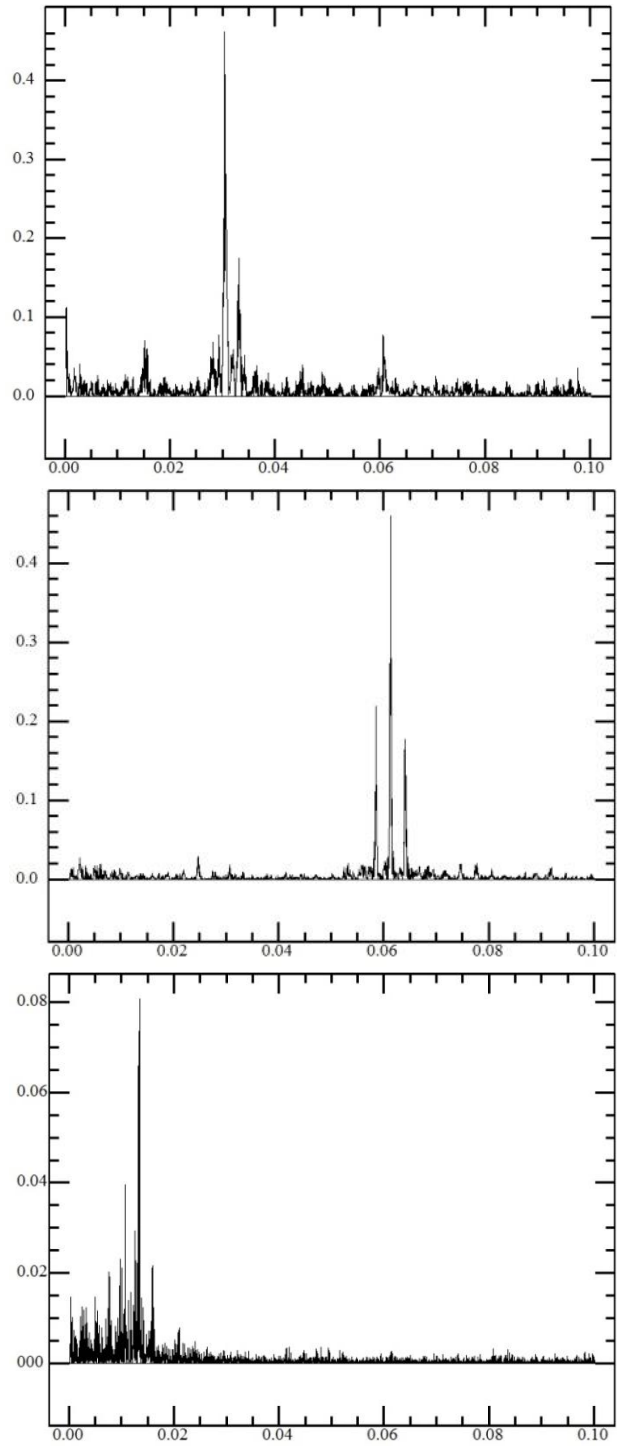


Figure 3: The periodograms for the RV Tau-type stars (from left to right) AD Aql, SZ Mon (group II) and TX Per (group III).

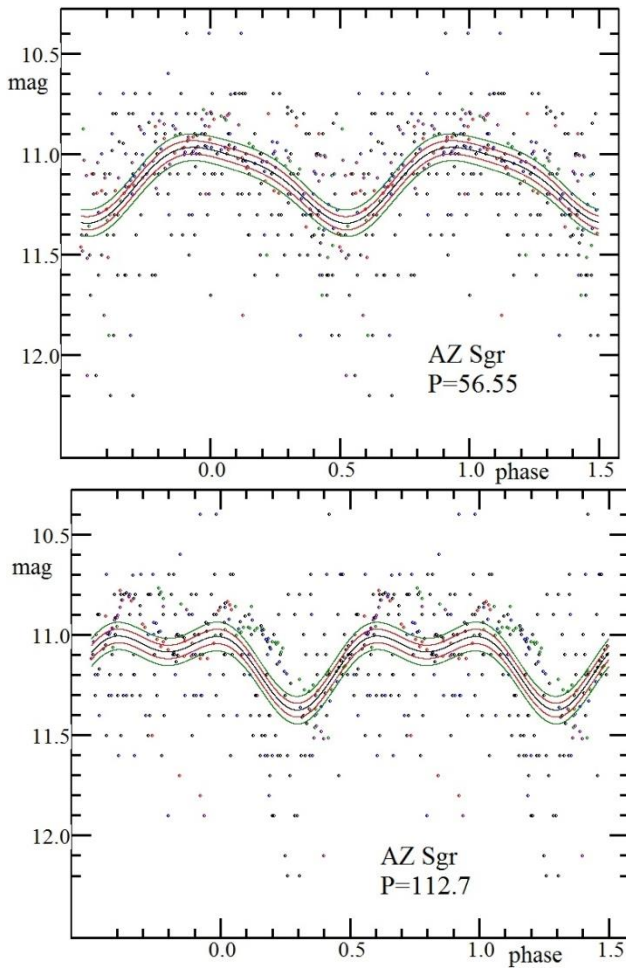


Figure 4: The mean light curve of AZ Sgr, obtained from observations by members AFOEV and ASAS. In all the figures of the light curves, the phase is set on the horizontal axis, and the brightness of the star is set on the vertical axis. The lines show the approximation and the corresponding $\pm 1\sigma$ and $\pm 2\sigma$ "error corridors".

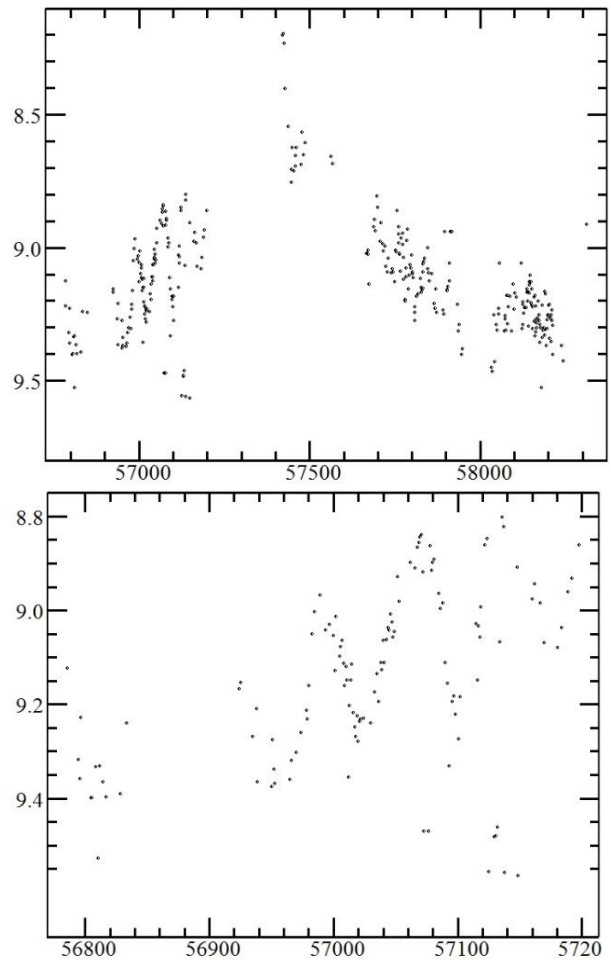


Figure 6: The light curve of IW Car obtained from observations by members ASAS (top). The "cyclic part" of the light curve (bottom).

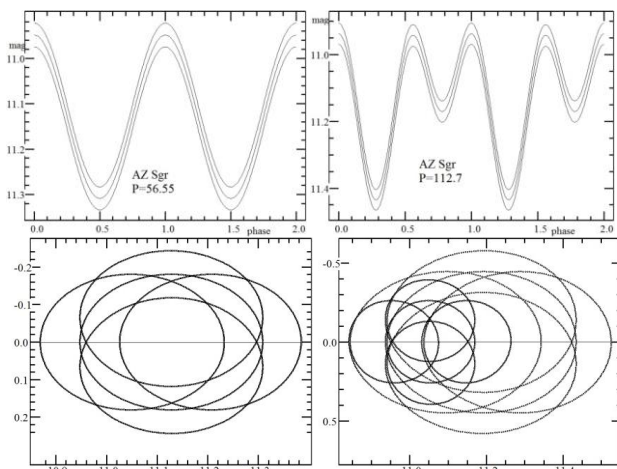


Figure 5: The mean light curves plotted with fundamental and formal periods and corresponding phase portraits for the AZ Sgr.

Even if we divide the ASAS observations into two parts (completely "chaotic" and "cyclical") and carry out the periodogram analysis of the cyclic part separately, with the obtained value of the period $P = 68 \pm 2^d$ it is impossible to calculate good mean light curve.

3. Conclusion

Thus,

- 1) from the form of the periodogram of IW Car, it can be assumed that it passes through the stage of stochastic self-oscillations, which then turn into chaotic ones.
- 2) The periodograms of several more stars have a similar form.
- 3) All stars that have been studied show beats in frequency spectra.
- 4) For stars from groups I and II, periodograms clearly show two peaks with a ratio of 2:1.

The table 1 contains basic information about the studied stars and the results of periodogram analysis.

Table 1. Characteristics of some studied RV stars.

Star	Group*	Sp _(GCVS)	P _{GCVS} , d	P, d	P ₂ /P ₁	N (obs)
AZ Sgr	I	F5V: F7-G0**	113.6	P ₁ =56.54±0.02 P ₂ =112.7±0.1 P=6305±112 P=324±1	1.99	322
GK Cyg	I		79.75	P ₁ =39.645±0.005 P ₂ =79.25±0.03 P=26.423±0.008 P=22.831±0.006	2.00	223
V 457 Cyg	I	G0	79.08	P ₁ =40.141±0.006 P ₂ =79.77±0.05 P=107.2±0.1 P=75.45±0.07	2.01	238
AD Aql	II	Fp(R)	66.03	P ₁ =33.045±0.003 P=5962±184 P ₂ =66.42±0.03 P=33.702±0.008	2.01	602
SZ Mon	II	F9-K5	32.685	P ₁ =16.3356±0.0006 P=466.1±2.4 P=16.265±0.003 P ₂ =32.64±0.01	2.00	1080
TX Per	III	G5e-K0e Gp(M2)- K0e(M2) **	78.	P=74.854±0.006 P=76.431±0.006 P=75.27±0.01 P=99.59±0.02		5128
IW Car	III	F7/8e F7/8+ A3/5Ib/II: **	72.1	P=1078±5 P=2308±80 P=276.7±0.9 P=71.6±0.1		573

* Kudashkina L. S., 2020

** <https://www.aavso.org/vsx>

References

- Andronov I.L.: 1994, *Odessa Astron. Publ.*, **7**, 49-54.
- Andronov I.L., Baklanov A.V.: 2004, *Astron. School's Rep.*, **5**, 264-272. DOI:10.18372/2411-6602.05.1264.
- Andronov I.L.: 2005, *ASP Conf. Ser.*, **335**, 37-53.
- Andronov I.L.: 2020, Knowledge Discovery in Big Data from Astronomy and Earth Observation, 1st Edition. Edited by Petr Skoda and Fathalrahman Adam. ISBN: 978-0-128-19154-5. Elsevier, 2020, p.191-224. DOI: <https://doi.org/10.1016/B978-0-12-819154-5.00022-9>.
- Andronov I.L., Breus V.V., Kudashkina L.S.: 2020, arXiv preprint arXiv:2007.14264.
- Andronov I.L., Chinarova L.L., Kudashkina L.S., Marsakova V.I., Tkachenko M.G.: 2016, *ASP Conf. Ser.*, **505**, 101.
- Andronov I.L., Kudashkina L.S.: 1988, *Astronomische Nachrichten*, **309**, Issue 5, 323-325. DOI: <https://doi.org/10.1002/asna.2113090505>.
- Andronov I.L., Kudashkina L.S., Grenishena L.V.: 2013, *Częstochowski Kalendarz Astronomiczny, ed. Bogdan Wszolek*, **9**, 211-216.
- Andronov I.L., Kudashkina L.S., Romanenko T.V.: 1992, *Perem. Zvezdy*, **23**, 23-33.
- Andronov I.L., Marsakova V.I.: 2006, *Astrophysics*, **49**, no. 3, 370-385. DOI: <https://doi.org/10.1007/s10511-006-0037-8>.
- Andrych K.D., Andronov I.L.: 2019, *Open European Journal on Variable Stars*, **197**, 65-70.
- Andrych K.D., Andronov I.L., Chinarova L.L.: 2017, *Odessa Astron. Publ.*, **30**, 57-62. DOI: <https://doi.org/10.18524/1810-4215.2017.30.118521>.
- Andrych K.D., Andronov I.L., Chinarova L.L.: 2020, *Journ. Phys. Studies*, **24**, No. 1, Article 1902, DOI: <https://doi.org/10.30970/jps.24.1902>.
- Andrych, K.D., Tvardovskyi, D.E., Chinarova L.L., Andronov, I. L.: 2020, *Contributions of the Astronomical Observatory Skalnaté Pleso*, **50**, no. 2, 557-559. DOI:10.31577/caosp.2020.50.2.557.
- Breus V.V., Andronov I.L., Hegedus T., Dubovsky P.A., Kudzej I.: 2012, *Advances in Astronomy and Space Physics*, **2**, 9-10. ADS: 2012AASP....2.....9B.
- Breus V.V., Andronov I.L., Dubovsky P., et al.: 2013, *Journal of Physical Studies*, **17**, 3902. ADS: 2013JPhSt..17.3901B.
- Kudashkina L.S.: 1999, *Vestnik Odessa State Univ.*, **4**, 55-58.
- Kudashkina L.S.: 2003, Kinematics and Physics of Celestial Bodies vol. 19, Issue 3, p. 193-233.
- Kudashkina L.S.: 2012, *Odessa Astron. Publ.*, **25/1**, 18-20.
- Kudashkina L.S.: 2019, *Astrophysics*, **62**, no. 4, 556-572.
- Kudashkina L.S.: 2020, *Annales Astronomiae Novae*, **1**, 199-204.
- Kudashkina L.S., Andronov I.L.: 2010, *Odessa Astron. Publ.*, **23**, 65-66.

- Kudashkina L.S.; Andronov I.L.: 2010, *Odessa Astron. Publ.*, **23**, 67-69.
- Kudashkina L.S., Andronov I.L.: 2017a, *Częstochowski Kalendarz Astronomiczny, ed. Bogdan Wszolek*, **14**, 283-290.; arXiv preprint: arXiv:1711.09029.
- Kudashkina L. S., Andronov I. L.: 2017b, *Odessa Astron. Publ.*, **30**, 93-97.
- Kudashkina L.S., Rudnitskij G.M.: 1994, *Odessa Astron. Publ.*, **7/1**, 66-69.
- Kudashkina L.S., Rudnitskij G.M.: 1988, *Perem. Zvezdy*, **22**, 925-926.
- Marsakova V.I., Andronov I. L.: 2006, *Astrophysics*, **49**, no. 4, 506-522. DOI: [https://doi.org/ 10.1007/s10511-006-0049-4](https://doi.org/10.1007/s10511-006-0049-4).
- Marsakova V.I., Andronov I.L.: 2007, *Astrophysics*, **50**, no. 1, 76-82. DOI: [https://doi.org/ 10.1007/s10511-007-0008-8](https://doi.org/10.1007/s10511-007-0008-8).
- Plachy E., Bódi A. and Kolláth Z.: 2018, *MNRAS*, **481**, 2986-2993. DOI: <https://doi.org/10.1093/mnras/sty2511>
- Rabinovich M.I.: 1978, *UFN*, **125**, no. 1, 123-177.
- Veldhuizen T., Percy J. R.: 1990, *JAAVSO*, **18**, 97-101.

DOI: <http://dx.doi.org/10.18524/1810-4215.2020.33.216277>

HD 121135: FEATURES OF ITS CHEMICAL COMPOSITION

T. Mishenina¹, Usenko I.^{1,2}, Kniazev A.³, Kovtyukh V.¹

¹ Astronomical Observatory, Odessa National University, 65014-UA Odessa, Ukraine, tmishenina@ukr.net

² Mykolaiv Astronomical Observatory, Obsevatorna 1, Mykolaiv 54030, Ukraine

³ South African Astronomical Observatory, P.O. 7925, Cape Town, South Africa

ABSTRACT. Low metallicity star HD121135 ($[Fe/H] = -1.5$) have been investigated spectroscopically. Its atmospheric parameters and elemental abundances have been determined, including elements of neutron (n-) capture processes, which are the keys in the study of early Galaxy enrichment. Na, Mg, Ni, Co, Sr, Y, Zr, Mo, Ba, La, Ce, Pr, Sm, Eu, Gd, Dy, Ho, Os, Th abundances were calculated using the synthetic spectrum method, factoring in the hyperfine structure (HFS) for the Eu II lines. Si, Ca, Sc abundances were determined using the equivalent widths of their lines. The carbon content was computed by the molecular synthesis fitting for the region of CH (4300-4330 Å). For the abundances determinations of C, Na, Mg, Ba, and Th the NLTE corrections have been applied.

We have determined for the first time the abundances of several n-capture elements and found that the behaviors of these elements do not show a significant trend with increasing atomic number. The elements ratios of $[Eu/Fe] = 0.06$, $[Ba/Eu] = 0.13$, $[Sr/Ba] = -0.05$ do not support the HD121135 status as a r-process enrichment star. We have obtained the thorium abundance $[Th/Fe] = 0.26$. The carbon content confirms the effect of canonical additional mixing in this star.

Keywords: stars: abundances – stars: atmospheres – stars: Population II – stars: individual (HD 121135).

АНОТАЦІЯ. Хімічні елементи, що утворювалися в результаті процесів захоплення нейтронів (n-), є ключовими у вивченні раннього збагачення Галактики. Їх великий вміст в зоряній атмосфері дозволяє тестувати процеси нуклеосинтезу. Перш за все, це важливо у випадку вивчення елементів швидкого захвату n (r-процес), що віддзеркалює, наприклад злиття нейтронних зірок або вплив магнітогідродинамічних наднових. Це також важливо для відстеження шляху збагачення цими елементами міжзоряного середовища в ранні галактичні часи. Для зірки HD121135 з металевістю $[Fe/H] = -1.5$ були визначені атмосферні параметри та розподіленість елементів.

Спектральний матеріал отримано за допомогою ешелє-спектрографа HRS Південноафриканського великого телескопа (SALT) у режимі середньої роздільної здатності ($R \sim 31000-41000$) з високим коефіцієнтом відношення сигнал до шуму, близько 100-200, в діапазоні довжин хвиль від 3900 до 8700 Å. Атмосферні параметри та хімічний склад зірки HD 121135 були визначені в підході ЛТР (локальної термодинамічної

рівноваги) з використанням моделей атмосфери Castelli & Kurucz (2004). Вміст Na, Mg, Ni, Co, Sr, Y, Zr, Mo, Ba, La, Ce, Pr, Sm, Eu, Gd, Dy, Ho, Os, Th розрахований за допомогою нової версії програмного забезпечення STARSP (Цимбал 1996), враховуючи надтонку структуру (HFS) для ліній Eu II, а вміст Si, Ca, Sc визначений з використанням еквівалентних ширин і WIDTH9 Р. Куруча. Вміст вуглецю розраховано за допомогою припасавання молекулярного синтезу до спостережного спектру в області CH (4300-4330 Å).

Для вмісту C, Na, Mg, Ba та Th ми розглянули оцінки поправок за рахунок відхилення від ЛТР.

Ми вперше визначили вміст деяких елементів нейтронного (n) захвату, включно з торієм, для HD121135. Ми виявили, що поведінка вмісту n- елементів не демонструє суттєвої тенденції росту зі збільшенням атомного числа. Співвідношення елементів $[Eu/Fe] = 0.06$, $[Ba/Eu] = 0.13$, $[Sr/Ba] = -0.05$ не підтримує визначення досліджуваної зірки як зірки зі збагаченням r-процесу. Ми отримали вміст торію зі значенням $[Th/Fe] = 0.26$. Вміст вуглецю підтверджує ефект канонічного додаткового змішування (Денисенков та Пінсон, 2008) у досліджуваній зірці.

1. Introduction

Metal-poor stars ($[Fe/H] < -1.0$) are considered to be among the oldest existing stars in the Galaxy (Beers & Christlieb, 2005; Frebel & Norris, 2015). Observations of these stars may be given an opportunity to get the data about the early conditions of nucleosynthesis for the Galactic stars, especially about the nucleosynthesis of rare elements, yields from early mergers of neutron stars (NSM) and supernovae (SN), and the chemical evolution of the Galaxy in general.

The low content of metals, primarily for the iron, indicates the possible contamination of interstellar clouds by a small number of stars producing chemical elements, especially at the very first, early stages of the Galaxy, at which the mixing of matter was still insignificant. Stars enrichment by the elements of the fast (r-) neutron capture process are very important for understanding of the early Galaxy chemical evolution (Snedden et al., 1996, Yong et al., 2013; Roederer et al., 2014; Hansen et al., 2018).

The sources of r-process elements production are in the active stage of researches. There are some transactions

that strongly support an early mergers of neutron stars (NSM) hypotheses (e.g. Lattimer & Schramm, 1974; Rosswog et al. 2014; Lippuner et al., 2017), but other authors suggest that not only NSMs can produce (create) r-process elements (e.g. Tsujimoto & Nishimura, 2015). At the same time, standard core-collapse supernovae most likely cannot produce the basic elements of the r-process (Arcones & Thielemann, 2013); however, the most likely candidate for yet another r-process formation site could be core-collapsed supernovae from strong magnetic stars (e.g. Winteler et al. 2012; Nishimura et al. 2017).

The study of r-process-enhanced, metal-poor stars are useful for identifying of the r-process sources types.

Besides, in this case, the detection of radioactive elements like Th and U is high, that provide cosmochronometric ages can also be determined (see, e.g., Holmbeck et al. 2018 and references therein).

The r-process-enhanced, metal-poor stars have historically been divided into two main categories (Beers & Christlieb 2005): the r-I stars have $0.3 < [Eu/Fe] < +1.0$, while r-II stars have $[Eu/Fe] > +1.0$; both require $[Ba/Eu] < 0$ to avoid contamination from the s-process. Variations in the lighter neutron-capture elements, such as Sr, Y, and Zr, have been observed in several stars (e.g., Spite et al. 2018) and a new limited r-process designation with $[Sr/Ba] > +0.5$ to classify stars with enhancements in these lighter elements was proposed by Frebel (2018). A subset of r-II stars (~30%) also exhibit an enhancement in Th and U that is referred to as an “actinide boost” (e.g., Hill et al., 2002; Mashonkina et al., 2014; Holmbeck et al., 2018a) – a complete explanation for this phenomenon remains elusive.

The main aim of this work is to study the elements abundances that have been formed due to n-capture processes in the atmosphere of HD 121135, with $[Fe/H]$ near -1.5. This object is one of the stars from our project to study the sources (sites) of r-process enrichment in the early Galaxy.

2. Observations and spectrum processing, radial velocities

The main characteristics of HD 121135 (HIP 67822) were taken from the SIMBAD database, in particular: Equatorial coordinates: $\alpha = 13\ 53\ 33$; $\delta = +02\ 41\ 41$ (2000) (GAIA DR2); Galactic coordinates: 336.90 ; $+61.40$ (2000).

Stellar magnitudes: $B = 10.14$; $V = 9.37$ (SIMBAD); distance = 755.00 pc (GAIA DR2); parallax (mas): 1.3245 [0.0532] (GAIA DR2); radial velocity (RV) in km/s = 125.60 [0.23] (GAIA DR2).

One spectrum of this star was obtained in 2020 with the 11-metre Southern African Large Telescope (SALT) (Buckley et al., 2006; O’Donoghue et al., 2006) and fibre-fed dual-beam echelle-spectrograph HRS (Barnes et al., 2008, Bramall et al., 2010, Bramall et al., 2012, Crause et al., 2014) in the medium resolution mode ($R \sim 31000$ - 41000) with a single exposure of 650s and a high S/N ratio near 100-200. HRS allows to provide the spectrum in the blue and red arms over the total spectral range from 3900 to 8700 Å. Primary reduction of HRS data, including over-scan correction, bias subtractions and gain corrections, was done with SALT science pipeline (Crawford et al., 2010).

All the data were processed using the software package developed by the authors based on the standard system of astronomical data reduction MIDAS. Further spectra processing, such as the continuum establishment, line depth and equivalent width (EW) measurements, etc., was conducted using the DECH30 software package by G.A. Galazutdinov <http://gazinur.com/DECH-software.html>. The radial and rotational velocities were measured by fitting of the observed spectra with models from Coelho (2014).

3. Atmosphere parameters determination

To determine the effective temperature T_{eff} , we have precised the value of T_{eff} based on the independence of the iron abundance obtained from given lines from the lower-level potential E_{low} of this line (Fig. 1). Gravity $\log g$ was determined from the ionization equilibrium balance for the Fe I and Fe II abundances. The microturbulent velocity V_t was obtained from the condition of independence Fe I abundance on the equivalent width EW (Fig. 2).

The metallicity $[Fe/H]$ was adopted as the iron abundance determined from the Fe I lines. The selection of the parameters was performed using an iterative procedure. Finally, the following parameters were adopted: $T_{\text{eff}} = 4950$ K; $\log g = 1.5$; $V_t = 1.8$ km/s.

Table 1 represents the comparison results of our data with those from other works. As can be seen in Table 1, there is a good agreement between T_{eff} , and $[Fe/H]$ obtained by different authors. However, some discrepancies are evident for $\log g$ and turbulent velocity V_t values.

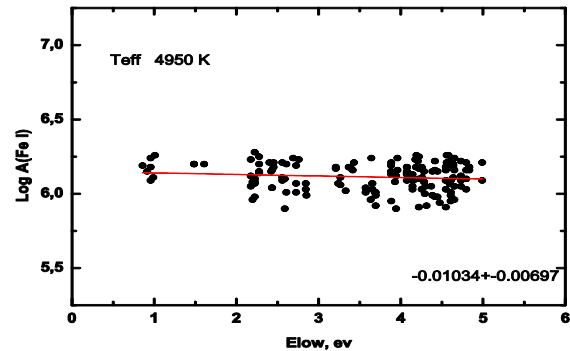


Figure 1. The dependence of $\log A(\text{Fe I})$ on E_{low}

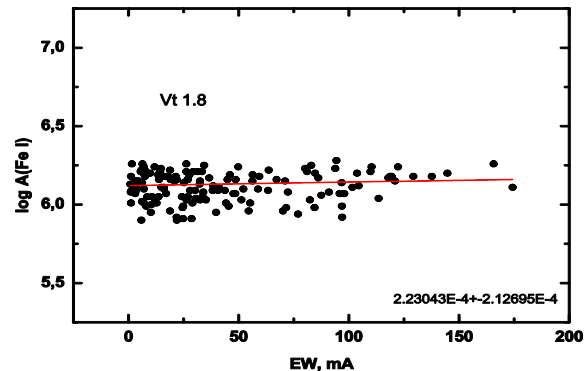


Figure 2. The dependence of $\log A(\text{Fe I})$ on EW.

Table 1. Comparison of parameters obtained by different authors

T_{eff}	$\log g$	[Fe/H]	V_t , km/s	reference
4950	1.5	-1.47	1.8	our
4934	1.91	-1.54 -1.37	1.6	Simmerer et al.2004
4934	-	-	-	Alonso et al.1999
4925	1.5	-1.57	2.1	Pilachowski et al., 1996
4927	-	--	-	Ramirez&Melendez, 2005
4925	1.5	-1.57	2.1	Burris et al. , 2000
5005	-	-	-	Gonzalez Hernandez & Bonifacio, 2009

Our determinations corroborate with the mean values of the parameters within the errors: $\langle T_{\text{eff}} \rangle = 4955 \pm 44$ K; $\langle \log g \rangle = 1.63 \pm 0.23$; $\langle [\text{Fe}/\text{H}] \rangle = -1.45 \pm 0.12$; $\langle V_t \rangle = 1.85 \pm 0.35$ km/s.

In the atmospheres of metal-poor stars the deviations from the Local Thermodynamic Equilibrium (LTE) may influence to the stellar parameters and abundance of iron (see, e.g., Lind et al., 2012). But, for such stars Roederer et al. (2014) shown that the Fe II abundance determined in the LTE approaches agree with those ones under non-LTE approximations within 0.02 dex. The obtained results enabled Roederer et al. (2014) to adopt the iron abundance derived from the Fe II lines as an indicator of metallicity [Fe/H]. Our values of the iron abundance obtained from the Fe I and Fe II lines are almost similar, and we used the Fe I abundance as metallicity [Fe/H].

4. Abundances determination

The elements abundances were determined using the LTE approximation and the atmosphere models by Castelli & Kurucz (2004). The choice of model for each star was made by means of standard interpolation for T_{eff} and $\log g$.

Na, Mg, Sr, Y, Zr, Mo, Ba, La, Ce, Pr, Sm, Eu, Gd, Dy, Ho, Os, Th abundances were calculated employing the synthetic spectrum method by a new version of the STARSP software (Tsymbol, 1996) and new version of the VALD2018 line list (Kupka et al., 1999), Si, Ca, Sc abundances using EWs of lines and WIDTH9 code by Kurucz R. Two lines of Eu II 4129 Å and 6645 Å with HFS taking into account (Ivans et al., 2006) were used. The carbon abundance was determined using the molecular synthesis fitting in the region of CH (4300-4330 Å).

For the Na, Mg, and Ba abundances determinations we have used the NLTE corrections: the NLTE departures for Na, Mg and Al at [Fe/H]~-1.5 varied from 0.03 to 0.15 dex depending on T_{eff} and $\log g$ (Andrievsky et al., 2010); the NLTE correction for the Ba lines at [Fe/H] close to -1.5 was about 0.1 dex (Korotin et al., 2015) and for 4019 Å Th line, for Sun it is 0.01 dex, and for [Fe/H] near -1.5 it is about 0.05 dex (Mashonkina et al., 2012).

The spectrum synthesis fitting of the Eu and Th lines to the observed profiles for star is shown in Figs. 3,4.

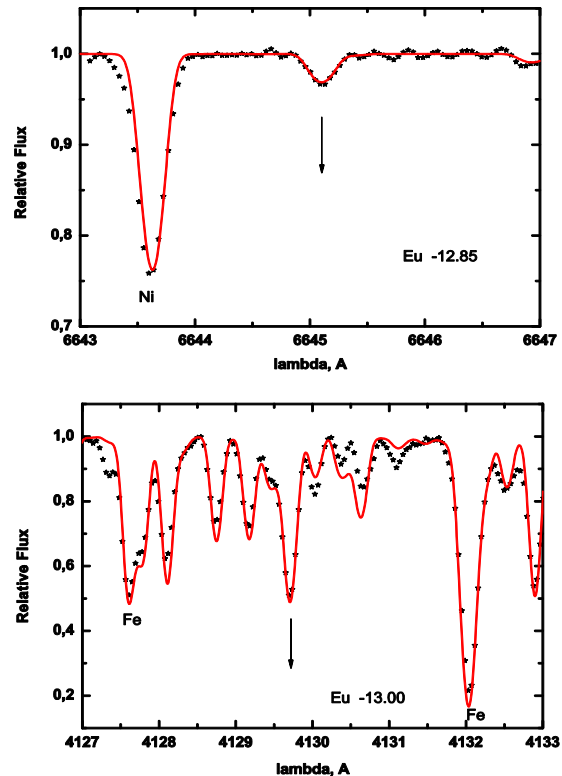


Figure 3. Observed (asterisk) and calculated (solid lines) spectra in the region of Eu II lines.

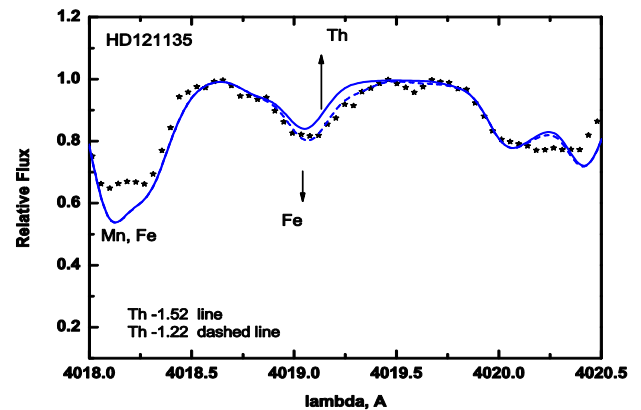


Figure 4. Observed (asterisk) and calculated (solid and dashed lines) spectra in the region of Th II line 4019 Å

To determine the systematic errors in the abundance estimates due to uncertainties in the atmospheric parameter determinations, we have derived the elemental abundances for the target star from several models with modified parameters ($\delta T_{\text{eff}} = \pm 100$ K; $\delta \log g = \pm 0.2$; $\delta V_t = \pm 0.1$). The total uncertainty due to the parameter and EW errors for the Fe I and Fe II are 0.11 and 0.12, respectively. The determination accuracy for other elements varies from 0.10 to 0.18 dex.

We compared our abundance determinations with those obtained by other authors (Pilachowski et al., 1996, Burris et al., 2001; Simmerer et al., 2004). As seen our data are in good agreement with those of other authors (Table 2).

The elemental abundances [E/H] as a function of the relevant atomic numbers for HD 121135 are depicted in Fig. 5.

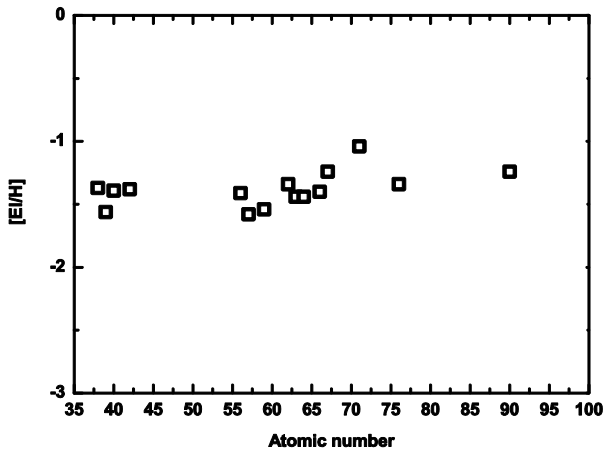


Figure 5. [E/H] vs. Atomic Number.

5. Results and discussions

We have studied HD 121135 both from the point of view of the advanced stages of stellar evolution of metal-poor stars, and in the context of n-capture elements enrichment.

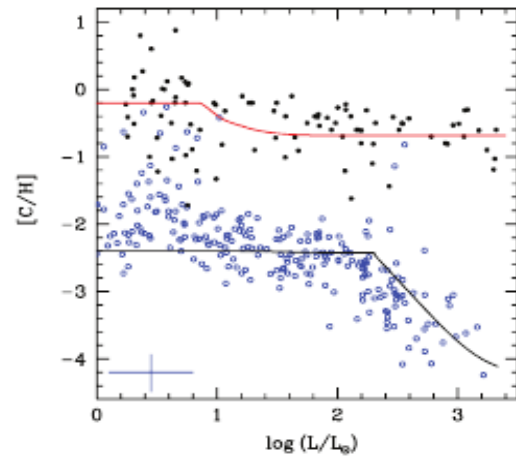
5.1. Stellar evolutionary effects

Stars in the advanced stages of their evolution may show some changes in the abundances of the certain chemical elements. Elements like Li, CNO, Na, Mg and Al may be expected these changes, which is the subject of long-term researches in the atmospheres of galactic clusters giants (e.g. Charbonnel C., 1994; 1995). Table 2 presents the abundances of the C, Na, Mg, Si, Ca, Sc, Ni, Ba and La/Eu ratio obtained in our research, as well as those reported in Pilachowski et al. (1996), Burris et al. (2001) and Simmerer et al. (2004).

Table 2. C, Na, Mg, Si, Ca, Sc, Ni, Ba abundances and La/Eu ratio

Elem	our	Pilachowski <i>et al.</i> , 1996	Burris <i>et al.</i> , 2001	Simmerer <i>et al.</i> , 2004
[C/Fe]	-0.53	--	--	-0.45
[O/Fe]	--	--	-	
[Na/Fe]	-0.04	-0.10	--	
[Mg/Fe]	0.43	0.44	--	
[Al/Fe]	--	--	--	
[Si/Fe]	0.50	0.48	--	
[Ca/Fe]	0.27	0.30		
[Sc/Fe]	-0.13	-0.06		
[Ni/Fe]	-0.02	-0.24		
[Ba/Fe]	0.19		0.20	
logA(La, Eu)	0.46(0.40)			0.37

A detailed analysis of mixing along the red-giant branch field stars within the metallicity range of $-2 \leq [\text{Fe}/\text{H}] \leq -1$ was carried out by Gratton et al. (2000). The abundances of light elements in lower-RGB stars (i.e. stars brighter than those with the first dredge-up luminosity and fainter than the RGB bump) are in agreement with the predictions made using classical evolutionary models.


 Figure 6. The carbon abundance vs. $\log L/L_{\odot}$; the figure corresponds to Figure 2 in Denissenkov&Pinsonneault (2008).

LTE analysis of several extreme metal-poor (EMP) giants in order to understand the CNO abundance variations found in some, but not all EMP field giants, considering mixing beyond the first dredge-up in the standard stellar models performed by Spite et al. (2006). They found out a C–N anti-correlation that corroborated the hypothesis that the surface abundances could be modified by the CNO processed material from the inner regions.

In our investigated star we found the carbon underabundance (Table 2) that may be agreement with the stellar evolution calculations and associated with canonical extra mixing (e.g., Denissenkov & Pinsonneault, 2008; for the CMEP stars). Figure 5 in their paper illustrated variations in the surface C and N abundances (black curve) due to canonical extra mixing with the depth $r_{\text{mix}} = 0.045 R_{\text{sol}}$ and rate $D_{\text{mix}} = 0.04 \text{K}$ in the RGB model with $M = 0.83 M_{\text{sol}}$ and $Z = 0.0001$, but the extra mixing depth does not seem to depend strongly on the metallicity (Denissenkov & Vandenberg, (2003). The authors called this universal non-convective mixing process “canonical extra mixing”

We compared our result with calculation of Denissenkov & Pinsonneault (2008). For that we have computed the value of $\log L/L_{\odot} = 2.60$ for HD121135 based on the classical formula:

$$\log L/L_{\odot} = \log M^*/M_{\odot} + 4\log \text{Teff}^*/\text{Teff}_{\odot} - \log g^*/g_{\odot}$$

were $\text{Teff}_{\odot} = 5780 \text{K}$, $\log g_{\odot} = 4.44$ and assuming the stellar mass $M^* = 0.85M_{\odot}$.

Fig. 6 presented the data by Denissenkov & Pinsonneault (2008) for canonical extra mixing at $\log L/L_{\odot} > 2.2$ (this figure correspond to black curves in Figures 2 in the cited paper). If we compare our values of $[\text{C}/\text{H}] = -2.00$ and $\log L/L_{\odot} = 2.60$ with the prediction reported in the aforementioned study, we can see that our star is located in the black curve which corresponds to canonical extra mixing for non-C-enhanced extremely metal-poor stars (Fig. 6).

5.2. Galactic n-capture element's enrichment

Based on the values of the components of spatial velocities taken from (Simmerer *et al.* 2004): U_{lsr} (km/s)= -8.2 ± 11.1 ; V_{lsr} (km/s)= -169.5 ± 24.4 ; W_{lsr} (km/s)= 111.3 ± 1.9 and the criterion for separating of stars belonging to the thick disk and the halo, for which the velocity component is equal $-V_{lsr} = 175$ km/c (Marsakov, Borkova 2005) , we can classify this star after study as a halo rather than thick disc.

The obtained pattern of the abundances of elements depending on their atomic numbers (for the elements with $AN > 50$, Fig.5), the abundance slightly increases with increasing atomic number) is in agreement with the results obtained by Sneden *et al.* (2003) for the star CS 22892-052 exhibiting a scaled solar system r-process abundance (as stars with no r-process enriched).

We compare also obtained Sr, Ba, Eu abundance with indicators of strong r-process evidence. Our values of $[Eu/Fe] = 0.06$, $[Ba/Eu]=0.13$, $[Sr/Ba]=-0.05$ do not support the definition of a star as enriched with r-process elements (r-I stars: $[Eu/Fe]>0.3$, $[Ba/Eu] < 0.0$, $[Sr/Ba]>0.5$).

6. Conclusion

- Carbon abundance confirms the operating of canonical extra mixing (Denissenkov&Pinsonneault 2008).
- The abundances of some n-capture elements were determined for the first time, including Th, $[Th/Fe] = 0.26$.
- Behavior of n-capture element's abundances don't show significant trend with atomic number increasing.
- Our values of $[Eu/Fe] = 0.06$, $[Ba/Eu]=0.13$, $[Sr/Ba]=-0.05$ do not support the definition of a star as enriched with r-process elements (r-I stars: $[Eu/Fe]>0.3$, $[Ba/Eu] < 0.0$, $[Sr/Ba]>0.5$).

References

- Alonso *et al.*: 1999, *A&AS*, **140**, 261.
 Andrievsky *et al.*: 2010, *A&A*, **509**, id. A88.
 Arcones A., Thielemann F-K.: 2013, *JPhG*, **40**, id. 013201.
 Barnes. *et al.*, 2008, *SPIE 7014*, 70140K.
 Beers T., Christlieb N.: 2005, *ARA&A*, **43**, 531.
 Bramall *et al.*: 2010, *SPIE 7735*, 77354F.
 Bramall. *et al.*: 2012, *SPIE 8446*, 84460A.
 Burris *et al.*: 2000, *ApJ*, **554**, 302.
 Buckley D.A.H., Swart G.P., Meiring J.G.: 2006, *SPIE*, 6267.
 Castelli F., Kurucz R.: 2004, *ArXiv Astrophysics e-prints astro-ph/0405087*.
 Charbonnel C.: 1994, *A&A*, **282**, 811.
 Charbonnel C.: 1995, *ApJ*, **453**, 41.
 Coelho P.R.T.: 2014, *MNRAS*, **440**, 1027.
 Crause *et al.*: 2014, *SPIE 9147*. 91476T.
 Crawford *et al.*: 2010, *SPIE 7737*, 773725.
 Denissenkov P., Pinsonneault: 2008, *ApJ*, **679**, 1541.
 Denissenkov P., VandenBerg D. A.: 2003, *ApJ*, **593**, 509.
 Galazutdinov G.: 2007, <http://gazinur.com/DECH-software.html>
 Gonzalez Hernandez J., Bonifacio P.: 2009, *A&A*, **497**, 497.
 Gratton, R.: 1989, *A&A*, **208**, 171.
 Frebel A.: 2018, *ARNPS*, **68**, 237.
 Frebel A., Norris J.: 2015, *ARA&A*, **53**, 631.
 Hansen *et al.*: 2018, *ApJ*, **858**, 92.
 Hill *et al.*: 2002, *A&A*, **387**, 560.
 Holmbeck *et al.*: 2018, *ApJ*, **859**, id. L24.
 Ivans *et al.*: 2006, *ApJ*, **645**, 613.
 Korotin *et al.*: 2015, *A&A*, **581**, 70.
 Kupka *et al.*: 1999, *A&ASuppl.*, **138**, 119.
 Lattimer J., Schramm D.: 1974, *ApJ*, **192**, 145.
 Lind *et al.*: 2012, *MNRAS*, **427**, 50.
 Lippuner *et al.*: 2017, *MNRAS*, **472**, 904.
 Marsakov V., Borkova T.: 2005, *AstL*, **31**, 515.
 Mashonkina *et al.*: 2014, *A&A*, **569**, 43.
 Mashonkina *et al.*: 2012, *A&A*, **540**, 98.
 Nishimura *et al.*: 2017, *ApJ*, **836**, 21.
 O'Donoghue D. *et al.*: 2006, *MNRAS*, **372**, 151.
 Pilachowski *et al.*: 1996, *AJ*, **111**, 1689.
 Ramirez I., Melendez J.: 2005, *ApJ*, **626**, 465.
 Roederer *et al.*: 2014, *AJ*, **147**, 136.
 Rosswog *et al.*: 2014, *MNRAS*, **439**, 757.
 Simmerer *et al.*: 2004, *ApJ*, **617**, 1091.
 Sneden *et al.*: 1996, *ApJ*, **467**, 819.
 Sneden *et al.*: 2003, *ApJ*, **591**, 936.
 Spite *et al.*: 2006, *A&A*, **455**, 291.
 Spite *et al.*: 2018, *A&A*, **611**, 30.
 Tsujimoto T., Nishimura N.: 2015, *ApJ*, **811**, 10.
 Tsybal V.: 1996, *ASP Conf. Ser.*, **108**, 198.
 Winteler *et al.*: 2012, *ApJ*, **750**, 22.
 Yong *et al.*: 2013, *ApJ*, **762**, 26.

DOI:<http://dx.doi.org/10.18524/1810-4215.2020.33.216278>

THE ON- AND OFF-STATE GENERATIONS IN CLASSICAL MICROQUASARS. 3-D NUMERICAL HYDRODYNAMICAL SIMULATIONS ON HIGH RESOLUTION GRID IN THE CASE OF INTERMEDIATE MASS TRANSFER RATE IN ACCRETION DISK OF MICROQUASAR CYG X-1

V.V. Nazarenko

Astronomical Observatory, Odessa National University,
Shevchenko Park, Odessa, 65014, Ukraine, nazaret@te.net.ua

ABSTRACT. In the present work we have computed the accretion disk time evolution over 50 orbital periods on high resolution grid (the grid size is equal to $140 \times 180 \times 140$) for microquasar CYG X-1 for the case of intermediate mass transfer rate (the initial one-point density is equal to $8.184 \cdot 10^{12} \text{ cm}^{-3}$, that corresponds to mass transfer rate order of $5 \cdot 10^{-9}$ solar mass per year). Our task in the present research is to generate ON-OFF-states (high/soft+low/hard states) in the accretion disk of the given microquasar. For this purpose we will simulate the precession motion of an accretion disk (the precession period is equal to 8 orbital ones in the present simulations). Thus, our key goal in the present work is to show that the precession motion in an accretion disk of microquasars results in ON-OFF state production. We have used the radiation cooling explicitly to obtain the real magnitudes of temperature in the calculations. The results show that in disk over the precession motion the mass accretion rate modulation occurs. This modulation is such that the states of low accretion rate replaced by the high accretion rate states, thus this replacement occur on the very short time scales, order of $15 \div 20$ minutes that in turn makes about of 0.0025 of orbital period. The relation of the magnitude of accretion rate between both states is by a factor of 100. The centre disk temperature also shows the strong modulations in the magnitudes. These temperature modulations are that that centre disk high temperatures are corresponding to the low mass accretion rate and centre disk low temperatures are corresponding to the high mass accretion rate. We interpret this situation as ON-OFF-state (high/soft - low/hard states) generation in our calculations. The ON-state time intervals are equal to OFF-state time intervals and these intervals are equal to 2 precession periods. The calculations also show that the time intervals of OFF-state are longer in space below

orbital plane relatively these intervals upper orbital plane. This circumstance is explained by as follows: the one-point stream motion is strong nonuniform over the precession motion. The most part of this stream is moving upper orbital plane and a gas is more dense in this space. Thus, a gas in space in the disk centre below orbital plane have the relatively small density and radiation cooling is not effective in this case. The temperatures are strong increased in this case and the jets are launched more often in the disk centre below orbital plane in our present research. Finally we may conclude that we show above how the precession mechanism of ON-OFF-state (high/soft - low/hard states) generation is working in our present research.

Keywords: Stars: binaries – stars: jets – methods: numerical – hydrodynamics.

АНОТАЦІЯ. В представленій роботі ми виконали чисельне обчислення еволюції акреційного диску протягом 50 орбітальних періодів з використанням числової сітки високого розділення (розмір сітки $140 \times 180 \times 140$) для мікроквазара CYG X-1, випадок проміжної швидкості переносу речовини, що дорівнює $5 \cdot 10^{-9} M_{\odot}/\text{рік}$ (початкова концентрація речовини в першій точці Лагранжа становить $8.184 \cdot 10^{12} \text{ cm}^{-3}$). Перед нами стояла задача згенерувати включені та виключені стани в акреційному диску даного мікроквазара. Для вирішення поставленої задачі нам потрібно було змодельовати прецесійний рух акреційного диску (в наших обчисленнях прецесійний період дорівнює восьми орбітальним періодам). Таким чином, ключовим завданням даної роботи було показати, що прецесійний рух акреційного диску приводить до генерації включених та виключених станів такого диску. Ми використовували радіаційне охолодження в явному виді, щоб одержати реальні значення температури в обчисленнях. Результати обчислень показали, що в диску

під час прецесійного руху модулюються сильні зміни швидкості акреції. Ці модуляції такі, що стани низької швидкості акреції змінюються станами високої швидкості акреції, це відбувається протягом дуже короткого проміжку часу, близько $15 \div 20$ хвилин, що відповідає 0.0025 орбітального періоду. Співвідношення між швидкостями високої та низької акреції складає величину близько 100 . Температура в центрі диску під час прецесійного руху також показує сильні модуляції за величиною. Ці модуляції такі, що висока температура в центрі диску відповідає низькій швидкості акреції та, навпаки, низька температура в центрі диску відповідає високій швидкості акреції. Ми інтерпретували наявність вказаних станів в наших обчисленнях як моделювання включених та виключених станів в акреційному диску. Обчислення показали, що часові інтервали виключених станів приблизно рівні часовим інтервалам включених станів і вони всі разом приблизно рівні двом прецесійним періодам. Обчислення також показали, що часові інтервали виключених станів в області нижче орбітальної площини за величиною значно більші аналогічних станів в області вище орбітальної площини. Це пов'язано з тим, що газовий потік, що рухається з першої точки Лагранжа, під час прецесійного руху диску рухається здебільшого вище орбітальної площини завдяки чому газ в центрі диску в цій області набагато щільніше, ніж газ в центрі диску нижче орбітальної площини. З цієї причини газ в області нижче орбітальної площини має високу температуру значно частіше завдяки тому, що тут радіаційне охолодження не ефективне. Та ж сама причина приводить до того, що в наших обчисленнях в області нижче орбітальної площини джети запускаються набагато частіше. Таким чином, в представлених обчисленнях ми показали як працює прецесійний механізм генерації включених та виключених станів на прикладі мікроквазара Cyg X-1.

1. Introduction

In the present research we have continued to simulate the ON- and OFF-states generations on the base of microquasar Cyg X-1 by the methods of 3-D numerical hydrodynamics (Nazarenko & Nazarenko, 2014, 2015, 2016, 2017; Nazarenko, 2018, 2019). The present work is devoted to ON- and OFF-states simulations in accretion disk on the base of classical microquasar Cyg X-1 in the case of high resolution grid. The goal of the present research is to compute the donor's wind, one-point-stream formation, its motion in Roche lobe of accretor, accretion disk formation and its slaved precession on high resolution

grid to see how the low numerical viscosity will be affects on the results. We have used such the overflow degree, that one is corresponding to the mass transfer rate order of $5 \cdot 10^{-9}$ solar mass per year.

2. The numerical algorithm

The description of the numerical algorithm in use in details is given in our previous works (Nazarenko & Nazarenko, 2014, 2015, 2016, 2017; Nazarenko, 2018, 2019). Shortly, this algorithm is as follows: to resolve the non-stationary Euler's hydrodynamical equations we have used the astrophysical variant of "large-particles" code by Belotserkovskii and Davydov (Belotserkovskii & Davydov, 1982); to simulate one-point-stream we use the donor's atmosphere model that in turn is constructed on the base Kurucz's grid (Kurucz, 1979) with the donor's parameters; we use the free-flow boundary conditions allowing to a gas to flow freely via the calculation area boundaries; to calculate mass flow real temperature we use the radiation cooling explicitly (Cox & Daltabuit, 1971). In the present calculation we use the rectangular coordinate system centred on the donor's centre. We have adopted the donor's mass to be equal to 40 solar mass and the accretor's mass to be equal to 10 solar mass. The precession period in the present simulations is about of 8 orbital periods. Hereafter all the distances will be given in units of the orbital separations; the temperature will be given in units of EV; the density will be given in units of 10^{11} cm^{-3} ; the times in the figures (see below) are given in units of the precession period. The initial one-point density is equal to $81,84$. In the present simulations the grid size is equal to $140 \cdot 180 \cdot 140$. The cell sizes in orbital plane are equal to 0.00755 and this size in the vertical direction is equal to 0.01 . The last means that in our present simulations the jets will be launched on highness of 10000 Schwarzschild radiuses.

3. The results

Before a starting precession we run our simulations over 2.6 precession periods to show a stationary state in disk over long time. The precession starting is on time equal to -0.25 . After a precession starting we run our simulation over $9 \div 10$ precession periods to have the results over long time. This time interval is containing two ON-states and two OFF-states. The mass accretion rate in a disk over OFF-states are equal to $2.5 \cdot 10^{-10}$ solar mass per year. The mass accretion rate in a disk over on states are equal to $5.5 \cdot 10^{-8}$ solar mass per year. We show mass accretion rate in a disk versus time on Fig. 1. This figure shows that to ON-states are corresponding high mass accretion rate and on contrary to OFF-states are

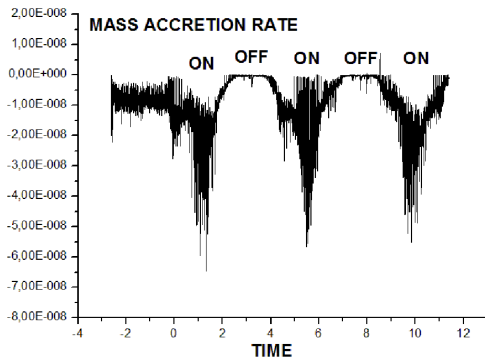


Figure 1: The mass accretion rate versus time.

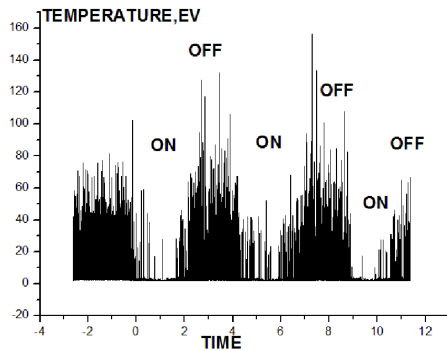


Figure 2: The central disk's temperature upper orbital plane versus time.

corresponding low mass accretion rate. This result is in the full corresponding with classical microquasars essential properties. The Fig. 2 and Fig. 3 show the central disk temperature upper and below orbital plane respectively. From these figures it is led that the transition between both states are occurring suddenly, on the very short time scale, order of 20 minutes of orbital time. The comparison of both the last two Figures show that the ON-state time intervals below orbital plane are much shortly relatively these intervals upper orbital plane. This circumstance is explained by the following: the distribution of one-point stream motion relatively the disk plane over the precession motion is strong nonuniform; the most part of this stream is moving upper orbital plane and this results in small density in the disk centre below orbital plane. As a result of it the OFF-state time intervals in the disk centre below orbital plane are very long. The last means that the jet launch below orbital plane must be occurring much often relatively this process upper orbital plane.

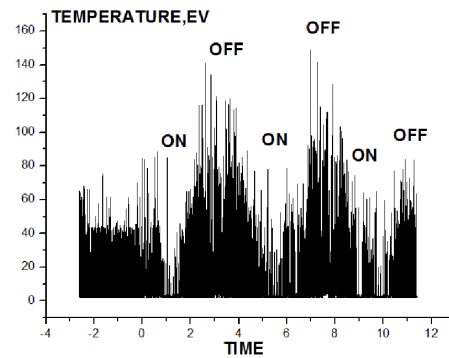


Figure 3: The central disk's temperature below orbital plane versus time.

4. Summary and conclusions

The present calculations show that in the case of intermediate mass transfer rate (order of $10^9 - 10^8$ solar mass per year) the time intervals of ON- and OFF-states are practically the same. The transition between both states is on very short time scale, order of 20 minutes of orbital plane. The low mass accretion rate is corresponding to OFF-states and high mass accretion rate is corresponding to ON-states. The relation between both mass accretion rates is order of 100 that is in good accordance with the observations commonly (Fender et al., 2003; Fender et al., 2004; Fabrika, 1993; Fabrika, 2004) and is in the very good accordance with observational data of Cyg X-1 (X-ray observations – Lachowicz et al., 2006) partially. The analyse of the present simulations show that the jet launch is occurring more often below orbital plane in comparison with this launch upper orbital plane.

References

- Belotserkovskii O.M., Davydov Yu.M.: 1982, "The large particles code in gas dynamics", Moscow: Nauka, 391.
- Cox D. P., Daltabuit E.: 1971, *ApJ*, **167**, 113.
- Fabrika S.N.: 1993, *MNRAS*, **261**, 241.
- Fabrika S.: 2004, *Astrophysics and Space Physics Reviews*, **12**, 1.
- Fender R.P., Gallo E., Jonker P.: 2003, *MNRAS*, **343**, L99.
- Fender R.P., Belloni T., Gallo E.: 2004, *MNRAS*, **355**, 1105.
- Kurucz R.L.: 1979, *ApJ. Suppl. Ser.*, **40**, 1.
- Lachowicz P. et al.: 2006, *MNRAS*, **368**, 1025.
- Nazarenko V.V., Nazarenko S.V.: 2014, *Odessa Astron. Publ.*, **27**, 137.
- Nazarenko V.V., Nazarenko S.V.: 2015, *Odessa Astron. Publ.*, **28**, 171.
- Nazarenko V.V., Nazarenko S.V.: 2016, *Odessa Astron. Publ.*, **29**, 82.
- Nazarenko V.V., Nazarenko S.V.: 2017, *Odessa Astron. Publ.*, **30**, 113.
- Nazarenko V.V.: 2018, *Odessa Astron. Publ.*, **31**, 90.
- Nazarenko V.V.: 2019, *Odessa Astron. Publ.*, **32**, 70.

DOI:<http://dx.doi.org/10.18524/1810-4215.2020.33.216284>

DETECTION OF EMERGENCE OF MAGNETIC FLUX TUBES IN THE PHOTOSPHERES OF DWARF 61 Cyg A, SUBGIANT β Aql AND GIANT β Gem

S.I. Plachinda^{1,2}, V.V. Butkovskaya^{1,2}

¹Main Astronomical Observatory of National Academy of Sciences of Ukraine,
Kyiv, Ukraine, psi1951@yahoo.com

²Crimean Astrophysical Observatory,
Nauchny, Crimea

ABSTRACT. Today, the study of stellar magnetic fields is one of the important research field in astrophysics because it provides us, in addition to physics, with information about space weather in the orbits of Earth-like planets in stars other than the Sun. Local magnetic fields on stars with convective envelopes are small-scale magnetic fields different in nature and structure from their global magnetic field. Unlike the Sun, through direct measurements we are able to measure only the magnetic field integrated over the visible disk of stars. However, we can register the magnetic field in the leading spot during the time interval when the corresponding magnetic flux tube already emerges on the surface of the star, and the magnetic flux tube of the following spot is still hidden in the interior under the photosphere. Our research is based on the spectropolarimetric observations carried out with 2.6m Shajn telescope equipped with the echelle spectrograph ESPL, CCD, and the Stokesmeter as a circular polarization analyzer. For measuring stellar magnetic fields the Single Line (SL) technique was developed at CrAO. This technique is based on the calculation of Zeeman effect in individual spectral lines. A key advantage of the SL technique is its ability to detect local magnetic fields on the surface of stars. Using SL technique emergence of large magnetic flux tubes at the surface of stars of V-IV-III luminosity classes (61 Cyg A, β Aql, β Gem) were first registered. We review the results of the study of local magnetic fields in these stars, including the results of modeling of magnetic field flux density and the size of their starspots. We also present the new results of spots modeling on β Aql. According to the considered geometric model, the rotational variability of the magnetic field and the extreme value of the field obtained from observations, we assume that the extreme radius of the spots at the surface of β Aql may exceed 9° .

Key words: stars, stellar magnetic activity, stellar magnetic fields.

АНОТАЦІЯ. Вивчення зоряних магнітних полів є одним із важливих напрямків астрофізики, оскільки воно надає нам інформацію не тільки про фізику зорі, але й про космічну погоду на орбітах землеподібних планет. Локальні магнітні поля у зірок з конвективними оболонками – це магнітні поля малого масштабу, що відрізняються за своєю природою та структурою від їх глобального магнітного поля. На відміну від Сонця, у зірок за допомогою прямих вимірювань ми можемо реєструвати лише магнітне поле, що інтегроване по видимому диску. Однак ми можемо реєструвати магнітне поле у головній плямі протягом часу, коли відповідна трубка магнітного потоку вже виходить на поверхню зірки, а трубка магнітного потоку хвостової плями все ще прихована у під фотосферою. Наші дослідження засновані на спектрополяриметричних спостереженнях, проведених за допомогою 2,6м телескопа ім. академіка Г.А.Шайна, оснащеного ешельним спектрографом ESPL, CCD та Стоксетром як аналізатором кругової поляризації. Для вимірювання зоряних магнітних полів в КраО була розроблена методика Single Line. Ця методика заснована на розрахунку ефекту Зеемана в окремих спектральних лініях. Ключовою перевагою техніки Single Line перед іншими є здатність реєструвати локальні магнітні поля на поверхні зірок. За допомогою техніки Single Line вперше було зареєстровано появу великих трубок магнітного потоку на поверхні зірок V-IV-III класів світності (61 Cyg A, β Aql, β Gem). Ми розглядаємо результати моделювання магнітних плям на 61 Cyg A і β Gem та представляємо нові результати моделювання магнітних плям на β Aql. Відповідно до розглянутої геометричної моделі, змінності магнітного поля з періодом обертання зорі та граничного значення поля, отриманого в результаті спостережень, ми припускаємо, що максимальний радіус плям на поверхні β Aql може

перевищувати 9° .

Ключові слова: зірки, магнітна активність зірок, магнітне поле зірок.

1. Introduction

Today, the study of stellar magnetic fields is one of the important research field in astrophysics because it provides us, in addition to physics, with information about space weather in the orbits of Earth-like planets for stars other than the Sun. Local magnetic fields in stars with convective envelopes are small-scale magnetic fields different in nature and structure from their global magnetic field. Local magnetic fields of different spatial scales are observed in the Sun. Solar local fields change at different time intervals from a few minutes to the 22-year Hale cycle. But, in contradiction to the Sun, the topology, evolution and variability of local and global magnetic fields of stars have not yet been studied in detail.

When active region is being formed on the surface of the Sun or a star, a magnetic flux tube of positive or negative sign first appears. The visible counterparts of magnetic flux tubes are solar or stellar spots. Sunspots usually appear in pairs of opposite magnetic polarities (leading and following sunspots). But magnetic flux tube of the opposite sign appears only after some time. Time delay between the appearance of the leading and following sunspots can reach a day. Unlike the Sun, through direct measurements we are able to measure only the magnetic field integrated over the visible disk of stars. This means that such direct measurements do not make it possible to estimate the local magnetic field in the spots if the active region has already formed on the surface of the star and contains spots of both polarities. However, we can register the magnetic field in the leading spot during the time interval when the corresponding magnetic flux tube already emerges on the surface of the star, and the magnetic flux tube of the following spot is still hidden in the interior under the photosphere. Observations of convective stars support this hypothesis. After emergence of the magnetic flux tube of the opposite sign, the opposite polarities cancel each other out and for given measurement accuracy we lose the ability to register the magnetic field of this active region.

A similar observational effect can be produced by a large unipolar spot. This interpretation can be accepted or rejected only if there are observations of the magnetic field in the next day. If in the next day the disk-integrated magnetic field returns to value expected at given rotation phase, this is evidence in favor of the emergence of magnetic flux tube. If in the next day (assuming the star is spinning slowly enough) the field remains anomalous, then, most likely, a unipolar spot has been registered. More detail-

led information can be obtained by comparing the theoretically modeled and observed Stokes profiles, or by measuring the magnetic field using sets of spectral lines, which formed mainly in the undisturbed photosphere and using another set of lines, which particularly formed in the spotted regions. It should be noted, on the Sun the probability of the formation of a unipolar spot is much less than the probability of the formation of a bipolar active region.

Performed at the CrAO observations allow us to assume that we registered the emergence of magnetic flux tubes of leading spots during the formation of the active regions in the stars of V-IV-III luminosity classes: 61 Cyg A (Sp K5 V, see Plachinda, 2004), β Aql (Sp G8 IV, see Butkovskaya et al., 2017), β Gem (Sp K0 IIIb, see Baklanova et al., 2011). Here, within the framework of this hypothesis, we discuss our earlier results of measuring the global and local magnetic fields of selected stars, as well as present new results of modeling the size and magnetic field of spots on β Aql.

2. Observational and diagnostic techniques for studying local magnetic fields

Since the 1980s, regular spectropolarimetric observations of nondegenerate stars of different spectral classes and evolution stages have been carrying out at the Crimean Astrophysical Observatory using the 2.6-m reflector named after academician Shajn (ZTSh). Today, for spectropolarimetric observations, the ESPL echelle spectrograph (Lagutin et al., 2019), the circular polarization analyzer (Stokesmeter) with a rotating input quarter-wave plate and a CCD detector ($2k \times 2k$) are used. The observations are carried out in the spectral range of 5000-6900 Å at the spectral resolution of $R \sim 51000$. To obtain the signal-to-noise ratio of ~ 250 -450, the duration of an exposure is from 120 seconds for stars of magnitude 0.^m0 to 1800-3000 seconds for stars of 5^m-6^m.

The key difference between solar and stellar spectropolarimetric observations is that the last ones give Stokes profiles mean-weighted over star's visible hemisphere. In this case the significant cancellation of the signal from active regions of mixed polarity is observed. Therefore, unlike solar observations, the local magnetic fields on stars often remain unresolved. Semel et al. (1993) proposed a multi-line technique to add the polarization signal originating from several spectral lines into one pseudo profile, with an higher signal to noise. But, in general, the atmospheres of cool non-degenerated stars are characterized by a complex of physical conditions: spatial temperature and gravity inhomogeneities; gradients of temperature, microturbulence, density, velocity and stratification of chemical elements with depth; inhomogeneity of

surface magnetic field (Plachinda et al. 2019). So, any multiline method, including the most popular Least Square Deconvolution (Donati et al., 1997), requires additional independent criteria for selecting spectral lines formed under the same physical conditions. Unlike multiline methods, we have developed and used Single Line method (SL-method), which calculates magnetic field using observed profiles of individual spectral lines (Plachinda & Tarasova, 1999; Plachinda, 2004; Butkovskaya & Plachinda, 2007; Plachinda, 2014) and is free from any model restriction.

3. Local magnetic fields of individual III-VI-V stars

Obtained at CrAO observational results allowed us to hypothesize that we have recorded the emergence of large magnetic flux tubes during the formation of an active region in stars of V-IV-III luminosity classes: 61 Cyg A (Sp K5 V), β Aql (Sp G8 IV), β Gem (Sp K0 IIIb) (Plachinda, 2004; Butkovskaya et al., 2017; Baklanova et al., 2011). Global and local magnetic fields of these stars folded with their axial rotation phases are illustrated in Figure 1.

3.1. 61 Cyg A

Integrated over the visible hemisphere of 61 Cyg A (Sp K5 V, $P_{\text{rot}} = 36.618 \pm 0.061$ days) magnetic field was estimated taking into account the contribution of spots of different sizes. Assuming the magnetic field of the spots is $B_{\text{spot}} = 4000$ G, the simulated spot sizes for different initial parameters are $4.8^\circ - 6.0^\circ$. In the top panel of Figure 1, open symbols marked values strongly out of the global magnetic field curve. Most likely, these outliers contain a significant contribution from the emerging magnetic flux tubes of active regions. For a more detailed description of data see Plachinda (2004). It should be noted that all outliers are of the same sign, as it should be during the same activity cycle. The arrows connect the values of consecutive dates. Thus, after almost a day, a lagging flux tube of an opposite sign compensates the magnetic flux of the tube that emerges first. This effect is well known from the physics of the Sun.

3.2. β Gem

Integrated over the visible surface of β Gem (Sp K0 IIIb, $P_{\text{rot}} = 491.5$ days) magnetic field was estimated taking into account the contribution of spots of different sizes. Assuming the magnetic field of the spots is $B_{\text{spot}} = 3000$ G, the simulated spot sizes for different initial parameters are $1.0^\circ - 1.55^\circ$. In the middle panel of Figure 1, open symbols marked values strongly out of the global magnetic field curve. As in the case of 61

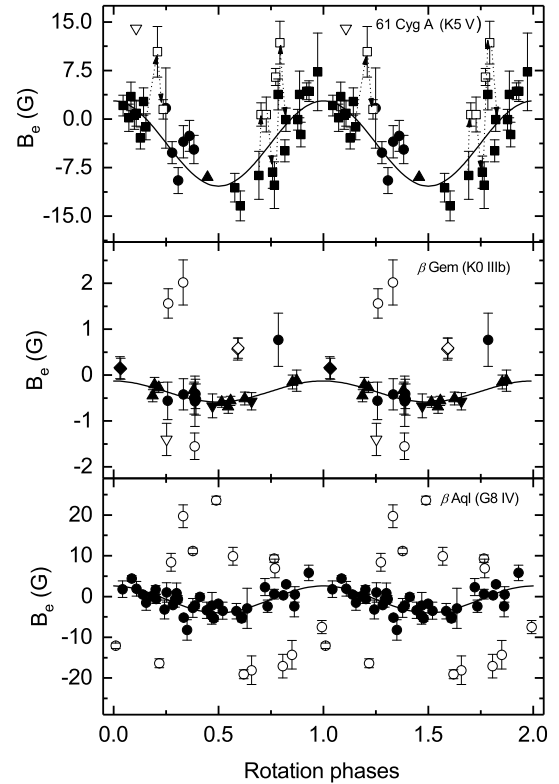


Figure 1: Global magnetic fields (filled symbols) and magnetic fields measured in dates when a strong spots contribution is supposed (opened symbols) of 61 Cyg A (top panel), β Gem (middle panel), β Aql (bottom panel) folded in phase with their axial rotational periods. The dipole fits are shown by solid lines. The arrows in the top panel connect the values of consecutive dates.

Cyg A, these outliers, most likely, contain a significant contribution from the emerging magnetic flux tubes of active regions. For a more detailed description, see Baklanova et al. (2011). It should be noted that, unlike to 61 Cyg A, observations of β Gem overlap several activity cycles of the latter. As a result, the positive as well as negative outliers from the magnetic curve are registered.

Baklanova et al. (2011) additionally tested the hypothesis of the detection of the emergence of a large magnetic field tube on β Gem. Assuming the radiation transfer in magnetic field does not distort the geometry of the magnetic field, geometric modeling of the contribution of an unipolar spot to the magnetic field of the Sun as a star was performed. The emerging magnetic tube was simulated by a dipole of a conventional unipolar sunspot without penumbra. The spot was placed on the central meridian. The following parameters were used in the simulation: the coefficient of the linear law of darkening to the edge

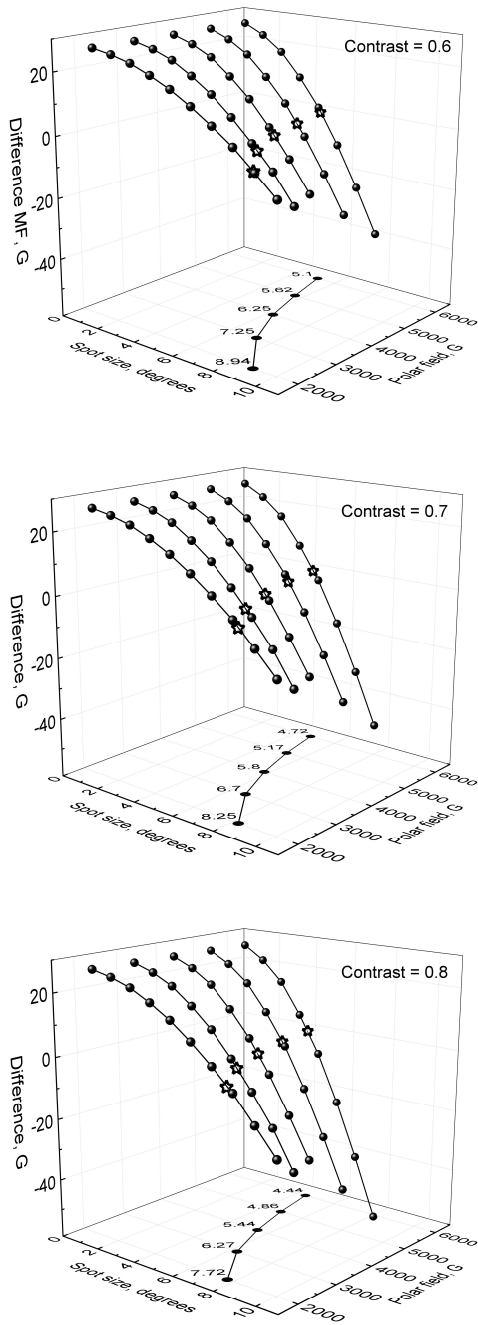


Figure 2: β Aql. For contrasts of the intensity in sunspot shadow to unperturbed photosphere equal to 0.6 (top panel), 0.7 (middle panel), and 0.8 (bottom panel), the dependencies of the discrepancy between calculated and measured longitudinal field component (Difference MF) on the spot radius (Spot size) and the field vector (Polar field) in the spot are presented. The asterisks mark points with minimal discrepancies between the observed and calculated magnetic field. Projections of these best fitted values on the lower plane Spot radius – Spot field are shown with indication of spot radius.

$u = 0.55$, the angle between the axis of rotation and the line of sight $i = 90^\circ$, the spot latitude $\phi = 30^\circ$, the ratio of the radiation intensity in the spot shadow to the unperturbed photosphere $\gamma = 0.4$, the tube radius $r = 1.5^\circ$, the magnetic field in the tube $B_{\text{tube}} = 4000$ G. The contribution of the magnetic flux tube to the global magnetic field of the Sun as a star was found to be only 1 G, this is in good agreement with the solar data. This geometric approach makes it possible to obtain a family of solutions that provides information on the radii of floating flux tubes and their magnetic fluxes.

3.3. β Aql

For β Aql (Sp G8 IV-V, $P_{\text{rot}} \sim 5.1$ days), all observations presented in the bottom panel of Figure 1 were obtained at the CrAO (Butkovskaya et al., 2017). As for the two previous stars, open symbols represent the magnetic field on dates, where, apparently, a significant contribution is made by the small-scale magnetic field associated with the emergence of the forming active regions.

In this work, for the date 2014 October 06, when strongly deviated magnetic field $B_e = 23.6 \pm 1.0$ G was registered, we modeled the possible sizes of magnetic spots for different magnetic fields in the spots (see Table 1 and Figure 2). The following parameters were used in the simulation: the coefficient of the linear law of darkening to the edge $u = 0.583$, the angle between the axis of rotation and the line of sight $i = 25^\circ$ (Butkovskaya et al. 2017), the latitude of the spot $\phi = 40^\circ$, the spot radius from 1° to 10° , magnetic field in spot from 2000 to 6000 G. The simulated spot was placed on the central meridian. With these parameters, the differences between the observed value of the longitudinal field $B_e = 23.6$ G and that simulated for the visible hemisphere with a spot were calculated. It should be noted that the radius of β Aql is $3.2R_\odot$, so the gas pressure in the atmosphere of β Aql is less than the gas pressure in the solar atmosphere. Therefore, to maintain the configuration of the magnetic field tube in atmosphere of β Aql, a smaller magnetic flux is sufficient. Therefore, we used a contrast value of 0.6 – 0.8, which is lower than that of the Sun.

According to Bunte & Saar (1993), for stars with temperatures and luminosities similar to β Aql, the typical magnetic field of spots range from 1800 to 3300 G. According to the top panel of Figure 2, this range of the magnetic field corresponds to the range of spot radii from 9° to 7.5° . With decreasing contrast (for the Sun ~ 0.3 - 0.4 in spot shadow), the radius of the magnetic flux tube (i.e. the radius of the spot) increases. According to the considered geometric model, the rotational variability of the magnetic field and the extreme value of the field obtained from observations, we assume that the extreme radius of

Table 1: Simulated sizes of magnetic spots (second column) for different magnetic fields in the spots (first column). Here spot sizes best fitted to $B_e = 23.6$ observed at 2014 October 06. The differences between observed B_e and calculated B_{calc} magnetic fields are presented in column 3.

B_{spot} , G	Spot size, °	$B_e - B_{\text{calc}}$, G
Contrast = 0.6		
2000	8.9	0.06
3000	7.3	0.13
4000	6.3	0.15
5000	5.6	-0.08
6000	5.1	-0.04
Contrast = 0.7		
2000	8.3	0.11
3000	6.7	-0.01
4000	5.8	-0.01
5000	5.2	-0.02
6000	4.7	-0.04
Contrast = 0.8		
2000	7.7	-0.08
3000	6.3	-0.10
4000	5.4	-0.02
5000	4.9	-0.01
6000	4.4	-0.07

the spots at the surface of β Aql may exceed 9° (1/40 of the circle). The radii of large solar spots at the same latitude are $\sim 1.5^\circ$. For such radii of spots on β Aql the magnetic field become abnormally big: $B_{\text{spot}} \sim 20000$ G. Thus, our geometric modeling allows us to conclude that the big spots at the surface of β Aql are several times larger than big sunspots.

4. Conclusions

In this paper we discuss the possibility of detection of activity regions by direct measurements of magnetic field in stars with convective envelopes. We present our results of registration of emergence of large magnetic flux tubes during the formation of an active region in selected stars of V-IV-III luminosity classes: 61 Cyg A (Sp K5 V), β Aql (Sp G8 IV), β Gem (Sp K0 IIIb). We also present the new results of modeling the size and magnetic field spots on β Aql. According to the considered geometric model, the rotational variability of the magnetic field and the extreme value of the field obtained from observations, we assume that the extreme radius of the spots on the surface of β Aql may exceed 9° (1/40 of the circle).

References

- Baklanova, D., Plachinda, S., Mkrtichian, D., Han, I., Kim, K. -M.: 2011, *Astron. Nachr.*, **332**, 939.
- Bünthe, M. & Saar, S.H.: 1993, *Astron. Astrophys.*, **271**, 167.
- Butkovskaya, V., Plachinda, S.: 2007, *Astron. Astrophys.*, **469**, 1069.
- Butkovskaya V.V., Plachinda S.I., Bondar' N.I., Baklanova D.N.: 2017, *Astron. Nachr.*, **338**, 896.
- Donati, J.-F., Semel, M., Carter, B.D., Rees, D.E., Collier Cameron, A.: 1997, *MNRAS*, **291**, 658.
- Plachinda, S.I.: 2004, Multi-Wavelength Investigations of Solar Activity, IAU Symposium, **223** /Ed. A.V.Stepanov, E.E.Benevolenskaya, A.G.Kosovichev, Cambridge, UK: Cambridge University Press, p.689-690.
- Plachinda, S.I.: 2014, *Bull. of the Crimean Astrophysical Observatory*, **110**, 17.
- Plachinda, S., Shulyak, D., Pankov, N.: 2019, *Astronomical and Astrophysical Transactions*, **31**, 323, arXiv:1910.01501.
- Semel, M., Donati, J.-F., Rees, D.E.: 1993, *Astron. Astrophys.*, **278**, 231.
- Plachinda, S.I., Tarasova, T.N.: 1999, *Astrophys. J.*, **514**, 402.

DOI:<http://dx.doi.org/10.18524/1810-4215.2020.33.216279>

PHOTOMETRY AND THE BLAZHKO EFFECT IN THE RR LYR VARIABLE STAR Y Vul

S. N. Udovichenko and L. E. Keir

Astronomical Observatory, Odesa National University,
Odesa, Ukraine, udovich222@ukr.net

ABSTRACT. The RR Lyr variable star Y Vul have been observed by using a CCD photometer during several seasons from 2011 to 2017. Nearly 5960 data points were obtained spanning over 53 nights. We found the amplitude and phase modulations with the amplitudes of 0.16 mag and 0.041 of the pulsating phase in V filter; 0.15 mag and 0.041 of the pulsating phase in R filter, respectively. The frequency Fourier analysis of the light curves with the help of Period04 software was performed, Blazhko modulation period (59.20 days) and triplet structures in the Fourier spectrum were detected. The pulsation frequency components in the Fourier spectrum were identified up to the 7th harmonic order, while the modulation side lobe frequencies – up to 9th order. The analysis of the light curves maxima resulted in the same value of the Blazhko period. The fundamental pulsation period of the star has been practically stable over a period of a hundred years.

АНОТАЦІЯ. У даній роботі ми досліджуємо змінну зорю типу RR Lyr – Y Vul, яка спостерігалась нами на протязі декількох спостережних сезонів з 2011 по 2017 роки за допомогою ПЗЗ фотометра. Було одержано біля 5960 вимірювань блиску протягом 53 ночей спостережень. Ми знайшли амплітудну і фазову модуляції кривих блиску з амплітудою 0.16 mag і 0.041 по фазі для V фільтра; 0.15 mag і 0.041 по фазі для R фільтра, відповідно. Для всіх кривих блиску був виконаний чисельний Фур'є аналіз за допомогою відомої програми для аналізу блиску змінних зір – Period04; знайдений період модуляції кривих блиску – ефект Блажко (59.20 днів) та триплетна структура Фур'є спектра. Частотні пульсаційні компоненти в Фур'є спектрі були ідентифіковані до 7 гармоніки, а модуляція в бокових пелюстках спектру – до 9 гармоніки. Аналіз моментів максимумів блиску дав аналогічний результат щодо періоду ефекта Блажко. В той же час основний фундаментальний період коливання блиску зорі був практично стабільний на протязі ста років.

Keywords: Stars: variables: RR Lyr stars – Y Vul.

1. Introduction

Y Vul (AN 1907.0004, Gaia DR1 - 286.0678990585, USNO-A2.0 1125 - 11247385), ($\alpha_{J2000.0} = 19^h04^m16.3^s$; $\delta_{J2000.0} = +24^\circ47'19.1''$) is known as the variable star for more than hundred years, but this RRab variable has been poorly investigated. The variability of the star was explored by van Biesbroeck and Casteels (1914), and they have defined that the star belongs to RR Lyr variables. However, in spite of their detailed observations, the authors haven't deduced the light curve elements. Using observation data, reported by van Biesbroeck and Casteels, Tse-sevich (1960) derived a period and epoch of Y Vul as follows:

$$MaxJD = 2419221.531 + 0^d.44941 \times E. \quad (1)$$

He pointed out the difference in height of the light curves maxima and suspected the presence of the Blazhko effect in Y Vul. Using photographic observations in the range JD 2433034-41492, Kazarovets and Shugarov (1973) determined elements of the light-curve variation more accurately:

$$MaxJD = 2438939.413 + 0^d.44945164 \times E. \quad (2)$$

Their estimated range of the light variation was $14^m.2 - 16^m.0$ (pg). The data reported in their study for Y Vul were included to the General Catalogue of Variable Stars (GCVS) (Samus' et al. 2017) and AAVSO Variable Star Index (VSX database, <https://www.aavso.org/vsx/index.php>).

2. Observations

The photometric CCD observations of Y Vul were obtained at the Astronomical station near Odesa during the observation seasons in 2011-12, 2014-16 years in V filter; later on, in 2017 year the observations were performed in R filter using the 48 cm reflector AZT-3 of Astronomical observatory of Odesa National University, equipped with CCD photometer and Peltier cooler

Table 1: The magnitudes of the comparison and check stars (NOMAD).

Star	α , δ_{2000}	magB	magV	magR
comA	19 04 12	14.63	13.76	13.09
	+24 45 20	-	-	-
comB	19 04 08	12.905	12.424	12.090
	+24 45 47	-	-	-
check	19 04 15	14.40	-	14.18
	+24 46 12	-	-	-
Y Vul	19 04 16	15.180	14.680	15.070
	+24 47 19	-	-	-

(Sony chip ICX429ALL, $\sim 600 \times 800$ pixels) in the f/4.5 Newtonian focus (Udovichenko 2012).

The datasets consists of 4290 V-band data points and 1665 Rc-band points obtained from over 53 nights of observations. Two stars were chosen as comparison and one as check stars as close as possible in B-V color. The magnitude of comparison star comB we have took from NOMAD catalogue (NOMAD 2005). We accepted these magnitudes and measured star comA relative to star comB on our frames. The resulting magnitudes for star comA are: V = 13.76, R = 13.09 with errors of 0.02 mag. The exposure time for variable and comparison stars was chosen to except a saturation of the frame and appointed as 120 sec. The BVR magnitudes of the variable, comparison and check stars from NOMAD catalogue; are summarized in Table 2.

The standard reduction of the CCD frames were carried out by using the MUNIPACK (Motl, <http://sourceforge.net/projects/c-munipack>) software. The procedures for an aperture photometry is composed of the dark-level and flat-field corrections, determination of the instrumental magnitudes and precision. The magnitude of comparison star "com A" was used to convert the differential magnitudes to the corresponding value of variable. The photometry was transformed to the standard VRc Johnson-Cousins system by means of the differential photometry method (Benson 1998). The transformation coefficient was determined from observations of standard stars (Udovichenko 2012). The finding chart with market-out variable, comparison and check stars is shown in Fig. 1, the whole dataset of observations is presented in Fig. 2. The errors in individual data points vary from $0^m.005$ to $0^m.02$.

3. Frequency spectrum analysis

All data on the light variation curves nearby maxima and minima have been approximated by polynoms of 2-7 degrees with the best fit option by using software MCV (Andronov and Baklanov 1998). Then amplitudes of light variations and times of maxima

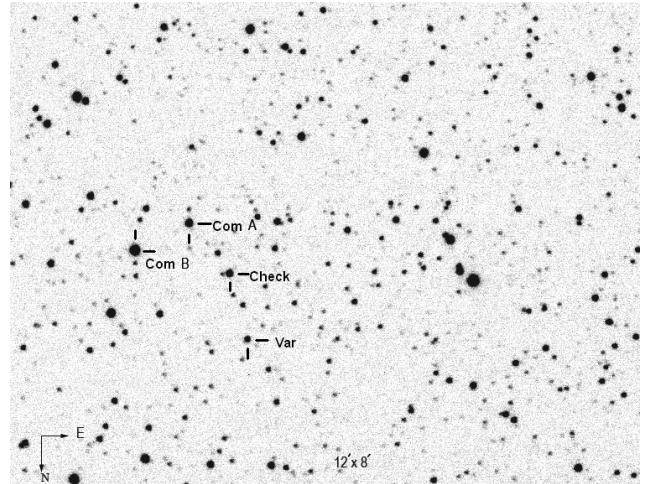


Figure 1: The finding chart of Y Vul with the variable, comparison and check stars marked.

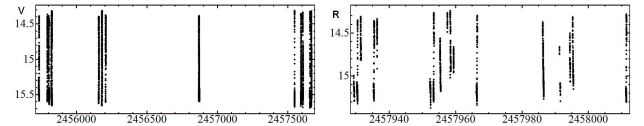


Figure 2: The all data set of observations of Y Vul.

have been defined. The observations of Y Vul shows the whole amplitude variation $1^m.05$ in Rc-band and $1^m.33$ in V-band. The modulation occurs at the maximum brightness and phase shift too. The brightness at maxima of the light curves in Rc-band vary from $14^m.265$ to $14^m.411$, the moderate Blazhko modulation of the amplitude reaches about 0.146; in V-band vary from $14^m.316$ to $14^m.478$, and the modulation reaches $0^m.162$. The phase shift modulation in both bands varies within about 0.041 of the pulsation phase. All light curves of the target star obtained by using V and Rc filters with the pulsating period, are shown on Fig. 3. These phase curves were computed by using GCVS elements, equation 2.

To analyse the modulation properties of the light curves for this star, we have used a common technique a Fourier decomposition. The frequency analysis was performed using a package of computer programs with sine-wave fitting by using utilize Fourier algorithms (program Period04), (Lenz and Breger 2005).

To capture longer time interval, we calculated observations, obtained with V-band and Rc-band.

The fundamental pulsation period was determined with the help of using the above-mentioned techniques as the highest peak on the Fourier amplitude spectrum. The observed harmonics and triplet were defined by pre-whitening data and Fourier analysis of the residuals. For each calculated harmonic and triplet, the signal-to-noise ratio has been estimated to retain only

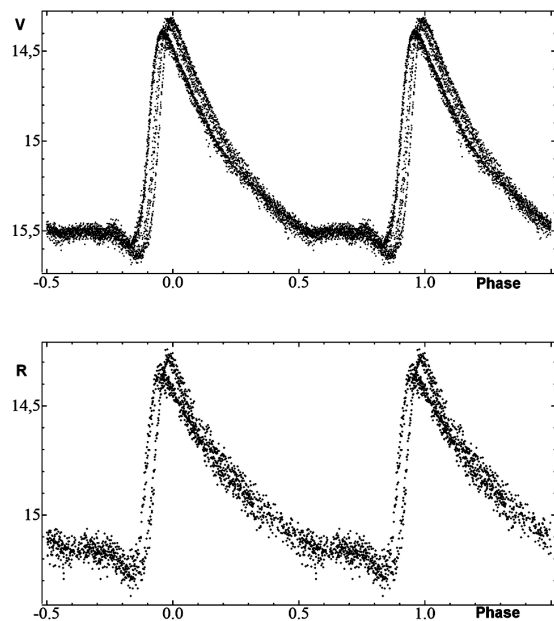


Figure 3: The phase curves of Y Vul in V and Rc filters.

significant signals greater than 4. The amplitude and phase for each frequencies, obtained with the best fitting, are given in Table 2.

The amplitude spectrum for the basic pulsating frequency and after pre-whitening are shown in Fig. 4. The harmonics of f_0 are significant to the 7th order, triplets $f_0 \pm f_m$ to 9th order. The fundamental pulsating period $P_0 = 0.44945177$ is very close to the GCVS value. The Blazhko frequency also was determined as the difference of frequencies $f_m = kf_0 - kf_0 \pm f_m$ and given in the last column of Table 2. Some of these frequencies contains an alias frequencies $\sim (1/365 = 0.0027)$ as a result of the several seasons of observations (2011–17). Keeping that in mind we only used non-aliased frequencies to determine the Blazhko frequency. The average value equals $0.01689 \pm 0.0004 \text{ cd}^{-1}$, which corresponds to the period of 59.20 ± 0.14 day.

The amplitude asymmetry is observed in the modulation components: $Q_i = (A_{i1}^+ - A_{i1}^-) / (A_{i1}^+ + A_{i1}^-)$, where $A_{i1}^+ = if_0 + f_m$, $A_{i1}^- = if_0 - f_m$. The asymmetry ratios for the first component $Q_1 = 0.36$; the triplet ratios in the side lobes $R_1 = A_{11}^+ / A_{11}^- = 2.16$. The amplitudes of the pulsation components which decrease with increasing orders are smooth while the amplitudes of the modulation components decrease irregularly.

4. Light curves maxima analysis

The times of maxima in the all light curves was performed with help of fitting the light curve near the maxima by a polynomial function an order from 2 to 7. The list of observed light curves maxima presents in Ta-

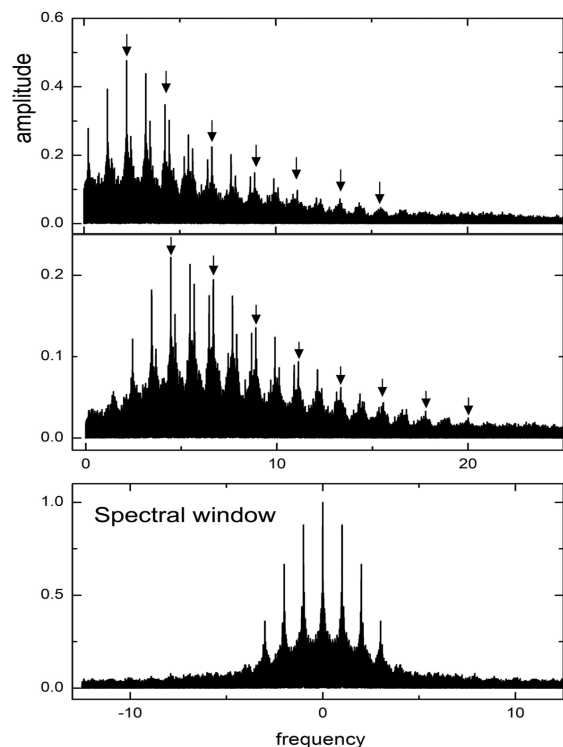


Figure 4: The Fourier amplitude spectrum of the basic frequency and after the first pre-whitening. In the above figure the arrows point to the basic pulsation frequency and its harmonics kf_0 . In the middle figure the arrows point to the modulation frequency triplets $kf_0 \pm f_m$ after the next pre-whitening. The bottom figure shows the spectral window.

ble 3. The modulation Blazhko period was determined by the (O-C) period analysis (using Period04). The both method (i.e. frequency spectrum analysis and (O-C) deviation at maximum) have shown the same value of a Blazhko period. The value from the light curves maxima analysis equal 59.20 ± 0.02 days. We selected the highest observed maximum and derived the elements of the Blazhko cycle:

$$MaxHJD_{Blazhko} = 2457548.505 + 59^d.20 \times E_{Blazhko} \quad (3)$$

The O-C diagram of Y Vul versus the Blazhko phase with sinusoidal fitting curve is presented in Fig. 5 (top). The O-C values are different in 9% of the pulsation period, the magnitudes at maximuma are different in 12–14% of the V and Rc amplitude.

The O-C diagram was constructed by using all the published observational data available (Tsessevich 1960; Kazarovets and Shugarov 1973) as well as the data, obtained in this study by using the GCVS elements. The resulting diagram with linear fit is plotted in Fig. 5 (bottom). The data covers the

Table 2: Identify frequencies, amplitudes, phases and modulation frequencies $f_m = kf_0 - kf_0 \pm f_m$ of the V and Rc light curve solutions of Y Vul.

Identification	f (cd^{-1})	amplitude, mag	phase, $\text{rad}/2\pi$	snr	f_m (cd^{-1})
V-band					
f_0	2.224936(2)	0.311(1)	0.084(1)	94.2	
$2f_0$	4.449874(3)	0.187(2)	0.303(2)	35.2	
$3f_0$	6.674817(3)	0.160(1)	0.845(2)	31.4	
$4f_0$	8.899735(3)	0.100(2)	0.203(3)	22.1	
$5f_0$	11.12464(1)	0.050(4)	0.63(1)	13.5	
$7f_0$	15.5717(6)	0.029(8)	0.06(2)	9.2	
$f_0 + f_m$	2.24188(3)	0.031(9)	0.07(1)	7.1	0.01694(3)
$f_0 - f_m$	2.20803(6)	0.027(8)	0.3(3)	6.7	0.01691(6)
$2f_0 - f_m$	4.433004(9)	0.051(2)	0.268(7)	5.6	0.01687(1)
$3f_0 + f_m$	6.691688(7)	0.046(2)	0.088(6)	9.3	0.01688(1)
$4f_0 + f_m$	8.91661(1)	0.040(2)	0.952(9)	9.5	0.01687(1)
$6f_0 - f_m$	13.33284(5)	0.038(9)	0.009(3)	11.4	0.01678(5)
$7f_0 + f_m$	15.59158(2)	0.018(3)	0.71(3)	4.5	0.01702(2)
$8f_0 - f_m$	17.78265(1)	0.017(2)	0.71(2)	4.0	0.01684(1)
$9f_0 + f_m$	20.0076(1)	0.09(1)	0.7(3)	7.2	0.0168(1)
R-band					
f_0	2.22491(6)	0.432(4)	0.992(2)	56.2	
$2f_0$	4.4497(1)	0.152(3)	0.715(8)	36.6	
$3f_0$	6.6744(4)	0.105(2)	0.415(4)	27.5	
$4f_0$	8.8994(4)	0.073(4)	0.813(8)	16.2	
$5f_0$	11.1235(7)	0.043(6)	0.62(2)	13.0	
$6f_0$	13.50(6)	0.022(8)	0.9(3)	5.0	
$7f_0$	15.575(1)	0.021(3)	0.19(1)	5.0	
$f_0 - f_m$	2.2094(3)	0.038(4)	0.17(1)	6.9	0.0151(3)
$2f_0 + f_m$	4.465(4)	0.035(9)	0.9(3)	8.4	0.015(4)
$3f_0 - f_m$	6.659(2)	0.037(8)	0.7(1)	9.6	0.016(2)
$4f_0 + f_m$	8.916(4)	0.038(3)	0.30(1)	8.4	0.016(4)
$5f_0 - f_m$	11.109(2)	0.028(9)	0.6(1)	8.3	0.016(2)
$8f_0 - f_m$	17.782(4)	0.016(3)	0.4(1)	4.6	0.017(4)

period of a hundred years. The O-C difference over such long period less than 0.02 day, which is less than the Blazhko phase change. It allows to assume, that Y Vul has practically no secular period changes. The scattering of dots is due to the Blazhko effect.

5. Conclusions

This paper describes the modulation of the light curves of a RR Lyrae variable Y Vul. Using the data obtained from the several observational seasons, we have found the Blazhko effect for the pulsating in the fundamental mode. The amplitude of the maximum brightness variation reaches $0^m.162$ with V filter and $0^m.146$ in Rc filter; the phase shift is 0.041 of pulsation phase. Using the Fourier analysis for these data we have derived the fundamental pulsating period of 0.4494517 ± 0.000001 day. The Blazhko period was defined using the O-C value at maxima and frequency spectrum analysis. The average period equal 59.20 ± 0.02 days. The modulation of the Y Vul light curves are described by the triplet frequencies $kf_0 \pm f_m$ and the modulation frequency f_m . In the frequency spectrum

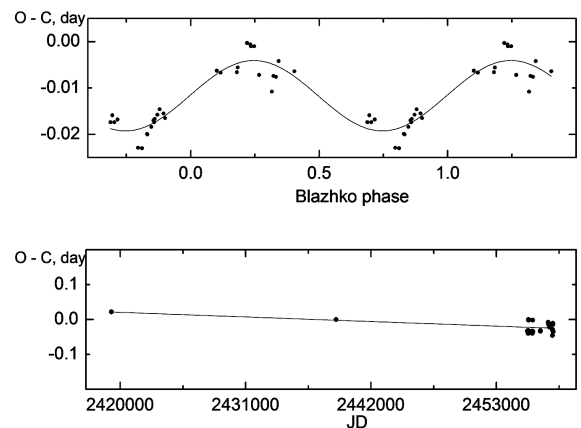


Figure 5: The O-C (day) diagram of Y Vul versus Blazhko phase with the sinusoidal fitting curve (top figure). The O-C (day) diagram of Y Vul during over a hundred years with the linear fitting (bottom figure).

Table 3: List of measured maxima of Y Vul

Maximum HJD	Error	Magnitude (V-C)	Error	Cycle	O - C	Phase	Error	Filter
2455735.4040	0.00019	0.6209	0.0028	37369	-0.0168	-0.0374	0.0004	V
2455793.3841	0.00021	0.6288	0.0027	37498	-0.0159	-0.0354	0.0004	V
2455801.4702	0.00025	0.6499	0.0034	37516	-0.0199	-0.0444	0.0005	V
2455802.3706	0.00018	0.6315	0.0027	37518	-0.0184	-0.0410	0.0003	V
2455805.5187	0.00071	0.6752	0.0112	37525	-0.0165	-0.0367	0.0015	V
2455824.4119	0.00028	0.5622	0.0049	37567	-0.0002	-0.0006	0.0006	V
2455825.3101	0.00023	0.5534	0.0034	37569	-0.0010	-0.0022	0.0005	V
2456156.5371	0.00031	0.6479	0.0034	38306	-0.0198	-0.0442	0.0007	V
2456158.3380	0.00023	0.6349	0.0030	38310	-0.0167	-0.0372	0.0005	V
2456180.3773	0.00020	0.5633	0.0033	38359	-0.0006	-0.0013	0.0004	V
2456181.2759	0.00026	0.5609	0.0041	38361	-0.0009	-0.0021	0.0005	V
2456207.3276	0.00048	0.6349	0.0055	38419	-0.0174	-0.0387	0.0010	V
2456208.2265	0.00024	0.6276	0.0021	38421	-0.0174	-0.0387	0.0005	V
2456868.4714	0.00023	0.6360	0.0030	39890	-0.0169	-0.0377	0.0005	V
2456869.3714	0.00022	0.6290	0.0029	39892	-0.0158	-0.0352	0.0005	V
2457548.5045	0.00027	0.5528	0.0048	41403	-0.0041	-0.0092	0.0006	V
2457593.4476	0.00031	0.6061	0.0040	41503	-0.0063	-0.0140	0.0007	V
2457594.3460	0.00030	0.6009	0.0050	41505	-0.0067	-0.0150	0.0006	V
2457606.4806	0.00022	0.5664	0.0027	41532	-0.0073	-0.0163	0.0004	V
2457657.2694	0.00028	0.5710	0.0045	41645	-0.0066	-0.0147	0.0006	V
2457665.3550	0.00029	0.5695	0.0044	41663	-0.0111	-0.0248	0.0006	V
2457666.2574	0.00040	0.5599	0.0069	41665	-0.0076	-0.0169	0.0009	V
2457899.5228	0.00043	0.5565	0.0078	42184	-0.0076	-0.0170	0.0010	V
2457930.5197	0.00033	1.2740	0.0062	42253	-0.0229	-0.0509	0.0007	R
2457931.4185	0.00038	1.2249	0.0043	42255	-0.0229	-0.0510	0.0008	R
2457935.4719	0.00051	1.2772	0.0060	42264	-0.0146	-0.0325	0.0011	R
2457936.3699	0.00073	1.2768	0.0075	42266	-0.0155	-0.0345	0.0016	R
2457953.4590	0.00034	1.1902	0.0054	42304	-0.0055	-0.0124	0.0007	R
2457958.4014	0.00070	1.1700	0.0064	42315	-0.0071	-0.0159	0.0015	R
2457966.4924	0.00036	1.1909	0.0074	42333	-0.0063	-0.0141	0.0008	R
2457993.4484	0.00066	1.2576	0.0089	42393	-0.0174	-0.0388	0.0014	R

the pulsation harmonic components are detected up to the 7th order; the modulation side lobe frequencies are detected up to 9th order. Thirty pulsation maxima from the observed light curves have been measured. The fundamental pulsation period of the star has been practically stable over a period of a hundred years.

References

- Andronov, I.L., Baklanov, A.V.: 2004, *Astronomical School's Report*, **5**, 264.
- Benson, P.J.: 1998, *Intern. Amateur-Professional Photoel. Photom. Communic.*, **72**, 42.
- Blazhko, S., Mitteilung uber veranderliche Sterne: 1907, *AN*, **175**, 325.
- Kazarovets, E. V., Shugarov, S. Y., 1973, *Peremennye Zvezdy Prilozhenie*, **1**, 455.
- Lenz P., Breger M.: 2004, *Comm. in Asteroseismology*, **146**, 53.
- Samus N.N., Durlevich O.V., Kazarovets E.V., Kireeva N.N., Pastukhova E.N., Zharova A.V. et al.: 2011, *General Catalogue of Variable Stars* (GCVS database, Version 2011Jan).
- Tsesevich V.P.: 1960, *Astronomicheskij Tsirkulyar*, **215**, 24.
- Udovichenko S.N.:2012, *Odessa Astron. Publ.*, **25**, 32.
- van Biesbroeck, G., Casteels, L.: 1914, *Annales de l'Observatoire Royal de Belgique Nouvelle serie*, **13**.
- Zacharias N. et al.: 2005, VizieR Online Data Catalog: NOMAD Catalog (Zacharias+2005), 1297.

DOI:<http://dx.doi.org/10.18524/1810-4215.2020.33.216285>

SPECTROSCOPIC INVESTIGATIONS OF GALACTIC CLUSTERS WITH ASSOCIATED CEPHEID VARIABLES. IV. COLLINDER 220 AND UW CAR

I. A. Usenko,^{1,2} A. Yu. Kniazev,^{3,4} I. Yu. Katkov,⁵ V. V. Kovtyukh,¹
T. V. Mishenina,¹ A. S. Miroshnichenko,^{6,7,8} D. G. Turner⁹

¹ Astronomical Observatory, Odessa National University, Shevchenko Park,
Odessa 65014, Ukraine, vkovtyukh@ukr.net

² Mykolaiv Astronomical Observatory, Obsevatorna 1, Mykolaiv 54030, Ukraine,
igus99@ukr.net

³ South African Astronomical Observatory, P.O. 7925, Cape Town,
South Africa, akniazev@saaao.ac.za

⁴ Southern African Large Telescope Foundation, P.O. 7925, Cape Town,
South Africa

⁵ New York University, Abu Dhabi, Saadiyat Island, P.O. 129188
Abu Dhabi, UAE, ik52@nyu.edu

⁶ Dept. of Physics and Astronomy, University of North Carolina at
Greensboro, P.O.Box 261170, Greensboro, NC 27402, USA, a_mirosh@uncg.edu

⁷ Main Astronomical Observatory of the Russian Academy of Sciences,
Pulkovskoe shosse 65–1, Saint-Petersburg, 196140, Russia

⁸ Fesenkov Astrophysical Institute, Observatory 23, Almaty, 50020, Kazakhstan

⁹ Dept. of Astronomy and Physics, Saint Mary's University,
923 Robie Street, Halifax B3H3C3, Nova Scotia, Canada, turner@ap.smu.ca

ABSTRACT. We present the results of a spectroscopic and photometric investigation of 18 probable members of the open cluster Collinder 220, which contains the Cepheid UW Car. Besides the Cepheid, we studied three K-giants, two B-giants, and twelve B-A-F main sequence stars. Radial velocities (RV), $v \sin i$, T_{eff} , and $\log g$ were determined using spectroscopic model fitting and atmosphere models. We have derived color-excesses, reddenings, and intrinsic colors for these stars using their T_{eff} and $\log g$ from comparison to the atmosphere models, especially for hot stars. Proper motions, RV, and the GAIA DR2 2018 parallaxes allowed us to determine their membership in the cluster and absolute magnitudes. We found that seven stars along with the Cepheid can be the cluster members with a high confidence. The parallaxes and reddenings of the 7 confident cluster members led to the distances in a range of 1900–2800 pc, while the other stars are probably foreground objects. All the members have $[\text{Fe}/\text{H}]$ near 0.1 dex. The B-giant HD 90435 located near the cluster's “turn-off” point has a low projected rotational velocity, and this fact allows us to determine its chemical

composition to compare with that of the Cepheid UW Car. The CNO abundances of HD 90435 are nearly solar, while the Cepheid shows a deficit of carbon, an overabundance of nitrogen, a nearly solar oxygen, and an overabundance of sodium. The confident cluster member, K-supergiant CPD –57°3199, has CNO- and Na abundances close to those of UW Car.

Key words: Open clusters: radial velocities; Stars: abundance; GAIA parallaxes; Cepheids; B - giants; K-giants; individual: Collinder 220, UW Car, CPD –57°3199, HD 90435, HD 90552, HD 302751, HD 302759, HD 302760, HD 302761, HD 302858, TYC 8608-1-1, TYC 8608-25-1, TYC 8608-33-1, TYC 8608-69-1, TYC 8608-153-1, TYC 8608-193-1, TYC 8608-213-1, TYC 8608-221-1, TYC 8608-1503-1.

АНОТАЦІЯ. Ми презентуємо результати фотометричних та спектроскопічних досліджень 18-ти вірогідних членів розсіяного скупчення Collinder 220, яке включає цефеїду UW Car. Окрім цефеїди, ми дослідили три К-гіганта, два В-гіганта та дванадцять В-А-Ф- зір головної послідовності. Радіальні швидкості RV, та параметри $v \sin i$, T_{eff} та

$\log g$ були отримані завдяки використанню фітінгу спектроскопічних моделей та моделей атмосфер. Ми вивели надлишки кольору, почервоніння, та справжні кольори для цих зір, використовуючи їх T_{eff} та $\log g$ шляхом порівняння з моделями атмосфер, особливо для гарячих зір. Власний рух, RV та паралакси з каталогу GAIA DR18 дозволяють встановити їх членство у скупченні та їх абсолютні магнітуди. Ми встановили, що сім зір з цефеїдою з високою вірогідністю можуть бути членами скупчення. Паралакси та почервоніння сімох надійних членів скупчення надають відстані у рамках 1900–2800 пс, тоді як інші зорі вірогідно є об'єктами переднього плану. Усі ці об'єкти мають $[\text{Fe}/\text{H}] = 0.1$ dex. В-гігант HD 90435, який міститься біля "точки повороту" скупчення, має низьку проекцію швидкості обертання, цей факт дозволяє отримати його хімічний склад, щоб порівняти з аналогічним у цефеїди UW Car. Вміст CNO у HD 90435 близький до сонячного, тоді як цефеїда показує дефіцит вуглецю, надлишок азоту, близький до сонячного вміст кисню та надлишок натрію. Дійсний член скупчення, К-надгігант CPD $-57^{\circ}3199$ має вміст CNO та Na близький до вмісту у UW Car.

Ключові слова: Розсіяні скупчення; променеві швидкості; Зорі: хімічний склад; паралакси GAIA; Класичні цефеїди; В-гіганти; К-гіганти; індивідуально: Collinder 220, UW Car, CPD $-57^{\circ}3199$, HD 90435, HD 90552, HD 302751, HD 302759, HD 302760, HD 302761, HD 302858, TYC 8608-1-1, TYC 8608-25-1, TYC 8608-33-1, TYC 8608-69-1, TYC 8608-153-1, TYC 8608-193-1, TYC 8608-213-1, TYC 8608-221-1, TYC 8608-1503-1.

1. Introduction

Collinder 220 is a rather poorly investigated open cluster. It contains 41 stars fainter than 10-mag of mostly B - and A - spectral types. Besides, it contains a 5.^d35 Cepheid UW Car as a possible member. According to Segel et al. (2019), the earliest spectral type stars in it are $B7$ – $B8$, $E(B - V) = 0.^m25 \pm 0.^m01$, the age near 370 Myr, and the metallicity $[\text{Fe}/\text{H}] = 0.00$ dex. Nevertheless there are some discrepancies between the distance moduli derived by different studies. In particular, $V_0 - M_V = 11.^m99 \pm 0.^m20$ (Segel et al. 2019), $11.^m48 \pm 0.^m24$ (Chen 2015) and $10.^m83$ (Dias et al. 2014). If the ratio of the total to selective extinction $R = A_V/E_{B-V} = 3.^m34 \pm 0.^m02$, we can assume that $A_V = 0.^m84 \pm 0.^m02$ for the color-excess from Segel et al. (2019). This way the following distances, 1698 ± 164 , 1342 ± 157 , and 995 pc have been derived, respectively. According to Cantat-Granden et al. (2018) (GAIA catalog), the distance to the cluster is ~ 2543 pc.

Kharchenko et al. (2013) gave $\langle RV \rangle = -13.0 \pm 0.2$ km s^{-1} for the cluster, while $\langle RV \rangle = -12.19 \pm 0.12$ km s^{-1} according to the GAIA DR18 catalogue. Collinder 220 has not been carefully studied spectroscopically except for UW Car (Luck & Lambert 2011). Therefore, the main goals of our investigation are as follows:

1) to measure the radial and rotational velocities of the cluster's stars, 2) to determine the atmospheric parameters, metallicities, CNO and Na abundances and compare the abundances of the objects of different spectral types, 3) to determine the distances using GAIA DR2 parallaxes and RV data, and to check their membership in the cluster.

2. Observations

Our observations were taken at the 11 m SALT (Southern African Large Telescope) equipped with HRS (High Resolution Spectrograph). HRS is a dual-beam (3700–5500 & 5500–8900 Å) fiber-fed, white-pupil, échelle spectrograph, which uses VHP gratings as cross dispersers. We obtained one spectrum for each object using the *medium mode* with the spectral resolving power $R = 40000$ and an average S/N over 100, which are sufficient to reach the goals of our study. These spectra have been used to derive the atmosphere parameters and chemical abundances for some elements of the open cluster members. The data were reduced using the *échelle* context in *MIDAS*. Also, the *feros* package developed for échelle data reduction from the Fiber-fed Extended Range Optical Spectrograph (FEROS) was used. Both FEROS and HRS provide very similar results.

We used the DECH30 package¹ designed to use the spectra in FITS format to measure the line depths and equivalent widths. The radial and rotational velocities were measured by fitting of the observed spectra with models from Coelho (2014). The object IDs, magnitudes, spectral types, proper motions, parallaxes from the GAIA DR18 catalogue, measured radial and rotational velocities for each spectrum are given in Table 1.

3. Results and Analysis

3.1 Radial and rotational velocities, proper motions and parallaxes

Distances derived from the Segel et al. (2019) and Cantat-Granden et al. (2018) data determine one of the main criteria for membership in the open cluster: a parallax range from 0.59 to 0.39 mas. According to Table 1, judging from the proper motion, radial velocity, and parallax measurements, seven objects are

¹<http://gazinur.com/DECH-software.html>

Table 1: General data for the observed objects in Collinder 220 and derived RVs.

Object	V	Sp.type	μ_α	μ_δ	$RV, \text{ km s}^{-1}$	$v \sin i, \text{ km s}^{-1}$	PLX (GAIA)
UW Car ¹	9.47	G0 Ib	-7.305	+3.590	+17.11±0.04	36.6±0.1	0.2631±0.0290
CPD -57°3199	10.86		-7.328	+2.680	+18.76±0.43	0.2±0.5	0.3463±0.0286
HD 90435	8.88	B7/8III/IV	-7.761	+3.658	+9.51±0.23	21.0±0.1	0.5164±0.0465
HD 90552	9.82	A4/7	-15.592	+4.086	+30.24±0.12	130.0±0.4	1.0433±0.0606
HD 302751	10.15	K2	-11.823	+8.164	+3.57±0.24	0.6±0.4	0.9386±0.0296
HD 302759	11.00	A	-9.162	+4.149	+9.35±0.25	54.0±0.4	0.5947±0.0332
HD 302760	11.00	A3	-2.414	+0.091	-2.72±0.02	21.3±0.1	0.8590±0.0328
HD 302761	10.28	F2	-9.068	+3.600	+5.76±0.19	68.6±0.2	1.9200±0.2500
HD 302858	11.46	A0	-6.330	+2.781	-0.78±1.10	174.0±0.4	0.6726±0.0381
TYC 8608-1-1	12.01		-8.612	+1.721	+4.84±0.24	39.9±0.2	0.3996±0.0299
TYC 8608-25-1	12.49		-8.321	+1.287	-4.40±0.09	149.6±0.1	0.4438±0.0290
TYC 8608-33-1	12.10		-0.5	+3.3	+11.45±0.31	46.3±0.2	
TYC 8608-69-1	11.92		-7.706	+3.257	+8.77±0.18	34.3±0.2	0.3548±0.0279
TYC 8608-153-1	11.59		-7.844	+2.164	+10.99±0.13	149.4±1.1	1.0902±0.0305
TYC 8608-193-1	10.87		-7.291	+3.146	-44.24±0.04	0.0±0.1	0.4448±0.0292
TYC 8608-213-1	12.30		-6.243	+5.414	+27.50±0.32	62.7±0.1	0.5156±0.0293
TYC 8608-221-1	10.66		-11.166	-1.933	-46.78±0.04	0.1±0.2	0.7723±0.0327
TYC 8608-1503-1	12.04		-7.572	+3.532	-7.61±0.02	34.1±0.4	0.3832±0.0323

1 - Phase 0.^P761 according to ASAS SN (Kochanek et al. 2017)

most likely foreground stars, and three others have an uncertain status.

It should be noted that our results are consistent with those from other sources: $RV = -13.00 \text{ km s}^{-1}$ (Mermilliod et al. 2008) and -12.19 ± 0.13 (GAIA DR2) for CPD -57°3199; $RV = 1.17 \pm 0.19 \text{ km s}^{-1}$ (GAIA DR2) for HD 302751 and $RV = 41.45 \pm 0.50$ (GAIA DR2) for TYC 8608-221-1, respectively. It is obvious that the majority of the confident cluster members have close RV s. As seen, these objects RV s lie in the range from -7.0 to $+19.0 \text{ km s}^{-1}$. As for UW Car, besides our estimate, there are two other estimates of the $RV = -14.80 \pm 0.9 \text{ km s}^{-1}$ (Gontcharov 2006) and $-1.08 \pm 14.14 \text{ km s}^{-1}$ (GAIA DR2).

As seen in Table 1, three K-giants CPD -57°3199, HD 302751, and TYC 8608-221-1 as well as the A-star TYC 8608-193-1 have evidently low $v \sin i$, the B-giant HD 90435 and the A-star HD 302760 have relatively low $v \sin i$, while other hot main-sequence (hereafter MS) stars are faster-rotating objects. It was very surprising to detect that the Cepheid UW Car has an unusually high $v \sin i$.

3.2 Color-indices, color-excesses, reddenings, and atmospheric parameters

As was mentioned above, only Segel et al. (2019) determined a color-excess for the cluster. It corresponds to a visual extinction of $A_V = 0.^m84 \pm 0.^m02$. To improve these parameters, we have used their T_{eff} and $\log g$ determined with the model fitting method. In the next step, the intrinsic color-indices $(B-V)_0$ were determined for the hot B- and A-type stars using the Kurucz

(1993) models and theoretical color-indices from Bessel et al. (1998). For more evolved stars of *FGK* spectral types with a large number of narrow metallic absorption lines we used the lines depth relationships to derive T_{eff} (Kovtyukh 2007) and a Fe ionization balance to derive $\log g$. These estimates give us an opportunity to determine corresponding $(B-V)_0$ for the *FGK*-stars.

Figure 1 demonstrates a “ $v \sin i - T_{\text{eff}}$ ” graph for the studied stars. As seen, the three *K* - giants, the Cepheid, the F- and A- MS-stars (12 objects) have a notable relation, while the hot giants group (6 objects) are located separately. This graph allows to separate stars of the different luminosity types in this cluster.

The described above results allowed us to determine the color-excesses, reddenings, and interstellar extinction. All these data are given in Table 2. We used the $(B-V)$ color-indices from TYCHO catalogue (Høg et al. 2000). Fig. 2 represents the reddening versus intrinsic color diagram for the cluster. There are two groups of hot stars: the first group (7 objects) has reddening values in a range of $0.^m00 - 0.^m34$ with a mean $A_V = 0.^m20 \pm 0.^m11$, while that for the second group is $0.^m86 - 1.^m41$ and a mean $A_V = 1.^m02 \pm 0.^m32$, respectively. The first group most likely consists of the confident cluster members (according to their parallaxes), and the second one consists of possible foreground objects. It is interesting that the possible foreground objects HD 90552 and HD 302760 fit well into the first group. TYC 8608-193-1, whose RV estimate differs noticeably from those of the other group, behaves similarly, while another possible foreground object TYC 8508-1-153 seems to belong to the second group. The reddening value $A_V = 0.^m84 \pm 0.^m02$ for the cluster derived from the color-excess suggested

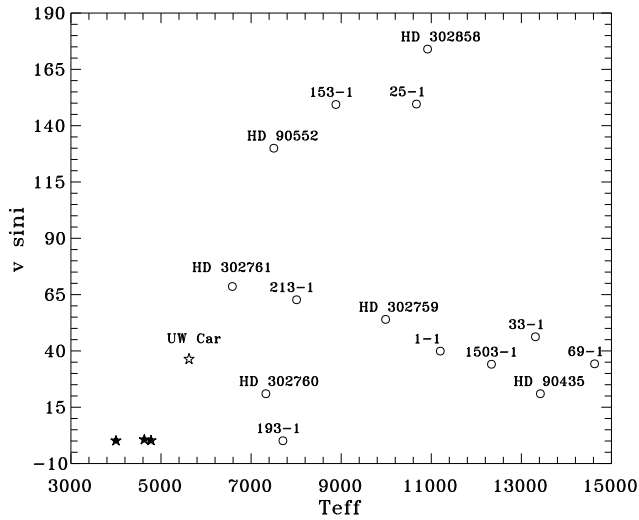


Figure 1: Relationship between the rotation velocity and T_{eff} for the objects from our list. Open circles show the main sequence B- and A- stars and B-giants, filled five-point stars show the K-supergiants, open five-point stars show the Cepheid.

by Siegel et al. (2019) is closer to that of the second group, and the same we can say about the A_V for the Cepheid UW Car. The average A_V for both groups comes to $0.^m65 \pm 0.^m18$.

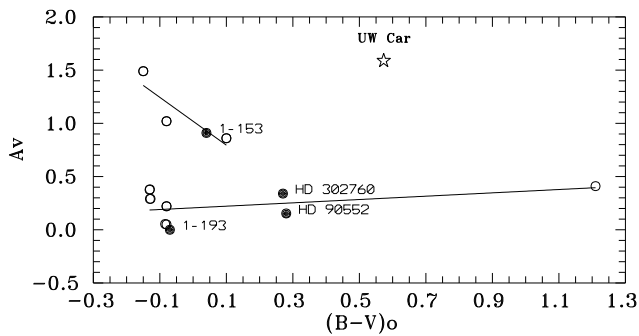


Figure 2: Reddening versus intrinsic color diagram for probable Collinder 220 members. Open circles represent probable confident members, filled circles show probable foreground objects, lines – linear approximations. Open star – Cepheid UW Car.

3.3 Absolute magnitudes and distances

Table 3 contains the absolute magnitudes of the Collinder 220 objects derived from the GAIA DR2 parallaxes and our T_{eff} and A_V data as well as from the $(B-V)_0$ color-indices and T_{eff} from to the Pecaut & Mamajek (2013) tables for MS stars. According to Table 3,

the absolute magnitude and distance, which were calculated by these two methods show an acceptable close range values only for three objects. Figure 3 represents the HR-diagram for the Collinder 220 objects. It shows that all the possible confident cluster members except for TYC 8608-193-1 lie well on the MS. TYC 8608-69-1 is located near the cluster's turn-off point, and it could probably be a blue giant. HD 90435 has already passed this point and is indeed a blue giant. It is interesting that possible foreground stars HD 302858 and TYC 8608-153-1 fall onto the cluster's MS. HD 90662, HD 302760, and TYC 8608-193-1 are not the cluster's members.

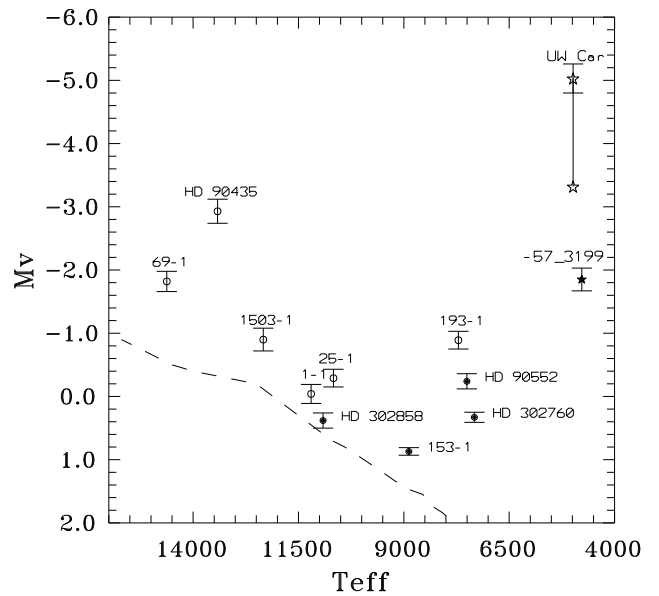


Figure 3: T_{eff} versus M_V diagram for the Collinder 220 possible members. The symbols represent the same objects as in Fig. 2., and filled star – K-giant CPD $-57^\circ 3199$. For UW Car M_V data according to GAIA DR18 parallax (with error bars) and Fernie et al. (1995) catalogue. Dashed line – main sequence according to Pecaut & Mamajek (2013).

Figure 4 represents a E_{B-V} versus $(V - M_V)$ variable - extinction diagram for the possible confident members of Collinder 220. This diagram shows that the distance modulus for the open cluster is $11.^m83 \pm 0.^m71$. Therefore, taken into account our reddening estimates of $0.^m20$ and $1.^m02$ we can derive the Collinder 220 distances of 2118 ± 590 or 1452 ± 405 pc, respectively. The former value takes into account the Cepheid UW Car, which belongs to the cluster, is more preferable. However, the intermediate value is closer to the color-excess and distance modulus from Segel et al. (2019), as mentioned above.

Table 2: Atmospheric parameters, rotational velocities, intrinsic colors, color-excesses, reddenings, and interstellar extinctions for the Collinder 220 objects.

Star	T_{eff}	$\log g$	$(B-V)_0$	E_{B-V}	A_V	R
UW Car ¹	4984±3	2.52±0.01	0.57	0.46	1.56	3.51
CPD -57°3199	4855±3	1.79±0.01	1.21	0.11	0.41	3.72
HD 90435	13420±2	3.76±0.01	-0.13	0.11	0.38	3.30
HD 90552	7504±5	3.43±0.01	0.28	0.05	0.15	3.39
HD 302751	4630±3	2.01±0.01	-	-	-	-
HD 302759	9985±6	3.29±0.00	-0.06	2.95	-	-
HD 302760	7327±6	2.47±0.03	0.27	0.10	0.34	3.40
HD 302761	6503±3	2.41±0.01	-	-	-	-
HD 302858	10917±4	3.92±0.01	-0.08	0.07	0.22	3.40
TYC 8608-1-1	11200±10	3.84±0.01	-0.08	0.02	0.05	3.35
TYC 8608-25-1	10669±0	3.43±0.00	-0.08	0.30	1.02	3.36
TYC 8608-33-1	13331±7	3.84±0.01	-0.13	0.09	0.29	3.30
TYC 8608-69-1	14626±6	3.32±0.01	-0.15	0.46	1.49	3.31
TYC 8608-153-1	8882±14	3.77±0.02	0.04	0.27	0.91	3.37
TYC 8608-193-1	7705±5	3.50±0.01	-0.07	0.01	0.00	3.36
TYC 8608-213-1	8010±1	3.52±0.01	0.15	-	-	-
TYC 8608-221-1	4000±3	2.25±0.01	-	-	-	-
TYC 8608-1503-1	12336±27	4.22±0.01	0.10	0.26	0.86	3.32

1 - T_{eff} , $\log g$, and $(B-V)_0$ for the pulsational phase of 0.761 according to Kochanek et al. (2017).

Table 3: Comparison between absolute magnitudes and distances, determined using the GAIA DR2 parallaxes and photometric data.

Object	M_V (GAIA)	M_V (P&M13)	d (pc) (GAIA)	d (pc) (P&M13)	Membership
UW Car	-5.03±0.23		3776±422		m
CPD -57°3199	-1.85±0.18		2888±239		m
HD 90435	-2.93±0.19	-0.32	1937±174	582	m
HD 90552	-0.24±0.12	+2.29	959±56	299	fg
HD 302751			1065±34		fg
HD 302759			1682±94		fg?
HD 302760	+0.33±0.08		1164±45		fg
HD 302858	+0.38±0.12	+0.60	1487±84	1342	fg?
TYC 8608-1-1	-0.04±0.15	+0.45	2503±187	2001	m
TYC 8608-25-1	-0.29±0.14	-0.42	2253±147	2389	m
TYC 8608-69-1	-1.82±0.16	-1.18	2819±222	2101	m
TYC 8608-153-1	+0.87±0.06	+1.89	917±26	575	fg
TYC 8608-193-1	-0.89±0.14	+0.70	2248±148	1081	m?
TYC 8608-213-1			1940±110		m?
TYC 8608-221-1			1295±55		fg
TYC 8608-1503-1	-0.90±0.18	-0.10	2610±220	1806	m

P&M13 - Pecaut & Mamajek (2013), [m] - confident member, [fg] - foreground star

3.4 Particular case 1. UW Car problem.

For this 5.^d35 Cepheid according to the Fernie et al. (1995) catalogue $M_v = -3.^m32$ and $d = 1844$ pc. According to Anderson (2018), its $(V - M_V) = 11.^m63 \pm 0.^m20$ and $M_V = -3.^m60 \pm 0.^m31$. However, according to the GAIA DR18 parallax, $M_V = -5.^m03 \pm 0.^m23$ and $d = 3776 \pm 422$ pc. Such a large data scatter rises doubts to the UW Car membership in Collinder 220. Although using our distance modulus for the cluster and our E_{B-V} for the Cepheid, we can derive $M_V = -4.^m17 \pm 0.^m71$ and $d = 2606 \pm 1008$ pc for UW Car.

3.5 Chemical abundances

When the atmospheric parameters were derived, we used the VALD oscillator strengths (Kupka et al. 1999) and LTE model atmospheres from Castelli &

Kurucz (2004) to determine the element abundances. In particular, we worked on three stars with relatively low projectional rotation velocities: UW Car, CPD -57°3199, and HD 90435. As seen from Table 3, two of these objects (except for the Cepheid) are true cluster members. Therefore, the chemical abundances of each object from our list are of interest. Table 4 presents the results of our investigation. It turned out that all these different spectral type stars have an equal iron content, solar-like abundances of α -, Fe-group, r- and s-process elements. Our elemental abundances are in good agreement with those derived by Luck & Lambert (2011). At the same time, the blue giant HD 90435 has a CNO-content close to the solar one, but the cooler Cepheid and K-giant have a deficit of C and an overabundance of N.

Table 4: Chemical abundances for single Collinder 220 objects.

Element	UW Car				76 (HD 90435)			69 (BD $-57^{\circ}3399$)		
	[El/H]	σ	NL	LL11	[El/H]	σ	NL	[El/H]	σ	NL
C I	-0.51	0.16	7	-0.17				-0.34	0.20	3
C II					0.34	-	1			
N I	0.55	0.07	3	0.46	0.17	0.38	4	0.21	0.13	2
O I	-0.13	0.20	3	0.18	0.19	-	1	0.13	0.07	3
Na I	0.26	0.10	2	0.18				0.39	0.07	2
Mg I				0.26				0.53	0.18	2
Mg II					0.99	0.33	2			
Al I	0.23	0.19	2	0.05				0.15	0.11	6
Al II					0.76	-	1			
Si I	0.04	0.14	7	0.14				0.09	0.04	6
Si II	-0.30	-	1		-0.17	0.09	4			
S I	-0.20	-	1					0.19	0.06	2
S II										
K I	0.16	-	1					0.23	-	1
Ca I	0.02	0.08	4	0.09				-0.10	0.06	3
Sc II								0.19	0.12	5
Ti I	0.03	0.08	17	0.19				-0.10	0.17	21
Ti II	0.18	0.08	2		0.85	0.18	4	0.29	0.14	4
V I	-0.09	0.19	4					-0.11	0.10	8
V II	-0.12	0.17	3					-0.13	0.08	2
Cr I	-0.19	0.16	16	0.05				-0.15	0.17	15
Cr II	0.13	0.16	16		0.11	-	1	0.36	0.08	5
Mn I	-0.15	0.12	4	-0.16				0.26	0.30	3
Mn II					0.86	0.11	2			
Fe I	0.09	0.10	137	0.09				0.10	0.15	217
Fe II	0.09	0.11	12	0.09	0.04	0.20	22	0.08	0.17	19
Co I	-0.22	0.13	8	-0.04				0.07	0.14	8
Ni I	-0.07	0.15	34	-0.04				-0.04	0.11	47
Ni II					0.46	-	1			
Cu I	-0.07	0.25	4					0.70	0.65	4
Zn I	-0.09	-	1					0.48	0.43	3
Rb I	0.17	-	1					-0.30	0.01	2
Y II	0.16	0.06	4	0.17				0.36	0.22	5
Zr II	-0.08	0.13	2					0.34	0.32	3
La II	0.09	0.14	4	0.27				0.40	0.10	5
Ce II	0.07	0.04	6	0.10				0.13	0.12	5
Pr II	-0.17	0.20	3	-0.15				0.23	0.09	4
Nd II	0.03	0.11	7	0.07				0.32	0.11	7
Sm II	-0.12	0.12	3	0.01				0.23	0.13	3
Eu II	0.03	0.20	2	0.22				0.23	0.18	3
Gd II	0.43	-	1	-				0.39	-	1

LL11 - Luck & Lambert (2011), NL is the number of spectral lines used for the abundance determination.

4. Summary

1. According to the derived RV, color-indices, and parallaxes, only 7 of the 18 investigated objects are confident members of Collinder 220. They are HD 90435, CPD $-57^{\circ}3199$, TYC 8608-1-1, TYC 8608-25-1, TYC 8608-69-1, TYC 8608-1503-1 and UW Car. TYC 8608-193-1, which was assumed to be as a confident member, probably do not belong to the open cluster. Other 11 objects are probably foreground stars.
2. The distances of the confident cluster members, determined from the GAIA DR2 2018 parallaxes, lie in a range of 1900–2800 pc. The Cepheid distance, which is near 3775 pc, is most likely over-estimated.
3. Among the confident cluster members, only TYC 8608-25-1 has a high projectional rotation velocity, while for other stars and Cepheid UW Car these estimates lie in a range of 24–40 km s^{-1} . The

K-giant CPD $-57^{\circ}3199$ has a very low value of $v \sin i$.

4. We have determined color-excesses E_{B-V} and reddening for the majority of objects from the list that allowed us to refine their intrinsic color-indices, especially for the hot stars.
5. Atmospheric parameters of the hot stars were determined by fitting method, while parameters of the Cepheid, K- giant, and blue giant were determined exclusively by the method of atmosphere models.
6. Using E_{B-V} , A_V , and R values derived by us for confident cluster members, we have determined the mean $A_V = 0.^m20 \pm 0.^m11$, distance modulus $V-M_V = 11.^m83 \pm 0.^m71$, and distance $d = 2118 \pm 590$ for the cluster. The Cepheid UW Car has an absolute magnitude of $-4.^m17 \pm 0.^m71$ and $d = 2606 \pm 1008$ pc.
7. The B-giant HD 90435 is located on the horizontal branch after the cluster's "turn-off" point, while

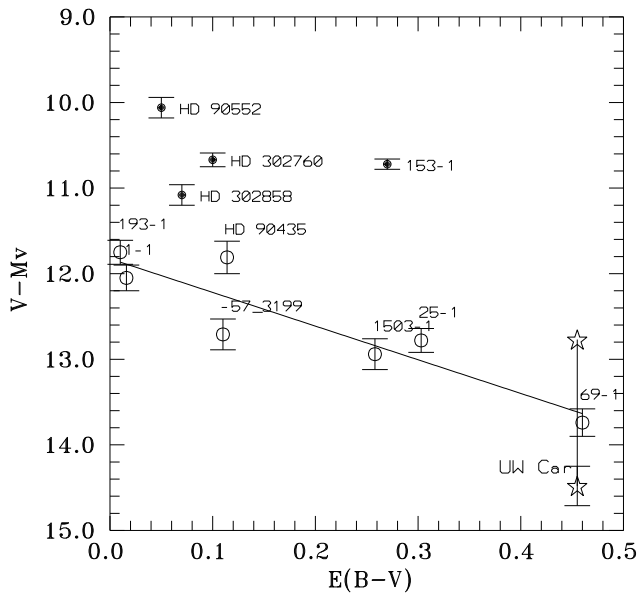


Figure 4: Variable-extinction diagram for possible Collinder 220 members. The symbols represent the same objects as in Fig. 2 and 3.

UW Car and CPD $-57^{\circ}3199$ are more evolved cool supergiants. Therefore the abundances of carbon, nitrogen, and oxygen in HD 90435 turned out to be close to the solar ones, while there is a deficit of C and an overabundance of N and Na with a solar-like O abundance for the cool supergiants. This fact indicates that the Cepheid and CPD $-57^{\circ}3199$ have already passed through the "first dredge-up" stage.

References

- Anderson, R.I.: 2018, *ApJ* **861**, 36.
- Bessell M.S., Castelli F. & Plez B.: 1998, *A&A*, **333**, 231.
- Cantat-Gaudin, T., Jordi, C., Vallenari, A. et al.: 2018, *A&A*, **618**, 93.
- Castelli, F. & Kurucz, R.L.: 2004, *arXiv: astro-ph/0405087*.
- Chen, X., de Grijs, R., Deng, L.: 2015, *MNRAS*, **446**, 1268.
- Coelho, P.R.T.: 2014, *MNRAS*, **440**, 1027.
- Dias, W.S., Monteiro, H., Caetano, T.C., Lepine, J.R.D., Assafin, M., Oliveira, A.F.: 2014, *A&A*, **564**, 79.
- Fernie, J.D., Beattie, B., Evans, N.R., Seager, S.: 1995, *IBVS*, **4348**, 1.
- GAIA DR2 Catalogue,; 2018, *CDS/ADS Collection of Electronic Catalogues*, 1345, 0.
- Gontcharov, G.A.: 2006, *AstL* **32**, 759.
- Høg, E., Fabricius, C., Makarov, V.V., et al.: 2000, *A&A* **355**, 27.
- Kharchenko, N.V., Piskunov, A.V., Schilbach, E., Roser, S., Scholtz, R.-D.: 2013, *A&A* **558**, 53.
- Kochanek, C.S., Shappee, B.J., Stanek, K.Z., et al.: 2017, *PASP* **129**, 104502.
- Kovtyukh, V.V.: 2007, *MNRAS* **378**, 617.
- Kupka, F., Piskunov, N.E., Ryabchikova, T.A., Stempels, H.S., Weiss, W.W.: 1999, *A&A*, **138**, 119.
- Luck, R.E., Lambert, D.L.: 2011, *AJ*, **142**, 136.
- Mermilliod, J.C., Mayor, M., Udry, S.: 2008, *A&A*, **485**, 303.
- Pecaut, M.J., Mamajek, E.E.: 2013, *ApJS*, **208**, 9.
- Segel, M.H., LaPorte, S.J. Porterfield, B.L., Hagen, L.M.Z., Gronwall, C.A.: 2019, *AJ* **158**, 35.
- Straizys, V.: 1981, *Metal-Deficient Stars*, "Mokslas", Vilnius.

DOI:<http://dx.doi.org/10.18524/1810-4215.2020.33.216289>

SPECTROSCOPIC INVESTIGATIONS OF THE POLARIS (α UMi) SYSTEM: RADIAL VELOCITY MEASUREMENTS, NEW ORBIT, AND COMPANION INFLUENCE FOR THE CEPHEID POLARIS Aa PULSATION ACTIVITY.

I. A. Usenko,^{1,2} A. S. Miroshnichenko,^{3,4,5} S. Danford,³ V. V. Kovtyukh,¹ D. G. Turner⁶

¹ Astronomical Observatory, Odessa National University, Shevchenko Park,
Odessa 65014, Ukraine, vkovtyukh@ukr.net

² Mykolaiv Astronomical Observatory, Obsevatorna 1,
Mykolaiv 54030, Ukraine, igus99@ukr.net

³ Dept. of Physics and Astronomy, University of North Carolina at Greensboro,
P.O. Box 261170, Greensboro, NC 27402, USA, a_mirosh@uncg.edu; danford@uncg.edu

⁴ Main Astronomical Observatory of the Russian Academy of Sciences,
Pulkovskoe shosse 65–1, Saint-Petersburg, 196140, Russia

⁵ Fesenkov Astrophysical Institute, Observatory 23, Almaty, 50020, Kazakhstan

⁶ Dept. of Astronomy and Physics, Saint Mary's University
923 Robie Street, Halifax B3H3C3, Nova Scotia, Canada, turner@ap.smu.ca

ABSTRACT. Thirty three spectra of the Polaris system obtained in August–December 2019 and February–April 2020 at the 0.81 m telescope of the Three College Observatory (TCO, North Carolina, USA) were used to determine the radial velocities (RV) and effective temperature of the Cepheid Polaris Aa. These new data have been added to the entire Polaris system RV data collection (over 2,500 measurements) to compute a new orbit of the Polaris Aa companion. Furthermore we have used our eight observational datasets taken in 2015–2020 and eight datasets taken in 2011–2018 by Anderson (2019) to check for possible influence of the orbital motion of Polaris Ab on the Polaris Aa pulsational activity. It was found that the mean pulsational period in 2015–2020 was quite stable (3.976 ± 0.012 days), while the pulsational amplitude showed evident changes: a growth before HJD 2457350 with a following decrease. This fact could be due to the Polaris Ab passing through the periastron.

Key words: α UMi (Polaris Aa and Polaris Ab) system; radial velocities; Polaris Aa effective temperatures; Polaris Aa pulsational period and amplitude; orbital elements.

АНОТАЦІЯ. Тридцять три спектри системи Полярної, отримані в серпні-грудні 2019 та лютому-квітні 2020 рр. на 0.81-м телескопі Обсерваторії Трьох Колледжів (ТСО, Північна Кароліна, США) були використані для отримання радіальних

швидкостей та ефективних температур цефеїди Полярної Аа. Ці нові данні були додані до загальної колекції радіальної швидкості Полярної (більш ніж 2500 оцінок), щоб розрахувати нову орбіту супутника цефеїди – Полярної Аб. Усі наші 187 спектри, що були отримані за період 2015–2020 рр. у восьми спостережних серіях за додатком восьми серій 2011–2018 рр. з роботи Андерсона (2019, 164 спектра) були використані, щоб перевірити можливий вплив орбітального руху Полярної Аб на пульсаційну активність Полярної Аа. Цей спостережний період є цікавим, тому що він охоплює час проходження через периастр та висхідний вузол супутника Полярна Аб. Було встановлено, що середній пульсаційний період у 2015–2020 рр. був досить стабільним (3.9722 ± 0.001 дб), тоді як амплітуда пульсації показує наявні зміни: зріст до HJD 2457350 з наступним зменшенням. Цей факт може бути пояснений проходженням Полярної Аб через периастр орбіти. Згідно з поведінкою пульсаційної амплітуди, ми можемо передбачити її поведінку у найближчому майбутньому. У зв'язку з цим, подальші отримання радіальних швидкостей системи Полярної Аа мають дуже важливе значення. Орбітальний рух зорі Полярної Аб має вплив на пульсаційну амплітуду Полярної Аа в залежності від орбітальної фази. А середня ефективна температура цефеїди Полярної Аа показує помітний зріст за кожний спостережний

сезон.

Ключові слова: Класичні цефеїди; система α UMi (Полярна Аа та Полятна Аб) ; Радіальні швидкості руху; Ефективні температури Полярної Аа; Пульсаційний період і амплітуда Полярної Аа ; Елементи орбіти.

1. Introduction

Radial velocity measurements of the Polaris system, in addition to studies of its pulsation period changes and the amplitude of the pulsation curve of the main component, the Cepheid Polaris Aa, are important for clarifying the properties of the Polaris Ab companion and the dynamics of this binary system. Over 2,500 RV estimates that cover four orbital cycles of Polaris Ab have been obtained in the last about 130 years (see Fig. 1).

The first orbital cycle (HJD 2414900 – 2426000) is the most covered compared to the second one (HJD 2426000 – 2436500), while the third cycle is the least covered. The observations taken between HJD 2445000 and 2447500 were carried out quite frequently. These data were obtained with photographic plates. A large fraction of the most recent observations taken during the fourth covered orbital cycle (since HJD 2447500) was obtained with CCD detectors.

An abrupt decrease of the pulsation amplitude is clearly visible in Fig. 1. It had began precisely in the “third orbit” time lag, especially near the ascending node of the orbit. Since the orbital motion of Polaris Ab is retrograde (Evans et al. 2018), the moment of its periastron passage occurs before passing through the point of the ascending node. It can be noted that no frequent spectroscopic observations were reported between 2007 and 2011 except for a few measurements. Our observations between 2015 and 2018 (Usenko et al. 2016, 2017, 2018) and those presented by Anderson (2019) were taken around these important orbital phases (see Fig. 2).

Additionally, according to our estimates, the pulsation period of Polaris Aa has increased compared to that of 2016–2017, and the pulsation amplitude showed a tendency to decrease (Usenko et al. 2018). However, Anderson (2019) indicates an amplitude constancy in 2011–2018. In this regard, the question arises: what are the roles of the orbital configuration and the orbital motion itself in changing the Polaris Aa pulsation amplitude?

To answer this question, we carried out further spectroscopic observations of the Polaris system from August 2018 to April 2020 and analyzed the results of the RV measurements relative to the orbital system’s motion. In particular, the following goals were set:

1. To choose short-term data sets (from 10 to 150

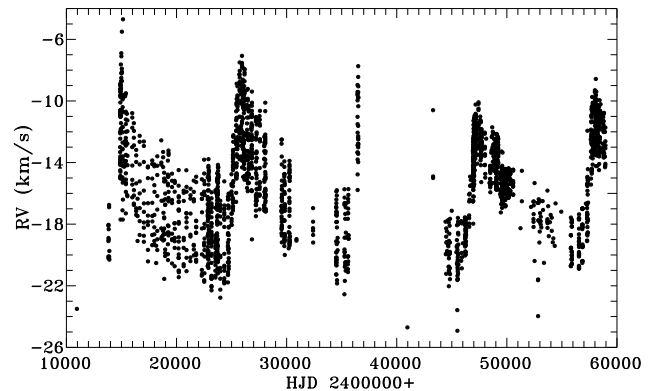


Figure 1: Polaris radial velocity estimations over the last \sim 130 years.

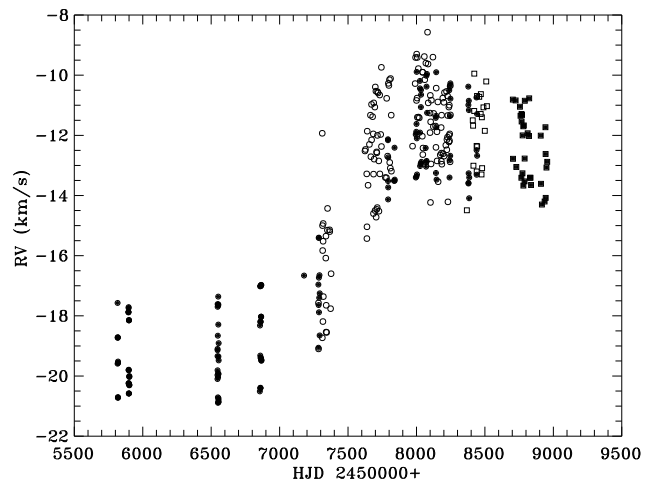


Figure 2: Radial velocity measurements of Polaris Aa from 2011 to 2020. Data from Anderson (2019) are shown by filled circles, our data obtained from 2015 to the first half of 2018 (open circles), September 2018 – January 2019 (open squares), second half of 2019 – first half 2020 (filled squares).

days) during which RV changes due to orbital motion could be neglected.

2. To obtain the best purely sinusoidal approximation for each of these data sets and to determine parameters of every orbit/pulsational cycle (period, amplitude, mean heliocentric velocity and the cycle’s initial phase).
3. To determine the mean heliocentric velocity values (γ -velocity) to calculate the orbit of Polaris system.
4. To subtract the orbital velocity values from the estimated heliocentric velocity ones.
5. To derive the pulsational cycle parameters from all our measurements.

Therefore we have used eight our observational sets, eight sets from Anderson (2019) data, and some earlier sets for a more precise determination of the Polaris system orbital period. The Kamper (1996) data were omitted due to a very small pulsational amplitude at that time period.

2. Observations and development of spectra

Fifty three spectra were obtained in the present data set: 20 in September 2018–January 2019, 24 in August–December 2019, and 9 in February–April 2020. All the observations were obtained with the 0.81 m telescope of the Three College Observatory (TCO) in North Carolina. This telescope is equipped with an échelle spectrograph manufactured by Shelyak Instruments¹. The instrument operates in the spectral range from 3850 to 7900 Å with a spectral resolving power of $R \sim 12,000$ and no gaps the between spectral orders. The average S/N ratio in the continuum was 150–200, while most spectral lines used in our analysis were taken from the range 4900–6800 Å. The data were reduced with the *échelle* package in IRAF.

The DECH 30 software package² was used to measure the line depths and RVs. The latter were measured by cross-correlation and the parabolic fitting methods. The uncertainty of the RV measurements is between 1.0 and 1.8 km s^{-1} . The line depths were used to determine the effective temperature. A method based on the depth ratios of selected pairs of spectral lines is the most sensitive to the temperature (Kovtyukh 2007). The method provides an internal accuracy of the T_{eff} determination of $\sim 10\text{--}30$ K (standard deviation of the average).

The derived values of T_{eff} and RV measured from hydrogen and metallic lines in each spectrum are presented in Table 1. These RV values are shown in Fig. 2.

3. Pulsation and orbital period analysis

The next step in the analysis was to use purely sinusoidal approximations for the data sets determined by the least squares method. As an example, one of these approximations is shown in Fig. 3, and the best-fit parameters are presented in Table 2. To derive a more precise orbital period of the Polaris A system, we have used the data from our observational seasons in combination with those from eight seasons published by Anderson (2019) and from six seasons published by Roemer (1965). The following general equation for the RV variations on an elliptical orbit was used for finding the best fits to the data:

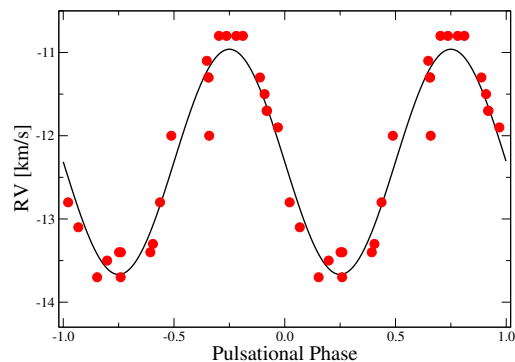


Figure 3: A sinusoidal least square method approximation for our HJD 2458704–2458837 observational set.

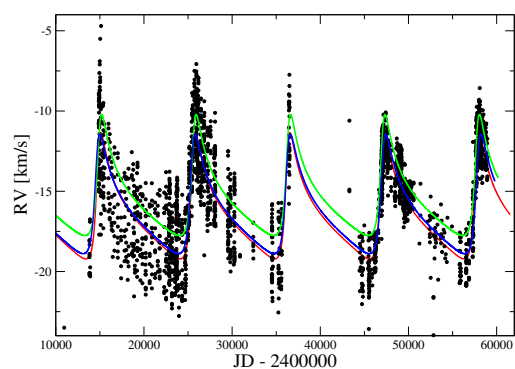


Figure 4: Comparison of the Polaris orbits: red line – Kamper (1996), green line – Anderson (2019), blue line – our data.

$$RV = \gamma + K(e \cos \omega + \cos(M + \omega)), \quad (1)$$

where K is the semi-amplitude of radial velocity variations, γ is the systemic RV , e is the orbital eccentricity (was always set to zero), ω - the argument of the periastron, M is the true anomaly.

Table 3 contains the orbital parameters of the Polaris system that had been published earlier and our new results. Figure 4 represents the median orbital RV curves of the Polaris A system using the orbital elements from Anderson (2019), Kamper(1996), and this work that have been calculated according to a selection of observational seasons from Table 2 and the data from Table 1. As seen from Table 3 and Fig. 4, our results are closer to those found by Kamper (1996). According to the orbital elements from Anderson (2019), Polaris Ab passed through periastron on 29 November 2016 and through the ascending node - on 18 October 2017, while using the elements from Kamper (1996) these dates are 1 April 2017 and 17 April 2018, respectively.

Figure 5 shows the pulsational period changes according to Anderson (2019) and to our data. As seen, these changes show some periodicity. If we use all our RV data with the orbital velocity subtracted, then we have a Fourier power spectrum (Fig. 6) with quite a

¹<http://www.shelyak.com>

²<http://www.gazinur.com/DECH-software.html>

Table 1: Observational data of α UMi (NL – number of lines)

HJD 2450000+	T_{eff} K	σ K	Phase	RV(km s^{-1})					
				Metals	σ	NL	H_{α}	H_{β}	H_{γ}
8368.5931	6058	21	0.934	-14.49	1.70	176	-14.45	-14.84	-14.67
8411.4928	6057	20	0.731	-11.50	1.77	159	-12.23	-9.93	-8.58
8413.5843	6055	19	0.258	-11.68	1.68	189	-12.23	-8.92	-10.96
8416.5683	6073	23	0.009	-13.01	1.61	173	-13.42	-7.80	-11.84
8421.6551	5984	18	0.289	-11.19	1.78	166	-11.20	-7.53	-10.24
8422.6439	5969	21	0.538	-9.95	1.86	157	-9.47	-4.03	-8.90
8439.6274	6038	22	0.812	-12.35	1.69	147	-12.07	-9.87	-11.31
8440.6117	6086	21	0.060	-13.20	1.91	155	-13.40	-10.75	-12.20
8442.6074	6050	21	0.562	-10.69	1.86	163	-10.18	-6.94	-8.58
8443.6292	6117	23	0.819	-12.37	1.60	153	-13.25	-8.88	-11.26
8458.6511	6074	21	0.600	-10.72	1.48	158	-11.30	-8.21	-8.81
8469.5308	6007	21	0.338	-11.29	1.47	159	-10.92	-8.52	-9.70
8470.5557	6083	25	0.596	-10.63	1.59	164	-10.74	-6.97	-9.46
8475.5715	6095	24	0.859	-13.30	1.20	161	-14.05	-9.15	-11.57
8477.5626	5948	20	0.360	-11.40	1.34	159	-10.33	-8.56	-9.44
8479.5699	6102	22	0.865	-13.09	1.45	170	-13.39	-10.70	-12.34
8489.5582	6041	20	0.379	-11.07	1.51	164	-10.38	-7.44	-9.77
8499.5614	6090	22	0.897	-11.85	1.37	160	-11.89	-8.81	-10.80
8509.5801	6050	22	0.418	-10.21	1.46	171	-10.12	-7.02	-8.83
8514.6088	6042	27	0.684	-11.03	1.63	170	-11.47	-9.57	-9.53
8704.6331	6011	20	0.557	-10.81	1.30	172	-10.82	-8.18	-10.98
8705.5884	6073	24	0.798	-12.78	1.30	164	-12.85	-11.23	-13.38
8724.5957	6058	19	0.588	-10.84	1.32	171	-10.43	-7.25	-10.49
8729.5863	6072	20	0.846	-13.05	1.38	181	-13.91	-8.96	-12.10
8755.7058	5931	23	0.429	-11.05	1.43	161	-11.09	-7.48	-10.23
8760.6257	6158	27	0.669	-11.35	1.52	164	-11.37	-9.05	-10.88
8766.6023	6032	29	0.176	-13.41	1.40	163	-14.03	-10.60	-12.85
8767.6403	6009	22	0.437	-11.29	1.26	164	-11.17	-7.81	-11.16
8768.6482	5985	26	0.691	-11.54	1.23	160	-11.54	-8.85	-11.43
8771.6134	6042	24	0.439	-11.32	1.48	159	-11.28	-8.25	-10.17
8774.5861	6078	23	0.188	-13.26	1.49	163	-14.76	-11.46	-12.86
8775.5933	6086	24	0.442	-12.00	1.29	164	-12.21	-9.79	-11.66
8780.5991	6049	18	0.703	-11.70	1.28	163	-11.95	-9.45	-11.51
8781.5251	6079	25	0.937	-13.67	1.37	158	-15.00	-11.83	-13.99
8784.5618	6078	23	0.702	-11.67	1.33	165	-11.20	-7.97	-10.52
8789.6421	6122	25	0.983	-13.53	1.54	170	-15.50	-12.51	-13.87
8790.5904	6057	25	0.222	-12.77	1.29	159	-14.39	-10.87	-12.06
8791.6463	5999	24	0.488	-10.85	1.46	160	-11.31	-7.85	-9.83
8812.5489	6056	21	0.756	-11.93	1.44	163	-12.30	-9.40	-10.66
8822.5455	6083	23	0.275	-12.02	1.45	168	-13.87	-10.18	-11.67
8823.5373	6050	20	0.525	-10.77	1.30	162	-10.54	-7.66	-9.60
8829.5468	6078	18	0.040	-13.41	1.47	161	-15.32	-11.08	-12.95
8833.5510	6040	26	0.049	-13.41	1.61	163	-15.63	-11.38	-13.32
8837.5157	6159	25	0.049	-13.65	1.62	192	-15.21	-11.81	-13.19
8907.6854	6031	20	0.734	-12.01	1.56	166	-12.26	-9.55	-10.86
8909.6695	6051	23	0.234	-13.61	1.63	196	-14.32	-14.73	-12.94
8916.6189	6121	23	0.986	-14.30	1.43	156	-14.86	-12.14	-13.28
8936.5658	6106	21	0.013	-14.20	1.85	197	-15.00	-11.32	-12.85
8942.5727	6034	22	0.527	-11.73	1.14	157	-11.45	-9.05	-10.31
8943.6633	6079	18	0.802	-12.62	1.17	153	-12.17	-9.44	-11.01
8944.6059	6145	24	0.040	-14.08	1.40	159	-15.15	-11.92	-13.34
8949.6344	6118	29	0.307	-13.07	1.49	157	-14.01	-10.48	-11.38
8955.5861	6100	23	0.807	-12.88	1.47	194	-12.85	-10.62	-11.78

Table 2: Polaris *RV* dataset during our and *HERMES* observational sets.

Source	JD range 2450000+	JD _{mid} 2450000+	NL	Period (days)	γ (km s^{-1})	K (km s^{-1})	T ₀ 2450000+ (days)
Roemer	14876–14951	14918	21	3.9585±0.002	-11.92±0.11	3.755±0.18	14874.591±0.025
Roemer	15378–15403	15391	16	3.9098±0.029	-13.27±0.50	2.358±0.79	15374.715±0.171
Roemer	18784–18878	18831	16	3.8087±0.020	-16.84±0.82	2.426±1.20	18778.901±0.292
Roemer	29792–29833	29816	11	4.0371±0.015	-16.79±0.03	2.047±0.15	29787.812±0.073
Roemer	34492–34576	34534	16	3.9847±0.005	-18.41±0.15	2.240±0.23	34488.449±0.054
Roemer	36440–36501	36472	8	3.9323±0.023	-10.75±0.10	2.288±0.13	36434.439±0.038
Hermes1	55816–55901	55872	10	3.9681±0.015	-19.18±0.23	1.466±0.33	55813.885±0.18
Hermes2	56546–56554	56550	9	3.9553±0.004	-19.17±0.02	1.675±0.03	56540.795±0.01
Hermes3	56855–56866	56862	11	3.9586±0.006	-18.73±0.04	1.821±0.05	56850.632±0.02
Hermes4	57283–57293	57288	9	3.9805±0.013	-17.20±0.07	1.829±0.13	57279.526±0.03
Hermes6	57994–58077	58033	22	3.9719±0.003	-11.67±0.08	1.775±0.12	57990.516±0.038
Hermes7	58141–58248	58196	14	3.9719±0.002	-11.77±0.09	1.733±0.13	58137.504±0.047
Hermes8	58379–58439	58402	9	3.9633±0.0028	-12.29±0.05	1.751±0.06	58375.814±0.024
TCO1	57283–57376	57332	21	3.9754±0.011	-16.72±0.41	2.052±0.60	57279.459±0.174
TCO2	57623–57744	57690	37	3.9787±0.009	-12.75±0.40	1.717±0.60	57617.046±0.218
TCO3	57772–57816	57798	12	4.0029±0.016	-11.78±0.17	1.592±0.20	57767.853±0.137
TCO4	57971–58109	58048	29	3.9633±0.004	-11.13±0.23	1.731±0.36	57966.927±0.109
TCO5	58120–58248	58196	38	3.9738±0.008	-11.65±0.24	1.115±0.36	58113.639±0.184
TCO6	58368–58514	58453	18	3.9754±0.005	-11.85±0.23	1.510±0.33	58363.854±0.139
TCO7	58704–58837	58778	24	3.9692±0.007	-12.31±0.20	1.353±0.27	58701.532±0.140
TCO8	58907–58955	58934	9	3.9659±0.007	-12.92±0.10	1.362±0.15	58904.094±0.065

Table 3: Orbital Parameters of Polaris systems.

Parameter	Roemer (1965)	Kamper (1996)	Turner et al. (2007)	Anderson (2019)	This work
P , yrs	30.46±0.10	29.59±0.02	29.71±0.09	29.32±0.13	29.25±0.03
e	0.639±0.012	0.608±0.005	0.543±0.010	0.620±0.008	0.633±0.044
T_0 , yr	1928.48±0.08	1928.48±0.08	1928.57±0.06	2016.19±0.1	1987.22±0.1
ω , deg	307.24±1.82	303.01±0.75	309.6±0.7	307.2±2.5	302.5±2.7
K , km s^{-1}	4.09±0.1	3.72±0.03	4.41±0.07	3.768±0.073	3.93±0.12
γ , km s^{-1}	-16.41	-16.42±0.03	-15.90±0.06	-15.387±0.04	-16.61±0.12

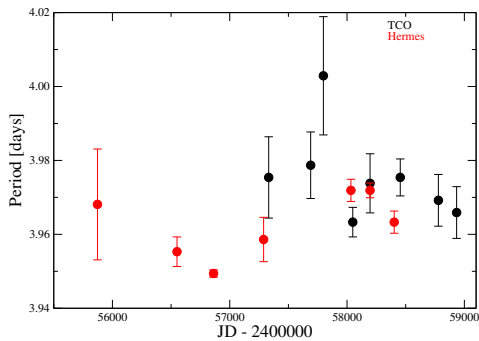


Figure 5: Polaris pulsational period changes in 2011–2020: red circles – Anderson (2019), black circles – our data.

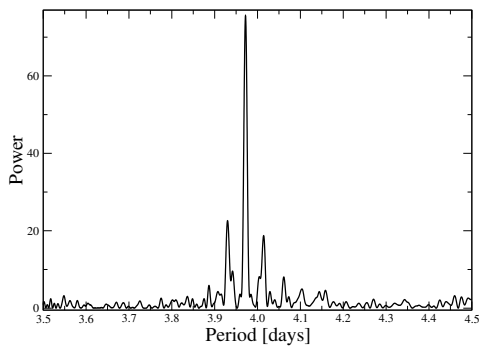


Figure 6: Fourier power spectrum of the Polaris Aa RV measurements for the 2015 – 2020 data.

constant pulsational period of 3.976 ± 0.012 days (see Table 2). Anderson’s data suggest a different value, because they were obtained on the ascending branch of the RV curve when the orbital velocity was significantly changing.

As seen in Fig. 7, the pulsational amplitude behaviour shows very noticeable changes during the time of our and Anderson’s observations. Our errors are somewhat higher because of a lower spectral resolving power and longer periods of pulsational cycles averaging. Two vertical lines denote the moments of the periastron passage according to Anderson (2019) (violet) and Kamper (1996) (blue). As seen, the pulsational amplitude growth could be connected immediately to the orbital motion of Polaris Ab and its passing through periastron. Moreover, we can predict a further decrease of Polaris Aa pulsational amplitude in the nearest future according to this graph.

4. Effective temperature changes

Figure 8 demonstrates the mean T_{eff} values estimated spectroscopically for each of our observational season jointly with earlier spectroscopic and photometrical ones. As seen, the mean T_{eff} of Polaris Aa during the last five years has been growing, and

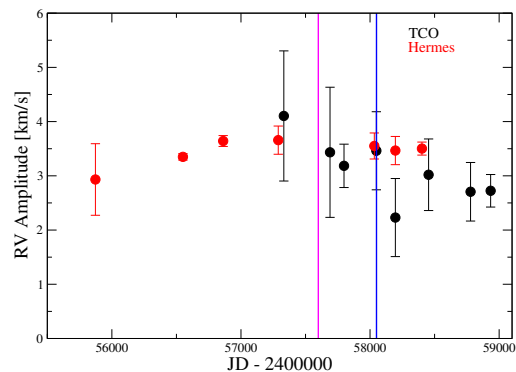


Figure 7: Pulsational amplitude of Polaris Aa according to data from Anderson (2019) (red) and our data from 2015 to 2020 (black). The violet and blue lines represent the moments of the periastron passage according to Anderson (2019) and Kamper (1996), respectively.

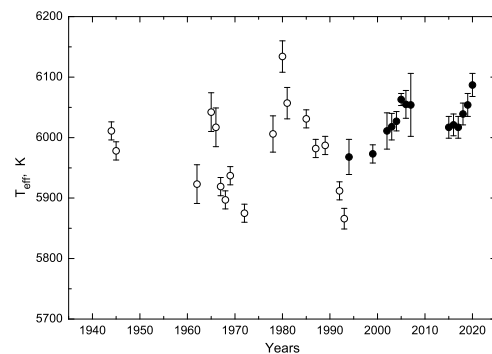


Figure 8: Variations of the mean T_{eff} of Polaris Aa during the last 75 years. Open circles - values from the $(B - V)$ vs. T_{eff} relationship by Gray (1992), filled circles - values from lines depth ratios (Kovtyukh 2007).

this phenomenon could be connected with the orbital motion of Polaris Ab.

5. Conclusions

The results of using 2585 RV data points during last 130 years we can suggest the following:

1. Our 187 *RV* observations obtained during last five years (8 observational seasons) along with 164 *RV* data points published by Anderson (2019) covered a fragment of the Polaris A orbit, which contained passages through a periastron and an ascending node.
2. The mean T_{eff} of Polaris Aa per season shows a gradual growth.
3. To check the influence of the Polaris Ab orbital motion on the Polaris Aa pulsational amplitude,

RV measurements from our data, those published by Anderson (2019), and some other sources have been analyzed.

4. Using these data, the orbit of the Polaris A binary system has been determined.
5. The mean pulsational period during five years demonstrates a certain stability.
6. The pulsational amplitude of Polaris Aa shows very strong changes, which contain a growth before HJD 2457350 with a subsequent decline. It is interesting that the decline has begun before the periastron passage.
7. Judging from the pulsational amplitude behaviour, we can predict its further decrease in the nearest future. Therefore further Polaris A *RV* observations are essential.
8. Orbital motion of Polaris Ab has an influence on the Polaris Aa pulsational amplitude depending on the orbital phase.

References

- Anderson R.I.: 2019, *A&A*, **623**, A146.
Evans N.R., Karovska M., Bond H.E., Schaefer G.H., Sabu K.C., Mack J., Nelan E.P., Gallenne A. & Tingle E.D.: 2018, *ApJ*, **863**, 187.
Gray D.: 1992, *Observations and Analysis of Stellar Atmospheres, 2nd edn. Cambridge Univ. Press, Cambridge*
Kamper K.W.: 1996, *JRASC*, **90**, 140.
Kovtyukh V.V.: 2007, *MNRAS*, **378**, 617.
Roemer E.: 1965, *ApJ*, **141**, 1415.
Usenko I.A., Kovtyukh V.V., Miroshnichenko A.S., Danford S.: 2016, *Odessa Astron. Publ.*, **29**, 100.
Usenko I.A., Kovtyukh V.V., Miroshnichenko A.S., Danford S.: 2017, *Odessa Astron. Publ.*, **30**, 146.
Usenko I.A., Kovtyukh V.V., Miroshnichenko A.S., Danford S.: 2018, *MNRAS*, **481**, L115.

RADIOASTRONOMY

DOI: <http://dx.doi.org/10.18524/1810-4215.2020.33.216305>

DISTRIBUTION OF THE OCCURRENCE OF THE INTENSIVE IONOSPHERE SCINTILLATIONS ON THE OBSERVATIONS OF THE COSMIC RADIO SOURCES AT THE DECAMETER WAVE RANGE

O. A. Lytvynenko, S. K. Panishko

Observatory URAN-4, Institute of Radio Astronomy NASU
Pushkinskaya str., 37, Odessa, 65125, Ukraine, spanishko@ukr.net

ABSTRACT. Effect of scintillations arises in the result of interaction of radio signal from the cosmic radio source with irregularities of ionosphere plasma which appears at the registration of observations as amplitude fluctuations. Wherein fluctuations of the different intensities and with the different long time periods can be observed. Scintillations of large intensity and with large characteristic times (periods) take an interest because its influence on records of the radio sources is very essential and can distort the record shape. In this case there is a need to consider the presence of the intensive fluctuations. In this sense it might be useful to investigate the frequency of occurrence of the intensive scintillation. Processing of the radio sources records was carried out on the observations of power cosmic radio sources at the passage through direction pattern of the radio telescope URAN-4 at frequencies 20 and 25 MHz during 1998-2007. Record's characteristics were obtained including ionosphere scintillation parameters. Also records with scintillations of large intensity and with long periods were marked. In this work daily distribution of intensive scintillations was analyzed. It was showed that occurrence of intensive scintillations changes in limits of 4-26% and it is larger on the lower frequency. Dependence of occurrence of scintillations from angle between direction on the radio source and line of geomagnetic field in the observation place was found. It was obtained that the maximum of the occurrence of the intensive scintillations for all observed radio sources appears on the nighttime of the day. Also local maximums of frequency of occurrence are exist which may be associated with the moments of sunrise and sunset.

Key words: radio source: ionosphere scintillations, decameter range, daily distribution of ionosphere scintillations

АНОТАЦІЯ. Ефект іоносферних мерехтінь виникає в результаті взаємодії радіосигналу від компактного космічного радіоджерела з неоднорідностями іоносферної плазми і проявляється при реєстрації спостережень як амплітудні флуктуації. При цьому можуть спостерігатись флуктуації різної інтенсивності і з періодами різної тривалості. Мерехтіння великої інтенсивності і з великим характерним часом (періодом) викликають інтерес так як їхній вплив на записи радіоджерел дуже вагомий і вони можуть значно спотворювати форму запису. В такому випадку виникає необхідність враховувати наявність інтенсивних флуктуацій. Тому може бути корисним

дослідити частоту появи інтенсивних іоносферних мерехтінь. На радіотелескопі УРАН-4 на частотах 20 і 25 МГц на протязі 1998-2007 років були проведені спостереження потужних космічних джерел з реєстрацією у вигляді записів при проходженні через діаграму направленості радіотелескопу, а також виконана обробка отриманих записів. В результаті обробки були отримані характеристики кожного запису в тому числі параметри мерехтінь. При цьому були відмічені записи з мерехтіннями великої інтенсивності і з великими періодами. В цій праці проаналізовано добовий розподіл появи інтенсивних мерехтінь. Показано, що частота появи інтенсивних мерехтінь змінюється в інтервалі 4-26% і їх ймовірність зростає на нижчій частоті. Знайдена залежність частоти появи інтенсивних мерехтінь від кута між напрямком на радіоджерело і силовою лінією геомагнітного поля. Отримано, що максимум частоти появи інтенсивних мерехтінь для всіх спостережуваних радіоджерел проявляється в нічний час. Також існують локальні максимуми, які, скоріше за все, пов'язані з моментами сходу і заходу Сонця.

Ключові слова: радіоджерело: іоносферні мерехтіння, декаметровий діапазон радіохвиль, добовий розподіл іоносферних мерехтінь.

1. Introduction

When the signal from the discrete cosmic radio source propagates through Earth's ionosphere it undergoes the amplitude fluctuations caused by interaction with irregularities of ionosphere plasma [Crane R. K., 1977]. Effect of scintillations is particularly essential for observations at the decameter wave range. Wherein amplitude fluctuations can to characterize by different intensities from weak up to saturated and by different characteristic time intervals (periods) from several seconds up to ten minutes. It is reflect the state of irregularity of ionosphere structure in the moment of observations. Scintillations with large intensities and periods take an interest because they largely distort the observations records of the cosmic radio sources. For example, fluctuations with large periods that comparable with size of radio telescope direction pattern can to distort the shape of records that caused the incorrecting processing results.

There is a need to take into consideration the presence of the intensive fluctuations at the processing of observations. In this sense it might be useful to investigate the frequency of occurrence of the intensive scintillation. The daily distribution of the intensive scintillations is presented in this work on the observations of the power radio sources at the decameter wave range.

2. Observations data

The regular observations of the 4-th power radio sources – 3C144, 3C274, 3C405, 3C461, were carried out on the radio telescope URAN-4 at frequencies 20 and 25 MHz during 1998-2007 [Derevyagin V. G. et al, 2019]. Several records of the passing through RT direction pattern of each radio source were registered during day. Observations data are stored in computer memory in the digital form. After data processing parameters that characterized each record and scintillation parameters were obtained. Under data processing the quality of the record was estimated including the presence or absence of intensive scintillations in form: '0' - absence; '1' – presence. All data processing was placed in the text files in chronological order for each source and on frequencies. The analysis of daily distribution of occurrence of intensive scintillations was fulfilled further on obtained estimations.

Table 1: Statistics of the occurrence of the intensive scintillations for 4-th radio sources at two frequencies during 1998-2007

NS	H	D	N20	S20	P20	N25	S25	P25
144	66	0	9881	990	0.10	8194	342	0.04
274	56	10	11318	1445	0.13	8859	606	0.07
405	84	19	10883	1761	0.16	11790	1045	0.09
461	77	37	8354	2201	0.26	8021	1177	0.15

3. Analysis and discussion the results on intensive scintillations

Examples of the records of radio sources with intensive scintillations obtained on radio telescope URAN-4 observations are showed in the Fig. 1 (Fig. 1b and 1c). Record with weak scintillations is demonstrated for comparison (Fig. 1a). Fig. 1 shows that in the case of weak scintillations the processing of record (that include the fitting of smooth curve) can to execute better than in second case and all the more in third case. Proceed from above-mentioned it is turns out to be important to know statistics and distribution of occurrence of intensive scintillations.

Data for radio sources that observed is contains in Table 1 at frequencies 20 and 25 MHz: N – total number of records; S – number of records with intensive scintillations; $P = S/N$ – relative value of occurrence of intensive scintillations. Also additional information on radio sources placed into Table 1: NS – number of source in catalogue 3C; H – height of source in culmination moment (degrees); D – angle between on source direction and line of geomagnetic field (degrees).

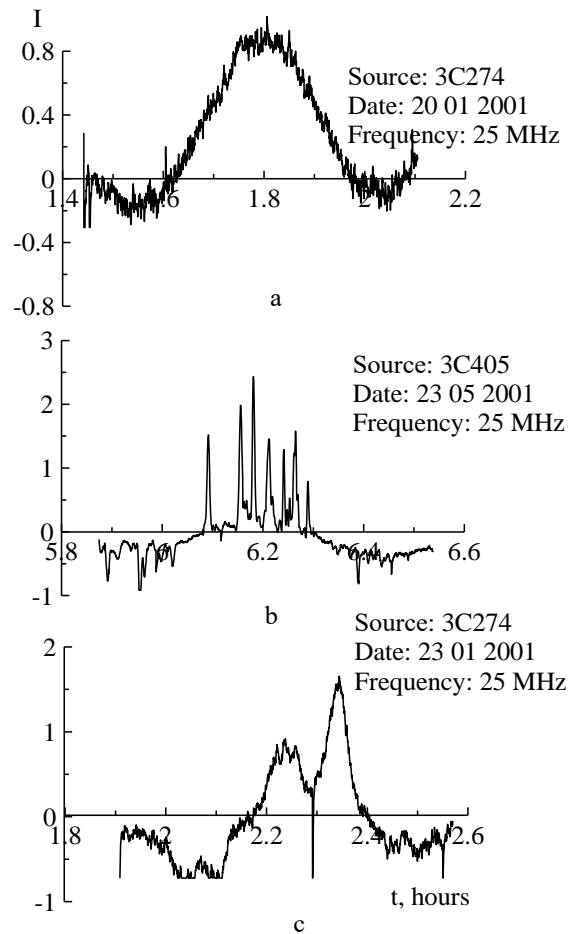


Figure 1: Samples of records of radio sources with scintillations of different intensities. Values of intensity are measured in relative units

Proceed from table data it is possible to say that frequency of occurrence of intensive scintillations changes in limits from 4 up to 26% and this value is larger almost in two times at 20 MHz than at 25 MHz that corresponds to increase of scintillation effect on lower frequency [Liu C. H. et al., 1986]. Also one can note that occurrence of intensive scintillations do not depends obviously on height on which radio source observed. However the dependence of frequency of scintillation occurrence from angle between on source direction and line of geomagnetic field in observation place (Fig.2) is observes: the larger this angle the higher probability of intensive scintillations. The similar dependence was got in the work [Lytvynenko O. A. et al, 2000] for such parameter of scintillations as period. Inversely proportional dependence exists for the scintillation index. It is demonstrates the role of geomagnetic field in manifestations of irregularity structure of ionosphere [Aarons J., 1982].

In order to analyze the behavior of intensive scintillations occurrence in time the daily distribution of such occasions was obtained by sum up within each hour from 0 up to 24. Distribution that obtained was normalized on maximum value. Result is shown in Fig. 3.

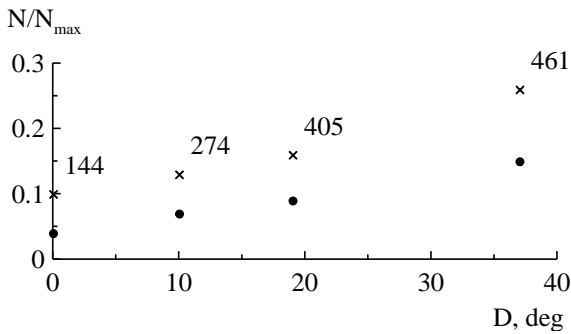


Figure 2: Dependence of the frequency of occurrence of the intensive scintillations from angle between direction on radio source and line of geomagnetic field in observation place. Data at the frequency 20 MHz marked by crests and at 25 MHz – by circles

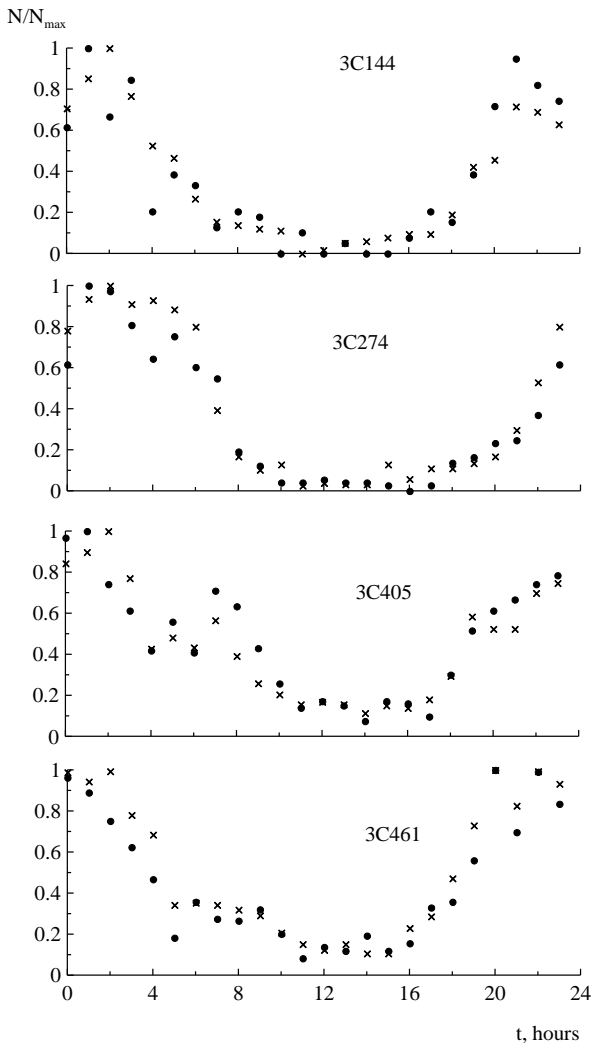


Figure 3: Frequency of the occurrence of intensive scintillations in dependence from time of day for 4-th radio sources at two frequencies; there are presented numbers of occasions divided by maximum value. Marks for two frequencies are correspond to marks in Fig. 2

Daily distribution of the frequency of intensive scintillations occurrence is observed for all radio sources with minimum in daytime and maximum in nighttime. Besides one can note that several local maximums of the frequency occurrence exist which may be associated with moments of sunrise and sunset.

4. Conclusions

The analysis of occurrence of scintillations with large intensity was fulfilled by observations of power cosmic radio sources (3C144, 3C274, 3C405, 3C461) obtained on the radio telescope URAN-4 at the frequencies 20 and 25 MHz during 1998-2007:

1. Frequency of occurrence of intensive scintillations changes in limits from 4 up to 26%.
2. Daily distribution of such scintillations was obtained: minimum observed in daytime and the probability to observe intensive scintillations increased in nighttime.
3. It is shown that relative frequency of intensive scintillations occurrence does not depend obviously from height of radio source observation.
4. The dependence of the frequency of scintillation occurrence from angle between source direction and line of geomagnetic field in observation place is observed: the larger this angle the higher probability of intensive scintillations.

References

- Crane R.K.: 1977, *Proc. IEEE*, **65**, 180.
 Derevyagin V.G. et al.: 2019, DOI: 10.31401/WS.2019.proc.
 Liu C.H. et al.: 1986, *Radio Science*, **21**, 363.
 Lytvynenko O.A. et al.: 2000, *Geomagnetizm i Aeronomiya*, **40**, № 4, 116 (in russian).
 Aarons J.: 1982, *Proc. IEEE*, **70**, No 4, 360.

SUN, SOLAR ACTIVITY AND ASTROBIOLOGY

DOI:<http://dx.doi.org/10.18524/1810-4215.2020.33.216444>

FEATURES OF THE DEVELOPMENT OF A CIRCULAR SOLAR FLARE

S. N. Chornogor, N. N. Kondrashova

Main Astronomical Observatory, National Academy of Sciences of Ukraine,
Kyiv, Ukraine, *chornog@mao.kiev.ua*

ABSTRACT. We present the results of the analysis of morphology and evolution of the circular solar flare using H-alpha images. H-alpha filtergrams were obtained with the Meudon spectroheliograph. The active region NOAA 9087 had a complex multipolar magnetic field configuration. New magnetic fluxes emerged during the evolution of this flare-productive active region. The high flare and surge activity was observed in the active region.

According to Solar Geophysical Data (SGD) the 3N/M6.4 class solar flare occurred on July 19, 2000 at 06:37 UT, peaked at 07:23 UT and lasted 2.5 hours. Two bright kernels appeared near large positive-polarity sunspot at the beginning of the flare. In a few minutes bright kernels occurred in the center of the active region near polarity inversion line. Space solar observatory Yohkoh detected a hard X-ray (HXR) coronal source in the 13.9-22.7 keV and 22.7-32.7 keV energy bands in this location.

New kernels appeared in the southern and eastern parts of the active region at the boundaries of the chromospheric network. They brightened sequentially clockwise, which may indicate a slipping reconnection. Magnetic reconnection was observed in the main phase of the flare in the eastern part of the active region. In the late flare phase arcade of post-reconnection EUV loops connected the main flare ribbon with the place of repeated reconnection. Additional heating may be required for the explanation of the long flare decay phase.

Flare ribbons of the circular shape were formed. The complex magnetic configuration of the studied active region and circular shape of the ribbons suggest that it had a fan-spine magnetic topology with null points. Possibly, flare ribbons are the locations of intersections of the fan quasi-separatrix layer with the chromosphere. They appeared as a result of heating or particle beam moving along a quasi-separatrix layer from a source in the corona.

Keywords: Sun, chromosphere, active regions, solar flares, magnetic reconnections, multi-wavelength observations.

АБСТРАКТ. В роботі представлено результати аналізу морфології та еволюції кругового сонячного спалаху із використанням Н-альфа зображень. Н-альфа фільтрограми отримано за допомогою спектрогеліографа обсерваторії в Медоні. Активна область NOAA 9087 мала складну конфігурацію багатополярного магнітного поля. Нові магнітні потоки з'явилися під час еволюції цієї спалахово-продуктивної активної

області. Багато спалахів та викидів спостерігались у цій активній області.

Згідно з Сонячними геофізичними даними (SGD) сонячний спалах класу 3N/M6.4 виник 19 липня 2000 року о 06:37 UT, досягнув максимуму о 07:23 UT і тривав 2,5 години. На початку спалаху з'явилося два яскравих ядра біля великої сонячної плями з позитивною полярністю. Через декілька хвилин в центрі активної області поблизу лінії інверсії полярності виникли яскраві ядра. Космічна сонячна обсерваторія Yohkoh виявила корональне джерело жорсткого рентгенівського випромінювання (HXR) в енергетичних смугах 13.9-22.7 та 22.7-32.7 кеВ у цьому місці.

Нові ядра з'явилися у південній та східній частинах активної області на межах хромосферної мережі. Вузли спалаху ставали яскравішими послідовно за годинниковою стрілкою, що може свідчити про ковзаюче магнітне перез'єднання. Повторне магнітне перез'єднання спостерігалось в основній фазі спалаху в східній частині активної області. У пізній спалаховій фазі аркада післяспалахових EUV петель з'єднувала основну спалахову стрічку з розташуванням місця повторного магнітного перез'єднання. Для пояснення тривалої фази спалаху може знадобитися додаткове нагрівання.

Спалахові стрічки мали круглу форму. Складна магнітна конфігурація досліджуваної активної області та кругла форма стрічок дозволяють припустити, що вона мала магнітну топологію типу "віяло-шип" з нульовими точками. Можливо, спалахові стрічки – це місця перетину шару віялової квазісепаратриси з хромосферою. Вони з'явилися внаслідок нагрівання або переміщення пучка частинок вздовж квазісепаратрисного шару від джерела в короні.

1. Introduction

Solar flares occur as a result of magnetic reconnections. Magnetic reconnections can be initiated at null points, on separators, in quasi-separatrix layers. Fluxes of energetic particles from the reconnection region or heating of the lower atmosphere cause the appearance of flare kernels and ribbons in the chromosphere.

The magnetic topology is very important for the occurrence and development of the flares (Priest and Titov, 1996). The attention of many authors is directed to the study of

three-dimensional magnetic field topology, containing 3D null points (eg, Aulanier et al., 2012, Guo et al., 2019).

The skeleton of the magnetic topology in the active region determines the geometry of flare ribbons (Guo et al., 2019). Flare ribbons can form at the intersection of the quasi-separatrix layer with the lower atmosphere (Mandrini et al., 1991). Study of morphology and evolution of flare kernels and ribbons can provide information about the topology of the magnetic field and mechanisms that contributed to flare occurrence and development.

We analyzed the sequence H-alpha images to study an evolution and morphological features of the two-ribbon solar flare on July 19, 2000 in the chromosphere of the active region NOAA 9087.

2. Active region, flare and observational data

The active region NOAA 9087 was observed on the solar disk from 15 to 27 July 2000. It had a multipolar magnetic field configuration, which became more complicated every day. Its flare activity increased gradually. A 3N/M6.4 flare occurred on July 19 at coordinates S18E10. It took up a large area on the disk. According to Solar Geophysical Data, the H-alpha flare began at 06:37 UT, its main maximum was at 07:23 UT, and the end was at 09:01 UT. It lasted for almost 2.5 hours and belonged to the class of long-term events (LDE - Long Duration Event).

In the paper (Chornogor and Kondrashova, 2020) the data of space-born and ground based observations of this flare were analyzed. The hard X-ray (HXR) and soft X-ray (SXR) data were obtained at the Yohkoh Telescopes (HXT and SXT) and Geostationary Operational Environmental Satellite (GOES). The full-disk magnetograms and EUV-images were provided by the Solar and Heliospheric Observatory (SOHO) Michelson Doppler Imager (MDI) and Extreme ultraviolet Imaging Telescope (EIT). Radio data were obtained with Learmonth Solar Radio Spectrograph, white light images in Big Bear Solar Observatory (BBSO).

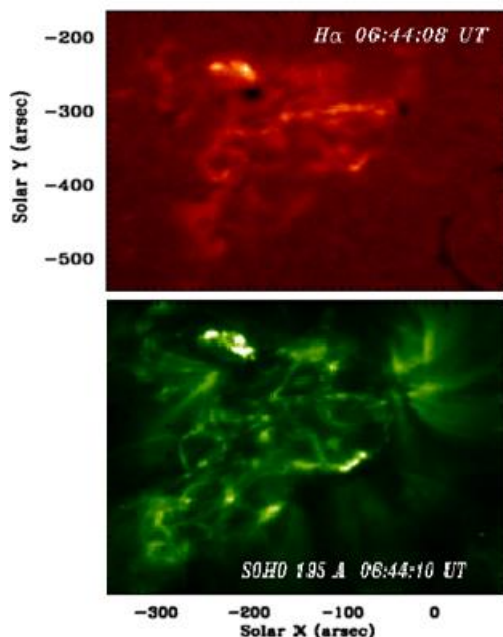


Figure 1: H-alpha image at 06:44:08 UT and SOHO 195A image at 06:44:10 UT

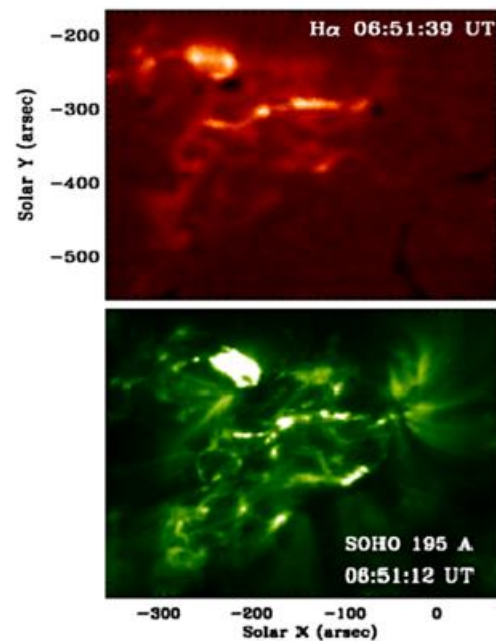


Figure 2: H-alpha image at 06:51:39 UT and SOHO 195A image at 06:51:12 UT

Wavelength light curves for hard X-ray and soft X-ray fluxes, radio solar flux, H-alpha intensity were presented. Times of burst peaks are given in table. H-alpha intensity peaks are 06:50:33, 07:01:11, 07:07:34, 07:18:12 UT. The main H-alpha peak of the flare was at 07:23 UT.

To study the flare evolution in the chromosphere, in this work we used the H-alpha line filtergrams. Filtergrams were obtained at the Meudon spectroheliograph in time steps from 30 seconds to 1 minute. EUV images also used in this work.

3. Flare evolution in the chromosphere

The flare studied began with the appearance of two bright kernels near a large spot of positive polarity (Fig. 1). The SOHO 195A image is also shown in the figure for comparison of the development of the flare in the chromosphere and the corona. A few minutes later, the intensity of the plages in the center of the group, near the polarity inversion line, increased (Fig. 2). In the first place of the flare, there was an arcade of post-flare loops.

A surge occurred at one of its footpoints, which then fragmented into several jets. Then a tunnel of bright loops appeared to the southwest of this place (Fig. 3). The flare kernels in the central part of the active region became very bright. Possibly, they were caused by a hard X-ray burst the peak of which was observed at 06:57 UT.

According to the data of the hard X-ray telescope HXT on board Yohkoh, the coronal source of hard X-ray radiation in the L (13.9-22.7 keV) and M1 (22.7-32.7 keV) bands located above the line of polarity inversion. A new kernels has appeared in the southern part of the active region (Fig. 4).

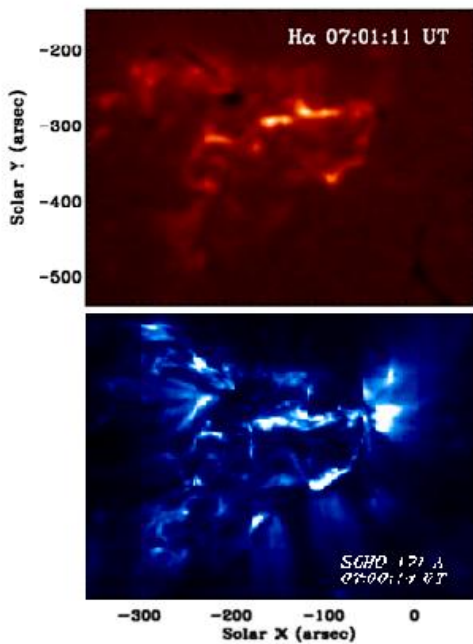


Figure 3: H-alpha image at 07:01:11 UT and SOHO 171A image at 07:00:14 UT

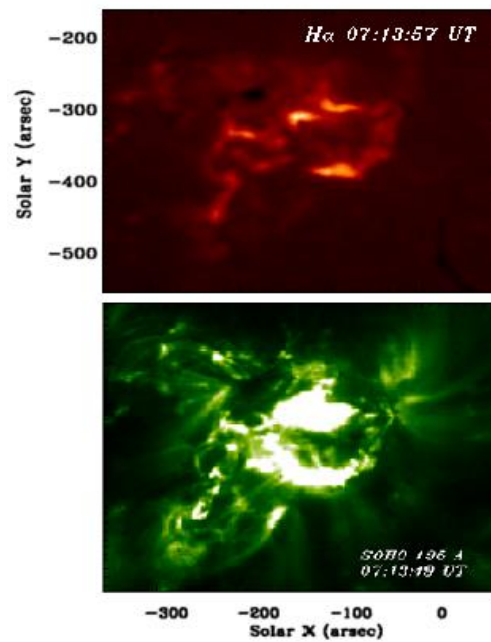


Figure 5: H-alpha image at 07:13:57 UT and SOHO 195A image at 07:13:49 UT

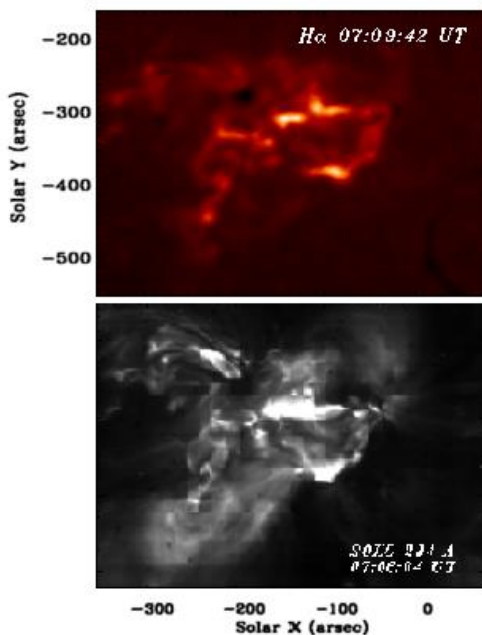


Figure 4: H-alpha image at 07:09:42 UT and SOHO 284A image at 07:06:04 UT

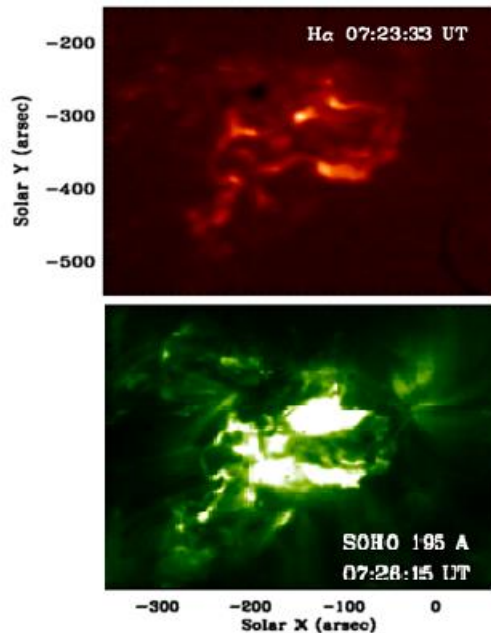


Figure 6: H-alpha image at 07:23:33 UT and SOHO 195A image at 07:26:15 UT

The flare ribbons formed had a circular shape. It can be assumed that the studied flare was circular. At 07:13:57 UT the flare occupied almost entire central and southern parts of the active region (Fig. 5). The SOHO 195 A and 304 A images also show the circular shape of the flare.

Circular flares are usually associated with a magnetic fan-spine topology containing 3D null points (Yang et al., 2015). Flare ribbons can be located at the intersection of the fan with the photosphere. The maximum brightness of all kernels was at the main H-alpha peak of the flare at 07:23 UT.

The images, obtained in the main phase of the flare, show the intersection of bright EUV-loops in the eastern part of the active region, indicating magnetic reconnection (Fig. 6). The response of the chromosphere is visible in the H-alpha images. Further development of the flare took place in the southern and eastern parts of the active region (Fig. 7).

The brightening of the kernels of the flare studied occurred mainly consistently in different places of the active region, which may indicate slipping reconnection (Aulanier et al., 2006). This type of magnetic reconnection can occur when field lines pass through the quasi-separatrix layer and

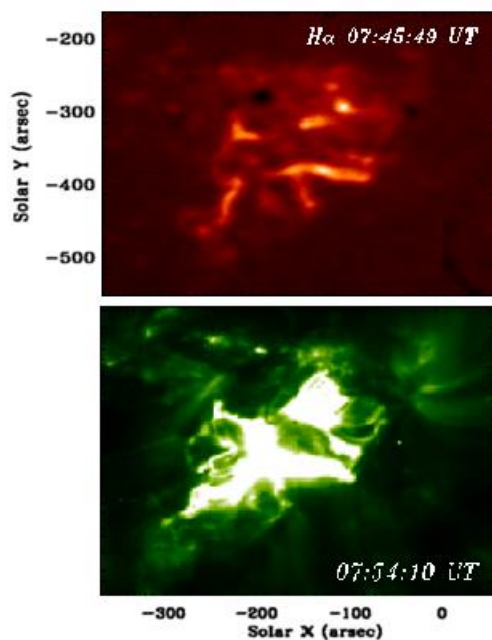


Figure 7: H-alpha image at 07:45:49 UT and SOHO 195A image at 07:54:10 UT

undergo continuous successive reconnections. In the flare studied, the brightening of kernels occurred clockwise in the main.

4. Conclusions

- The evolution of the two-ribbon 3N/M6.4 flare on 19 July 2000 in the chromosphere was analyzed on the base of the H-alpha filtergrams. Analysis of H-alpha images shows that the state of the chromosphere was constantly changing during the flare. The energy was released sequentially in different places of the active region.

- The kernels appeared along the polarity inversion line sequentially and were located at the boundaries of the chromospheric network.

- The successive appearance of flare kernels may indicate slipping magnetic reconnection in the flare. The flare ribbons were round. It can be assumed that there was a magnetic topology of the fan-spine type, containing null points. In the main phase of the H-alpha flare, the images show loops intersecting over in the eastern part of the active region, which are clearly visible in observations of EIT 195 A. They indicate magnetic reconnection.

- The arcade of the EUV loops after reconnection connected the main flare ribbon with the location of these loops in the late phase in one and a half hour after the flare maximum. Additional heating may be required to explain the long decay phase of the flare.

Acknowledgements. We are grateful to the observer teams of Meudon, Yohkoh, and SOHO who have provided free access to their results.

References

- Aulanier G., Janvier M., Schmieder B.: 2012, *A&A*, **543**, id.A110, 14 p.
- Aulanier G., Pariat E., Demoulin P., DeVore C. R.: 2006, *Solar Phys.*, **238**, № 2, 347.
- Chornogor S. N., Kondrashova N. N.: 2020, *KPCB*, **36**, № 3, 140.
- Guo J., Wang H., Wang J., et al.: 2019, *ApJ*, **874**, № 2, article id. 181, 10 p.
- Mandrini C.H., Demoulin P., Henoux J.C., Machado M.E.: 1991, *A&A*, **250**, 541.
- Priest E. R., Titov V. S.: 1996, *Philosophical Transactions: Mathematical, Physical and Engineering Sciences*, **354**, № 1721, 2951.
- Yang K., Guo Y., Ding, M. D.: 2015, *ApJ*, **806**, №2, article id. 171. 13 p.

DOI: <http://dx.doi.org/10.18524/1810-4215.2020.33.216446>

RELATIONSHIP OF SCR, CME AND CORONAL SHOCK WAVES WITH THE PARAMETERS OF TYPE IV AND II SOLAR RADIO BURSTS

E.A. Isaeva

Institute of Radio astronomy of NAS of Ukraine, isaevaode@gmail.com

ABSTRACT. This paper presents the results of a comparative analysis of the relationship between solar cosmic rays (SCR), coronal mass ejections (CME), and coronal shock waves (CSW) with the parameters of solar continual type IV radio bursts, as well as with the parameters of type II radio bursts. The sample under study contains 147 proton events accompanied by type IV continuum radio bursts in the 25-15400 MHz range, type II radio bursts in the 25-180 MHz range, as well as CME and coronal shock waves. For the analysis, we used original records of solar radio emission at 8 fixed frequencies in the range 245-15400 MHz according to data from RSTN (Radio Solar Telescope Network), original records of dynamic spectra from SRS (Solar Radio Spectrograph) in the range of 25-180 MHz, as well as original records intensity of the flux of SCR protons with proton energies in the range $> 1-100$ MeV according to data from the GOES spacecraft. A comparative analysis showed that the relationship between the intensity of the SCR proton flux and the CME velocity is, on average, much stronger with the parameters of type IV radio bursts than with the parameters of type II radio bursts, which indicates the dominant role of the SCR acceleration process in the flare region, rather than shock waves. However, detailed studies of the fine structure of type II radio bursts have shown that there is a fairly strong relationship between the intensity of the flux of mean-relativistic protons I_p and the frequency $f_{min,1}$ at the fundamental harmonic (at the 1-st harmonic) at the time t_{min} corresponding to the minimum relative distance b_{min} between the harmonics of type II radio bursts. Detailed studies of the fine structure of type II radio bursts have also shown that there is a strong relationship between the intensity of the SCR proton flux I_p and parameter V_{II} , which characterizes the displacement of the shock front with time t_i in a narrow frequency range of 25-60 MHz.

АНОТАЦІЯ. У даній роботі наводяться результати порівняльного аналізу зв'язку сонячних космічних променів (СКП), корональних викидів маси (КВМ) і корональних ударних хвиль (КУХ) з параметрами сонячних континуальних радіосплесків IV типу, а також з параметрами радіосплесків II типу. Досліджувана вибірка містить 147 протонних подій, що супроводжуються континуальними радіоспесками IV типу в діапазоні 245-15400 МГц, радіоспесками II типу в діапазоні 25-180 МГц, а також КВМ і корональними ударними хвилями. Для аналізу використовувалися оригінальні запи-

си радіовипромінювання Сонця на 8 фіксованих частотах в діапазоні 245-15400 МГц за даними з RSTN (Radio Solar Telescope Network), оригінальні записи динамічних спектрів з SRS (Solar Radio Spectrograph) в діапазоні 25-180 МГц, а також оригінальні записи інтенсивності потоку протонів СКП з енергією протонів в діапазоні $> 1-100$ MeV за даними з апаратів GOES. Порівняльний аналіз показав, що зв'язок інтенсивності потоку протонів СКП і швидкості КВМ в середньому значно сильніше з параметрами радіосплесків IV типу, ніж з параметрами радіосплесків II типу, що вказує на домінуючу роль процесу прискорення СКП у спалахової області, а не ударними хвилями. Однак детальне дослідження тонкої структури радіосплесків II типу показали, що існує досить сильний зв'язок між інтенсивністю потоку середньорелятивістських протонів I_p і частотою $f_{min,1}$ на основній гармоніці (на 1 гармоніці) на момент часу, відповідний мінімальній відносній відстані b_{min} між гармоніками радіосплесків II типу. Детальні дослідження тонкої структури радіосплесків II типу також показали, що спостерігається сильний зв'язок між інтенсивністю потоку протонів СКП I_p і параметром V_{II} , що характеризує зміщення фронту ударної хвилі з плином часу t_i у вузькому частотному діапазоні 25-60 МГц.

Keywords: Proton events, solar cosmic rays (SCR), coronal mass ejections (CME), coronal shock waves (CSW).

1. Introduction

Prediction of proton events is one of the topical problems in solar radiophysics. Modern methods for predicting proton events are based on the relationship between the parameters of solar cosmic rays (SCR) and the parameters of solar radio bursts (Akinyan et al., 1977, 1978; Chertok, 1982; Chertok et al., 1987; Melnikov, Epifanov, 1979; Melnikov et al., 1986, 1991). Proton events have a characteristic U and W - shaped type of frequency radio spectrum with maxima in the centimeter and meter wavelength ranges and a deep minimum in the decimeter range (Podstrigach and Fasahova, 1981). It is known that the parameters of microwave bursts can be used to judge the total number of accelerated particles and their energy spectrum (Chertok, 1982), while the parameters of meter-decameter radio bursts can be used to judge the conditions for the escape of accelerated particles into interplanetary space.

The presence of a sufficiently powerful meter-long component indicates favorable exit conditions, while the absence indicates unfavorable exit conditions (Akinian et al., 1977). It was shown in (Melnikov et al., 1986) that the presence of a strong coupling between the flux of mean relativistic electrons of solar cosmic rays (SCRs) and the integral flux of microwave bursts (μ -bursts) indicates that the SCR electrons and the electrons generating the radio burst are accelerated in a single process. Based on this, statistical models were obtained that relate the fluxes of protons and electrons to the parameters of microwave bursts (Melnikov et al., 1991).

In this paper, present the results of a comparative analysis of the relationship between SCR, coronal mass ejections (CMEs), and coronal shock waves with the parameters of type IV continuum radio bursts in the range 245-15400 MHz and with the parameters of type II radio bursts in the 25-180 MHz range. In this work, the emphasis is on studying the relationship between the SCR proton flux and the parameters of type II radio bursts and on comparing the results with what is obtained from the parameters of microwave bursts. Earlier, in (Tsap and Isaeva, 2011, 2012, 2013), some issues were considered regarding the relationship between the SCR proton flux and the parameters of type II radio bursts. In the course of studies of the relationship between the frequency drift velocity of meter-decameter type II bursts and the intensity of the proton flux I_p of different energies, two families of events were discovered, which, according to Tsap (Isaeva and Tsap, 2011), suggests the generation of shock waves both in the region of the flare energy release and a moving coronal mass ejection (CME). In works (Isaeva and Tsap, 2011; Tsap and Isaeva, 2012, 2013), the results of studying the efficiency of SCR acceleration by coronal and interplanetary shock waves are presented, as well as arguments in favor of the model of a two-step proton acceleration process (Wild et al., 1963). A comparative analysis showed that the acceleration of protons by coronal shock waves is more efficient than by interplanetary shock waves, and that the main acceleration of protons occurs in the flare region and additional acceleration by shock waves (Tsap, Isaeva, 2012). Study of the fine spectral structure of meter-decameter type II radio bursts showed that there is a fairly strong relationship between the proton flux I_p and the relative distance $b_i = (f_{i2}-f_{i1})/f_{i1}$ between the 1-st and 2-nd harmonics at a given time t_i , where the correlation coefficient r between the studied values $r \approx 0.70$, while the relationship between the drift velocity V_{drift} and the proton flux I_p turned out to be weak, where the correlation coefficient r between I_p and V_{drift} does not exceed $r \approx 0.40$ (Tsap and Isaeva, 2013). However, further studies of the fine spectral structure of meter-decameter type II radio bursts in the 25-180 MHz range showed that if instead of the drift velocity V_{drift} , the parameter $V_{\text{II}} = (f_2-f_1)/(t_1-t_0)$ is used, which to some extent characterizes the velocity displacement of the shock front with time t_i , where f_2 and f_1 are frequencies at the 2-nd and 1-st harmonics at a given time t_i , and t_0 is the time of the onset of a type II burst at the 1-st harmonic at a frequency of 180 MHz, then a fairly strong relationship is observed between the intensity of the flux of protons I_p and V_{II} , where the correlation coefficient r between the studied values is $r \approx 0.79$ (Isaeva, 2018), which is quite compara-

ble with what is obtained from the parameters of microwave bursts (Melnikov et al., 1991; Isaeva, 2018). It should also be noted that a strong connection between the proton flux intensity I_p and parameter V_{II} is observed in a narrow frequency range of 25-60 MHz. Moreover, detailed studies of the dynamics of the fine structure of type II radio bursts revealed a number of features. It was shown that the relative frequency b_i between the harmonics of type II radio bursts monotonically changes with time. For all 112 type II radio bursts are characterized by a monotonic decrease in the relative distance b_i between harmonics to the minimum value b_{min} with a subsequent increase (Isaeva, 2019, 2020). It was also shown that the relationship between the intensity of the proton flux I_p and the parameters of type II radio bursts changes with time t_i and reaches a maximum value when the relative distance b_i becomes minimum, i.e. $b_i = b_{\text{min}}$ (Isaeva, 2018, 2019).

2. Relation of the SCR proton flux with the parameters of type IV continual radio bursts in the range 245-15400 MHz and with the parameters of type II radio bursts in the 25-180 MHz range

It is currently believed that SCRs can be accelerated either in the region of flare energy release or at the fronts of shock waves, which can be generated by both flares and CME (Reames, 1999). The results obtained to date do not allow making an unambiguous conclusion about which of the acceleration processes is dominant.

Significant progress in solving this problem can be achieved due to detailed studies of the relationship between the SCR proton flux and the parameters of type IV and II radio bursts in a wide wavelength range. In this regard, the author of this work carried out studies in a wide range of wavelengths. For the analysis, we used the original records of solar radio emission at 8 fixed frequencies 245, 410, 610, 1415, 2695, 4995, 8800, 15400 MHz (<https://www.ngdc.noaa.gov/stp/space-weather/solar-data/solar-features/solar-radio/rstn-1-second/>), original records of dynamic spectra of solar radio emission in the 25-180 MHz range according to data from SRS (Solar Radio Spectrograph), original records of proton flux intensity I_p with proton energy $E_p > 1 - 100$ MeV according to data from GOES (https://satdat.ngdc.noaa.gov/sem/goes/data/new_avg/), as well as a list of proton events (<ftp://ftp.swpc.noaa.gov/pub/indices/SPE.txt>). The sample under study contains 147 proton events for the period from 06-02-1986 to 14-10-2014. Proton events were selected according to the generally accepted criteria for protonity. It is known that for events with a U or W-shaped type of radio frequency spectrum with maxima in the meter and centimeter wavelength ranges and with a minimum in the decimeter range, the best correlation is observed between the parameters of μ -bursts and the intensity of the flux of mean-relativistic electrons and SCR protons. Confirmation of this fact can be seen in fig. 1a) (left), which shows the relationship between the integral flux of continuous μ - bursts at a frequency of 8800 MHz and the intensity of the flux of protons I_p with an energy $E_p > 30$ MeV. For such events, the correlation coefficient r between $\int F_{\mu} dt$ and $I_p \approx 0.80$. At the same time, the relationship between the proton flux intensity I_p and the integral flux of continual radio bursts largely depends on the radio burst frequency f see fig. 1b) (left) and the proton energy E_p

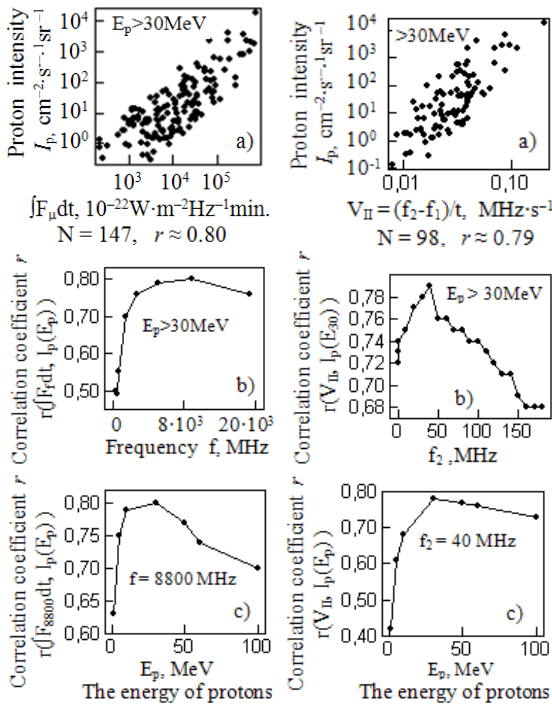


Figure 1: Relationship between the intensity of the SCR proton flux I_p with the integral flux of μ -bursts $\int F_{\mu} dt$ (left) and with parameter V_{II} , which characterizes the displacement velocity of the shock front (right).

see fig. 1c) (left). The relationship between I_p and the integral flux of radio bursts $\int F_{\mu} dt$ sharply decreases in the decimeter range and is practically absent in the meter range, see Fig. 1b) (left). The strongest relationship between I_p and $\int F_{\mu} dt$ is observed for average relativistic protons with an energy $E_p > 30$ MeV and an integral flux of μ -bursts, see fig. 1c) (left), which is quite consistent with the results of other authors (Melnikov et al., 1991).

The presence of a strong connection between the flux of SCR protons and the parameters of μ -bursts definitely indicates the acceleration of SCR protons in the flare region. However, there are many indications that shock waves also play an important role in the acceleration of solar cosmic rays (Gopalswamy et al., 2002; Cliver et al., 2004). In this regard, detailed studies of the parameters of the fine structure of type II radio bursts and their relationship with SCR were carried out.

Earlier in the article (Tsap, Isaeva, 2013), the relationship between the intensity of the SCR proton flux I_p ($E_p > 1-100$ MeV) with the drift velocity V_{drift} and with the relative distance b_i between the harmonics of a type II radio burst at a given time t_i was investigated. Comparative analysis showed that with an increase in the proton energy ($E_p > 40-100$ MeV), a significant increase in the correlation coefficient r between I_p and b_i from 0.40 to 0.70 is observed, while the correlation coefficient r between I_p and the drift velocity V_{drift} at the maximum does not exceed 0.30. A significant increase in the correlation r between I_p to Tsap (Tsap, Isaeva, 2013), indicates a significant contribution of shock waves to the acceleration of high-energy protons. The presence of a low correlation ($r < 0.30$) between

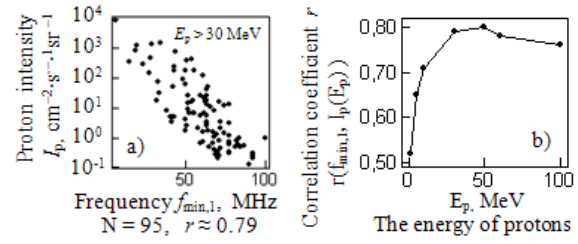


Figure 2: The relationship between the intensity of the proton flux I_p and the frequency $f_{\text{min},1}$ at the 1-st harmonic at the time t_{min} of the minimum relative distance b_{min} between the harmonics of type II radio bursts and b_i with an increase in the proton energy E_p , according

I_p and the drift velocity V_{drift} , according to Tsap (Tsap, Isaeva, 2013), can be explained by significant changes in the conditions of shock wave propagation from event to event due to the strong dependence of the shock wave intensity on the parameters of the medium. In the case of using the relative distance b_i , which characterizes the plasma inhomogeneity, this effect is leveled.

Later, in works (Isaeva, Tsap, 2017; Isaeva, 2018; 2019), on the basis of a larger sample of proton events, containing 112 proton events (previously there were 69) accompanied by type II radio bursts in the range 25-180 MHz, detailed studies of the fine structure of radio bursts were carried out type II using a new regression model (1) (Isaeva, Tsap, 2017). This model (1) gives a fairly good approximation for 95% of type II radio bursts, which made it possible to study the dynamics of the parameters of type II radio bursts over time t_i .

$$\lg f_{i,j} = a_j \cdot \sqrt{t_i} + b_j \quad (1)$$

In model (1), $f_{i,j}$ are the frequency values at the 1-st and 2-nd harmonics at time t_i , i - is the count number, j - is the harmonic number, a_j and b_j are the linear regression coefficients, which were found using the method of least squares (MLS).

Detailed studies have shown that there is a fairly strong connection between the intensity of the proton flux I_p and parameter V_{II} (2), which to some extent characterizes the displacement of the shock front over time t_i , where f_1 and f_2 are the frequency values at the 1-st and 2-nd harmonics at a given time t_i , t_0 is the start time at the fundamental (at the 1-st harmonic) at a frequency of 180 MHz.

$$V_{II} = \frac{f_2 - f_1}{t_i - t_0} \quad (2)$$

In fig. 1a) (right) shows the dependence of the proton flux intensity I_p with an energy $E_p > 30$ MeV on the value of the parameter V_{II} , where the correlation coefficient r between I_p and $V_{II} \approx 0.79$, which is quite comparable with what is obtained from the parameters of μ -bursts. A comparative analysis also showed that the relationship between I_p and V_{II} reaches maximum values in the range 25-60 MHz (see fig. 1b) (right) for protons with energies $E_p > 30$ MeV (see fig. 2c) (right) (values for the frequency f_2).

Further studies of the fine structure of type II radio bursts showed that the intensity and the relative distance between the harmonics of a type II radio burst changes over time, as well as the relationship between the proton flux intensity I_p and the parameters of type II radio bursts (Isaeva, 2019). It was shown that there is a fairly strong relationship between the proton flux intensity I_p and the frequency $f_{\min,1}$ at the fundamental (at the 1-st harmonic) at the time t_{\min} of the minimum value of the relative distance b_{\min} (3) between the harmonics of a type II radio burst, where the correlation coefficient r between I_p and $f_{\min,1} \approx 0.79$ (see fig. 2 a) and 2b)).

$$b_{\min} = \frac{f_{\min,2} - f_{\min,1}}{f_{\min,1}} \quad (3)$$

3. Connection of CME with the parameters of type IV continual radio bursts in the range 245-15400 MHz and with the parameters of type II radio bursts in the 25-180 MHz range

Earlier in the article (Isaeva, Tsap, 2017), the relationship between the CME velocity V_{CME} and the parameters of continual radio bursts in the range 245-15400 MHz was investigated. Comparative analysis showed that there is a strong relationship between V_{CME} and the integrated flux of μ -bursts $\int F_{\mu} dt$ in the 2695-15400 MHz range.

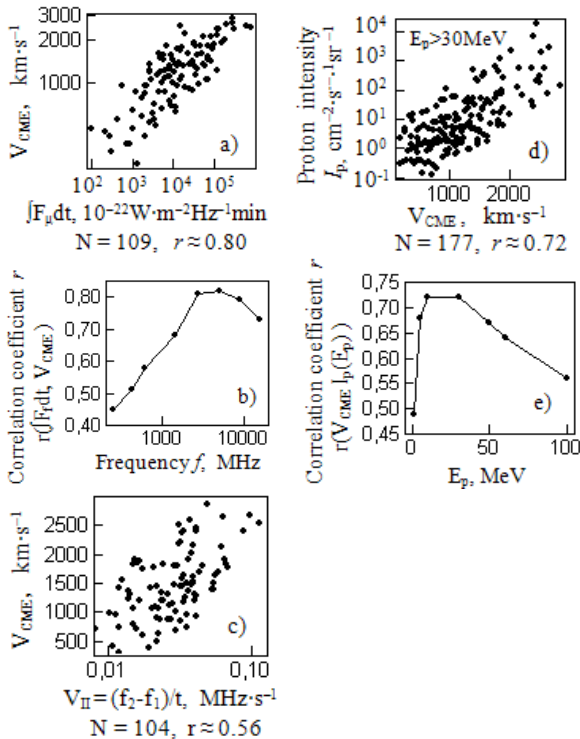


Figure 3: On a) and b) shows the relationship between the CME velocity V_{CME} and the integral flux $\int F_{\mu} dt$ of continual radio bursts in the 245-15400 MHz range, as well as with the parameter V_{II} of type II radio bursts in the 25-180 MHz range (see c)); On d) and e) the relationship between the proton flux intensity I_p and the CME velocity V_{CME} is shown;

In fig. 3a) shows the relationship between V_{CME} and $\int F_{\mu} dt$ at 8800 MHz, where N is the number of events and r is the correlation coefficient between the quantities under study. For the overwhelming majority of proton events, the correlation coefficient r between V_{CME} and $\int F_{\mu} dt$ is ≈ 0.80 . The relationship between the integral flux of microwave bursts and the CME velocity can be well represented using a linear regression model (4), where $V_{\text{CME},\mu}$ - calculated value of CME velocity.

$$\log_{10} V_{\text{CME},\mu} = 0.2322 \cdot \log_{10} \int F_{\mu} dt + 2.1108 \quad (4)$$

It was also shown that the relationship between V_{CME} and the integral flux of continual radio bursts $\int F_{\mu} dt$ decreases significantly with decreasing frequency, and already in the meter range at a frequency of 245 MHz, the correlation coefficient between V_{CME} and $\int F_{\mu} dt$ does not exceed 0.45 (see fig. 3b).

In fig. 3c) shows the relationship between the CME velocity and the parameter of type II radio bursts, which characterizes the displacement of the shock front with time. Figures 3a) and 3c) show that the relation between the CME velocity is much higher with type IV radio bursts than with type II radio bursts, where the correlation coefficient does not exceed 0.60.

Almost all proton events are accompanied by coronal mass ejections (CMEs). The presence of a high correlation between the CME velocity and the integral flux of μ -bursts during proton events indicates the flare origin of CME. Such CMEs are formed in the region of flare energy release and are associated with the ejection of high-energy particles into interplanetary space.

In this regard, in work (Isaeva, 2018), the relationship between the proton flux intensity I_p and the CME velocity V_{CME} was investigated. The sample under study contained 177 CMEs associated with proton events from 04-11-1997 to 26-01-2015. For the analysis, we used the tabular data of the CME velocity V_{CME} (https://cdaw.gsfc.nasa.gov/CME_list/UNIVERSAL/text_ver/univ_all.txt). Comparative analysis showed that there is a fairly strong relationship between the intensity of the flux of mean-relativistic protons I_p and the CME velocity V_{CME} . In fig. 3d) shows the relationship between I_p with the proton energy $E_p > 30$ MeV and the CME velocity, where the correlation coefficient r between the investigated quantities is ≈ 0.70 , which is in good agreement with the results in (Grechev et al., 2015). In fig. 3e) shows the dependence of the correlation coefficient r between I_p and V_{CME} as a function of the proton energy E_p .

4. Relationship between coronal shock waves and the parameters of type IV and II radio bursts

It is known that shock waves can be generated by both solar flares and CMEs. It is believed that type II meter bursts are associated with shock waves arising in flares (Wagner et al., 1983; Vrsnak et al., 1995), while bursts in the decameter-hectometer range are associated with the propagation of interplanetary shock waves generated by CME (Gopalswamy et al. 1998; Classen et al. 2002). The most reliable indicator of shock waves in the Sun's

corona are slowly drifting type II bursts. It is believed that the plasma mechanism of radio emission is responsible for their generation (Cairns et al., 2003).

Earlier in work (Isaeva, Tsap, 2017), the relationship between coronal shock waves and the parameters of μ -bursts was investigated. For the analysis, we used the original records of solar radio emission at 8 fixed frequencies in the range 245-15400 MHz. Comparative analysis showed that there is a fairly strong relationship between the parameter a_j in the regression model (1), which characterizes the decrease of the frequency drift rate in the 25-180 MHz range and the rise time t_μ μ -bursts at 8800 MHz. The correlation coefficient between t_μ and a_j is ≈ 0.66 see fig. 4a).

Due to the fact that flares differ significantly in intensity and duration, therefore, the rise time t_μ is expressed as a percentage of the duration of μ -bursts. In this case, the duration of the burst for each event was equal to 100%. The relationship between the velocity of shock waves V_{shock} and the integral flux $\int F_\mu dt$ μ -bursts at a frequency of 8800 MHz was also investigated. The correlation coefficient between $\int F_\mu dt$ and $V_{\text{shock}} \approx 0.55$ see fig. 4b). The lower relationship between the shock wave velocity and the integral flux of μ -bursts is most likely due to the fact that different stations give averaged estimates of the shock wave velocity at different times. And due to the fact that the velocity of the shock wave decreases very quickly over time, therefore, when using tabular data, a fairly large variance between $\int F_\mu dt$ and V_{shock} will be observed. But in spite of this, the connection between $\int F_\mu dt$ and V_{shock} is quite clearly traced for most proton events, see fig. 4b).

In the present work, also investigated the relationship between the velocity of coronal shock waves V_{shock} and various parameters of type II radio bursts. Comparative analysis showed that the strongest relationship is observed between the velocity of coronal shock waves V_{shock} and the frequency $f_{\text{min},1}$ at the fundamental harmonic (at the 1-st harmonic) at the moment t_{min} of the minimum value of the relative distance b_{min} , where the correlation coefficient r between $f_{\text{min},1}$ and $V_{\text{shock}} \approx 0.68$, see fig. 4c).

5. Conclusion

On the basis of the carried out comprehensive studies of the relationship between SCR, CME, and coronal shock waves with the parameters of solar radio bursts of type IV and II, a number of regularities were revealed, part of which fully agree with the previously obtained results of other authors. For example, the presence of a strong connection between the SCR proton flux and the parameters of type IV continual μ -bursts (Isaeva, Melnikov, Tsvetkov, 2010). Also in (Isaeva, Melnikov, Tsvetkov, 2010), it was confirmed that the accuracy of estimating the SCR proton flux is largely determined by the conditions for the release of accelerated particles, which can be judged from the parameters of type IV meter-decameter continuum radio bursts. Also, based on the studies carried out, it can be concluded that, for the overwhelming majority of proton events, the main acceleration of particles occurs in the region of flare energy release and additional acceleration

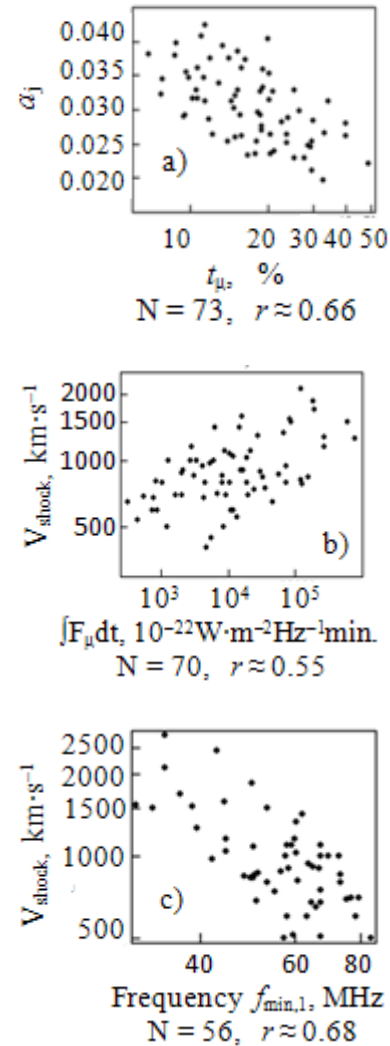


Figure 4: On a) the relationship between the parameter a_j and the rise time t_μ of type IV microwave bursts at a frequency of 8800 MHz is shown;

On b) the relationship between the velocity of coronal shock waves V_{shock} and the integral flux $\int F_\mu dt$ of type IV μ -bursts at a frequency of 8800 MHz is shown;

On c) shows the relationship between the velocity of coronal shock waves V_{shock} and the parameter of type II radio bursts $f_{\text{min},1}$, where $f_{\text{min},1}$ is the frequency at the fundamental harmonic at the moment the minimum relative distance b_{min} between the harmonics of a type II radio burst:

at the fronts of shock waves (Tsap, Isaeva, 2012; Tsap, Isaeva, 2012). At the same time, new patterns were identified. For example, detailed studies of the dynamics of the fine structure of type II radio bursts in the 25-180 MHz range over time have shown that all proton events accompanied by type II radio bursts are characterized by a monotonic decrease in the relative distance b_i between harmonics to a minimum value b_{min} with a subsequent increase (Isaeva, 2019; Tsap, Isaeva, Kopylova, 2020). It was shown that there is a strong relationship between the intensity of the proton flux I_p ($E_p > 30$ MeV) with the fre-

quency $f_{\min,1}$ at the fundamental harmonic (at the 1-st harmonic) at the time of the minimum value of the relative distance b_{\min} (3) between the harmonics of radio bursts II type, where the correlation coefficient r between $f_{\min,1}$ and $I_p \approx 0.79$ (Isaeva, 2019), which is more fully commensurate with what is obtained from the parameters of μ -bursts. It was also shown that there is a strong relationship between the intensity of the SCR proton flux and parameter V_{II} (2), which characterizes the displacement of the shock front with time t_i , where the correlation coefficient r between V_{II} (2) and $I_p \approx 0.79$ (Isaeva, 2018). It should also be noted that the presence of a strong coupling between V_{II} and I_p is most likely realized in a narrow frequency range of 25-60 MHz for all 112 proton events.

As a result of detailed studies, a fairly strong connection was also revealed between the rise time t_μ of μ -bursts at a frequency of 8800 MHz and the parameter a_j in the regression model (1), which characterizes the decrease in the drift velocity of type II radio bursts with time t_i , where the correlation coefficient r between t_μ and $a_j \approx 0.66$ (Isaeva, Tsap, 2017). The revealed regularity may also indicate that for the overwhelming majority of proton events, coronal shock waves are generated in the region of flare energy release and are associated with flares, which is quite consistent with the conclusions of other authors in (Wagner et al., 1983; Vrsnak et al., 1995).

In this work, it was also shown that there is a fairly strong relationship between the velocity of coronal shock waves V_{Shock} (tabular data with NGDC) and the frequency $f_{\min,1}$ at the fundamental harmonic at the time of the minimum relative distance b_{\min} between the harmonics of a type II radio burst, where the correlation coefficient between $f_{\min,1}$ and $V_{\text{Shock}} \approx 0.68$.

It should be noted that the revealed new patterns require further detailed studies in order to confirm or refute the results.

References

- Akin'yan S., Fomichev V., Chertok I.: 1977, *Geomagnetizm i aeronomiya*, **17**, № 1, 10.
- Akin'yan S., Fomichev V., Chertok I.: 1978, *Geomagnetizm i aeronomiya*, **18**, № 4, 577.
- Cairns I., Knock S., Robinson P., Kuncic Z.: 2003, *Space Sci. Rev.*, **107**, 27.
- Classen H. et al.: 2002, *A&A*, **384**, 1098.
- Clover E., Kahler S. and Reames D.: 2004, *Astrophys. J.*, **605**, 902.
- Gopalswamy et. al.: 1998, *Geophys. Res.*, **103**, 307.
- Gopalswamy, N., Yashiro, S., Michalek, G., et al.: 2002, *Astrophys. J.*, **572**, 103.
- Grechev V., Kiselev V., Meshalkina N. et al.: 2015, *Solar Physics*, **290**, 2827.
- Isaeva E., Mel'nikov V., Tsvetkov L.: 2010, **106**, № 1, 42.
- Isaeva E., Tsap Yu.: 2011, *Bull. of the Crimean Astrophys. Observ.*, **107**, 78.
- Isaeva E., Tsap Yu.: 2017, *Odessa Astron. Publ.*, **30**, 222.
- Isaeva E.: 2018, *Odessa Astron. Publ.*, **31**, 132.
- Isaeva E.: 2019, *Odessa Astron. Publ.*, **32**, 122.
- Mel'nikov V., Yepifanov O.: 1979, *Simp. po KAPG po solnechno-zemnoy fizike*, M.: Nauka, 115.
- Mel'nikov V., Podstrigach T., Kurt V., Stolpovskiy V.: 1986, *Kosmicheskiye issledovaniya*, **24**, 610.
- Mel'nikov V., Podstrigach T., Daybog E., Stolpovskiy V.: 1991, *Kosmicheskiye issledovaniya*, **29**, 95.
- Podstrigach T., Fasahova M.: 1981, *Geomagnetizm i aeronomiya*, **21**, № 1, 22.
- Reams D.: 1999, *Space Sci. Rev.*, **90**, 413.
- Tsap Yu., Isaeva E.: 2012, *Bull. of the Crimean Astrophys. Observ.*, **108**, 52.
- Tsap Yu., Isaeva E.: 2012, *Geomagnetism and Aeronomy*, **52**, № 7, 921.
- Tsap Yu.T., Isaeva E.A.: 2013, *Cosmic Research*, **51**, № 2, 108.
- Tsap Yu., Isaeva E., Kopylova Yu.: 2020, *Astron. Lett.*, **46**, № 2, 144.
- Chertok I.: 1982, *Geomagnetizm i aeronomiya*, **22**, № 2, 182.
- Vrsnak B. et al.: 1995, *Solar Phys.*, **158**, 331.
- Wagner W. et al.: 1983, *A&A*, **120**, 136.
- Wild J., Smerd S., Weiss A.: 1963, *Ann. Rev. Astron. Astrophys.*, **1**, 291.

DOI:<http://dx.doi.org/10.18524/1810-4215.2020.33.216449>

THE ROLE OF MACROSCOPIC TURBULENT DIAMAGNETISM IN ENSURING LONG-TERM STABILITY OF SUNSPOTS

V.N. Krivodubskij

Astronomical Observatory, Taras Shevchenko National University of Kyiv, Kyiv, Ukraine
krivod2@ukr.net

ABSTRACT. We investigated the role of macroscopic turbulent diamagnetism in ensuring the long-term stability of the equilibrium state of the sunspots. The physical meaning of macroscopic diamagnetism of turbulent plasma is expulsion of a large-scale magnetic field from areas with increased turbulence intensity to areas with reduced turbulence. We follow the idea of Krause & Rüdiger (1975) that a strong magnetic field of a sunspot modifies the structure of turbulence in spot umbra, so it becomes two-dimensional. In addition, we take into account the strong magnetic suppression of turbulence in the spot, where it becomes less intense than the turbulent convection around the spot. As a result, a relatively thin transitional vertical layer of permeable convection (convective overshoot layer) should be formed between these sections, in which the intensity of turbulent pulsations decreases noticeably in the transverse direction during the transition from the convection section to the spot. In this permeable convection layer, the effect of turbulent diamagnetic displacement of the magnetic field from the convection region to the sunspot occurs. Owing to the two-dimensional turbulent diffusion, the magnetic field of the spot spreads outwards, while the intense turbulent pulsations in the convection region return the magnetic field in the opposite direction, back to the spot. Therefore, these two oppositely directed processes of magnetic field transfer in the horizontal plane compete with each other. As a result, the magnetic fields that are transferred due to turbulent diffusion outward from the sunspot will be thrown backward into the spot due to strong external turbulent convection. In our opinion, this effect should ensure long-term stability of the equilibrium state of the magnetic field of sunspots and support them in the form of isolated vertical unipolar magnetic force tubes.

Keywords: sunspots, magnetic fields, turbulence, convective overshoot layer, macroscopic turbulent diamagnetism.

АНОТАЦІЯ. Ми дослідили роль макроскопічного турбулентного діамagnetизму у забезпеченні довготривалої стабільності рівноважного стану сонячних плям. Фізичний сенс макроскопічного діамagnetизму турбулентної плазми полягає у витисненні крупномасштабного магнітного поля із ділянок з підвищеною інтенсивністю турбулентності в ділянки зі зниженою турбулентністю. Ми дотримуємось ідеї Краузе та Рюдігера (Krause & Rüdiger, 1975) про те, що сильне магнітне поле сонячної плями змінює структуру

турбулентності в тіні плями, тому тут вона стає двовимірною. Крім того, ми беремо до уваги сильне магнітне пригнічення турбулентності в плямі, де вона стає менш інтенсивною, ніж турбулентна конвекція навколо плями. В результаті між цими ділянками повинен утворитися відносно тонкий перехідний вертикальний шар проникної конвекції (конвективний овершут шар), в якому інтенсивність турбулентних пульсацій значно зменшується в поперечному напрямку при переході від ділянки конвекції до плями. У цьому шарі проникної конвекції виникає ефект турбулентного діамagnetизму витиснення магнітного поля із ділянки конвекції до сонячної плями. Завдяки двовимірній турбулентній дифузії магнітне поле плями поширюється назовні, тоді як інтенсивні турбулентні пульсації у ділянці конвекції повертають магнітне поле в зворотному напрямку, назад до плями. Тому ці два протилежно спрямовані процеси перенесення магнітного поля в горизонтальній площині конкурують між собою. В результаті, магнітні поля, які внаслідок турбулентної дифузії переносяться назовні із сонячної плями, будуть відкинуті назад в пляму через сильну зовнішню турбулентну конвекцію. На наш погляд, цей ефект повинен забезпечити довготривалу стійкість рівноважного стану магнітного поля сонячних плям і підтримувати їх у вигляді ізольованих вертикальних однополярних магнітних силових трубок.

Ключові слова: сонячні плями, магнітні поля, турбулентність, шар проникної конвекції, макроскопічний турбулентний діамagnetизм.

1. Introduction

Observations show a strange property of surface magnetic fields on the Sun, which tend to spontaneously concentrate into widely spaced isolated magnetic flux tubes (MFT) of the same polarity in the form of sunspots. The question arises of how to explain the long-term stability of the equilibrium state of the spot after the fields float to the surface, when the MFTs in the subphotosphere layers are close to the vertical position, despite the mutual repulsion of fields of the same polarity. In connection with this problem, we investigated the role of macroscopic turbulent diamagnetism in ensuring the equilibrium state of vertical MST.

2. Macroscopic turbulent diamagnetism of plasma

Turbulent viscosity of plasma in absence of magnetic field is described by the following relationship

$$v_T \approx (1/3)ul, \quad (1)$$

where u and l are the rms effective velocity and the characteristic scale of turbulent vortices. Zeldovich (1956) discovered, and Weiss (1966) then confirmed, that vortices in turbulent plasma are capable of expulsion magnetic flux out of the turbulent region. Later, Rädler (1968) called the revealed phenomenon as “the macroscopic diamagnetic effect”. The physical sense of macroscopic diamagnetism of turbulent plasma (Krause & Rädler, 1980; Vainshtein, Zel’dovich & Ruzmaikin, 1980; Zeldovich, Ruzmaikin & Sokoloff, 1983) is expulsion of the mean (large-scale) magnetic field from areas of high-conductivity plasma with increased intensity of turbulent motions to places with less developed turbulence along the gradient of turbulent viscosity v_T with the effective rate

$$\mathbf{U}_\mu = -\nabla v_T / 2. \quad (2)$$

The expulsion of initially homogeneous magnetic field from the region of highly conductive plasma with turbulent vortex motions can be explained as follows. At first, the magnetic field frozen into the highly conductive plasma is strongly entangled by vortices and its scale decreases rather quickly. When the scale becomes small enough, the ohmic dissipation (which is determined by magnetic viscosity $v_m = c^2/4\pi\sigma$, σ is the gas-kinetic conductivity of plasma, and c is the speed of light) enters into action, and the field almost disappears in this region. Ultimately, this phenomenon can be interpreted as the expulsion of the field from the region with turbulent motions.

Within the framework of macroscopic magnetohydrodynamics, the decay process of the mean magnetic field \mathbf{B} in turbulent plasma is described by the diffusion equation

$$\partial\mathbf{B}/\partial t = \text{rot}(\mathbf{U}_\mu \times \mathbf{B}) + (v_m + v_T)\Delta\mathbf{B}. \quad (3)$$

The first term in the right side of this equation describes magnetic field transfer due to macroscopic turbulent diamagnetism, while the second term describes magnetic field attenuation due to ohmic dissipation and turbulent diffusion.

It is important to remember that there are frequent situations in space and in the solar plasma in particular when characteristic sizes of vortices are large enough to form zones between turbulent convective structures and regions without perturbations, where gradual decrease in turbulent vortices intensity occurs. This structure, referred to as “the convective overshoot layer”, is formed at the boundary between the solar convection zone (SCZ) and the radiative interior of the Sun (Roxburgh, 1978; Spiegel & Weiss, 1980; Van Ballegooijen, 1982).

A noticeable positive radial gradient of the turbulent velocity near the bottom of the SCZ in the overshoot convection layer causes an intense downward diamagnetic displacement of the field, which acts against magnetic

buoyancy and thus contributes to the long-term retention of the field (Krivodubskij, 1984, 2005; Kryvodubskij, Rüdiger & Kitchatinov, 1994).

We believe that favorable conditions for the appearance of a convective overshoot layer can also be created near the surface of the Sun at the transverse transition from the vertical MFT of the sunspot to the environment convection region. Let's explore in more detail how these conditions are created.

3. Turbulence degeneration at strong magnetic field in sunspot

It is well known that strong magnetic fields appreciably suppress the turbulent eddies intensity. However, laboratory experiments by Kit & Tsinober (1971) showed that a strong magnetic field does not completely suppress turbulence. Rather, it leads to a change in the spatial structure of turbulence. By a strong magnetic field turbulence is caused to become two-dimensional: a variation of the turbulent velocity in the direction parallel to the magnetic field is strongly inhibited.

It should be expected that the strong magnetic field in a sunspot will cardinaly modify the structure of turbulent motions in the sunspot umbra in comparison with the turbulent convection in sunspot vicinity in the more profound layers of the SCZ. Indeed, according to Krause & Rüdiger (1975), the turbulent motions in deep sunspot layers by the influence of the strong homogeneous vertical magnetic field ($B \approx 3000$ G) degenerates into a two-dimensional structure, which does not changes along the magnetic field (Fig. 1). It was believed that the processes causing the decay of the magnetic field take place in the deeper layers, where the field can be assumed vertical. Thus, this model does not take into account the magnetic lines of force spread in the upper layers near the surface of the Sun. In this case, the rate of magnetic field decay in a

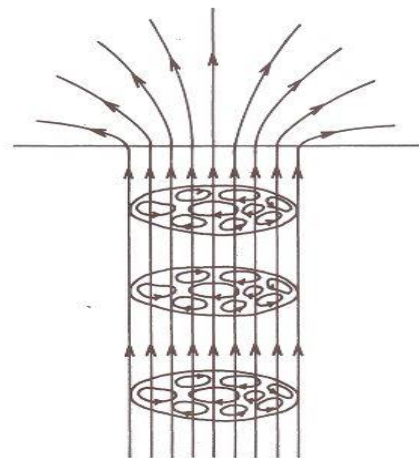


Figure 1: Sunspot magnetic field model. The magnetic field is assumed to be directed perpendicular to the Sun's surface. The turbulent motions in deep sunspot layers by influence of the strong homogeneous vertical magnetic field degenerate into a two-dimensional structure. Figure was taken from the paper (Krause & Rüdiger, 1975).

transverse direction is determined by the two-dimensional turbulent viscosity (Krause & Rüdiger 1975),

$$v_T^{(2)} \approx (1/2)ul. \quad (4)$$

In addition, a strong magnetic field causes noticeably suppression of turbulent convection (which leads to decrease in the parameters u and l) in the sunspot umbra (Obridko & Teplitskaya, 1978; Krat, Karpinsky & Pravdjuk, 1972). Therefore it should be expected that the turbulent viscosity in the sunspot will be smaller than this one in the convective region outside of the spot.

4. Vertical turbulent overshoot layer in the vicinity of the sunspot

We will proceed from the above mentioned model of the magnetic field of the sunspot. According to Solov'ev (1976) the magnetic field decreases sharply from 2000-4000 G in the sunspot to 500-700 G in the convective region. We believe that in the convective region with a weak magnetic field, intense turbulent convection has a three-dimensional structure, while in the sunspot with a strong magnetic field, turbulent convection degenerates into a weak two-dimensional structure. As a result, on the spot outer boundary a relatively thin vertical transitional layer of permeable convection (convective overshoot layer) should be formed in which the intensity of turbulent pulsations decreases noticeably in the transverse direction during the transition from the convective region to the sunspot (Fig. 2). Therefore, favorable conditions appear in this boundary layer for transverse (horizontal) macroscopic diamagnetism that can affect the reconstructing of the sunspot magnetic field. Intense turbulent pulsations in the convection region return the magnetic field backward to the sunspot, which permeates due to turbulent diffusion in the opposite direction, outward from the sunspot.

Therefore, two oppositely directed processes of magnetic field transfer in the horizontal plane compete with each other. Namely, the magnetic fields that are transferred due to turbulent diffusion outward from the sunspot to the convection region (the second term in the right side of eq. (3)) will be thrown backward into the sunspot due to the gradient of turbulent viscosity in overshoot layer (the first term in the right side of this equation). In our opinion, this effect must keep magnetic fields of sunspots and support them in the form of long-term isolated vertical MFTs.

5. Transverse (horizontal) turbulent diamagnetic transfer of fields from the convection region to the sunspot

To verify our assumption how turbulent diamagnetism helps the sunspot magnetic fields to keep their structure in for a long time, we calculated the coefficient of turbulent viscosity outside a sunspot in the convection region and compare it with the calculated turbulent viscosity in the sunspot.

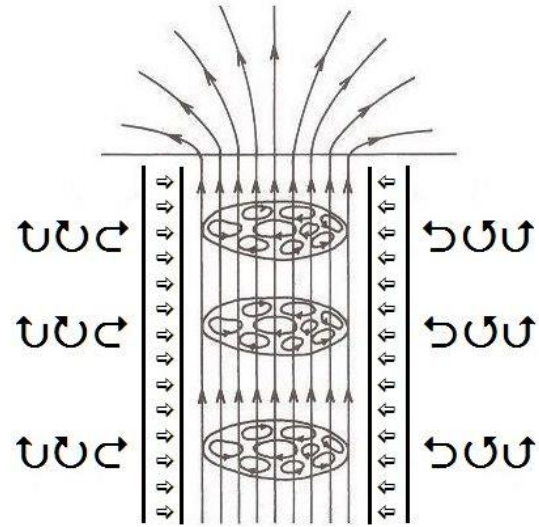


Figure 2: Vertical turbulent overshoot layer at the boundary between an MFT and surrounding convection region. In this layer (with thickness d) the intensity of turbulent pulsations decreases noticeably in the transverse direction at the transition from the convective region to the sunspot. Due to weak two-dimensional turbulent viscosity in sunspot the magnetic field permeates outwards, however intense three-dimensional turbulent vortices in the convection region (large eddies) return this magnetic field backward to the sunspot. The direction of the macroscopic diamagnetic field transfer to the spot (with the rate $U_\mu = -\nabla v_T / 2$) is shown in the overshoot layer by light arrows.

For the convective region we use the following values of turbulent parameters at a depth of $z \approx 400$ km in the SCZ model by Stix (2003): $u \approx 2 \times 10^5$ cm/s, $l \approx 4 \times 10^7$ cm. Then the turbulent viscosity in the convection region is estimated to be $v_T \approx (1/3)ul \approx 3 \times 10^{12}$ cm²/s.

As noted above, the strong magnetic field of sunspot stimulates the degeneration of three-dimensional turbulence into two-dimensional one (Krause & Rüdiger, 1975). The following turbulent parameters for sunspot umbra were taken for calculating: $u \approx 1.3 \times 10^5$ cm/s (Obridko & Teplitskaya, 1978); $l \approx 1.5 \times 10^7$ cm (Krat, Karpinsky & Pravdjuk, 1972). As a result of calculations, the following estimate was obtained: $v_T^{(2)} \approx (1/2)ul \approx 2 \times 10^{12}$ cm²/s.

It is essential that turbulent viscosity in the convective region exceeds this one in the sunspot. Therefore, our estimates confirm that the effect of turbulent diamagnetic expulsion (in the horizontal plane) of magnetic field from the convection region toward the sunspot must inevitably appear in the boundary overshoot layer (which occurs between a vertical MFT and surrounding medium).

Following (Solov'ev, 1976), we assume that the thickness d of the transitional layer of penetrating convection between the vertical MCT of the spot and the surrounding three-dimensional turbulence is 100 km.

We can estimate the velocity of diamagnetic transfer (“dragging”) of magnetic field from the convection region

to the sunspot using the obtained parameters of turbulent viscosity

$$U_{\mu} \approx -(\nu_T - \nu_T^{(2)})/2d \approx -(\nu_T - \nu_T^{(2)})/2d \approx -10^5 \text{ cm/s}. \quad (5)$$

The minus sign indicates that the magnetic field is expelled from the convection region to the sunspot. The time of diamagnetic “dragging” of the field toward the sunspot is next: $t_{\mu} \approx d/|U_{\mu}| \approx 100$ s.

Therefore, the regime of stable keeping the magnetic field in the sunspot is settled fairly fast (over the time that is less than the lifetime of granulation cells on solar surface) due to macroscopic turbulent diamagnetic effect in the convection region. The disintegration of the sunspot at its inner side is determined by slow magnetic diffusion due to relatively low turbulent viscosity of the sunspot umbra. The sunspot decay at its outer side is due to diffusion under conditions of enhanced turbulent convection intensity, which yields an accelerated rate of magnetic attenuation that can be interpreted as an “expulsion” of the magnetic field from surrounding medium backward to the sunspot umbra. It is this second accelerated rate of magnetic field attenuation at the outer side of the sunspot that plays an essential role in long-term stability of equilibrium state of vertical MFTs in sunspots (effect of macroscopic diamagnetic field expulsion from the convection region to the sunspot).

6. Conclusion

We considered the difference in turbulent vortices intensities between the sunspot umbra (where turbulent vortices are suppressed by a strong magnetic field) and the surrounding plasma without magnetic fields (the convection region, where suppression of turbulent vortices due to magnetic field is absent). As a result, a relatively thin transitional vertical convective overshoot layer must be formed between these sections, in which the intensity of turbulent pulsations decreases significantly in the transverse direction during the transition from the convection region to the spot.

This approach enabled us to reveal the effect of macroscopic diamagnetic expulsion of magnetic field from the convection region to the sunspot (transverse turbulent diamagnetism), which can play an essential role in long-term stability of equilibrium state for vertical MFTs.

Acknowledgements. This study was funded by grant number 19BF23-03 of Taras Shevchenko National University of Kyiv.

References

- Kit L.G., Tsinober A.B.: 1971, *Magnitnaja gidrodinamika*, **1971/3**, 27.
- Krat V.A., Karpinsky V.N., Pravdjuk L.M.: 1972, *Sol. Phys.*, **26**, 305.
- Krause F., Rädler K.-H.: 1980, *Mean Field Magnetohydrodynamics and Dynamo Theory*, Berlin: Akademie-Verlag.
- Krause F., Rüdiger G.: 1975, *Sol. Phys.*, **42**, 107.
- Krivodubskij V.N.: 1984, *Soviet Astronomy*, **28**, No.2, 205.
- Krivodubskij V.N.: 2005, *Astron. Nachr.*, **326**, No.1, 61.
- Kryvodubskij V.N., Rüdiger G., Kitchatinov L.L.: 1994, *Visnyk Kyiv. Universytetu. Astronomija*, **33**, 55.
- Obridko V.N., Teplitskaya R.B.: 1978, *Itohi Nauki Tekh.*, Ser.: Astron., **14**, 7.
- Rädler K.-H.: 1968, *Z. Naturforsch., A: Astrophys., Phys., Phys. Chem.*, **23**, 1841.
- Roxburgh I.W.: 1978, *Astron. Astrophys.*, **65**, 281.
- Solov'ev A. A.: 1976, *Astron. Zh.*, **53**, 140.
- Spiegel E.A., Weiss N.O.: 1980, *Nature*, **287**, 616.
- Stix M.: 2003, *The Sun*. Berlin: Springer.
- Vainshtein S. I., Zel'dovich Ya. B., Ruzmaikin A. A.: 1980, *Turbulent Dynamo in Astrophysics*, Moscow: Nauka, 352 p. [in Russian].
- Van Ballegooijen A.A.: 1982, *Astron. Astrophys.*, **113**, 99.
- Weiss N.O.: 1966, in *Proc. Roy. Soc. London*, **A293**, 310.
- Zel'dovich Ya. B.: 1956, *Zh. Eksp. Teor. Fiz.*, **31**, 154.
- Zeldovich Ya.B., Ruzmaikin A.A., Sokoloff D.D.: 1983, *Magnetic Fields in Astrophysics*, New York: Gordon and Breach, 381 p.

DOI: <http://dx.doi.org/10.18524/1810-4215.2020.33.216451>

ANOMALOUS WIDENING OF 5434.5 LINE IN SUNSPOTS: SUPER-STRONG MAGNETIC FIELDS?

V.G. Lozitsky¹, S.M. Osipov², M.I. Stodilka³¹ Astronomical Observatory of the Taras Shevchenko National University of Kyiv, Kyiv, Ukraine, lozitsky_v@ukr.net² Main Astronomical Observatory of National Academy of Science, Kyiv, Ukraine, osipov@mao.kiev.ua³ Astronomical Observatory of Ivan Franko National University of L'viv, L'viv, Ukraine, m.stodilka@gmail.com

ABSTRACT. We present results of spectral observations of two sunspots in six metal lines near Fe I 5434.5 Å, which have effective Lande factors g_{eff} from -0.014 to 2.14 . The observations were made on July 8 and August 25, 2015, with the ATsU-5 telescope of GAO NAS of Ukraine using a circular polarization analyzer and spectra registration with the SBIG ST-8300 CCD camera. The following line parameters are compared: observed splitting of $I \pm V$ profiles, the width and depth of the Stokes I profiles. Significant differences of the measured magnetic field strengths B_{eff} were found in separate places of the spots and by lines with different g_{eff} values. The Fe I 5434.5 Å line ($g_{\text{eff}} = -0.014$) shows measurable splitting in some locations of the sunspots, which corresponds to the magnetic field $B_{\text{obs}} \approx 20$ kG. Comparison of the widths and depths of the line profiles revealed several special places in the sunspots, where the Fe I 5434.5 Å line was expanded additionally by ≈ 15 – 35% , whereas other lines with larger Lande factors did not have such a feature. One of the reasons for this expansion could be a sharp and local increase of turbulent velocities, but no active processes such as solar flares or significant Doppler flows were observed at these locations. A semi-empirical model constructed for the first sunspot by FeI 5434.5 line using inverse code with Tikhonov's stabilizers shows an anomalous feature – the maximum of microturbulent velocities in the upper photosphere and the temperature minimum zone instead of the usual small increase of microturbulence at these heights. This may be the effect of very strong magnetic fields of mixed polarity or unresolved turbulent structures. As to first case, the estimated value of the magnetic field in such locations of sunspots is $\sim 10^5$ G, which requires additional careful verification.

Keywords: Sun, solar activity, sunspots, magnetic fields, spectral lines, the Zeeman effect, semi-empirical model, turbulent velocities, superstrong magnetic fields.

АНОТАЦІЯ. Представлені результати спектральних спостережень двох сонячних плям у шести лініях металів поблизу лінії Fe I 5434.5 Å, які

мають ефективні фактори Ланде g_{eff} від -0.014 до 2.14 . Спостереження були виконані 8 липня і 25 серпня 2015 р. на телескопі АЦУ-5 Головної астрономічної обсерваторії НАН України з використанням аналізатора кругової поляризації і з реєстрацією спектру з допомогою камери SBIG ST-8300 CCD camera. Були співставлені такі параметри ліній: спостережене розщеплення профілів $I \pm V$, ширини і глибини профілів Стокса I . Виявлені суттєві розбіжності вимірюваних магнітних полів B_{eff} у окремих ділянках сонячних плям а також по лініях з різними величинами g_{eff} . Лінія Fe I 5434.5 Å ($g_{\text{eff}} = -0.014$) виявляє достовірне розщеплення у деяких місцях плям, яке відповідає магнітному полю $B_{\text{obs}} \approx 20$ кГс. Співставлення ширин і глибин профілів ліній показало, що у деяких місцях лінія Fe I 5434.5 Å додатково розширена на ≈ 15 – 35% , тоді як інші лінії з більшими факторами Ланде не мають такої особливості. Однією з причин такого розширення могло бути різке й локальне зростання турбулентних швидкостей, однак ніяких активних процесів типу сонячних спалахів або значних доплерівських потоків не було помічено у цих місцях. Напівемпірична модель першої плями, побудована за даними в лінії FeI 5434.5 інверсним методом з використанням стабілізаторів Тихонова для забезпечення стійкості розв'язків рівнянь переносу випромінювання, має цікаву особливість – максимум мікротурбулентних швидкостей у верхній фотосфері і зоні температурного мінімуму замість слабого зростання мікротурбулентності на цих висотах. Це може бути внаслідок дуже сильних магнітних полів змішаної полярності або ж внаслідок присутності просторово нероздільних турбулентних структур. Щодо першого випадку, то наближена оцінка магнітного поля у цих місцях плям дорівнює $\sim 10^5$ G, що потребує додаткової ретельної перевірки.

Ключові слова: Сонце, сонячна активність, сонячні плями, магнітні поля, спектральні лінії, ефект Зеємана, напівемпірична модель, турбулентні швидкості, надсильні магнітні поля.

1. Introduction

Magnetic fields in sunspots are measured, as a rule, using spectral lines with the largest Lande factors. This provides the highest accuracy of measurements and the ability to determine such an important characteristic as the modulus of the magnetic field strength, in addition, regardless of instrumental polarization, the inclination of the field vector to the line of sight and the scattered light. Although in this case, there are some methodological problems that are encountered when comparing data from different observatories (Lozitska et al., 2015). As for the most mass magnetographic measurements to date, they usually give a longitudinal component of the magnetic field and, moreover, are not corrected for changing the profile of the spectral line due to non-magnetic changes in the transition from the photosphere to the sunspot. As a result, the most reliable measurements of magnetic fields in sunspots today are traditional spectral measurements or modern Stokes diagnostics using realistic models of the solar atmosphere. However, in the latter case, lines with large Lande factors are also commonly used. This automatically limits the range of magnetic field strengths available for measurements. Regarding direct data for cases corresponding to the filling factor f close to unity (i.e., $f \approx 1$), the strongest magnetic fields in the spots were found to be within 5.5–6.1 kG (Livingston et al., 2006; Lozitsky et al., 2018). However, sunspots with such superstrong fields are rare; for the most part, the typical magnetic field strength in developed sunspots (with shadow and penumbra) is in the range of 2–3 kG.

Subtle effects were found in line profiles which indicate that the magnetic field strength in spatially unresolved elements of sunspots can be 7–8 kG (Van Noort et al., 2013; Lozitsky, 2016). The filling factor for such elements can reach values $f = 0.2$ – 0.3 , and the Doppler shifts correspond to plasma lifting with speeds of 2–3 km / sec. However, in the article by Van Noort et al. (2013) the conclusion is different: the substance in the subtelescopic elements goes down with speeds of about 20 km / sec. A possible reason for the difference between these findings is that in the papers by Lozitsky (2016) the umbra of large spots was studied, whereas in the article by Van Noort (2013) – penumbra of sunspots.

It should be noted that the particularly strong magnetic fields in the range of 7–8 kG are, in fact, close to the upper limit of detectable (measurable) fields when to use the spectral lines like Fe I 5250.2 or Fe I 6302.5 with large Lande factors. The mentioned authors analyzed the spectral lines of Fe I 6301.5 and 6302.5 with effective Lande factors 1.67 and 2.50, respectively, which in case of high magnetic strengths are split so strongly that their Zeeman σ components begin to overlap mutually, complicating the diagnosis of fine photometric effects in the adjacent spectral continuum. This is especially true in the sunspot umbra where the numerous and variable molecular blends can occur. That is why it is better to use spectral lines with small Lande factors ($g_{\text{eff}} \leq 1$) to measure even stronger magnetic fields.

It is important to note that modern methods of measuring magnetic fields in sunspots are mainly oriented on observations of fields of regular polarity, which give characteristic manifestations in the Stokes parameters Q ,

U and V . However, for spatially unresolved magnetic fields of mixed polarity, the corresponding observed manifestations in these parameters may be close to zero, i.e. not detectable. At the same time, strong mixed-polarity fields can be detected by the Stokes I profile, that is, by the integral intensity, on the basis of observations of significant expansion of this profile. However, in practice, this parameter is almost never analyzed when interpreting observations.

In this study, we use both of the mentioned methodological factors: spectral lines with very small Lande factors and data on the line profiles in the integral intensity. The purpose of our work is to obtain new data for the problem of the upper limit of the magnetic field in the sunspots using the spectral data obtained with a circular polarization analyzer.

2. Observations

Observational material for our study was obtained with the horizontal solar telescope ATsU-5 of Main Astronomical Observatory of National Academy of Science of Ukraine. The telescope is well tested and has a half-width of the instrumental profile ≈ 20 mÅ for $\lambda = 6328$ Å (Osipov, 2015). During observations, the spectra of sunspots and surrounding areas were recorded using an SBIG ST-8300 CCD camera in the wavelength range about ± 4 Å around Fe I 5434.5 Å line. To obtain the spectra $I + V$ and $I - V$, a polarization mosaic by Skomorovsky (1974) and a quarter-wave plate were used.

In this paper, we analyze the observations of two sunspots which were observed on July 8 and August 25, 2015. The second sunspot was in the tail part of the active region of NOAA 2403, which was located from the center of the disk at a distance $\rho/R = 0.415$, $\mu = 0.91$. The diameter of the penumbra of this spot was about 45 Mm; the spot was irregular in shape, especially its umbra (Fig. 1).

The exposure of the spectrum of this spot was made at the following time interval: 07^h36^m–07^h46^m UT. During the exposure, the entrance slit of the spectrograph crossed the spot in the north-south direction on the disk, as it is shown in Fig. 1.

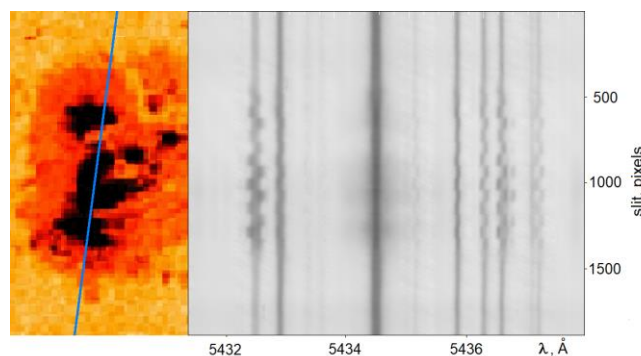


Figure 1: The images of the sunspot of 25 August, 2015 in white light according to the SOHO data (left), and its spectrum according to observations on the ATsU-5, which is analyzed in this paper (right). The strongest spectral line in the middle part of this spectrum is Fe I 5434.5 Å line ($g_{\text{eff}} = -0.014$).

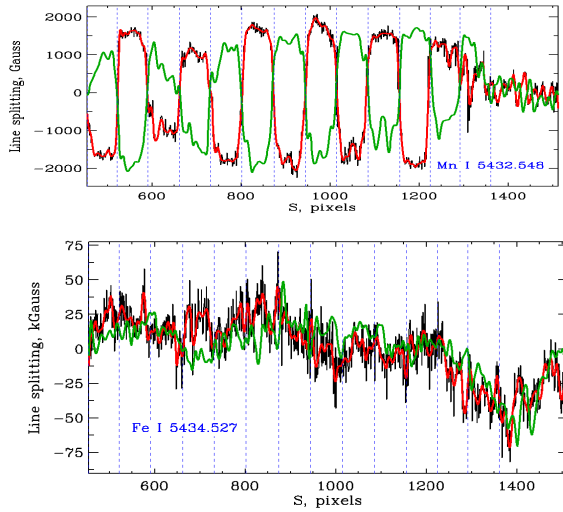


Figure 2: Shift of ‘center of gravity’ of spectral lines with Lande factors $g_{\text{eff}} = 2.143$ and $g_{\text{eff}} = -0.014$ for sunspot of 28 Aug 2015. Red and green lines represent calibrated positions of ‘center of gravity’ of $I + V$ and $I - V$ profiles along direction of entrance slit of spectrograph.

First sunspot was observed on July 8, 2015, in active region NOAA 2381. Beginning of exposure of this sunspot was at 7^h 12^m UT.

3. Effective magnetic fields

The effective (averaged) magnetic fields B_{eff} were measured by the displacement of the centers of gravity of the profiles $I + V$ relative to $I - V$. For a uniform magnetic field and incomplete splitting of the Zeeman π and σ components, this should give a value close to the longitudinal component of the magnetic field.

Figure 2 shows, for illustration, distribution of spectral positions of two lines with very different Lande factors, $g_{\text{eff}} = 2.143$ (upper graph) and $g_{\text{eff}} = -0.014$ (lower graph). These positions are presented along direction of entrance slit of spectrograph for two orientations of quarter-wave plate, $+45^\circ$ and -45° relatively optical axis of polarization mosaic. Along the horizontal axis on Figures, the horizontal coordinates of corresponding places on the Sun are given in numbers of pixels (slit, pxl). We will denote this parameter in the short form as S below.

One can see the following well-visible effects in line with large Lande factor: (a) periodical deviations of line position when to transit from given band of mosaic to the next, and (b) discrete change of the sign of deviation to the opposite one for different orientations of quarter-wave plate. Namely such effects demonstrate the magnetic nature of these manifestations. On this Figure, equivalent width of the mosaic strip is 3.3 Mm on the Sun.

In order to determine the magnitude of the measured magnetic field according to these graphs, it is necessary to take for each specific strip of the mosaic half the difference of the position of the line with different orientation of the quarter-wave plate. For example, in Fig. 2 in the abscissa interval $S = 800\text{--}870$ the line posi-

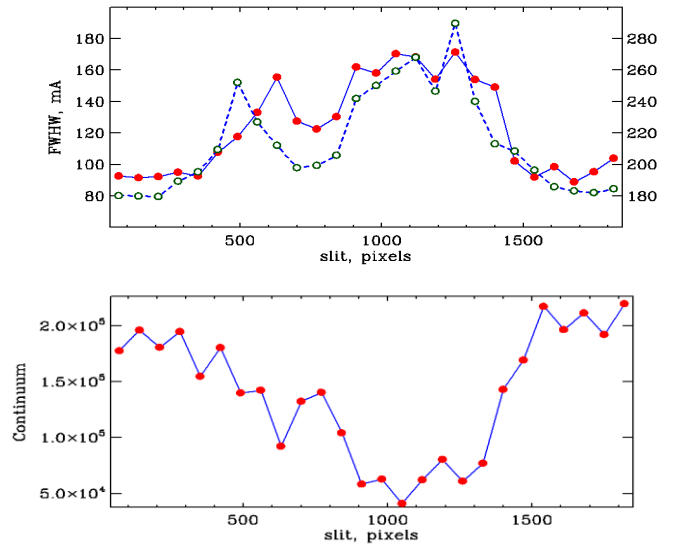


Figure 3: Comparison of the half-widths of lines with $g_{\text{eff}} = 2.143$ and -0.014 , versus the intensity in the spectral continuum (lower graph). It can be seen that line with $g_{\text{eff}} = -0.014$ (stroke line) has a sharp jumps at position slits ≈ 500 and 1260 .

tions correspond to values of $+1800$ G and -2000 G. Subtracting the second value from the first and taking half of it, we have an average field in this strip, equal to 1900 G.

A similar examination of the observational data for line with very small Lande factor (-0.014) shows that in some places of the sunspot it also has similar evidence of Zeeman splitting. For example, this is seen in the abscissa intervals $S = 670\text{--}720$ and $820\text{--}830$, where, at different positions of the plate $\lambda / 4$, the ‘‘center of gravity’’ of the line deviates in opposite directions relative to the direction of spectral dispersion. If to interpret it as a manifestation of the Zeeman effect, then the corresponding magnetic field should be at the level of ≈ 20 kG. Another conclusion follows from Fig. 2: the corresponding places in the sunspot with particularly strong fields are quite local, with a typical scale, probably $1\text{--}3$ Mm.

4. Stokes I

Comparison of the half-widths of the Stokes I profiles for the same lines as in Fig. 2 is shown in Fig. 3. One can see that line with large Lande factor (solid line on upper graph on the Figure) has the largest broadening exactly in such places where the intensity in spectral continuum is minimal.

This is well expected effect if we take into account that strongest magnetic fields, as rule, are localized in sunspot umbra. However, the line with a very small Lande factor (dashed line in the Figure 3) behaves differently: in two places, at $S \approx 500$ and 1260 , it has sharp jumps of the half-width. This is surprising because it does not coincide with the darkest places in the sunspot.

Of course, for more confident conclusions, it is necessary to compare the widths of a larger number of spectral lines. This is shown in Fig. 4 for six lines, which presents the relative increase in the line half-width as a function of the

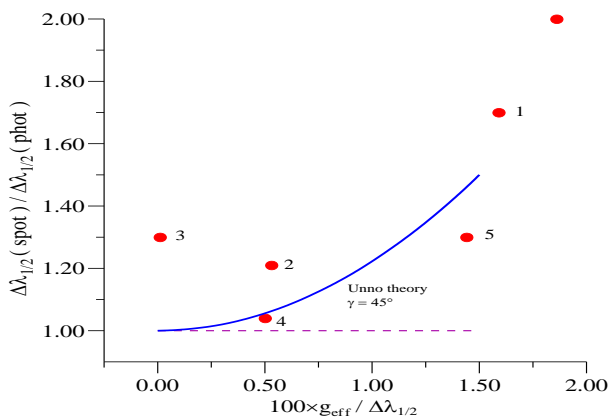


Figure 4: Comparison of the relative increasing of the Stokes profile I for six spectral lines with different Lande factors observed by S.M. Osipov on ATsU-5 in the sunspot on August 25, 2015.

magnetic sensitivity normalized to the line half-width. The filled circles with numbers indicate the observations; the blue curve is Unno (1956) theory for a uniform magnetic field. One can see that the line №3 ($g_{\text{eff}} = -0.014$) deviates significantly from the theoretical dependence. This means that this line really "falls out" of the theoretical regularity that is expected for a uniform magnetic field of the "kilo-Gaussian" level.

5. Semi-empirical model

Similar effects were found also in the first sunspot, which was observed on July 8, 2015. For this sunspot, a semi-empirical model was build using Stodilka's (2003) code. This model presents the photospheric layers of the sunspot and was constructed on a base of observations of FeI 5434.5 line by solving the inverse problem for non-equilibrium radiative transfer problem using Tikhonov stabilizers. The main peculiarity of the model is following: it has an anomalous feature – the maximum of microturbulent velocities in the upper photosphere and the temperature minimum zone instead of the usual small increase of microturbulence at these heights (detailed presentation of this model is planned in a separate study). This may be the effect of very strong magnetic fields of mixed polarity or unresolved turbulent structures. In the first case, the estimated value of the magnetic field in such locations of the sunspot is $\sim 10^5$ G, which, naturally, requires additional careful verification. Notice, similar magnetic fields were suspected in solar flares (Lozitsky, 2009) on a base of observations also in FeI 5434.5 line.

6. Conclusions

The present study confirms the assumption of Severny (1957) that magnetic fields of several tens of kilogauss can exist in sunspots. Indications of such very strong fields follow from both polarization effects and unpolarized light data. The latest data are especially interesting because they lead to the conclusion about the possible existence of even stronger fields of the $\sim 10^5$ G level. In this respect, diagnostics of magnetic fields by the FeI 5434.5 line are especially attractive for future research. The current research narrows the search for such extremely strong fields. Firstly, it is not necessary to have extremely high resolution to detect them. In particular, even a low resolution of 1-3 Mm may be sufficient, since the filling factor, rather than the direct resolution limit, seems to play an important role here. Secondly, data in unpolarized light can be very valuable, but it requires simultaneous analysis of several lines with different Lande factors. Thus, even old observations of sunspots without polarizing optics can contain important information about especially strong magnetic fields in the sunspots.

Acknowledgements. This study was funded by the Taras Shevchenko National University of Kyiv, project No.19БФ023-03, by Main Astronomical Observatory of National Academy of Sciences of Ukraine, project No. 352B, and by Ivan Vranko National University of L'viv, project No. AO91-Φ.

References

- Livingston W., Harvey J.W., Malanushenko O.V.: 2006, *Solar Phys.*, **239**, 41.
- Lozitska N.I., Lozitsky V.G., Andryeyeva O.A. et al.: 2015, *Adv. Space Res.*, **55**, 897.
- Lozitsky V.G., Yurchyshyn V.B., K. Ahn K. et al.: 2018, *Odessa Astron. Publ.*, **30**, 152.
- Lozitsky V.G.: 2009, *Journ. Phys. Studies*, **13**, No. 2, id.2903 (8p.).
- Lozitsky V.G.: 2016, *Adv. Space Res.*, **57**, 398.
- Osipov S.N.: 2015, *Kinem. Phys. Cel. Bodies*, **31**, 261.
- Severny A.B.: 1957, *Astronomicheskii Zhurnal*, **34**, 684.
- Skomorovsky V.I.: 1974, *Issled. Geomagn., Aeronomii i Fizike Solnza*, **26**, 220.
- Stodilka M.I.: 2003, *Kinem. Fizika Nebesnykh Tel*, **19**, 334.
- Unno W.: 1956, *Publs. Astron. Soc. Japan*, **8**, 108.
- Van Noort V., Lagg A., Tiwari S.K. et al.: 2013, *Astron. & Astrophys.*, **557**, id.A24, 14 pp.

DOI:<http://dx.doi.org/10.18524/1810-4215.2020.33.216453>

ON THE POSSIBLE EXISTENCE OF SUPERSTRONG MAGNETIC FIELDS IN A LIMB SOLAR FLARE

I. I. Yakovkin, V.G. Lozitsky

Astronomical Observatory of the Taras Shevchenko National University
of Kyiv, Kyiv, Ukraine, yakovkinii@gmail.com, lozitsky_v@ukr.net

ABSTRACT. We present the simultaneous observations of the K Ca II 3933.7 Å, H δ 4101.7 Å and He I 4471.5 Å lines in the limb solar flare of July 17, 1981. For two moments of the flare we analyzed Stokes $I \pm V$ and V profiles of these lines from observations made on the Echelle spectrograph of the horizontal solar telescope of the Astronomical Observatory of Taras Shevchenko National University of Kiev. In the flash phase of the flare, all named lines had very wide emissions, with a wing length of 6–8 Å. An interesting feature was observed in the violet wings of these lines, namely, narrow emission peaks with a width of only 0.25–0.35 Å. The Zeeman splitting of these emission peaks correspond to magnetic field strength in range 1300–2900 G at altitudes of 10–15 Mm above the level of the photosphere. Magnetic fields of ‘kilogauss’ range (up to 3200 G) were found for some locations also in post-peak phase of the flare. Likely, the true local magnetic fields in the flare could be even larger, since the obtained results represent a longitudinal component of the magnetic field assuming that the filling factor equals unity. A new indication of the existence of superstrong magnetic fields follows from a comparison of the kinetic temperatures and turbulent velocities found from the narrow emission component in the flash phase of the flare. Considering this emission component to be optically thin, we found that there is an anti-correlation between temperature and turbulent velocity. Such a dependence seems unlikely and, possibly, the widths of the line profiles reflect, in our case, not turbulent velocities, but very strong magnetic fields. The corresponding estimates of the magnetic field by the K Ca II line lead to the value $B = 8.3$ kG, and by the He I 4471.5 line - to the value $B = 6.7$ kG. Considering that the He I line is clearly closer to the case of an optically thin layer, the closeness of these estimates is very encouraging. Our results are apparently the first indications of superstrong magnetic fields of 6–7 kG at an altitude of about 10 Mm in a solar flare.

Keywords: Sun, solar activity, solar flares, magnetic fields, spectral lines, the Zeeman effect, temperatures, turbulent velocities, superstrong magnetic fields.

АНОТАЦІЯ. Представлено результати одночасних спостережень ліній K Ca II 3933,7 Å, H δ 4101,7 Å і He I 4471,5 Å у лімбовому сонячному спалаху 17 липня 1981 року. Для двох моментів спалаху були проаналізовані стоксові профілі $I \pm V$ та V цих ліній на

основі спостережень, проведених на ешельному спектрографі горизонтального сонячного телескопа Астрономічної обсерваторії Київського національного університету імені Тараса Шевченка. У флеш-фазі спалаху всі названі лінії мали дуже широкі емісії з довжиною крил 6–8 Å. Цікава особливість спостерігалась у фіолетових крилах цих ліній, а саме – вузькі емісійні піки з шириною лише 0,25–0,35 Å. Земанівське розщеплення цих емісійних піків відповідає напруженостям магнітного поля в діапазоні 1300–2900 Гс і висотам 10–15 Мм над рівнем фотосфери. Магнітні поля діапазону «кілогауссового» (до 3200 Гс) були знайдені у деяких місцях також в інший момент, що відповідає фазі після максимуму спалаху. Ймовірно, дійсні локальні магнітні поля у спалаху можуть бути ще більшими, оскільки отримані результати представляють собою позовжно складову магнітного поля, вважаючи, що коефіцієнт заповнення дорівнює одиниці. Нове свідчення існування надсильних магнітних полів впливає з порівняння кінетичних температур і турбулентних швидкостей, знайдених по вузькій емісійній компоненті у флеш-фазі спалаху. Вважаючи цей компонент оптично тонким, ми виявили, що існує антикореляція між температурою та турбулентною швидкістю. Така залежність уявляється малоімовірною, і, можливо, ширина лінійних профілів відображає, у нашому випадку, не турбулентні швидкості, а дуже сильні магнітні поля. Відповідні оцінки магнітного поля по лінії K Ca II дають величину $B = 8,3$ кГс, а по лінії He I 4471,5 - величину $B = 6,7$ кГс. Враховуючи, що лінія He I явно ближче до випадку оптично тонкого шару, близькість цих оцінок дуже обнадійлива. Отримані нами результати, можливо, є першими свідченнями надсильних магнітних полів рівня 6–7 кГс на висоті близько 10 Мм у сонячній спалаху.

Ключові слова: Сонце, сонячна активність, сонячні спалахи, магнітні поля, спектральні лінії, ефект Зеємана, температури, турбулентні швидкості, надсильні магнітні поля.

1. Introduction

At present, there are very little data in the literature about magnetic fields in limb solar flares. The first such measurements were made by Koval (1977) using the H α

line. It was found that the magnitude of the magnetic field, measured by the relative splitting of the line in orthogonal circular polarizations (i.e., in the $I + V$ and $I - V$ spectra, where I and V are the corresponding Stokes parameters), is typically several hundred gauss (G). However, a case of a rather significant relative displacement of the $I \pm V$ profiles corresponding to a magnetic field of 9000 G was also detected. Named author had the following point of view: "However, such large values are unlikely in the light of existing ideas about the structure of magnetic fields in the solar atmosphere". It should be noted that even magnetic fields of $\sim 10^2$ G are 'too strong' for limb flares. Indeed, if the magnetic field tube is homogeneous and non-twisted, then the upper limit of B_{\max} in the tube can be estimated from the simple condition of the equality of the magnetic pressure $B^2/8\pi$ inside the tube and the gas pressure $P = nkT$ outside the tube. Limb solar flares occur in the chromosphere and lower corona, where the gas pressure in undisturbed atmosphere is $\sim 10^{-1} \div 10^2$ dyn/cm². However, at such pressure, B_{\max} should be in range $1 \div 50$ G, which is at least an order of magnitude less than observed. Furthermore, given that observations with a circular polarization analyzer give a mainly longitudinal component of the magnetic field, the magnitude of the magnetic field may be even larger. As it was pointed above, such strong magnetic fields, maybe, can occur in strongly twisted magnetic structures like force-free ropes.

The magnetic fields of 200 G were measured using the H α line also in the limb solar flare of $M 7.7$ class of 2012 July 19 (Kirichek et al., 2013). The results obtained refer to a rather high altitude above the limb, about 40 Mm. In this case, a significant lack of parallelism of the bisectors of $I \pm V$ profiles was observed too, with a maximum of their splitting at a distance of 0.4 Å from the center of the emission profile. In the named paper, a theoretical MHD force-free model was proposed that allows explain the existence of such strong fields in the corona due to the strong twisting of the power lines. According to numerical estimations in frame of the model, the magnetic field strength increases by about 2 orders in comparison with the weak external field of 1-2 G level which is typical for the solar corona.

Recently, Kuridze et al. (2019) reported on the unique observation of flaring coronal loops at the solar limb using high-resolution imaging spectropolarimetry in Ca II 8542Å line from the Swedish 1 m Solar Telescope. They found magnetic field strengths as high as 350 G at heights up to 25 Mm above the solar limb. As to field order, these measurements are similar to above-named data by Kirichek et al (2013).

2. Observations

The solar flare of 1981 July 17 occurred on the eastern limb of the Sun, in the vicinity of the place with coordinates 7°S, 90°E. According to the bulletin "Solnechnyie Dannyie" (1981), the flare was associated with the active region № 325, which appeared on the Sun's disk the next day, 1981 July 18.

This flare was observed with the Echelle spectrograph of the horizontal solar telescope of the Astronomical

Observatory of Taras Shevchenko National University of Kyiv (Lozitsky, 2016), starting from about 8^h15^m UT. Observers were N.I. Lozitska, V.G. Lozitsky and P.M. Polupan. The flare emission was observed initially in a spectroheliograph, which allows observe the entire "royal" (near the equatorial) zone of the Sun's disk in light of the H α line. Natalia Lozitska, identifying the flare position in white light at the entrance slit of the Echelle spectrograph, noticed an interesting detail: this flare was visible for some time also in white light as a small arched feature on Sun's limb. As we know from the literature, limb solar flares were no longer observed in the white light. It should be noted that in order for such observational manifestations to be possible, the optical thickness in the continuum τ_c must be close to unity. Since $\tau_c \approx n_H L$, where n_H is the concentration of neutral hydrogen atoms, L is the effective linear length of the flare, the condition $\tau_c \approx 1$ can be fulfilled even when the plasma density is less than photospheric one ($\sim 10^{15}$ cm⁻³). If for the flare the effective length is written through L_{fl} and for the photosphere through L_{ph} , then we can expect that $L_{fl} / L_{ph} = 10-100$. This means that to observe a limb flare in white light, it is sufficient that $n_H \sim 10^{13} \div 10^{14}$ cm⁻³.

According to our estimation, the optical flare class was $2B$, which is higher than by bulletin "Solnechnyie Dannyie" (SB). However, we did not perform the exact measurements of the flare area required to strictly determine its class. The main value of our observations is that a wide spectrum interval, from 3800 to 6600 Å, was recorded simultaneously where bright and interesting emissions of hydrogen, helium, and ionized calcium lines were observed. Another advantage of our observations is that $I + V$ and $I - V$ spectra were obtained simultaneously, on separate adjacent bands of the spectrum (see Fig. 1 below). This was made thanks to the fact that the circular polarization analyzer was composed on a base of a $\lambda / 4$ plate in front of the entrance slit of the spectrograph and a two-beams splitting prism (analogous to the Wollaston prism) behind the entrance slit. Therefore, $I + V$ and $I - V$ spectra relate to the same moment of time and to the same places on the Sun.

The flare spectrum was photographed on WP1 ORWO photo-plates with exposures of $10 \div 30$ sec. In the 8^h17^m \div 9^h51^m UT time interval, six exposures were made. Below, the first Zeeman spectrogram obtained in 8^h17^m UT with exposure of 10 sec is analyzed. This time corresponds, apparently, to the flash phase of the flare that is evident due to the very wide wings of the spectral lines (Fig. 1).

3. Line profiles

A visual inspection of the 8^h17^m spectrogram shown that it contains bright emissions of about ten lines of hydrogen, helium and Ca II. In this study we present results obtained from the K Ca II 3933.7 Å, H δ 4101.7 Å and He I 4471.5 Å lines.

For flash phase of the flare, 8^h17^m, the shape of the K Ca II 3933.7 Å and He I 4471.5 Å lines clearly indicates that there were at least two emission components in these lines: wide and narrow, 1.8–2 Å apart in

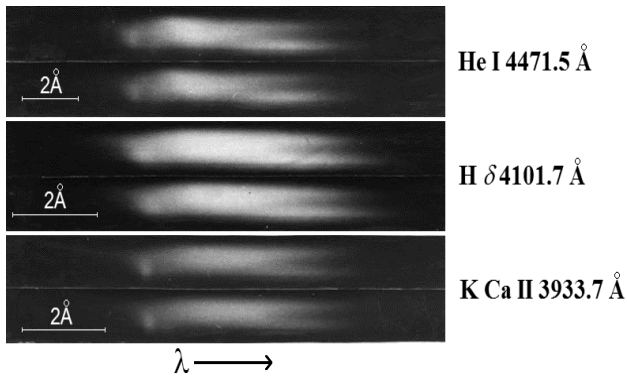


Figure 1: Positive images of the He I 4471.5, H δ 4101.7 and K Ca II 3933.7 lines on the spectrogram for 8^h17^m UT. Each line is represented by two images that correspond to the $I + V$ and $I - V$ spectra. The width of each stripe corresponds to approximately 32 arc sec or 23 Mm on the Sun.

wavelength (Fig. 1). It can be seen from this Figure that the total widths of the emission lines of K Ca II and H δ are almost the same. This directly indicates that non-thermal mechanisms play the main role in the expansion of lines. In case if the profiles of these lines were expanded only by temperature, the width of the K line would be approximately 6.5 times narrower than the hydrogen line.

16 minutes after the flash phase, at 8^h33^m, the emissions in the spectral lines were divided into several discrete components corresponding to relative radial velocities up to 170 km/s. The narrow component of the emission has disappeared till this moment; it was not visible even in the H and K Ca II lines. At least 3 separate emission components are present in the lines under study. These emissions correspond to the heights of up to 20 Mm above the level of photosphere

A detailed study of the profiles of these lines was carried out in two ways: by the traditional method using an M Φ -4 microdensitometer and using an Epson Perfection V 550 scanner, which allows obtain two-dimensional scans of images recorded on transparent films or on photo-plates. In the first case, in order to convert the density into intensity, it is necessary to take into account the characteristic curve of the photographic material as well as the scattered light on the photographic plate. In the second case, it is necessary to take into account two characteristic curves, namely, the curve of the photo-emulsion and the curve of the scanner itself. Both curves are nonlinear and require preliminary determination by special methods. In order to do this, we used a step attenuator, for which transmittances are precisely known. As a result, we could compare the data obtained with the microdensitometer and the scanner, and it turned out that these data are very well consistent with each other.

For 8^h17^m, the photometric line profiles clearly show the presence of a discrete narrow component in the ‘violet’ wing of the observed profiles (Fig. 2). This is most clearly seen in the K Ca II line, where this effect can be traced for about 10 Mm in the direction of the entrance slit, i.e. by flare height.

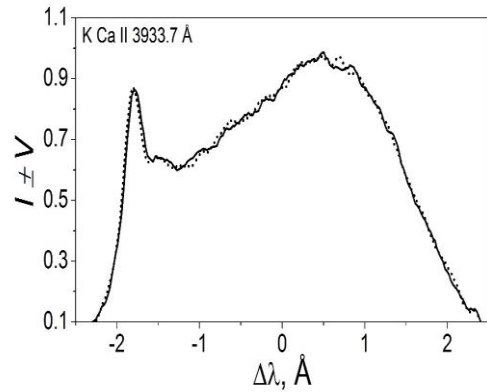


Figure 2: The $I \pm V$ profiles of the K Ca II line in the studied flare for 8^h17^m observed at a height of about 12 Mm above photosphere. One can see the presence of a narrow component in the ‘violet’ wing of the flare emission (at $\Delta\lambda \approx -1.8$ Å).

4. Magnetic fields

We used various methods to measure magnetic field in the flare. In particular, we estimated the longitudinal component to the line of sight, B_{LOS} , using weak-field approximation, when

$$V = (\partial I / \partial \lambda) \Delta \lambda_{\text{H}} \quad (1)$$

where V and I are Stokes parameters, $\partial I / \partial \lambda$ is Stokes I gradient in a spectral line, $\Delta \lambda_{\text{H}}$ is its Zeeman splitting. For example, for K Ca II 3933.7 Å line (which has effective Lande factors $g_{\text{eff}} = 1.167$)

$$B_{\text{LOS}} = B \cos \gamma = 1.186 \cdot 10^5 \times [V / (\partial I / \partial \lambda)], \quad (2)$$

where magnetic field strength B_{LOS} is expressed in gauss (G), and wavelength λ – in Å. In practice, we determined the Stokes V amplitude, V_{max} , and compared one with corresponding parameter of $(\partial I / \partial \lambda)_{\text{max}}$.

For flash phase of the flare, we measured magnetic field also by Zeeman splitting of the narrow component after extraction this component in the explicit form and its approximation by Gaussian. In this case, we fixed shift of the ‘center of gravity’ of these Gaussian in $I + V$ and $I - V$ spectra. For after-peak phase (8^h33^m), the Zeeman splitting was measured by wide profiles of lines. In order to reduce the noise-like fluctuations in wings of profiles, only those portions of the line profiles were taken into account that directly adjoined its apex and corresponding to the upper half of its maximum intensity.

It was found that for 8^h17^m magnetic field strengths in the flare were in range 1300-2900 G at altitudes of 10–15 Mm above the level of the photosphere. Magnetic fields of ‘kilogauss’ range (up to 3200 G) were found for some locations also in post-peak phase of the flare (8^h33^m). The typical errors of our measurements are, as rule, ± 150 G.

5. Temperatures and turbulent velocities

In order to determine the temperature T and the turbulent velocity ξ_{turb} in the flare, only narrow component of emission was analyzed (Figs. 1 and 2). For this purpose, it was necessary to extract this component in its pure form, without superposing on the wide component. In order to separate the narrow component from the wide one, we approximated the wide component by the most acceptable Gaussian profiles. Moreover, since we could not approximate the entire wide component with a Gaussian distribution, we chose the most suitable Gaussian profile only for those sections of the wide component that were directly adjacent to the narrow component. In fact, these were sections in the range from -3 to -1 Å in Fig. 2.

We found that shape of extracted narrow component was close to the Gaussian distribution. This circumstance, likely, means that approximation of the optically thin layer is suitable. In this case, we can determine the temperature T and the turbulent velocity ξ_{turb} using well-known simple formula:

$$\Delta\lambda_D = (\lambda_0/c) \times (2kT/m + \xi_{\text{turb}}^2)^{1/2}, \quad (3)$$

where $\Delta\lambda_D$ is Doppler widths, λ_0 is the unperturbed wavelength of the spectral line, c is the speed of light, k is the Boltzmann constant, m is the mass of the atom.

Results of comparison of ξ_{turb} vs. T are presented on Fig. 3. One can see well visible tendency to anti-correlation of these parameters.

This seems strange because, based on general considerations, we can expect that turbulent velocities should also increase with increasing temperature in the plasma. This leads us to suspect that the additional (compared to temperature) broadening of the line profiles is actually caused not by turbulent velocities, but by strong magnetic fields of mixed polarity.

The corresponding estimates of the magnetic field were made in assumption, that turbulent velocities should be the same for different temperatures. Likely, this leads us to some

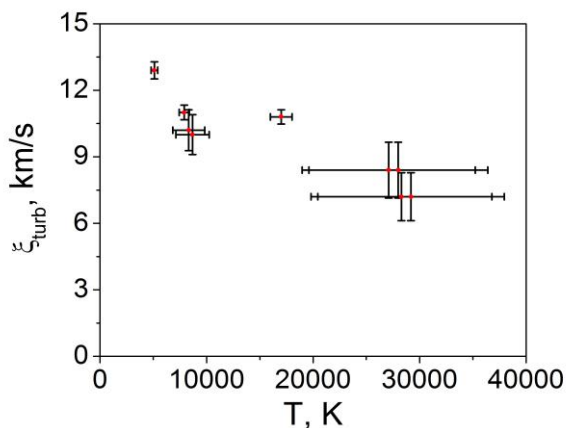


Figure 3: Comparison of temperatures and turbulent velocities in the explosive phase of the flare, found from the widths of the narrow component of the emission.

lower estimation of the mixed polarity magnetic fields. For this case we found $B = 8.3$ kG by the K Ca II line and $B = 6.7$ kG by the He I 4471.5 line. Considering that the He I line is clearly closer to the case of an optically thin layer, the closeness of these estimates is very encouraging. Our results are apparently the first indications of superstrong magnetic fields of 6-7 kG at an altitude of about 10 Mm in a solar flare.

6. Conclusion and Discussion

The main conclusion of our work is that in the limb solar flare of July 17, 1981, there were very strong magnetic fields up to about 3 kG in two moments: in its explosive phase and 16 min after it. Such magnetic fields were observed at altitudes of 10-18 Mm, i.e. in lower solar corona. It is important to note that true local magnetic fields in the flare could be even larger, since the obtained results represent a longitudinal component of the magnetic field assuming that the filling factor equals unity.

Another interesting feature of the flare is that very narrow emissions were observed in the K Ca II and He I lines against the background of broad emission typical of the explosive phase of the flare. If we consider these emissions to be optically thin, then we get an anti-correlation of temperatures and turbulent velocities. Physically, this is unlikely and may reflect the expansion of the line profiles not by turbulent velocities, but by very strong magnetic fields of mixed polarity. This assumption allows to obtain an estimation of the mixed polarity magnetic fields, namely, $B = 8.3$ kG by the K Ca II line and $B = 6.7$ kG by the He I 4471.5 line. It is also possible that in other flares the assumed turbulent expansion of the profiles is actually magnetic expansion. For example, a very local in height increase in turbulence in a powerful flare on October 28, 2003 (Lozitsky et al., 2017) could be caused, in fact, due to very strong 'entangled' magnetic fields.

Acknowledgements. This study was funded by the Taras Shevchenko National University of Kyiv, project No. 19БФ023-03.

References

- Byull. Solnech. Dannye Akad. Nauk USSR: 1981, No.7.
 Kirichek E.A., Solov'ev A.A., Lozitskaya N.I., Lozitskii V.G.: 2013, *Geomagn. & Aeronomy*, **53**, 831.
 Koval A.N.: 1977, *Bull. Crimean Astrophys. Obs.*, **57**, 133.
 Kuridze D., Mathioudakis M., Morgan H., Oliver R. et al.: 2019, *Astrophys. J.*, **874**, art. id. 126, 12 pp.
 Lozitsky V.G., Yakovkin I.I., Lozitska N.I.: 2020, *Journ. Phys. Studies*, **24**, No. 2, id.2901 (6p.).
 Lozitsky V.G.: 2016, *Adv. Space Res.*, **57**, 398.
 Lozitsky V.G., Baranovsky E.A., Lozitska N.I., Tarashchuk V.P.: 2017, *Journ. Phys. Studies*, **21**, No. 3, id 3902 (7 p.).

SOLAR SYSTEM

DOI: <http://dx.doi.org/10.18524/1810-4215.2020.33.216427>A NEW WIDE-FIELD TELESCOPE WITH
A MIRROR DIAMETER OF 600 MM FOR THE TELESCOPE
NETWORK OF THE ODESSA OBSERVATORYFashchevsky N.N.¹, Podlesnyak S.V.¹, Bondarenko Yu.N.¹,
Andrievsky S.M.¹, Romanyuk Ya.O.²¹ Astronomical Observatory of Odessa National University,
Odessa, Ukraine, *astronomical_observatory@onu.edu.ua*² Main Astronomical Observatory, Kiev, Ukraine

ABSTRACT. Optical scheme of the new wide-field telescope of the telescope network of Odessa Observatory is described. The telescope optical layout is designed as a mirror-lens system with a Ross-type two-lens corrector and a hyperbolic primary mirror with diameter of 600 mm. The prime focus corrector is capable of imaging a field of 2 degrees, the root-mean-square radius of the diffraction spot is about 4.5 μm , which is 2.5 times larger than that of the diffraction-limited spot (Airy disk).

Keywords: Astronomical instrumentation, methods and techniques

АНОТАЦІЯ. Після появи професійних оптичних CCD-матриць з високою чутливістю з'явилася можливість застосування телескопів з малим дзеркалом для вирішення широкого кола важливих наукових завдань. Використання телескопів з малим дзеркалом дозволяє не обмежувати кількість часу на спостереження. Крім того, невеликі телескопи незамінні для реалізації дослідницьких програм ближнього космосу (навколосемного, Сонячної системи). Такі інструменти використовуються для вивчення метеорів, астероїдів, комет, планет разом зі своїми супутниками, а також штучних об'єктів в космосі.

У цій роботі розглядаються перші етапи проектування телескопа з діаметром первинного дзеркала 600-мм, який має унікальний оптичний дизайн та широке поле зору. Оптичну схему телескопа розробив науковий співробітник Астрономічної обсерваторії Одеського національного університету Микола Фащевський у кінці своєї дуже плідної наукової та практичної діяльності, цю схему він назвав "Гіперболічний Росс". Ця оптична система дуже схожа на дволінзовий коректор, який був розроблений

Россом (1935) для параболічного первинного дзеркала 200-дюймового (5 м) телескопа Хейла обсерваторії Маунт Паломар.

У роботі наданий опис оптичної схеми нового телескопа з широким полем зору, який створюється для мережі телескопів Астрономічної обсерваторії Одеського національного університету. Оптична схема складається з дзеркально-лінзової комбінації з дволінзовим коректором Росса і гіперболічним дзеркалом, діаметр якого складає 600 мм. Коректор первинного фокусу дає змогу отримати поле зору до двох градусів. Середньоквадратичний радіус дифракційного кола розсіювання складає 4.5 мікрон, що у 2.5 рази більше, ніж дифракційна межа (диск Ері). Проектування та виробництво оптичної системи 600-мм телескопа вже завершено, і зараз закінчується побудова труби телескопа та модернізація астрономічного паралактичного штатива, який повинен нести вагу труби.

Ключові слова: Астрономічне приладобудування, методи і техніка

1. Introduction

Just a few decades ago astronomy with small telescopes seemed to be receding into the past. Such views stretched from a growing number of optical telescopes with mirrors of larger diameters, which had been built and put in operation in those days. However, it soon turned out that small telescopes managed to carve a niche for themselves in areas related to astronomy. It is mainly due to the fact that the operational time on large telescopes is quite costly, and it is allocated among numerous observation programmes with a wide range of objectives, which are usually focused on deep space exploration. Telescopes with small mirrors, by contrast, are often employed within the

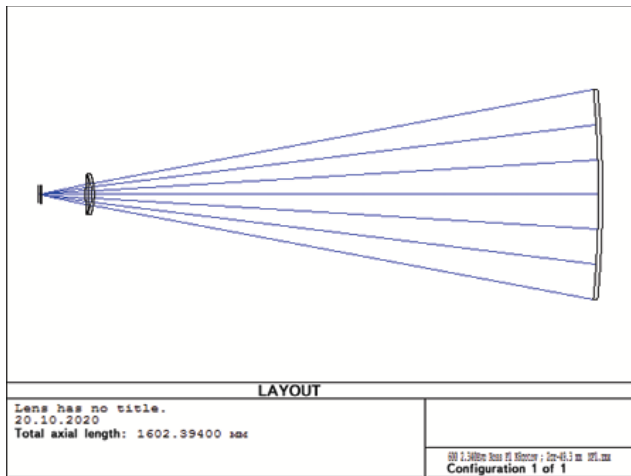


Figure 1: Original optical layout of the 600-mm telescope

scope of a particular programme, thus putting no limits on the amount of operating time for an individual observer. Besides, small telescopes are indispensable to the implementation of near-space (near-Earth, Solar System) research programmes. Such instruments are used to study meteors, asteroids, comets, planets along with their satellites, as well as man-made objects in space. One of the good examples related to the Odessa Observatory telescope network is OMT-800 (Andrievsky et al., 2013).

The optical layout of the telescope is designed as a mirror-lens system with a Ross-type two-lens corrector and a hyperbolic primary mirror (Figure 1).

The present paper discusses the first stages of the design and construction of a telescope with a 600-mm diameter primary mirror, unique optical design and a wide field of view.

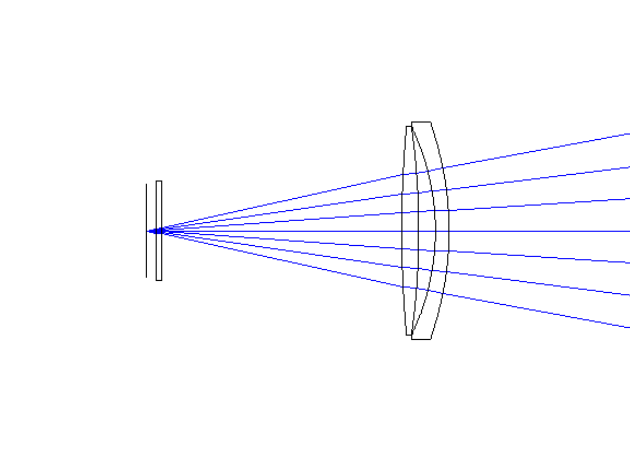


Figure 2: A Ross-type two-lens corrector of the telescope optical system

2. Optical layout of the 600-mm telescope

A research scientist of Astronomical Observatory of Odesa National University, Nikolay N. Fashchevsky, at the end of his fruitful scientific career and practical activities, performed complex computations of an original optical design for the telescope, which he named “Hyperbolic Ross” (Figure 2).

This optical system is very similar to the doublet lens corrector designed by Ross (1935) for the parabolic primary mirror on the 200-inch (5-m) Hale Telescope at the Mount Palomar observatory. However, the optical design developed by Fashchevsky has several distinguishing features. The original Ross corrector consists of two lenses made of optical glass of the same grade with zero optical power; it was designed specifically for correcting coma of mirrors exclusively (that is, as a coma-corrector). In our optical system, the corrector is comprised of different types of optical glass, namely F1 and K8, with low positive optical power of 0.8-dioptres. The primary mirror is a hyperboloid of high asphericity, which allows us to have a sufficient number of free parameters for practical correction of all five third-order aberrations. The result obtained is illustrated in the spot diagrams for images, presented in Figure 3.

As is seen from the spot diagrams above, the prime focus corrector is capable of imaging a field of 2 degrees, the root-mean-square radius of the diffraction spot is about $4.5 \mu\text{m}$, which is 2.5 times larger than that of the diffraction-limited spot (that is, the radius of the Airy disc). This is quite a good result for such a field of view.

Key characteristics of the computed optical design, along with some additional parameters, are listed in the table presented below in scheme (Figure 4).

Nikolay Fashchevsky made a report on the results obtained to the Scientific Council of the Astronomical Observatory of Odesa National University, and the Council made a decision approving optics manufacturing. The manufacturing process got underway. The primary mirror was polished and configured, getting it preliminary ready for operation. Regretfully, Nikolay Fashchevsky did not have time to proceed with all the works planned. The mirror was lying idle for several years. Under such circumstances, the Head of the Observatory, Sergey M. Andrievsky, came to a decision to resume the optical-system manufacturing activities.

To further the work, first of all, it was needed to design, construct and test a prototype of the optical system, in particular to manufacture a compensating spherical mirror of 400 mm in diameter and a set of alignment mirrors. We managed to accomplish all these works successfully. The test (reference) layout

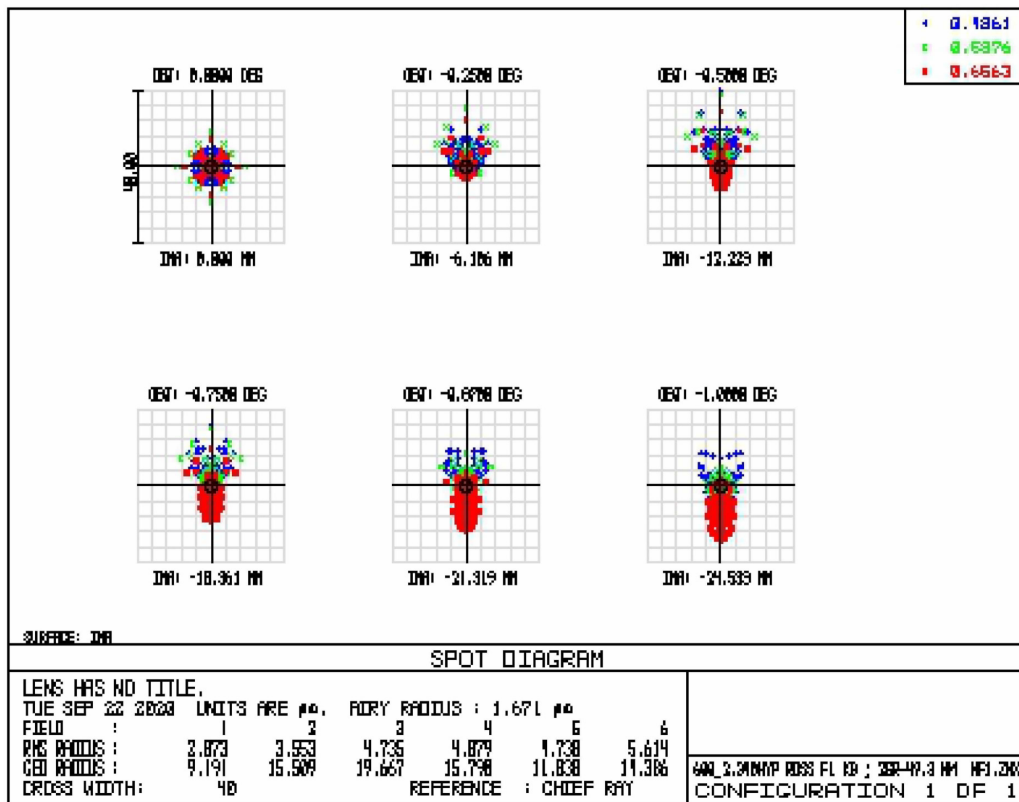


Figure 3: Resulting spot diagrams for images

Dapert. = 600 Fequiv. = 1365.79 1/Aequiv. = 2.28 1/2 field (deg.) = 1.00

Surf	Comment	Radius	Thickness	d Surf	Glass	Conic (e^2)	Semi-Diametr
OBJ	Object at infinity	Infinity	Infinity			0	
1	Primary mirror	3230.17	1442.34	0	MIRROR	1.576	300
2	Lens 1	170.76	7.1	1442.34	F1	0	57.529
3		126.5	8.8	1449.44		0	55.21
4	Lens 2	397.6	9	1458.24	K8	0	55.213
5		-600.12	124.488	1467.24		0	54.912
6	Protective glass	Infinity	3.2	1591.728	QUARTZ	0	26.207
7		Infinity	5.334	1594.928		0	25.725
IMA	Chip	Infinity	-	1600.262		0	24.542

Thickness 5 = 126.8
124.488

Glass Catalog GOST SCHOTT MISK

Wavelength (μm)	F1	K8	Quartz
0.48613	nF = 1.6246518934	1.5219510778	1.4631264824
0.58756	nd = 1.6129259062	1.5163676780	1.4584636856
0.65627	nC = 1.6080589841	1.5138911579	1.4563666190

Fpr. mirror = 1615.09 1/Apr. mirror = 2.69
Fequiv. = 1365.79 1/Aequiv. = 2.28
Field (mm)/ (1 deg.) = 49.041 DFfocal= 1600.262
mm/1' = 0.409 optical
mm/1" = 0.007 corr. power= 0.92506938
Airy disk = 0.0027

Figure 4: Optical system data

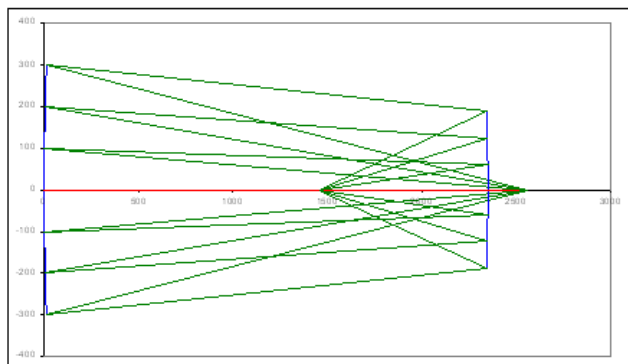


Figure 5: Test (reference) optical layout.



Figure 6: General view of the optical system prototype during test procedures.

of the primary mirror is depicted in Figure 5. It is a well-known Maksutov (1948) optical layout upgraded as suggested by Fashchevsky (2010). At the reference output point of the optical layout, an image is formed with a diffraction-spot radius of $8 \mu\text{m}$, which is close to the diffraction limit.

The optical system prototype was assembled and aligned in the immediate vicinity of the polishing machine in the optical workshop of the Astronomical Observatory of Odesa National University; it enabled us to test the surface quality not removing the mirror from the polishing machine frame (Figure 6).

Then, the mirror had to be polished to form the desired shape. In so doing, the main challenge was associated with too high asphericity of the primary mirror, which was almost beyond our abilities; in particular, the eccentricity square was to be 1.58, the deviation from the best-fitting sphere – $11.8 \mu\text{m}$, and the longitudinal spherical aberration – 25 mm . It was not feasible to attain the computed targets using classical methods and techniques. This is why, in order to solve



Figure 7: Two corrector lenses.

such an issue, we selected a special polishing resin and manufactured specific polishing pads. As a result, the primary mirror was polished to a shape that was very close to the computed one within the errors.

Meanwhile, the Ross-type corrector lenses were manufactured. The first corrector concave-convex lens, made of F1 optical glass, and the second double convex lens, made of K8 glass, were polished and centred to the desired radii and thicknesses. After polishing, the lenses were treated with diluted acetic acid as an anti-reflection coating. The finished corrector lenses are shown in Figure 7.

3. Conclusion

All activities related to the design and manufacturing of the optical system of the 600-mm telescope have been accomplished, and we are currently finishing constructing the telescope tube and modernising the astronomical parallactic tripod, which is to bear the tube's weight.

Acknowledgements. The authors are grateful to Ya.S. Yatskiv, L.E. Keir and O.Sh. Shakhrukhanov for help with the implementation of this project.

References

- Andrievsky S.M., Molotov I.E., Fashchevsky N.N., Podlesnyak S.V., Zhukov V.V., Kouprianov V.V., Kashuba S.G., Kashuba V.I., Mel'nichenko V.F., Gorbanev Yu.M., 2013, *Odessa Astron. Publ.*, **26**, 6.
 Fashchevsky N.N.: 2010, *Astronomicheskiye teleskopy i astronomicheskaya optika*, Odessa.
 Maksutov D.D.: 1948, *Izgotovleniye i issledovaniye astronomicheskoy optiki*, M.: Gostekhizdat.
 Ross F.E.: 1935, *Ap. J.*, **81**, 156.

DOI: <http://dx.doi.org/10.18524/1810-4215.2020.33.216430>

GROUPS OF METEORITE-PRODUCING METEORIODS AND METEORITES IN ASTEROIDAL ORBITS AND THEIR SOURCES

Yu. M. Gorbanev¹, N. A. Konovalova², N. Kh. Davruqov³¹ Astronomical Observatory of Odessa National University, Ukraine, skydust@ukr.net² Institute of Astrophysics of the Academy of Sciences of the Republic of Tajikistan, nakonovalova@mail.ru³ Institute of Astrophysics of the Academy of Sciences of the Republic of Tajikistan, naqqosh89@mail.ru

ABSTRACT. This paper presents the results of the analysis of possible existence of nine near-Earth meteorite-producing groups in asteroidal orbits, consisting of sporadic fireballs from the IAU MDC 2007 database, sporadic meteors from the SonotaCo database, meteorites – namely, L5, L6 and H4-H6 ordinary chondrites and an ureilite, for which atmospheric and orbital parameters are known from instrumental observations – and their plausible parent bodies, that is, near-Earth asteroids (NEAs). Orbits of the selected members of meteorite-producing groups were classified as asteroidal according to the Tisserand parameter $T_J > 3.1$.

In order to test the link between meteorite-producing groups in asteroidal orbits and their plausible parent bodies, we carried out an investigation into the possible existence of some known NEAs that move in similar orbits. Based on the orbital similarity, determined using the Drummond (D_D) and Southworth & Hawkins (D_{SH}) orbital similarity criteria, some associations between the identified NEAs, known meteorites in asteroidal orbits and small, as well as meteorite-dropping, meteoroids have been suggested. As a result, several meteorite-dropping sporadic fireballs and small meteors, whose orbits are currently similar to the orbits of known meteorites, have been detected and reckoned as possible members of the groups in asteroidal orbits; their plausible source regions have also been considered.

Keywords: meteorite-producing group – meteor – fireball – meteorite – ordinary chondrite – asteroid – Earth-crossing orbit.

АНОТАЦІЯ. У статті представлені результати аналізу існування в навколоземному просторі дев'яти метеоритоутворюючих груп на астероїдних орбітах, що включають спорадичні боліди з бази метеорних даних IAU MDC 2007, спорадичні метеори з бази даних SonotaCo і метеорити – звичайні хондрити типів L5, L6, H4-H6 і Ureilite, з відомими по інструментальним спостереженням атмосферними і орбітальними даними, та їх можливі батьківські тіла – навколоземні астероїди. Належність орбіт відібраних членів груп до астероїдного типу визначалася за значенням параметра Тіссерана $T_J > 3.1$.

Динамічний зв'язок членів виявлених метеоритоутворюючих груп з астероїдними орбітами і їх батьківських тіл NEAs перевірялася з використанням критеріїв близькості орбіт: D_D -критерію Друммонд і D_{SH} -критерію Саутворта і Хокінса.

В результаті кілька спорадичних метеоритоутворюючих болідів і малих метеорів, орбіти яких в даний час аналогічні астероїдним орбітам 9-ти відомих метеоритів, були знайдені в якості можливих членів метеоритоутворюючих груп, і були розглянуті їх можливі батьківські тіла – навколоземні астероїди. На підставі орбітальної подібності були виявлені асоціації між відібраними навколоземними астероїдами і 9-ма метеоритоутворюючими групами на астероїдних орбітах, що включають відомі метеорити, спорадичні боліди і малі метеори.

1. Introduction

The notion that meteoroid streams could originate from asteroids was suggested by Hoffmeister [1] and Fesenkov [2]. Halliday *et al.* [3], having analysed the fireball data from the Meteorite Observation and Recovery Project (MORP) and the Prairie Network, inferred the asteroidal origin of some fireball streams. The authors suggested existing of four possible meteorite-producing groups, among which group 1 included the Innisfree meteorite. Shestaka [4] examined a swarm of meteorite-producing bodies, which produced the Innisfree and Ridgedale fireballs, and found out that the investigated swarm was also related to nine small meteoric swarms, several asteroids and 12 fireballs. Greenberg & Chapman [5] reckoned meteorites might be pieces of large main-belt asteroids, derived primarily by cratering collisions rather than disruptive fragmentation of the parental body. Jopek & Williams [6] considered the possibility that a meteoroid stream of asteroidal origin could have formed through the ejection of fragments from an asteroid due to its collision with another body (an impact as the formation mechanism). In such a case, a portion of the fragmented parent body in the form of small particles and bigger fragments, such as cobbles and pebbles, survives as debris

in its orbit. The authors have suggested that a collision will only produce a meteoroid stream if it involves relatively large bodies, with the asteroid-impactor being of several tens of metres in diameter. The fragments of asteroid Vesta expelled in the collision with the impactor and subsequently found on Earth as meteorites – vestoids, can serve as an example of the formation of meteorites associated with impact events [7].

Spurny *et al.* [8] supposed the existence of a meteor stream, which might be produced by tidal disruption of a heterogeneous, rubble-pile asteroid. The evidences of high macroporosities in the interiors of some asteroids, for instance, (253) Mathilde, (1620) Geographos and (216) Kleopatra, as well as close-up images of the surface of asteroid (25143) Itokawa [9], suggest that a considerable portion of asteroids may have surface cracks (or fractures) and a rubble pile structure. Such aggregates are only held together by a relatively weak gravity and may eventually disrupt.

The fact that asteroids can indeed eject dust in such a manner (the so-called “dusty asteroids”) was proved by the LINEAR (the Lincoln Near-Earth Asteroid Research project) image of comet-like asteroid P/2010 A2 with a dust tail, formed in a collision between two asteroids that had occurred in February or March 2009 [10]. Williams [11] claimed that meteoroid streams, formed through the dust ejection from an asteroidal body, would contain far less mass and be far more diffuse than those of cometary origin. In that case, the spatial density of a meteoroid stream of asteroidal origin should be lower while its meteor activity should differ from the activity of major meteor streams of cometary origin.

As the problem of asteroid impact hazard to Earth’s biosphere has gained increasing attention in recent years, the international project “Asteroid & Comet Hazard” was launched. This project involves systematic monitoring of the sky, aimed primarily at detecting near-Earth asteroids, whose orbits are similar to Earth-crossing orbits of meteoroid streams, especially short-period ones, which are close to the ecliptic and may pose an impact hazard to Earth.

2. Methods for detecting groups of meteorites and fireballs in asteroidal orbits using meteor databases

Annual activity of 2,373 bright shower and sporadic fireballs, observed from across Canada and documented in the Millman Fireball Archive, was studied in [12]. From the resulting solar-longitude distribution of the cumulative number of fireballs, representing an annual fireball activity profile, the peaks in the activity of fireballs from known meteor showers were identified. The peaks in the activity profile of fireballs from four meteorite-producing groups, which could be related to meteor streams of asteroidal origin, were identified as well. In the paper [13], the authors analysed data on the time of observation of superfireballs and meteorite falls in Spain, based on the reports in newspapers collected for the period covering the last 150 years. The analysis revealed statistically significant peaks corresponding to stronger fireball activity for some periods of the year, which was not associated with known meteor streams.

The study [14] yielded histograms of the annual activity of sporadic bright fireballs, meteors and

meteorites, which were constructed on the basis of data adopted from two meteor databases [15, 16]. Six major (Maj) and two minor (Min) peaks in the activity of the investigated bodies, which were not connected with the dates of peak activity of known meteor showers, were identified from the plotted histograms.

All data on the detected periods of the observed activity of sporadic fireballs, meteors and meteorites laid the groundwork for addressing the issue of clustering the data on near-Earth sporadic meteorite-producing meteoroids. Data on atmospheric paths, radiant and heliocentric orbits for 24 known meteorites, instrumentally observed in different years, have been published in scientific journals to date. Of these 24 Earth-crossing orbits for known meteorites, four orbits of CI and CM carbonaceous chondrites and six orbits of L3.5 and H5 ordinary chondrites are Jupiter-family comet-like orbits, while 14 orbits of L5, L6, H4-H6 chondrites and an ureilite are recognised as asteroidal.

A search for fireballs and meteors with orbits similar to Earth-crossing asteroidal orbits of 14 known meteorites was carried out in two meteor databases. We used the following method for detecting groups of meteorites and fireballs in asteroidal orbits: the data on a known meteorite – in particular, its orbital elements, radiant coordinates and date of observation – were employed as a reference for the search of members of the relevant meteorite-producing meteoroid group. The selection of meteorite-producing meteoroids as members of a specific group was performed by comparing respective data of the meteorite and potential members of the group; in so doing, meteoroids in orbits proven to be similar by the specified orbital similarity criteria were only selected. The search among 14 known meteorites in Earth-crossing asteroidal orbits yielded groups of meteorite-producing meteoroids linked to nine of the known meteorites, namely Innisfree, Novato, Villalbeto de la Peña, Lost City, Križevci, St. Robert, Grimsby and Almahata Sitta.

3. Groups of meteorite-producing meteoroids in asteroidal orbits and their plausible parent bodies

In the present study, we investigated the possibility of the existence of near-Earth meteorite-producing groups in asteroidal orbits, consisting of sporadic meteoroids, meteorite-dropping fireballs and instrumentally observed meteorites. The selection of members of the groups was carried out as follows: sporadic meteorite-dropping fireballs, which could survive the flight through Earth’s atmosphere with a non-zero terminal mass, were selected from the IAU MDC 2007 database [15], and sporadic meteors – from the SonotaCo database [16]. As a group-membership criterion to be met for the selection of meteorite-producing sporadic fireballs, meteoroids and meteorites, we used the similarity of orbits of a group’s members to the orbit of a known, instrumentally observed meteorite that fell within the time span of the observed occurrence of fireballs from the group and that was taken as a reference for the search of potential group members.

The similarity between the orbits was established applying two known criteria, used as a quantitative measure of the distance between the orbits, namely the

Southworth-Hawkins D_{SH} criterion [17] and the Drummond D_D criterion [18]. The following limit values of the orbital similarity criteria were used for selecting into the groups: $D_D \leq 0.15$ and $D_{SH} \leq 0.3$. Orbits of the selected fireballs, meteors and instrumentally observed meteorites were recognised as asteroidal according to the Tisserand parameter $TJ > 3.1$.

The search, based on the orbital similarity, duration of observations (1.5-2 months) and radiant positions ($\Delta\alpha_R < 15^\circ$), ($\Delta\delta_R < 30^\circ$) of meteorite-producing meteoroids and meteors, selected from the meteor databases, resulted in the detection of associated groups of meteorite-producing meteoroids for 9 of 14 meteorites of asteroidal origin with observationally known atmospheric and orbital parameters. Details about nine detected meteorite-producing groups are listed in the Table below, providing the following data for each of the groups: a meteorite's name; year, month and date of observations; radiant co-ordinates – the right ascension (α_R) and declination (δ_R); the entry (pre-atmospheric) velocity (V_∞); orbital elements, including the perihelion (q), semi-major axis (a), orbital eccentricity (e) and inclination (i), the argument of perihelion (ω), the longitude of the ascending node Ω ; the orbital similarity criteria D_D and D_{SH} , and also parameters of the respective mean orbit, for which the number of meteorite-producing meteoroids that are members of the group is included in round brackets.

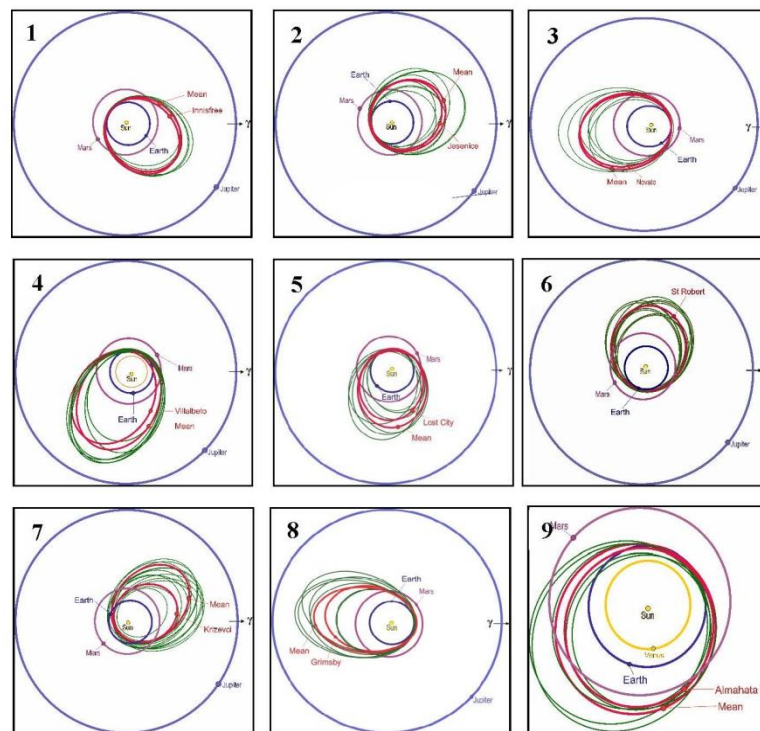
Orbits of nine meteorite-producing groups are illustrated in Figures 1; in particular, each figure depicts a meteorite's instrumentally determined orbit, the mean orbit of the respective group and also orbits of the group members, that is, meteorite-dropping fireballs in asteroidal orbits.

4. Conclusions

In the present study, the search among objects, selected from the IAU MDC 2007 and the SonataCo Network databases by the orbital similarity criteria, duration of the observed activity and radiant co-ordinates, has yielded nine meteorite-producing groups of sporadic fireballs and meteors in asteroidal orbits, which include nine known, instrumentally observed meteorites – namely, L5, L6, H4-H6 ordinary chondrites and an ureilite. The analysis of the search in the meteor databases for plausible meteorite-producing groups for four meteorites, namely the Peekskill, Morávka, Bunburra Rockhole and Buzzard Coulee meteorites, with instrumentally determined atmospheric paths and orbital parameters has not shown any results with regard to meteorite-producing groups found for these meteorites in the available meteor and fireball databases.

Table 1: The detected groups of meteorites and meteorite-dropping fireballs with similar orbits (at epoch 2000.0).

Name	Year	M	D	α_R	δ_R	V_∞	q	a	e	i	ω	Ω	D_D	D_{SH}
The Innisfree (L5) meteorite group														
Mean (14)	-	02	09	41.0	54.0	13.7	0.990	1.868	0.470	8.0	185.0	319.0	0.00	0.00
Innisfree	1977	02	06	6.7	66.2	14.5	0.990	1.868	0.470	12.0	178.0	317.0	0.03	0.10
The Jesenice (L6) meteorite group														
Mean (11)	-	04	01	139.5	51.8	13.9	0.977	1.838	0.456	8.4	192.7	21.8	0.00	0.00
Jesenice	2009	04	09	159.9	58.7	13.8	0.996	1.750	0.431	9.6	190.5	19.2	0.03	0.05
The Novato meteorite group														
Mean (12)	-	10	01	289.8	-26.1	13.8	0.982	2.132	0.534	2.7	314.6	21.4	0.00	0.00
Novato	2012	10	18	268.1	-48.9	13.7	0.988	2.090	0.526	5.5	347.4	24.9	0.11	0.33
The Villalbeto de la Peña (L6) meteorite group														
Mean (7)	-	12	27	321.1	4.2	15.9	0.921	2.379	0.607	5.3	142.3	278.1	0.00	0.00
Villalbeto	2004	01	04	311.4	-18.0	16.9	0.860	2.300	0.630	0.0	132.3	283.7	0.05	0.12
The Lost City (H5) meteorite group														
Mean (10)	-	01	01	249.9	26.0	14.1	0.956	1.802	0.464	7.1	165.2	285.8	0.00	0.00
Lost City	1970	01	04	315.0	39.1	14.2	0.967	1.660	0.417	12.0	161.0	283.8	0.06	0.11
The Križevci (H6) meteorite group														
Mean (19)	-	02	21	137.0	17.8	18.9	0.783	2.075	0.614	3.4	242.2	328.6	0.00	0.00
Križevci	2011	02	04	131.2	19.5	18.2	0.740	1.544	0.521	0.6	254.4	315.6	0.09	0.11
The St. Robert meteorite group														
Mean (16)	-	06	02	187.9	12.0	13.3	0.994	2.085	0.517	4.2	191.5	71.6	0.00	0.00
St. Robert	1994	06	15	176.0	6.0	13.0	1.016	1.900	0.480	0.7	179.0	83.7	0.04	0.08
The Grimsby (H4-6) meteorite group														
Mean (8)	-	09	17	251.9	49.8	19.4	0.997	2.290	0.554	24.4	171.5	175.7	0.00	0.00
Grimsby	2009	09	26	242.6	55.0	20.9	0.982	2.040	0.518	28.1	159.9	182.9	0.05	0.10
The Almahata Sitta (Ureilite) meteorite group														
Mean (7)	-	09	23	339.5	13.9	14.4	0.888	1.413	0.312	6.1	235.4	187.4	0.00	0.00
AhS	2008	10	07	348.1	7.6	12.4	0.900	1.308	0.312	2.5	234.4	194.1	0.02	0.07



Figures 1: Nine groups of meteorites and meteorite-dropping fireballs in asteroidal Earth-crossing orbits.

According to one of possible scenarios, the similarity of orbits of the group members, that is, members of a genetically associated group, could have formed through the disruptive fragmentation of the parent body (NEA) and thus become a group of genetically related members. Porubčan et al. [19] pointed out that they only included as real genetically related pairs of meteoroids and plausible parent NEAs those for which the orbital evolution was proven to be similar over 5,000 years. In an alternative scenario, such a relationship between meteoroids within a certain group could have formed randomly. Both scenarios do not rule out possible existence of meteorite-producing meteoroids related to the investigated groups.

The feasibility of identifying a plausible parent body related to a specific group and determining the age of the group of genetically associated meteoroids is crucial for establishing relationships between groups of meteorite-producing meteoroids and their parents, that is, comets or asteroids, and also for studying mechanisms of formation of the investigated meteorite groups.

Within the framework of the project addressing the problem of asteroid impact hazard to the environment and Earth's biosphere in particular, it is essential to systematically monitor the sky at the radiant points specified for meteorite-producing groups during periods of their activity. Ultimately, it is extremely important to detect potentially hazardous meteorite-producing meteoroids in near-Earth space well before they enter Earth's atmosphere.

References

- Hoffmeister C.: 1937, *Astronomische Nachrichten*, **262**, Is. 3, 45.
- Fesekov V.G.: 1958, *Astron. zhurnal*, **35**, № 3, 327.
- Halliday I. Blackwell A.T., Griffin A.A.: 1990, *Meteoritics*, **25**, 93.
- Shestaka I.S.: 1994, *Astronom. Vestnik*, **28**, No. 6, 94.
- Greenberg R., Chapman C.R.: 1984, *Icarus*, **57**, Is. 2, 267.
- Jopek T.J.; Williams I.P.: 2013, *MNRAS*, **430**, Is.3, 2377.
- Pieters C. M., Binzel R. P., Bogard D., Hiroi T., Mittlefehldt D. W., Nyquist L., Rivkin A., Takeda H.: 2006, *IAUS*, **229**, 273.
- Spurny P., Olberst J., Heinlein D.: 2003, *Nature*, **423**, 151.
- Miyamoto H., Nakamura A. M., Nakamura R., Sasaki S. and Uesugi K.: 2006, *Science*, **312**, 1330.
- Jewitt D.: 2012, *AJ*, **143** (3), 66J, 14.
- Williams I. P. & Wu Z. 1993, *MNRAS*, **262**, 231.
- Beech M.: 2006, *Journal of WGN IMO*, **34**, 104.
- Zamora S., Ocana F., Sanchez de Miguell A. and Mole M.: 2015, in *Proc. of the International Meteor Conference, Mistelbach, Austria, 27-30 August 2015* /Eds.: Rault, J.-L.; Roggemans, P., International Meteor Organization, 187.
- Konovalova N.A., Gorbanev Yu.M., Davruqov N.Kh.: 2018, *Odessa Astron. Publ.*, **31**, 174.
- <http://www.astro.sk/~ne/IAUMDC/Ph2007/database.html>
- SonotaCo database. <http://sonotaco.jp/doc/SNM/index.html>
- Southworth R.B., Hawkins G.S.: 1963, *Smiths. Contrib. Astrophys.*, **7**, 261.
- Drummond J.D.: 1981, *Icarus*, **45**, 545.
- Porubčan V., Kornos L., Williams I.P.: 2004, *Earth, Moon, Planets*, **95**, 697.

DOI:<http://dx.doi.org/10.18524/1810-4215.2020.33.216432>

SPECIFIC FEATURES OF STRUCTURES IN THE INNER COMA OF COMET C/2017 T2 (PANSTARRS) AS OBSERVED WITH THE OMT-800 TELESCOPE OF THE ODESSA OBSERVATORY TELESCOPE NETWORK

V.V. Kleshchonok¹, S.G. Kashuba², S.M. Andrievsky², Yu.M. Gorbanev²¹ Astronomical Observatory, Taras Shevchenko National University of Kyiv, Kyiv, Ukraine, klev@observ.univ.kiev.ua² Astronomical Observatory of Odessa National University, Odessa, Ukraine, vladimir.kashuba@gmail.com, andrievskii@ukr.net, skydust@ukr.net

ABSTRACT. Observations of the comet were carried out using the OMT-800 telescope (the primary mirror diameter $D = 80$ cm; the focal length $F = 214$ cm) of the Odessa Observatory telescope network from January to June 2020. Image processing was performed through standard methods using subtraction of dark and flat field frames. The resulting frames were employed to analyse the morphology of the cometary inner coma using digital filters. Isophotes of the coma and images of its structures appearing as fans and jets were obtained. The presence of a strong fan, which distorts the coma's standard appearance and makes it elongated perpendicularly to the Sun-comet line, is observed over the period from January to April. Later on, a weak jet that hardly affects the coma's standard shape appears to replace the fan. The jet reaches its peak intensity near perihelion and then gets fainter rapidly. Such behaviour of the coma structures is indicative of the presence of two active areas on the cometary nucleus surface, for which the matter outflow is governed by the Sun illumination conditions. One of these areas, being more active, is responsible for the appearance of a strong fan. The other area, which is far less active, generates a jet that manifests itself near perihelion. The peak dust production of the comet 120–150 days before perihelion is due to the presence of an active fan in the inner coma.

Keywords: Comets: individual: C/2017 T2.

АНОТАЦІЯ. Особливості структур внутрішньої коми комети C/2017 T2 (PANSTARRS) за спостереженнями на телескопі OMT-800 мережі телескопів одеської обсерваторії. Спостереження комети проводились на телескопі OMT-800 ($D=80$ см, $F=214$ см) мережі телескопів одеської обсерваторії протягом січень–червень 2020 р. Обробка зображень проводилася стандартним способом з врахуванням темнових кадрів та

кадрів плоского поля. Отримані таким чином кадри використовувалися для аналізу морфології внутрішньої коми комети з використанням цифрових фільтрів. Були отримані ізофоти коми та зображення структур у вигляді фенів і джетів. Було відмічено існування потужного фену в період січень – квітень, який спотворює стандартний вигляд коми і робить її витягнутою перпендикулярно напрямку Сонце комета. Пізніше на зміну фену з'являється слабкий джет, який майже не впливає на стандартний вигляд коми. Він досягає максимальної інтенсивності близько перигелію, а потім швидко слабшає. Така поведінка структур свідчить про наявність двох активних ділянок на поверхні ядра комети, режим витоку речовини яких регулюється умовами освітленості Сонцем. Одна більш активна ділянка відповідає за появу потужного фену. Друга значно менш активна породжує джет, який проявляє біля перигелію. Наявність активного фену пояснюється максимумом пилопродуктивності комети за 120–150 днів до перигелію.

Ключові слова: Комети: індивідуальні: C/2017 T2.

1. Introduction

Comet C/2017 T2 (PANSTARRS) was discovered on 2 October 2017 at a distance of 9.2 au from the Sun using a 1.8-metre (60-inch) diameter telescope in Hawaii (<http://www.ifa.hawaii.edu/info/press-releases/PS1/>). C/2017 T2 (PANSTARRS) is a long-period near-parabolic comet. It passed through perihelion at a heliocentric distance of 1.615 au on 4 May 2020. Most of the comet's observations have been conducted earlier in 2020 when the comet reached its peak brightness; hence, there have been almost no results of studies of this comet published so far.

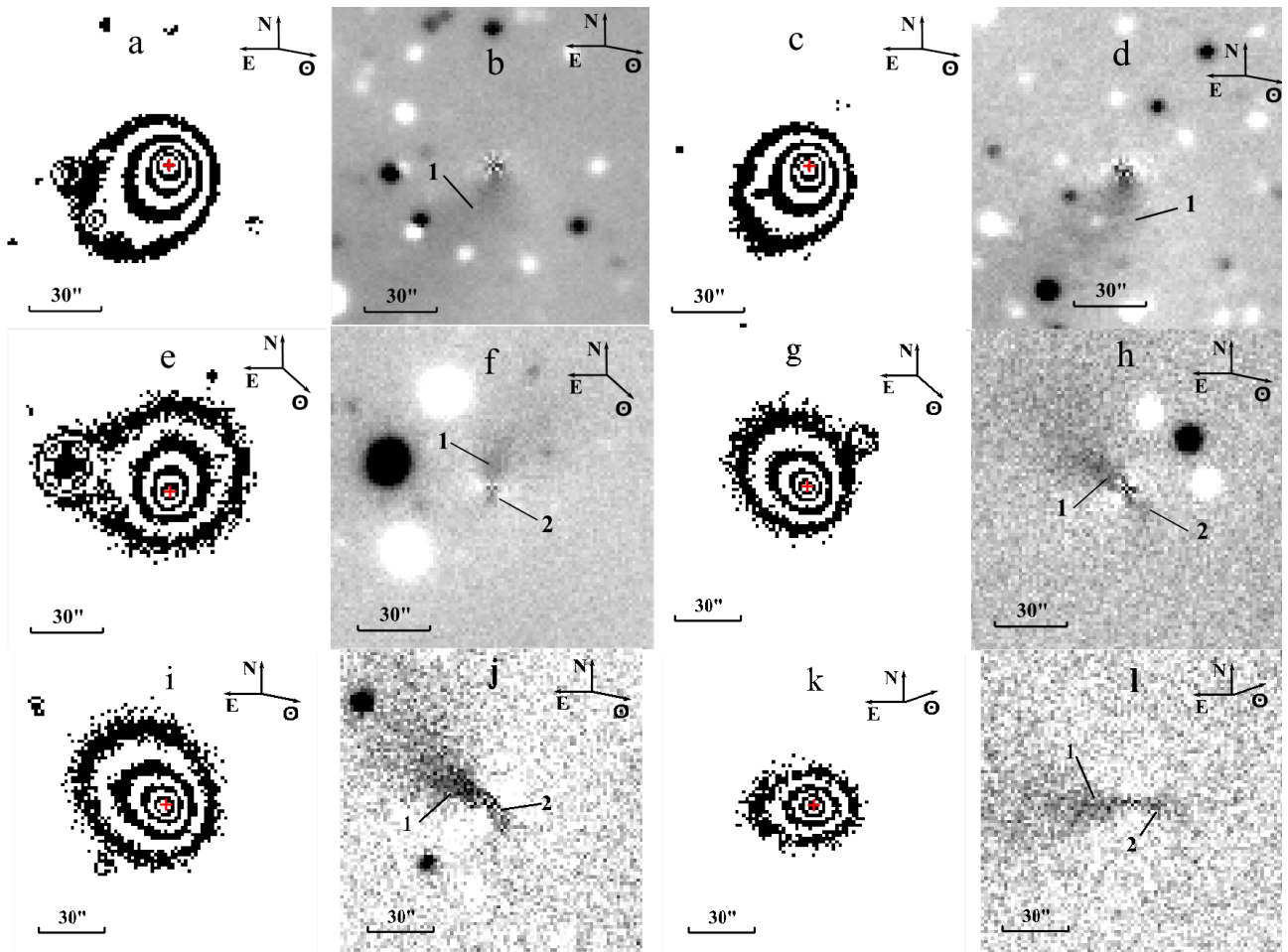


Figure 1: Digitally processed images of comet C/2017 T2 (PANSTARRS) obtained with the OMT-800 telescope. Figures 1a, 1c, 1e, 1g, 1i and 1k illustrate isophote lines superimposed on the processed images. Figures 1b, 1d, 1f, 1h, 1j and 1l depict the images digitally enhanced using the rotational gradient filter (negative). Figures 1a and 1b present images obtained on 24 January 2020; 1c and 1d – 25 January 2020; 1e and 1f – 23 April 2020; 1g and 1h – 10 May 2020; 1i and 1j – 13 May 2020; 1k and 1l – 08 June 2020. Arrows indicate the direction to the Sun (S), North (N) or East (E).

C/2017 T2 is an inactive comet. Even though the comet is dynamically new and it passed fairly close to the Sun, it remains relatively faint. It apparently suggests a small size of the comet nucleus of 10–15 km. According to the CARA (Cometary Archive for Afrho; <http://cara.uai.it>) data, comet C/2017 T2 exhibits unusual behaviour with respect to dust activity. The comet's dust production ($Af\rho$) reached its maximum 150–120 days before perihelion (in December 2019 – January 2020). Moreover, there was a secondary peak 50 days before perihelion (in March 2020). After the perihelion passage, a noticeable and regular decrease in dust production has been observed. The present paper explains such behaviour of the comet through analysis of morphological changes in the inner coma.

2. Observations and analysis

Observations of the comet were carried out using the OMT-800 telescope (the primary mirror diameter $D = 80$ cm; the focal length $F = 214$ cm) at Mayaki observing station of Astronomical Observatory of Odesa National University (Andrievsky et al., 2013). The observational data are listed in Table 1, which presents the date of observation, the heliocentric distance – r , the geocentric distance – δ , the phase angle – α , respective magnitudes of the comet, as well as exposures used to capture the comet in the frame and number of frames with a given exposure.

Preliminary processing of the obtained frames was performed using standard methods. A master dark frame was created from a set of 9–15 dark frames with an exposure equal to that for light frames using median

Table 1: Log of the observations of comet C/2017 T2 (PANSTARRS)

#	Date	r (au)	δ (au)	α (deg)	mag*	T_{exp} (sec)	N
1	24 Jan 2020	2.096	1.593	26.7	9.6	16,60	12,45
2	25 Jan 2020	2.087	1.599	27.0	9.4	60	48
3	23 Apr 2020	1.622	1.723	34.8	9.0	16	40
4	10 May 2020	1.617	1.680	35.6	8.6	16	103
5	13 May 2020	1.619	1.674	35.7	8.4	16	253
6	08 Jun 2020	1.682	1.681	35.2	9.0	16	32

*Adopted from <https://cobs.si>

Table 2: Structures in the inner coma of comet C/2017 T2 (PANSTARRS)

#	Date	Structure 1			Structure 2		
		φ (deg)	ω (deg)	ρ (104 km)	φ (deg)	ω (deg)	ρ (104 km)
1	24 Jan 2020	170	77	3.9	-	-	-
2	25 Jan 2020	169	72	3.2	-	-	-
3	23 Apr 2020	2	45	2.3	176	32	0.7
4	10 May 2020	53	33	5.8	209	27	1.3
5	13 May 2020	65	30	6.0	214	33	1.5
6	08 Jun 2020	100	34	5.2	237	41	1.3

filtering technique. A master flat frame was created in a similar way. The master dark was subtracted from each light frame with subsequent division of the resulting frame by the master flat. All images were digitally processed to amplify and extract specific structural features of the inner coma. The coma isophotes were plotted for different observation dates. The isophotes were drawn so that their intensity was decreasing by a factor of $\sqrt{2}$ when shifting towards the coma edges. Images of the comet were also digitally enhanced employing the rotational gradient filter (Larson & Sekanina 1984). The results are shown in Figure 1.

The isophotes indicate a significant asymmetry of the inner coma. In January, the coma is elongated southwards and almost perpendicular to the Sun's direction. In April, the coma is elongated southward, which is also greatly different from usual anti-solar direction. At later observation dates, the coma is elongated in anti-solar direction due to the contribution of the cometary tail to the total brightness of the coma. Fans and jets can be seen in the images processed using the rotational gradient filter. Such structures were also highlighted in the study by Manzini et al. (2020). A wide and contrast fan-shaped structure can be seen in the images taken in January. Two oppositely directed jets with substantially different intensities and extensions can be observed in the images obtained in April. Observations in May and June 2020 show two structures: a flat (low contrast) structure (b) is a low intensity jet; a more prominent structure (a) in anti-solar direction is the cometary tail that has not manifested itself in earlier observations. Parameters of the jets are given in Table 2, which presents the observation date, the position angle $-\varphi$, the cone angle (width) $-\omega$ and the extension of the jet $-\rho$.

3. Interpretation and discussion of the results

The appearance of comet C/2017 T2 depends significantly on the presence and activity of jet structures. A strong fan-shaped structure can be observed in images taken in January (Figure 1b and 1d); this fan forms the comet into a peculiar shape, which is elongated almost perpendicularly to the Sun's direction (Figure 1a and 1c). When approaching the perihelion, the fan gets fainter, and the second very weak jet appears (Figure 1f), which results in decreasing compression ratio of the coma (Figure 1e). Observations in May and June show a weak jet (jet 2 in Figure 1h, 1j and 1l) that has reached its peak activity shortly after passing the perihelion and then became weaker. Structural feature 1 in the same images practically coincides with the anti-solar direction and has a noticeable extension, which suggests that in this case we observe the cometary tail. Such behaviour of structures in the inner coma, as well as changes in its shape and dust production rate around perihelion, is very similar to the behaviour of well-studied comet 2P/Encke (Sekanina, 1979; Rosenbush et al., 2020). There are two active areas in the nucleus of comet 2P/Encke that have been existing for a sufficiently long period of time. Due to the location of these active sites in the nucleus of comet 2P/Encke, as well as orientation of the rotation axis of the cometary nucleus, it turns out that one active area is illuminated for the greater part of the comet's rotation period, except for a very short period of time near perihelion. However, depending on the mutual position of the comet and Earth, this active area can produce either a wide fan-shaped structure or narrower jets. When such a wide fan is observed in the cometary coma, the coma is elongated in the direction

not coinciding with the anti-solar direction. During this time, the yield by this active area contributes markedly to the emission of matter by the remaining part of the nucleus. The presence of such an active area in the nucleus of comet 2P/Encke also results in a shift in the peak brightness with respect to the time of perihelion passage. The second active area in comet 2P/Encke is far less productive, being illuminated by the Sun just for a short period of time when the comet is near perihelion. Similar behaviour of these two comets allows us to suggest a similar explanation of such behaviour, in particular, by the presence of two active areas with different production rates in the cometary nucleus. Engaging additional observations of comet C/2017 T2 will enable us to determine the orientation of its rotation axis and location of active areas on the nucleus of this comet.

4. Conclusions

Peculiarities of changes in the shape of coma and behaviour of its specific structural features are indicative of the presence of two active areas in the nucleus of comet C/2017 T2. The presence of an active high-productive area in the nucleus of comet C/2017 T2 enables us to explain specific features of dust activity of the comet, in particular, reaching the maximum dust production 120–150 days before the perihelion passage.

Acknowledgements. The research of V. Kleshchonok was supported in part by the 16BF023-02 project of the Taras Shevchenko National University of Kyiv.

References

- Andrievsky S.M. et al.: 2013, *Odessa Astron. Publ.*, **26**, 6.
Larson S.M. et al: 1984, *A.J.*, **89**, 571.
Manzini F. et al.: 2020, *The Astronomer's Telegram.*, No **13698**.
Rosenbush V. et al.: 2020, *Icarus.*, **348**, id. 113767.
Sekanina Z.: 1979, *Icarus.*, **37**, 420.

DOI:<http://dx.doi.org/10.18524/1810-4215.2020.33.217120>

CENTENARY OF THE BIRTH OF THE FAMOUS UKRAINIAN RESEARCHER OF RADIOMETEORS PROF. B.L.KASHCHEYEV (1920-2004), HIS HERITAGE AND TRAJECTORY MEASUREMENTS TODAY

S.V. Kolomiyets, K.A. Kolomiets, I.Yu. Kyrychenko, Yu.D. Prymachov

Kharkiv National University of Radio Electronics
14 Nauky ave., Kharkiv, Ukraine, svitlana.kolomiyets@nure.ua

ABSTRACT. The development of meteor radar research was stimulated during World War II by air defense requests to rule out false alarms of radars on meteoroid intrusions. After the war, many air defense radars were involved in scientific observations of meteors. An additional stimulus for interest in the study of radiometeors was the phenomenon of the Draconid meteor shower in 1946, which was recorded by the radio method as extraordinary. We can talk about the scientific and technological revolution of this period, associated with the use and boom in the development of radio technology and missile technology. The ballistics of the movement of airborne objects in the Earth's atmosphere (and outside the atmosphere since 1957) of artificial and natural origin is becoming increasingly complex. Radio technology could not have developed without knowledge of the ionosphere and the effects of the Sun on radio communications, along with the effects of the Sun on the ionosphere. In the ionosphere, a layer at altitudes of 70-130 km is called the meteor zone, i.e. the zone where cosmic bodies, burning in the Earth's atmosphere, cause the appearance of ionized meteor tracks, which interact with radar radiation and reflect it. This allows the radar receiver to record the reflected signal. In the presence of three receivers spaced 3-5 km apart (and located approximately at the vertices of a right triangle), it is possible to determine the guiding cosines of the trajectory of the meteoroid in the Earth's atmosphere. Continuing the trajectory of the meteoroid to the intersection with the celestial sphere at infinity, we obtain a point called the meteor radiant. In basic optical meteor observations, the trajectory is determined differently than in the radio method. The article highlights the significance of the event of the centenary of the birth of the famous Ukrainian researcher of radiometeors Prof. Kashcheyev B.L. (1920-2004) and its legacy, as well as the problems and solutions of trajectory measurements today.

Keywords: meteors, ionosphere, trajectory measurements, meteor radar, Kashcheyev heritage.

АНОТАЦІЯ. Розвиток метеорних радіолокаційних досліджень було стимульовано під час другої світової війни запитами протиповітряної оборони на виключення хибних спрацьовувань радарів на метеороїдні вторгнення. Після закінчення війни багато радарів протиповітряної оборони були залучені до наукових спостережень за метеорами. Додатковим стимулом інтересу до дослідження радіометеорів стало явище метеорного доща Драконід в 1946 році, яке саме було зафіксоване радіометодом як надзвичайне. Можна казати про науково-технічну революцію цього періоду, пов'язану з застосуванням та бумом розвитку радіо технологій та ракетних технологій. Балістика руху повітряних об'єктів в атмосфері Землі (і за межами атмосфери з 1957) штучного та природного походження стає пов'язаною зі все більш складними задачами. Радіотехнології не могли розвиватися без знань про іоносферу і про вплив Сонця на радіо зв'язок разом з наслідками сонячного впливу на іоносферу. В іоносфері виділяється прошарок на висотах 70-130 км під назвою метеорна зона, тобто зона, де космічні тіла, згоряючи в Земній атмосфері викликають появу іонізованих метеорних слідів, які взаємодіють з падаючим на них випромінюванням радіолокаторів та віддзеркалюють його. Це дає змогу зафіксувати відбитий сигнал приймачем радіолокатора. При наявності трьох приймачів, рознесених у просторі на 3-5 км (та розташованих приблизно у вершинах прямокутного трикутника) можна визначити направляючі косинуси траєкторії руху метеороїда в атмосфері Землі. Продовжуючи траєкторію руху метеороїда до перетину з небесною сферою на нескінченності ми отримуємо точку, яка зветься метеорним радіантом. При базисних оптичних метеорних спостереженнях визначення траєкторії проводиться інакше, чим при радіометоді. Стаття висвітлює значення події сторіччя від дня народження відомого українського дослідника радіометеорів проф. Кашчєєва Б.Л. (1920-2004) та його спадщини, а також проблеми і рішення траєкторних вимірювань сьогодні.

Ключові слова: метеори, іоносфера, траекторні вимірювання, метеорний радар, спадщина Кащеева.

1. Introduction. Researcher B.L. Kashcheyev

Science of the XXI century, in particular, related to the study of meteors, has its own special history with a powerful layer of the Ukrainian scientific and technical heritage of the XX century in this area. An important milestone in this history is 1957 and the associated program of the International Geophysical Year (IGY-1957) and the fifth section of this program "Ionosphere. Meteors" (Hocking & Kolomiyets, 2020; Kolomiyets et al., 2016; Tsesevich, 1957). In this section, the best world-level results in meteor radar studies were obtained by the Kharkiv scientific group of meteor researchers headed by B.L. Kashcheyev and with his direct participation (Lebedev & Sollogub, 1960). The significant contribution of B.L. Kashcheyev to the IGY-1957 program was awarded a certificate and badge "Gold IGY-1957" in connection with the fiftieth anniversary of the IGY 1957 program in 2007 (Kolomiyets et al., 2016). Kashcheyev B.L. (1920-2004) – a famous Ukrainian scientist, Honored Scientist of Ukraine, Professor, Doctor of Technical Sciences, Honorary Professor of the Kharkiv National University of Radio Electronics. He organized and directed the Kharkiv radar meteor research, starting with the registration of radiometeors for the first time in Ukraine in Kharkiv in 1954 for almost fifty years (Kolomiyets, 2012).

Meteor Scientific Group led by B.L. Kashcheyev began to conduct meteor research at the Kharkiv Polytechnic Institute (KhPI), and in July 1971 one was transferred to the Kharkiv National University of Radio Electronics (NURE) as part of the Department Fundamentals of Radio Engineering together with the Balakliia observatory base.

In 2021 it will be 50 years since the beginning of the deployment of research under the leadership of B.L. Kashcheyev within the walls of the NURE on scientific research meteor topics, including in the field of meteor radio astronomy (Kolomiyets, 2012). In 2007, the meteor radio astronomy direction was formalized in a separate research laboratory of radio astronomy named after B.L. Kashcheyev inside the scientific research department of NURE. In the name of B.L. Kashcheyev also named asteroid 6811 in 2000 (Kolomiyets et al., 2016). The merits of B.L. Kashcheyev as the organizer of science and a high rating of world-class scientific achievements of the team of scientists of NURE under his leadership, not only in the field of meteor radio astronomy, but also in the field of meteor geophysics, as well as in the applied aspects of meteor research. The encyclopedia "Names of Ukraine in Space" (Kolomiyets, 2003) confirmed the fact that

the names of three minor planets are associated with the University of NURE. In addition to the asteroid "Kashcheev" there are also the asteroids "KhTURE" and "Voloshchuk". This underlines the significant world-class contribution to science made by the research meteor department of the University under the leadership of B.L. Kashcheyev, as well as the role of the University in creating opportunities for B.L. Kashcheyev and his scientific group. Significant monographs co-authored by B.L. Kashcheyev, contain theoretical and experimental developments, here we note the following: "Meteor phenomena in the atmosphere of the Earth", 1967 (Kashcheyev et al., 1967), "Meteors and meteor substance", 1989 (Voloshchuk et al., 1989). B.L. Kashcheyev, together with the scientific team headed by him, along with achievements in theoretical research, had world recognition in conducting meteor experiments (Kolomiyets, 2012; Kashcheyev & Tkachuk, 1980; Novoselova & Tkachuk, 1971). Meteor radar systems of several generations created under his leadership, including MARS (Meteor Automated Radar System) of the period 1968-1978, have always been at the level of world standards or exceeded world standards. In 2004, the one of the modification of the NURE MARS, updated under the leadership of B.L. Kashcheyev at the end of the twentieth century was included in the list of objects of national heritage of Ukraine under the name "Multipurpose geophysical complex for studying the atmosphere and the influx of meteor matter", Balakliia district (List of objects that make up the national heritage – NAS of Ukraine 2013).

In 1968-1970 B.L. Kashcheyev with the scientific team from Kharkiv together with P.B. Babadjanov and the scientific team from Dushanbe carried out meteor scientific experiments in Somalia, Mogadishu. This event was named the Soviet Equatorial Meteor Expedition. Meteor observations at the equator were made for the first time in the world (Catalog, 1975). The name of B.L. Kashcheyev is inseparable from the most significant geophysical projects of the second half of the 20th century. The IGY-1957 project mentioned above was, among other things, the first global project of joint experiments in the field of geophysics and astronomy (Tsesevich, 1957) on the widest range of topics with measurement research inclusive. These joint astronomical and geophysical studies were continued in the project under the previous program called "International Geophysical Cooperation 1959" (Lebedev & Sollogub, 1960; Kashcheyev & Tsesevich, 1965; Ovezgeldyev et al., 1986).

The level of meteor research in Kharkiv was very high, which made it possible to consider and solve the issues of the methodology of radiometeor observations (Kashcheyev & Nechitaylenko, 1983), create models, including engineering ones (Andreev et al., 1987), and make progress in applied aspects (Kashcheyev et al., 1996).

2. Trajectories. Meteors. Ballistics

According to (Astapovich, 1958) et al. the visible meteor trajectory on a sphere is the segment of its path between the points of appearance and disappearance of the meteor, usually expressed in degree. The true trajectory of a meteoroid is called a segment of the path in space, between the corresponding points in the Earth's atmosphere. The trajectory of a meteoroid relative to an observer on the Earth's surface is called atmospheric or topocentric, relative to the center of the Earth – geocentric, with respect to the Sun – a heliocentric trajectory (orbit). Determination of the orbit (trajectory) of meteoroids, which they describe around the Sun as small bodies of the Solar system, is based on observations of a small part of their path (trajectory) that they cover in the Earth's atmosphere. A meteor phenomenon accompanying the movement of a meteoroid in a certain part of its path in the Earth's atmosphere (meteor zone) is observed by us for a very short time. If it is possible to obtain from observations the velocity of the meteoroid in magnitude and direction, the problem of finding its orbit will be solved, since the coordinates of the meteoroid relative to the Sun are known: they are determined by the position of the Earth at the time of observation. Trajectory elements for each type of trajectory have a special terminology.

In general, the problem of the motion of a meteoroid in the Earth's atmosphere in the range of Earth's speeds and in narrower applications is considered a problem of external ballistics. One of the special tasks of ballistics – the movement of a rocket, the mass of which decreases – is mathematically identical to the problem of the movement of a meteor body, and even then with reservations (for certain altitude intervals above sea level, for a meteoroid that retains part of its mass, etc.). For practical convenience, the motion of a meteoroid is distinguished in several sections of its trajectory in the Earth's atmosphere: higher, upper, middle, low and lower. The physical theory of meteors describes the physical processes accompanying the entry of a meteor body into the Earth's atmosphere: glow and ionization of the atmosphere, reflection of radio waves from a meteor trail (Levin, 1956; Kashcheyev et al., 1967; Voloshchuk et al., 1989).

The first "artificial meteors" were projectiles and bullets (for example, experiments with high-speed bullets were carried out in the Astrobballistics Laboratory of the US Navy (Astapovich 1958), appeared others technologies for laboratory studies of high-speed movement of objects (i.e., with speeds of 3-90 km/s). The velocity of the meteoroid in the Earth's atmosphere is 11-72 km/s, (39,000 – 259,000 km/h). The maximum speed of the projectiles can reach 0.3 km/s (1000 km/h). The speed of sound in air is 340 m/s (0.34

km/s or 1.224 km/h). The North American X-15 was a hypersonic rocket-powered aircraft operated by the United States Air Force and the National Aeronautics and Space Administration as part of the X-plane series of experimental aircraft. As of September 2015, the X-15 holds the official world record for the highest speed ever recorded by a manned, powered aircraft. It could reach a top speed of 2 km/s (7.274 km per hour).

Important information about the laws of motion of meteoroids can be gleaned from meteoritics, the science of meteorites and cosmic dust falling onto the Earth's surface. This branch of astronomy studies the movement of meteor bodies and their interaction with the atmosphere when cosmic matter falls to the Earth. Scientific research in meteoritics includes the collection, identification, and classification of meteorites and the analysis of samples taken from them in a laboratory. One of the main tasks of meteoritics is to find a dropped object. Annually, about 100 thousand tons of meteor bodies invade the Earth's atmosphere, among them about 800 (Kruchinenko, 2012) fall in the form of meteorites.

Numerical methods, analytical solutions using a modern computer base, modeling in the study of the movement and destruction of meteoroids and fireballs in the Earth's atmosphere in the form of information technologies have long been an integral part of meteor science (Moreno-Ibáñez, 2020; Dmitriev, 2015; Bouquet et al., 2014; Clark & Wiegert, 2011; Ceplecha, 1987). One of the new methods is determining the fate of the fireball using the $\alpha - \beta$ criterion (Sansom et al., 2019).

Fireball networks, which are particularly effective at detecting meteorites, have become another technology to improve the methods and means of observing meteors. Now successful meteor networks of amateurs and professionals are deployed in the USA and Canada (CAMS, CMN etc. (Gural, 2012)), Japan (SonotaCo), Europe (Fripion).

Among the observational methods of meteor astronomy (visual, optical/photographic, television, etc./, radar, "in situ" and others) from the point of view of trajectory measurements, we distinguish two types: 1) optical methods, connecting to them visual, 2) radar methods. One of the main tasks of observational meteor astronomy is to determine the orbit of a meteor body through the parameters of the trajectory in the Earth's atmosphere. An important parameter of the movement of a meteoroid is the meteor radiant (a point on the celestial sphere). In optical methods, the trajectory of a meteoroid in the Earth's atmosphere is recorded as a projection onto the celestial sphere in the form of an arc of the celestial sphere (Astapovich, 1958). Special techniques have been developed for determining the parameters of the meteor trajectory by optical methods (Astapovich, 1958), where the deter-

mination of the coordinates of the meteor radiant precedes the determination of other parameters of movement. In the radar method, the direction cosines of the trajectory in the Earth's atmosphere are determined first, and secondly, the coordinates of the meteor radiant (Kashcheyev et al., 1967). The fundamental difference between radar observations and optical ones is that during optical observations the energy emitted by the meteor is recorded, and during radar observations the electromagnetic energy of the transmitter of the radar station reflected or scattered by the electrons of the meteor trail is recorded. The parameters of the Kharkiv meteor radar "MARS II" in the period 1972-1978 are as follows (Table 1):

Table 1: Ratings MARS II

Operating frequency/wavelength	31.1MHz 9.6m
Pulse Transmitter Power	up to 1 MW
Pulse Repetition Rate	500 Hz
Pulse duration	30 kgB·m/s
Antenna type (main antennas)	Corner
Antenna gain coefficient, (main/remote)	~250/16
Direction, altitude, latitude, longitude	east, 45°, 5°, 30°
Minimum detectable receiver signal	5μV
Type of registered meteor trails	~10 ¹¹ em ⁻¹
Minimum detectable mass	~10 ⁻⁶ g

The principles of construction and a complete description of MARS are given in (Kashcheyev et al., 1977). MARS was a multidisciplinary observation tool and made it possible to solve diverse problems of geophysics and astronomy (Fedynsky et al., 1976). The capabilities of MARS in trajectory measurements were as follows. The meteor radar determined and printed 37 parameters of the meteoroid motion and related characteristics, including: 1) the orbit of the meteoroid; 2) slant range; 3) time; 4) velocity; 5) time shifts of the signal at remote points in relation to the main point; 6) azimuth and zenith angle of the radiant; 7) the height of the meteor (the height of the reflecting point on the trail); 8) the elevation angle of the reflecting point. Additionally, a separate study was devoted to altitude measurements (Novoselova & Tkachuk, 1971).

Observational experiments in Kharkiv (at an observation base near Balakliia) for almost 40 years after 1957 left behind a legacy in the form of radiometeor databases (digitized and not digitized). The digitized base of radiometeor data from 1972-1978 (Voloshchuk et al., 2018) can be used as a research tool for various tasks. Let us demonstrate this for studying the motion of meteor bodies with a velocities of less than 23 km/s. These are the velocities inherent in meteorites (Levin, 1957). Fig.1 shows an illustration of the theoretical meteorite collection cone according to (Simonenko, 1975). Meteorites vary greatly in size. Most of

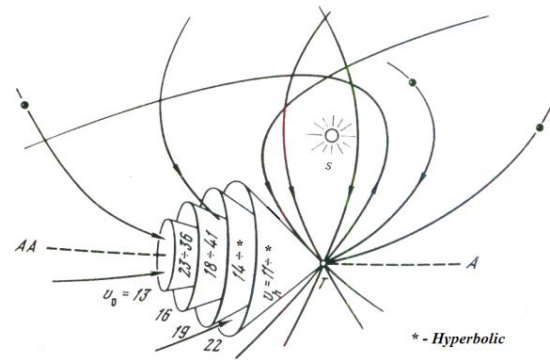


Figure 1: "Cones of collection" of meteorites.

the meteorites have a mass of several grams to several tens of tons. There are micrometeorites too.

A meteor that reached +1M at a speed of 40 km/s, appeared at an altitude of 100 km, and disappeared at an altitude of 80 km at a distance of 150 km from the observer, will have a flight time of 1.5 seconds, a size of 0.6 mm and a mass of 6 mg. The permeability of photographic methods is limited by meteors +4M. Television and electro-optical instruments make it possible to increase the sensitivity of the method, for example, the Dushanbe data (Narziev, 2019) refer to meteors brighter than +5M. Radar techniques provide even more opportunities for observing weaker meteors, i.e. to conduct research on meteoroids with lower masses. In the 70s information about weaker meteors (from +6.5M to +13M) in Harvard, Obninsk, Kharkiv and Kazan was obtained by the radar method. The features of the influx of meteor substances into the Earth's atmosphere are well demonstrated in Fig. 2, credit (Ceplecha, 1998), which shows the complexity of this process. The Kharkiv MARS in 1972-1978 recorded an influx of meteor substance in the mass range 10⁻⁶ – 10⁻³ g, it was considered one of the most highly sensitive radars in the world, as it recorded the orbits of radiometeors up to +12M, and the number of radiometeors up to +14M. It is believed that the New Zealand meteor radar AMOR, when registering meteor orbits, had a sensitivity of up to +13M, although the reliability of these data is possibly somewhat lower compared to the Kharkiv data. The currently active orbiting meteor radars CMOR (Canada) and SAAMER (Tierra del Fuego, Argentina) have a sensitivity of up to +8M.

3. Results and discussion

What can the Kharkiv meteor data tell about meteorites in such a difficult situation with the meteor substances influx into the Earth's atmosphere and why? Kharkiv meteor data are statistically secured and reliable. Meteoroids from any mass range are part of the

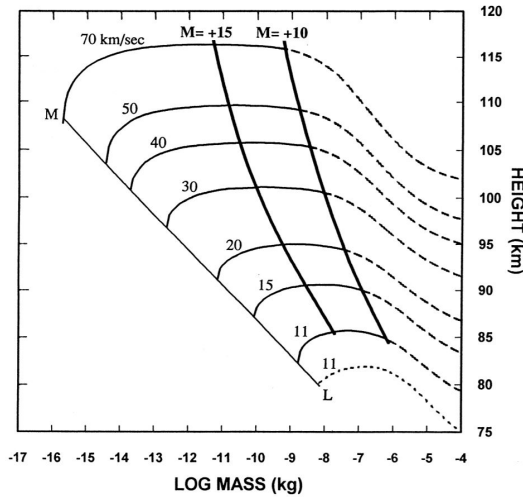


Figure 2: Credit (Ceplecha, 1998), Heights of meteor ablations as a function of mass and velocity

world around us and carry partial information about this world. It remains only to correctly extract this information. In meteor astronomy, the techniques and methods of probability theory and mathematical statistics are widely used, the representativeness of samples is taken into account. In meteor astronomy, the distributions of the number of cases are analyzed for selected parameters. The trajectories of objects from the class of the Solar system small bodies and the laws of their motion are closely related. The bodies falling to the Earth are endowed with general patterns in their orbital dynamics. For smaller bodies, the statistical security is higher and, therefore, a higher probability of establishing a pattern. From the aforementioned Kharkiv meteor database, we selected for analysis meteoroids in the amount of about 160,000 pieces, for which orbits were determined. Also, other samples from this database were used, first of all, a sample of meteoroids orbits with velocities characteristic of meteorites was taken, i.e. $V_g < 23$ km/s. Fig.3 shows the distribution of the number of orbits by parameters: a) $N = N(V_g)$ for $Q > 100$ AU (among 159318), b) $N = N(Nu, V_g)$ for 1978 (all orbits); c) $N = N(\alpha, \delta)$ for $Q < 1.5$ and $V_g < 23$ km/s (denote the Near Earth environment); d) $N = N(Nu, V_g)$ for $Q < 1.5$ and $V_g < 23$ km/s; e) $N = N(\alpha, \delta)$ for $1.5 < Q < 3.8$ and $V_g < 23$ km/s (denote the Asteroids Main Belt); d) $N = N(Nu, V_g)$ for $1.5 < Q < 3.8$ and $V_g < 23$ km/s.

By analyzing the specified database of meteor data, we have established the following patterns. In Fig. 3, a we see that the orbits of meteoroids with $V_g < 23$ km/s may have aphelions Q exceeding 100 AU (Kolomiyets, 2018); the distribution of the number of orbits over the coordinates of the radiant for the selected areas of their aphelions near the Earth and

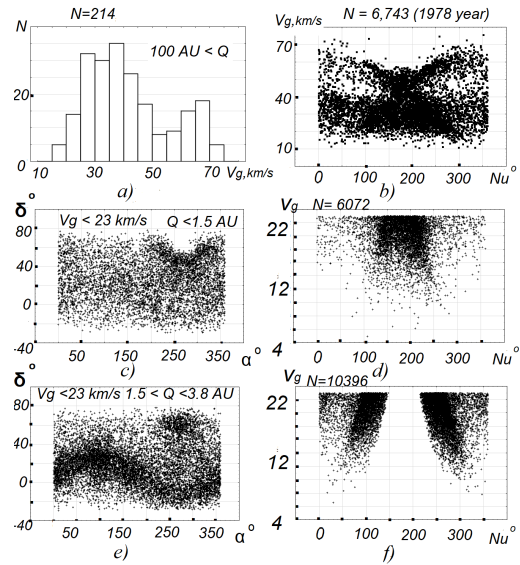


Figure 3: Distribution of the number of orbits of meteoroids according to the selected parameters, including under the condition $V_g < 23$ km/s (c-f).

near the Main Belt of Asteroids have specific features. It turned out that all the orbits of meteoroids with $V_g < 23$ km/s have an inclination less than 90 degrees (e.g. Fig. 4, d). The distributions of orbital elements (eccentricity, argument of perihelion, perihelion distance, inclination) for the selected areas of their aphelions near the Earth and near the Main Belt of Asteroids have the following course (Fig. 4, a-d, $Q < 1.5$ AU – white (top) and $1.5 < Q < 3.8$ AU – gray (bottom), respectively). The concept of the meteor sky, set forth in (Kolomiyets, 2018), was used for a differentiated study of the orbital dynamics of small bodies in the Solar System from the meteor statistics of the database with the selected parameters.

4. Conclusion

The purpose of this research was: 1) to show that in the history of Ukraine there are facts indicating a significant contribution to world and national science of Kharkiv scientists under the leadership of B.L.Kashcheyev in the field of research of meteors by the radar method; 2) to demonstrate the existence of these achievements and the stages of their acquisition in connection with the centenary of the birth of B.L.Kashcheyev in 2020; 3) once again to point out the complexity of trajectory measurements in meteor science and other ballistics application, show different approaches to solving problems of the movement of meteoroids; 4) to use the statistical properties of the Kharkiv meteor database of weak radiometers to study the orbital motion of space objects, incoming

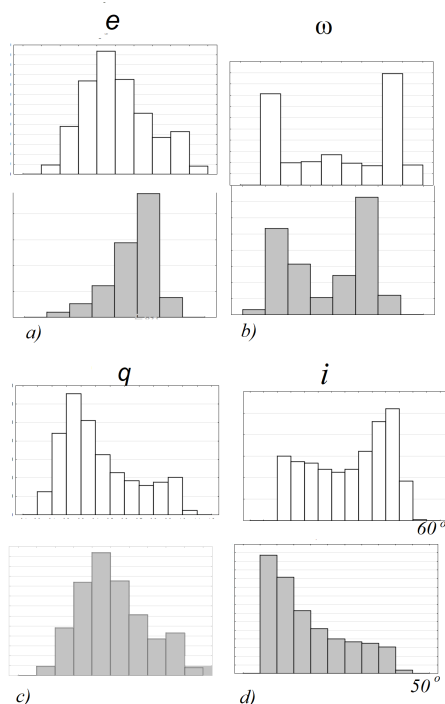


Figure 4: Distributions of meteor orbital elements for a sample of Near-Earth aphelions, aphelions in the Main Asteroid Belt and $V_g < 23$ km/s

into the Earth's atmosphere with geocentric velocities less than 23 km/s, and others aspects. It was found that in the studied meteor database for the sample $V_g < 23$ km/s, there are no orbits with reverse motion (i.e., there are no orbits with inclination $i > 90^\circ$), and the aphelions distances of their orbits may have values from 0.98 to 100 AU and higher.

References

- Andreev V.V., Babadzhyanov P.B., Barsukov V.L. et al.: 1987, *GOST 25645.128-85. Meteor substance, spatial distribution model*, M.: Izd. standartov, 23 p.
- Astapovich I.S.: 1958, *Meteor phenomena in the atmosphere of the Earth*, M.: Fizmatgiz, 640 p.
- Bouquet A., Baratoux D., Vaubaillon J. et al.: 2014, *Planetary and Space Science*, **103**, 238.
- Catalog: Dec. 1968 – Jul. 1970, Moscow, 1975, 167.
- Cepelcha Z.: 1987, *Bull. of the Astron. Inst. of Czechoslovakia*, **38**, 222.
- Clark D., Wiegert P.: 2011, *Meteorit. Planet. Sci.*, **46**, 1217.
- Gural V.P.: 2012, *Planetary Science*, **9**, 1405.
- Dmitriev V., Lupovka V., Gritsevich M.: 2015, *Planetary and Space Science*, **117**, 223.
- Hocking W.K., Kolomiyets S.V.: 2020, *Radiotekhnika: All-Ukr. Sci. Interdep. Mag.*, **201**, 78.
- Fedynsky V.V., Kashcheyev B.L., Voloshchuk Yu.I. et al.: 1976, *Bull. of the USSR Academy of Sciences*, **10**, 89.
- Jenniskens P. S., Gural L., Dynneson B. J. et al.: 2016, *Icarus*, 40.
- Kashcheyev B.L., Koval Yu.O., Gorbach V.I. et al.: 1996, *Meteors today*, K.: Tekhnika, 196 p.
- Kashcheyev B.L., Nechitaylenko V.A.: 1983, *Meteor research*, **8**.
- Kashcheyev B.L., Lebedinets V.N., Lagutin M.F. et al.: 1967, *Meteor phenomena in the Earth's atmosphere*, M.: Nauka, 260p.
- Kashcheyev B.L., Tkachuk A.A.: 1980, *Catalogue of meteor orbits to +12M*, Moscow, 232 p.
- Kashcheyev B.L., Tsesevich V.P.: 1965, *The study of circulation of atmosphere in the meteor zone. Instruction manual*, M.: Nauka, 64 p.
- Kashcheyev B.L., Voloshchuk Yu.I., Dudnik B.S. et al.: 1977, *Meteor research*, **4**, 11.
- Kolomiyets S.V.: 2012, *IEEE*, 46.
- Kolomiyets S.V.: 2018, in: *Proc. of the IAU Symposium 339, New York*, **14**, 215.
- Kolomiyets S.V.: 2003, *Scientific-encyclopedic vision /Ed. I.B. Vavilova & Plachinda, Lviv, Kyiv*, 654 p.
- Kolomiyets S.V., Voloshchuk Yu.I., Slipchenko M.I. et al.: 2016, *Radiotekhnika*, **184**, 6.
- Kruchinenko V.G.: 2012, *Mathematical and physical analysis of the meteoric phenomenon: monograph*, MAO NASU, K.: Nauk. Dumka, 294 p.
- Lebedev T.S., Sollogub V.B.: 1960, *Informatsionnyy byulleten' (Newsletter)*, **2**, 3.
- Levin B.Yu.: 1956, *Physical theory of meteors and meteoric matter in the solar system*, Publ. house of the Academy of Sciences of the USSR, 293 p.
- List of objects that make up the national heritage: 2013, *NAS of Ukraine* [Electronic resource].
- Moreno-Ibañe M. et al. 2020, *MNRAS*, **494**, 316.
- Narziev M.: 2019, *Planetary and Space Science*, **173**.
- Novoselova N.V., Tkachuk A.A.: 1971, *Radiotekhnika*, **16**, 18.
- Ovezgeldyev O.G., Kashcheyev B.L., Nechitaylenko V.A. et al.: 1986, *Radiotekhnika*, **9**, 83.
- Sansom et al.: 2019 *ApJ*, **885**, 115.
- Sidorov V.V., Kolomiyets S.V.: 2007, in: *Proc. IEU SS5 Cambridge Univ. Press*, 189.
- Simonenko A.N.: 1975, *Atlas*, 68.
- Tsesevich V.P.: 1957, *International Geophysical Year [1957-1958]*, M.: Gostekhizdat, 184 p.
- Tsesevich V.P.: 1957, *Astronomical problems of the International Geophysical Year*, M.: Znaniye, 40 p.
- Voloshchuk Yu.I., Kashcheyev B.L., Kruchinenko V.G.: 1989, *Meteors and meteor substance*, K.: Nauk. dumka, 296 p.
- Voloshchuk Yu.I., Kolomiyets S.V., Cherkas Yu.V.: 2018, *Analysis of data on the small bodies of the solar system using information radio technologies: Catalog of meteor orbits. monograph.*, 344. DOI:10.30837/978-966-659-249-4 Corpus ID: 213952314.

DOI:<http://dx.doi.org/10.18524/1810-4215.2020.33.207036>

IMAGING POLARIMETRY OF GEOSTATIONARY SATELLITE EXPRESS-AM5

N. Kosaka¹, Y. Itoh¹, T. Saito¹, M. Tozuka¹,
T. Endo², T. Ando²

¹ Nishi-Harima Astronomical Observatory, Center for Astronomy,
University of Hyogo, Hyogo, Japan, yitoh@nhao.jp

² Information Technology R&D Center, Mitsubishi Electric Corporation,
Kanagawa, Japan

ABSTRACT. This paper reports on the optical imaging polarimetry of geostationary satellite Express-AM5. Precise optical polarimetry was carried out using the Nayuta 2-m telescope at Nishi-Harima Astronomical Observatory and a polarimeter. *V*-band images were continuously taken in 312 minutes. The degree of polarization decreased with time until the minimum phase angle was reached at midnight, and then, it increased until morning. This change in the degree of polarization is well explained by the reflection of sunlight from monocrystalline solar panels of the satellite and possibly from other satellite components such as the antenna dishes and/or bus.

Keywords: Polarization, Planets and satellites: individual: artificial satellite.

АНОТАЦІЯ. Штучні супутники мають спостерігати за допомогою різних астрономічних приладів. Отримавши колір супутника за допомогою фотометричних спостережень, можна оцінити поверхневий матеріал супутника. Кольори супутників, як правило, червоніші за сонячний спектр і супутники різних виробників мають різні кольори. Багато спроб ідентифікувати поверхневий матеріал супутника за допомогою дистанційного зондування було зроблено за допомогою спектроскопії. Ця стаття повідомляє про дослідження оптичної поляриметрії зображень геостационарного штучного супутника Землі Express-AM5. Високоточну оптичну поляриметрію проводили за допомогою 2-метрового телескопа Наюта (Nayuta) в астрономічній обсерваторії Ніші-Харіма (Nishi-Harima) та поляриметра. На протязі 312 хвилин у фотометричній смузі *V* послідовно отримувалися зображення цього супутника. Було отримано що ступінь поляризації зменшувалася з часом, поки близько опівночі не був досягнутий мінімальний фазовий кут, а потім ступінь поляризації супутника збільшувалася до самого ранку. Ступінь поляризації зменшувалася з початку спостережень, і залишалася на

надзвичайно низькому значенні, менше 2%, між 22:51 і 24:42 (JST), а потім зросла до 14% у кінці спостережень. Кут поляризації зменшувався протягом ночі. Було досліджено поляризацію як функцію фазового кута супутника. Фазовий кут розраховували за допомогою веб-сайту Calsky. Фазовий кут зменшився з початку спостережень і досяг мінімуму 23,5° о 23:50 а потім збільшувався до самого кінця спостережень. Супутник показав великий ступінь поляризації під великим фазовим кутом. Для одного і того ж фазового кута ступінь поляризації була майже однаковою до і після мінімального фазового кута, що вказує на те, що компонент, що відбиває сонячне світло, був однаковим до і після мінімального фазового кута. Ця зміна ступеня поляризації добре пояснюється відбиванням сонячного світла від монокристалічних сонячних панелей супутника Express-AM5 і, можливо, від інших супутникових компонентів, таких як антенні тарілки та/або інші прилади.

1. Introduction

Artificial satellites have been observed using various astronomical techniques. By obtaining the color of the satellite through photometric observations, one can estimate the surface material of the satellite. Schmitt (2020) carried out optical *B*-, *V*-, *R*-, and *I*-band photometry of 61 geostationary satellites. They reported that the colors of the satellites are generally redder than the solar spectrum and that satellites from different manufacturers have different colors.

Many attempts at identifying the surface material of a satellite through remote sensing have also been made using spectroscopy. Jorgensen et al. (2004) presented the optical spectra of two satellites. One satellite exhibited a significant increase in reflectance in the wavelengths of the *U*- and *B*-bands. The authors considered this to be due to the presence and orientation of the solar panels. They also noticed a broad absorp-

tion feature at nearly 8500 Å in the spectra of both the satellites, which was attributed to the presence of aluminum.

Polarimetry is a powerful tool for investigating the surface of a solid body. An asteroid is an astronomical object with a solid surface reflecting sunlight. The reflected light is polarized, and by measuring the degree of polarization, one can estimate the size of the regolith on the surface. Kuroda et al. (2018) observed an extremely low-albedo asteroid in 1998, KU₂. They obtained linear polarization degrees of 44.6% and 44.0% at a phase angle (Sun–asteroid–observer angle) of 81.0° in the *Rc*- and *V*-bands, respectively. These values are the highest for the known airless bodies in the Solar system at similar phase angles. They attributed this high degree of polarization to a highly microporous regolith structure comprising nano-sized carbon grains on the surface of the asteroid.

An artificial satellite has a solid surface. Speicher (2015) observed eight satellites using a 20-inch telescope and a polarimeter. The polarimeter used had a polarizing beam splitter and took horizontally and vertically polarized images simultaneously. A large degree of polarization was observed during dusk and dawn and a small degree polarization at midnight.

Express-AM5 is an active geostationary satellite. This Russian communication satellite was launched in 2013, and it is located in the geostationary orbit at 140° east longitude. The satellite is three-axis stabilized.

In this study, we conducted optical imaging polarimetry of Express-AM5 using a unique polarimeter by which the fluxes of four polarimetric components were recorded simultaneously. We carried out the most continuous polarization measurements of a geostationary satellite to date.

2. Observations

Optical polarimetry of Express-AM5 was carried out on January 19, 2019 using a simultaneous imaging/spectroscopic polarimeter, called POL (Fujita et al. 2009), mounted at the Cassegrain focus of the Nayuta 2-m telescope at Nishi-Harima Astronomical Observatory, Japan (35.025° N, 134.336° E). POL has an unpolarized beam splitter and two Wollaston prisms, which divide light into four channels corresponding to linearly polarized light with polarization position angles of 0°, 45°, 90°, and 135°. The four channels were simultaneously captured in a single image. Each channel has a field of view of $\sim 0.7' \times 2.5'$. The optical magnitude of Express-AM5 was approximately 10 mag in the *V*-band. The celestial coordinate was calculated from a two-line element set. The satellite remained at 9.9° east from the south with an elevation of 48.9° in the sky. We observed the satellite between 21:46 and 27:48 (JST). A total of 162 frames

were obtained with a 90-s exposure in the *V*-band. After observing the satellite, we observed HD 154892 as an unpolarized standard star and HD 154454 and HD 161056 as polarized standard stars (Turnshek et al. 1990). All images were taken at a position angle of -29.5° for operational reasons. The seeing size was approximately 1.5". Dark and flat frames were also taken. We think that the light reflected by the flat screen is polarized because a halogen lamp illuminates the screen in the dome from the lower side. We set the rotation angle of the Cassegrain rotator, to which the POL is attached, to 0°, 45°, 90°, and 135°, and took flat frames at each angle.

Data were processed with the Image Reduction and Analysis Facility (IRAF). The object frames were calibrated in a standard manner, namely dark subtraction and flat fielding with the dome-flat frames. The flat frames taken at four rotation angles of the Cassegrain rotator were combined into a single frame. The fluxes of the satellite and standard stars were measured using aperture photometry. The aperture radius was set to 2.5". We calculated the degree of polarization, P , and polarization angle, α , as follows:

$$\frac{Q}{I} = \frac{F_{0^\circ} - F_{90^\circ}}{F_{0^\circ} + F_{90^\circ}} \quad (1)$$

$$\frac{U}{I} = \frac{F_{45^\circ} - F_{135^\circ}}{F_{45^\circ} + F_{135^\circ}} \quad (2)$$

$$P = \sqrt{\left(\frac{Q}{I}\right)^2 + \left(\frac{U}{I}\right)^2} \quad (3)$$

$$\alpha = \frac{1}{2} \tan^{-1}\left(\frac{U}{Q}\right), \quad (4)$$

where F_θ is the flux density for the light polarized at θ , and Q/I and U/I are the normalized Stokes parameters. In astronomy, $\theta = 0^\circ$ indicates north and $\theta = 90^\circ$ indicates east. The degree of polarization of the unpolarized standard star was measured as 1.54 %. The polarization was caused by the telescope and/or instrument. We subtracted 0.0121 from Q/I and added 0.0095 to U/I such that the degree of polarization of the unpolarized standard star was zero. The same correction was applied to the data on the polarized standard stars and satellite. The measured degree and angle of polarization of the polarized standard stars were different from those described in the literature. The measured Q/I and U/I were transformed using the scaling and rotation matrix on the $Q/I - U/I$ plane; thus, the differences between the measured polarization and that described in the literature were minimum. Based on these differences, we consider the uncertainties to be 3/100th of the polarization degree and 5° in the polarization angle. The same matrix was applied to the satellite data. Among the 163 frames of the satellite data, background stars overlapped the satellite in 9 of the frames, and we did not further use these 9 frames.

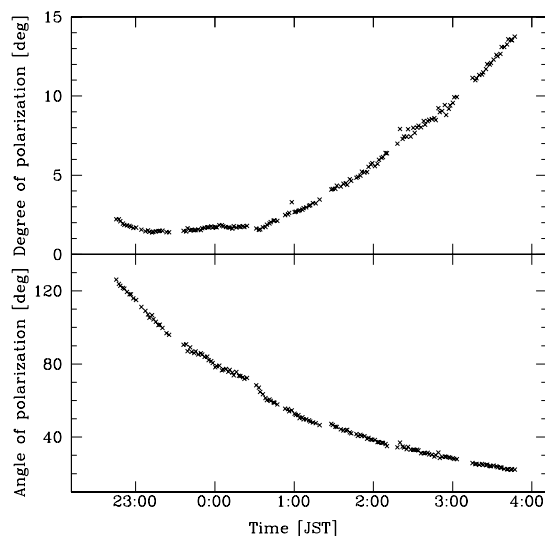


Figure 1: Degree and angle of polarization of Express-AM5 as functions of the observation time.

3. Results

The polarization of Express-AM5 was detected throughout the night (Figure 1). The degree of polarization decreased from the beginning of the observation, and remained at an extremely low value of less than 2% between 22:51 and 24:42 (JST) and then increased to 14% until the end of the observations. The polarization angle decreased throughout the night. Figure 2 shows the polarization as a function of the phase angle of the satellite. The phase angle was calculated using the *Calsky* website. The phase angle decreased from the beginning of the observations and reached a minimum of 23.5° at 23:50 and then increased until the end of the observations. The satellite showed a large degree of polarization at a large phase angle. For the same phase angle, the degree of polarization was almost the same before and after the minimum phase angle, indicating that the component reflecting the sunlight was the same before and after the minimum phase angle.

4. Discussion

The polarization of light reflected by the satellite components was investigated with laboratory measurements. Beamer (2018) measured the polarization of light reflected by a monocrystalline solar panel, a polycrystalline solar panel, a cylinder and a cubic box as a model of a satellite bus, a painted dish antenna, and a painted dish antenna with a fiberglass wire mesh. The intensity of light reflected by the sample in a specific direction was measured using a power meter. The bus and antennae of a geostationary satellite are nadir pointing. To measure the light reflected from the bus

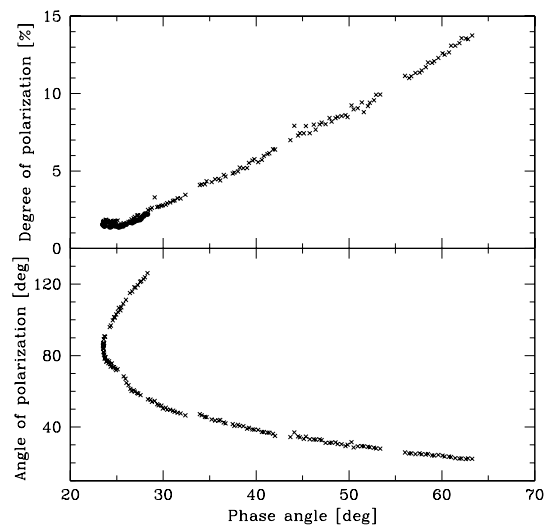


Figure 2: Degree and angle of polarization of Express-AM5 as functions of the phase angle. In the upper figure, the degree of polarization before the minimum phase angle is indicated by the filled circles and that after the minimum phase angle is indicated by crosses.

and antenna components, those and the power meter were mounted on a rail. A halogen lamp was set separate from the rail, and by changing the orientation of the rail with respect to the halogen lamp, the incidence angle of light to the sample was changed. The solar panels of a geostationary satellite are oriented towards the sun. For measurement, the solar panel was not mounted on the rail but was set normal to the halogen lamp. The reflection angle of the light to the solar panel was changed as the power meter moved. They measured the degree of polarization using an incidence or reflection angle between 15° and 83° . The monocrystalline solar panel showed a degree of polarization of less than 2% at a reflection angle between 20° and 30° and a degree of polarization of $\sim 10\%$ at a reflection angle of $\sim 60^\circ$. The painted dish antenna, the cylinder bus, and the cubic bus showed a degree of polarization of $\sim 10\%$ even at a small angle of incidence. The polycrystalline solar panel and dish antenna with a wire mesh exhibited a low degree of polarization at all incidence and reflection angles.

Cognion et al. (2013) claimed that the sunlight reflected from the front of the solar panels dominates the reflection light of a satellite at a phase angle below 85° .

The degree of polarization of Express-AM5 is $\sim 2\%$ at a phase angle less than 30° and 13% at 60° . This degree of polarization is roughly consistent with that of the light reflected by a monocrystalline solar panel. We consider the polarization of light reflected from Express-AM5 to be mainly caused by its solar panels.

Nevertheless, the observed degree of polarization of Express-AM5 is 2%–3% larger than the measured de-

gree of polarization of a monocrystalline solar panel. Different solar panels may exhibit larger degrees of polarization. Horváth et al. (2010) indicated that solar panels made by different companies exhibit different patterns of polarization. Száz et al. (2016) verified that an anti-reflective coating changes the polarization properties. Other satellite components, i.e., the bus or dish antennae, may also contribute to the polarization. Endo et al. (2016) found a $B - V$ color variation of approximately 1 mag for Express-AM5, indicating the reflection of sunlight by multiple components. Express-AM5 has three 1.2-m diameter dishes and three larger dishes. All dishes have smooth surface. The diameter of the larger dish seems to be twice that of the small dish (Amyotte et al. 2013). The total surface area of six dishes is 17 m², which is larger than the projected area of the bus. The area of the solar panels of Express-AM5 is 84 m². If 20% of the reflected light comes from the antennae and 80% from the solar panels, the degree of polarization increases by approximately 2%–3% at a phase angle of 30° and 1%–2% at a phase angle of 60°, compared to the reflection solely by the solar panels.

Speicher (2015) measured the polarization of eight satellites. The polarimeter had a polarizing beam splitter and two optical CCDs, allowing the simultaneous collection of two-channel polarimetry data. The instrument was set to obtain horizontally polarized ray, F_h , and vertically polarized ray, F_v ; then, $S_1/S_0 = (F_h - F_v)/(F_h + F_v)$ was calculated. Because an alt-azimuth telescope was used and an instrument rotator was not applied, S_1/S_0 differed from Q/I . Two polarized images were obtained for each satellite every 15 min with a 20-s exposure. A negative S_1/S_0 was observed with a large absolute value during dusk and dawn and with a small absolute value at midnight. A negative S_1/S_0 with a large absolute value indicates strong vertical polarization. They considered that the bus or antennae exhibited strong vertical polarization, whereas the solar panels provided only a small contribution to the overall optical signature during dusk and dawn owing to their edge-on geometry. However, as shown in Figure 1, the polarization angle of light reflected by Express-AM5 changed over time because the scattering plane rotated over time. A measurement of linearly polarized light with four polarization angles is mandatory for the polarimetry of a satellite.

When the phase angle is at its minimum, the projected point of the satellite onto the Earth, the projected anti-solar point on the Earth (the anti-sub solar point), and the observer are along a single line. This line is an intersection of the scattering plane and the Earth's surface. Both planes are orthogonal. The position angle of this line is $90^\circ + \tan^{-1}\left(\frac{35.025^\circ}{134.336^\circ - 140^\circ}\right) = 9.2^\circ$ west from the north. Assuming a vertical polarization to the scattering plane, the polarization angle of the reflection light is 80.2° at the time of the minimum phase angle. The minimum phase angle was observed

at 23:50, and the measured polarization angle was 85.9° at that time. The angle reached 80.2° approximately 10 min later. Because the uncertainty of the measurement is 5° in terms of the polarization angle, we do not consider a discrepancy of 5.7° to be significant.

Unpolarized light is 100% polarized if the incidence angle equals the Brewster's angle. Because the refractive index of a vacuum is 1 and that of a solar panel glass is 1.5, the Brewster's angle of a solar panel is 56°. Speicher (2015) reported that there was no significant increase in the degree of polarization at a phase angle of 56°. In our observations, we also did not find such an increase. Speicher (2015) speculated that an anti-reflective coating on the surface of the solar panel reduces the total reflected light, creating a small polarization. However, as noted by Beamer (2017), a solar panel of a satellite always faces the sun, and thus, the incidence angle of sunlight does not equal the Brewster's angle even when the phase angle is 56°.

Each component of a satellite has its own color. The antennae of Express-AM5 are white, black, or gold, whereas the solar panels of some satellites are bright in the blue and ultraviolet wavelengths. A bus consists of numerous materials. Multi-band imaging polarimetry may resolve the shape, orientation, and surface material of a satellite.

5. Conclusion

We measured the polarization of sunlight reflected by the Russian geostationary satellite, Express-AM5. The degree of polarization in the V -band ranged from less than 2% at approximately the minimum phase angle to 14% at the end of the observations. The polarization vector rotated clockwise in the sky. We concluded that the solar panels, and possibly the antenna dishes and/or bus, contribute to the polarization of the reflected light.

Acknowledgements. This study was supported by a fund from Mitsubishi Electric Corporation.

References

- Beamer, D. K.: 2018, *Ph. D. Thesis, University of Dayton*
- Cognion, R. L.: 2013, *Proc. of AMOS Conf.*
- Endo, T. et al.: 2016, *Proc. of AMOS Conf.*, 922
- Fujita, K., Itoh, Y., Mukai, T.: 2009, *Adv. Space Research*, **43**, 325
- Horváth, G. et al.: 2010, *Conservation Biology*, **24**, 1644
- Jorgensen, K., Africano, J., Hamada, K., et al.: 2004, *Ad. Sp. Res.*, **34**, 1021
- Kuroda, D., Ishiguro, M., Watanabe, M., et al.: 2018, *Astron. & Astrophys.*, **611**, A31
- Schmitt, H. R.: 2020, *Adv. Space Research*, **65**, 326
- Speicher, A.: 2015, *Ph. D. Thesis, University of Denver*
- Száz, D. et al.: 2016, *J. of Insect Conservation*, **20**, 663
- Turnshek, D. A., Bohlin, R. C., Williamson, R. L. II: 1990, *Astron. J.*, **99**, 1243

DOI: <http://dx.doi.org/10.18524/1810-4215.2020.33.216464>

SIMULTANEOUS MULTI-SITE PHOTOMETRY OF LEO SATELLITES TO CHARACTERISE THEIR ROTATION STATES

Koshkin N.¹, Shakun L.¹, Melikyants S.¹, Korobeynikova E.¹, Strakhova S.¹, Bilinsky A.², Vovchuk Ye.², Kudak V.³, Motrunich I.³, Neubauer I.³, Kozhukhov O.⁴, Romanyuk Ya.⁵, Ryabov A.¹, Terpan S.¹, Dragomiretsky V.¹, Golubovskaya T.¹

¹ Astronomical observatory of Odessa I.I.Mechnikov National University

² Astronomical observatory of Lviv I.Franko National University

³ Uzhhorod National University, Laboratory of Space Researches

⁴ National Space Facilities Control and Test Centre of State Space Agency of Ukraine

⁵ Main Astronomical Observatory of NAS of Ukraine

ABSTRACT. The photometry of space objects (SO) makes it possible to determine their state of rotation around the center of mass, orientation of the rotation axis and rotation speed in the most cost-effective manner. However, the methods for determining the attitude parameters from photometric data from a single observation site (OS) require long series of high-quality and high-frequency measurements. We propose a method for determining the orientation parameters of slowly rotating SO based on simultaneous multi-site photometry with a high temporal resolution. Preconditions for planning and building a local photometric network that can accomplish such a task have been tested via computer simulation. Synchronous observations of the unoperated spacecraft TOPEX/Poseidon were carried out. They were attended by the observatories of Odessa, Lvov and Uzhgorod universities, as well as the observation station of the State Space Agency of Ukraine in Zalistsi, Khmelnytsky region, took part. Synchronous network-based photometric observations from three OSs enable us to calculate time lags between correlated light-curve segments and promptly determine the direction of rotation, as well as the spatial orientation of a SO's spin axis and its angular spin rate. A local network of several distributed observation sites for synchronous monitoring of the rotation of various SO in LEO will make it possible to determine the rotation parameters of also slowly rotating objects that do not exhibit glints within their light curves.

Key words: space object (SO), rotation, attitude, photometry, synchronous observation.

АНОТАЦІЯ. Фотометрія космічних об'єктів (КО) дозволяє визначити їхній стан обертання навколо центру мас, орієнтацію осі обертання та швидкість обертання найбільш економічним способом. Однак методи визначення параметрів орієнтації на основі фотометричних даних з одного пункту спостереження (ПС) потребують довгих серій високоякісних та високочастотних вимірювань. В роботі запропоновано метод визначення параметрів орієнтації КО, що повільно обертаються, на основі одночасної багатопунктової

(мережевої) фотометрії з високою тимчасовою роздільною здатністю. Передумови для планування та побудови локальної фотометричної мережі, яка може виконати таке завдання, перевірені за допомогою комп'ютерного моделювання. Були проведені синхронні спостереження космічного корабля TOPEX/Poseidon, що вже не працює. У них взяли участь обсерваторії Одеського, Львівського та Ужгородського університетів, а також станція спостереження Державного космічного агентства України в м.Заліссі Хмельницької області. Синхронні мережеві фотометричні спостереження з трьох ПС дозволяють розрахувати затримки часу між корельованими сегментами кривих блиску та швидко визначити напрямок обертання, а також просторову орієнтацію осі обертання КО та кутову швидкість його обертання. Локальна мережа з кількох розподілених місць спостереження для синхронного моніторингу обертання різних низькоорбітальних КО дасть можливість визначити параметри обертання також об'єктів, що повільно обертаються та не мають періодичних спалахів у своїх кривих блиску.

Ключові слова: космічний об'єкт (КО), обертання, орієнтація, фотометрія, синхронні спостереження.

1. Introduction

Photometric observations of artificial satellites orbiting Earth are traditionally used as a source of information on the rotation about the centre of mass, spatial orientation and, finally, geometric shape of the observed object. Multi-hertz sample rate photometry is especially valuable as man-made SOs are commonly designed with smooth surfaces, they have non-convex overall shapes and can spin fast, etc. This results in periodic variations in the SO brightness amid rapidly changing phase and observation angles as the SO moves in its trajectory (see Fig. 1) (Kurosaki *et al.*, 2005; Koshkin *et al.*, 2018). Notably, such brightness variations are characterised by the so-called "apparent" period, that is, the observed period of the SO light curve which can vary significantly during a flyby of the SO over the ground OS as

the line-of-sight direction changes. Mathematically, it is expressed using vector addition of constant angular spin rate of the SO about its centre of mass and variable angular velocity of the phase-angle bisector (PAB), which depends on the SO orbital motion relative to a topocentric observer (Hall & Kervin, 2014). It is this condition that makes it possible, when solving the inverse photometric problem, to estimate the spatial orientation (in the inertial reference frame) of the SO spin-axis vector. Theoretically, the problem solution can result from processing of photometric observations during a single pass of the LEO SO over an OS. However, until recently, the described method for the real-time determination of rotation parameters of the SO could not be widely employed due to a lack of the required observing instruments and facilities. Therefore, researchers were often confined to only apparent (or synodic) rotation period measured from the light curve averaged out (or convoluted) in one way or another, since the “inertial” or sidereal rotation period could not be estimated separately from finding a solution to the SO spin-axis orientation.

The duration of the visibility of a LEO SO during its single pass is defined by the geometry of its visibility from the OS and is limited to several minutes. During this time span, a change in the phase angle (the angle Sun-SO-observer) can make up about 90° or slightly greater. A change in the “phase angle projection” onto the plane perpendicular to the satellite spin axis can be of the same order of value. It is the last value that determines the “apparent” period variation during a single pass. If the rotation period of a LEO SO is just several tens of seconds, an observer will see several complete revolutions made by the SO during each pass, which will allow the analysis of

the “apparent” period variation in order to find a solution to the SO spin-axis orientation. These estimates indicate that a relative change in the “apparent” period in the given example is just a few percentage points; hence, to measure it reliably, the LEO SO brightness must be recorded at a sample rate of at least 10-100 Hz. It is fairly feasible using a conventional set of instruments and equipment traditionally employed by different researchers to conduct photometric observations (Gasdia *et al.*, 2017; Hall *et al.*, 2006).

Meanwhile, it is known that many SOs experience a rapid decline in the angular spin rate resulting from their interaction with the Earth’s magnetic field. Consequently, the rotation period can exceed (and even significantly) the duration of viewing a LEO SO during its single pass (see Figure 2). Our experience of monitoring observations of a large number of satellites rendered inoperable, as well as upper-stages of rocket bodies, shows that the light curves of such targets become non-periodic and often do not have “features”. If that is the case, there is just a vague hope that the SO spin parameters can be inferred from single-site photometric data. In the present paper, we offer a problem-solving technique for such cases. This technique assumes creating local networks of multiple OSs and acquiring multi-site synchronous photometric observations of slowly rotating SOs. Methods of multi-site synchronous photometric observations have been already discussed in papers of other researchers (Hall *et al.*, 2007; Gasdia *et al.*, 2017; Schafer, 2017), though there has not been enough emphasis therein placed upon the fact that this is actually the only feasible way to estimate the spin parameters of “slow” SOs.

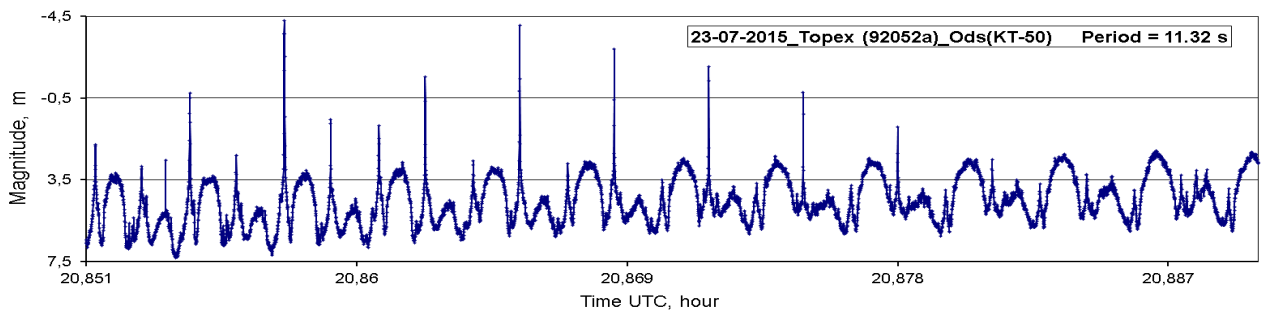


Figure 1: A light curve of the inactive Topex/Poseidon satellite (NORAD ID 22076; $i = 66.039^\circ$, $h = 1350$ km) obtained in Odessa with the KT-50 telescope on 23 July 2015. The length of the presented light-curve portion is 2.34 minutes (140 seconds). The apparent or synodic rotation period $P_{syn} = 11.32$ sec. During the observing session, the phase angle changed by 37° .

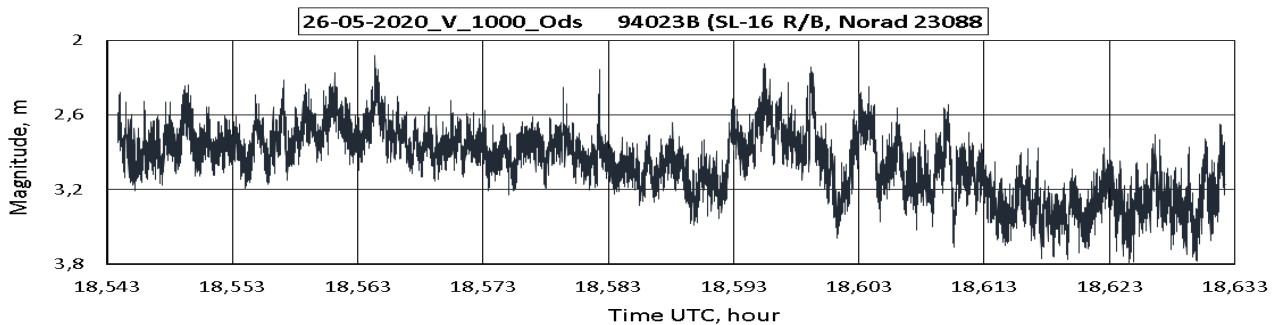


Figure 2: A light curve of the upper-stage SL-16 (NORAD ID 23088) obtained in Odessa with the KT-50 telescope on 26 May 2020 within the framework of the IADC (the Inter-Agency Space Debris Co-Ordination Committee) international campaign for the analysis of space debris (upper-stage rocket bodies) rotation. The length of the presented light-curve portion is 5.2 minutes (312 seconds).

2. Model computation to simulate multi-site synchronous photometric observations

We performed computer simulation of conditions for acquiring multi-site synchronous photometric observations of SOs. Our satellite model is a geometric representation of six identical, symmetrically located polyhedra, which are randomly oriented with respect to each other and partially penetrate each other's facets in order to minimize their mutual shading (Figure 3). Photometric properties of all flat facets of the model are identical; the reflection of light from each facet is quasi-specular, that is, the indicatrix is noticeably elongated in the direction of the specular reflection (the half-intensity indicatrix width is ~ 2 degrees). The position of the spin axis related to the body of such a model does not matter; what is important is that the spin-axis orientation remains the same in all computations. Such a large number of flat facets integrated into the model is required to ensure that at varying spatial orientations of the model spin axis, as well as at different observer's locations, the light curve of the spinning model exhibits several almost randomly temporally-distributed glints given off of different facets over an interval shorter than the time required to complete a single revolution.

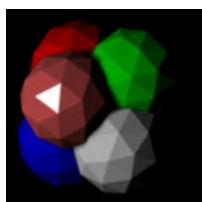


Figure 3: An optical-geometric satellite model represented as six polyhedra partially penetrating each other (a specular flash or glint given off a flat facet can be seen on one of the polyhedra).

The position of a source of parallel light rays (the Sun) is specified in the inertial equatorial co-ordinate frame with two angles: the right ascension $\alpha = 0^\circ$ and declination $\delta = 0^\circ$. Then, the directions for five observer's locations in the same co-ordinate system are specified with the following pairs of co-ordinates α and δ : ($71^\circ, +01^\circ$); ($73^\circ, -05^\circ$); ($75^\circ, 00^\circ$); ($76^\circ, +05^\circ$); ($78^\circ, -03^\circ$). Thus, the phase angle during simulation of this model is about 75° while the satellite-centric angular distance between individual modelled observing sites varies from 3 to 10 degrees. Figure 4 shows all five light curves simulated for the given observer's locations and position of the Sun, upon rotating the model 215° around the spin axis, whose spatial orientation is specified with $\alpha_\Omega = 40^\circ$ and $\delta_\Omega = 75^\circ$. The rotation phase in a degree (an analogue to time scale) is plotted on the X-axis against the light intensity (apparent brightness) of the model in relative units on the Y-axis. As is seen, at different observer's locations, from five to eight glints of varying intensity occur within each light curve of this model. Mutual positioning of individual glints, that is, the phase delay (or time lag) between individual flares, recurs for

some of adjacent pairs throughout different light curves. This enables us to calculate an overall phase shift between different light curves, that is, between different synchronous records (measurements) of brightness variations of one and the same spinning model.

In this computational experiment, the modelled satellite does not move along its orbit, that is, geometric conditions of its visibility, such as the phase angle, etc., remain unaltered. The entire simulated light curve can therefore be considered as a continuous curve with the same phase shift relative to any other light curve, taken as a "reference" one. Computing the observed phase differences between the simulated light curves (through calculating the cross-correlation function), followed by superimposing the light curves on each other with a phase shift corresponding to the resulting phase differences, yielded a pattern illustrated in Figure 5. The light curves, appearing as a series of sharp maxima, are superimposed on each other quite well throughout the entire length, demonstrating synchronous occurrence of glints as viewed by several observers (in different combinations of the observing locations). In a few cases, the phase of an individual glint within one of the light curves is shifted with respect to several other glints that are well-synchronised. It is associated with a random temporal (or phase) coincidence of glints produced when the light is reflected off some other flat facet in this complex model. Nevertheless, these synchronously occurring glints (flares) suffice to perform calculations of the phase difference (or time lag) between all simulated light curves.

An analysis of the observed time lags between "similar" events within the light curves (or correlated light-curve segments) recorded by three OSs enables us to compute a local direction in which a quasi-specularly reflected spot of light travels along the Earth's surface. In Figure 6, numbers denote locations of three ground-based observation sites; the circle marks a spot of light reflected off of a satellite's facet, and the thick black arrow points in the direction of the spot-of-light's motion. The Y-axis is directed towards the celestial pole while the X-axis is parallel to the equator. By measuring delays in time of the peak brightness occurrence as viewed from each OS, we can compute a direction of the spot-of-light's motion at each location, that is, the inclination of the small-circle arc along which the spot of light is moving at a given local network location (the angle γ in Figure 6), and also its angular velocity. Calculating the satellite's spin-axis orientation (co-ordinates of the rotation pole) requires estimating the inclination of the arc, along which the spot of light is moving, at least at two different positions.

A preliminary conclusion can be inferred from the simulation results. Specular flares from flat facets, which serve as excellent markers within the SO light curve, can only be observed quasi-synchronously from three or more OSs that form a local photometric network if a certain ratio between the distance to the satellite and distance between these OSs is maintained. The satellite-centric angular distance between OSs should not markedly exceed 0.2 radians. In such a case, it is quite feasible to acquire correlated light-curve segments from several adjacent OSs.

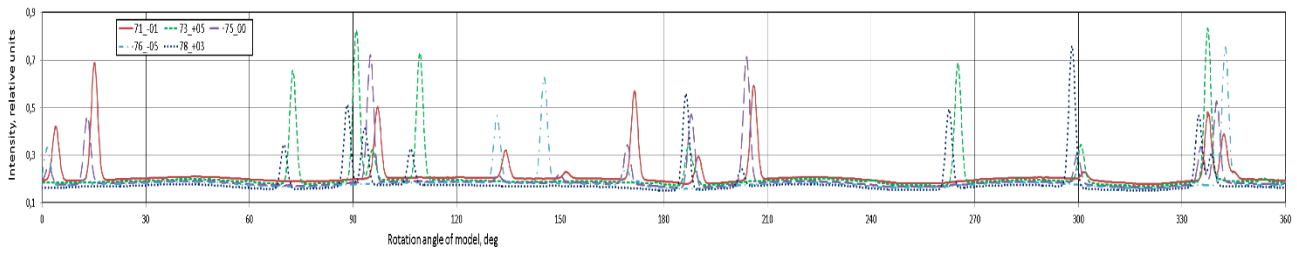


Figure 4: Superimposing five light curves of the satellite model simulated for five different modelled OSs forming a local photometric network.

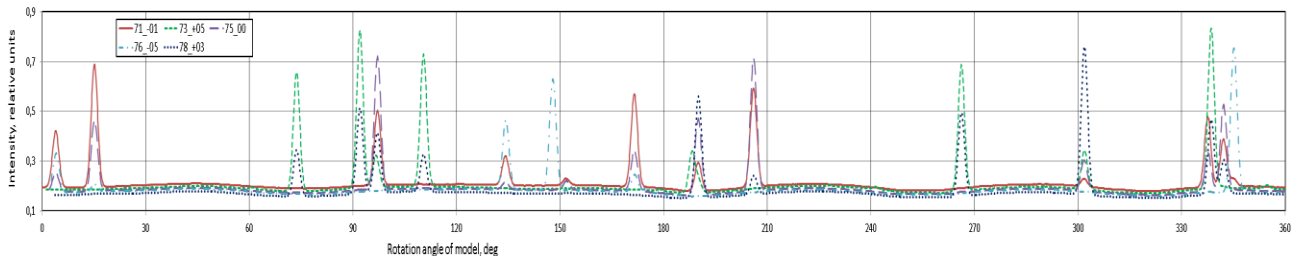


Figure 5: Superimposing five light curves of the satellite model simulated for five different modelled OSs, forming a local photometric network, after compensation for the actually observed phase shift between the light curves.

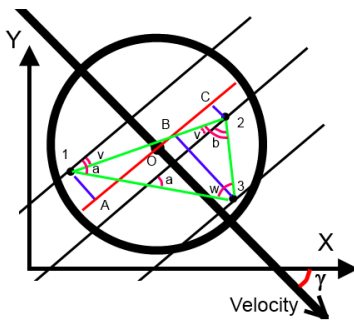


Figure 6: A pattern for calculating the direction, in which a “spot of light”, quasi-specularly reflected off of the satellite surface, travels along the Earth’s surface.

3. Synchronous observations of the Topex/Poseidon satellite by the Ukrainian network of observatories

There are several astronomical observatories in Ukraine that conduct photometric observations of artificial satellites and space debris. Taking that into consideration, in order to test the feasibility of obtaining synchronous network-based (that is, multi-site) photometric observations of such space objects, a campaign for observing inactive satellite Topex/Poseidon and the Experimental Geodetic Satellite Ajisai was carried out. Astronomical observatories of Odessa, Lviv and Uzhgorod universities, as well the observing station of the National Space Facilities Control and Test Centre of Ukraine in Zalistsi, participated in the campaign. Astronomical Observatory of Kharkiv University, located in Grakovo village, has also attempted to join the campaign, but failed so far. During the periods from 02 to 13 August and from 21 to 30 September 2020, synchronous observations of the afore-listed satellites were acquired from OSs that have the following co-ordinates: (Odessa: 30.75569° longitude, 46.47775° latitude, 54 m

altitude; Bryukhovichy: 23.9544°, 49.9176°, 360 m; Uzhgorod: 22.2986°, 48.6334°, 176 m; Derenevka: 22.4538°, 48.5636°, 226 m; and Zalistsi: 26.7183°, 48.8483°, 389.8 m). In so doing, the average distances between OSs were as follows: 680 km between Odessa and Uzhgorod; 640 km between Odessa and Lviv; 185 km between Lviv and Uzhgorod; 400 km between Odessa and Zalistsi; 320 km between Uzhgorod and Zalistsi, and 235 km between Lviv and Zalistsi. Given that the target satellites orbit at an altitude of about 1.5 thousand kilometres, each of the Odessa-Uzhgorod and Odessa-Lviv distances slightly exceeds the limiting/optimal estimated distance, which ensures a good correlation between quasi-specular flares within the light curves, while the distances between the other OSs are optimal. Figure 7 depicts portions of two light curves of the Topex/Poseidon satellite generated from synchronous observations in Odessa and Derenevka (an observing site of Uzhgorod National University) on 02 August 2020 at 20:32 (UTC), after performing a 0.25 sec time shift on one of the light curves.

The total length of the light curve acquired in Odessa is 10.1 minutes (with a short gap near zenith wherein the alt-azimuth mounted telescope KT-50 have got blind spot); the duration of the light curve obtained in Derenevka is 8.6 minutes (8.4 minutes of which correspond to synchronised guiding of the telescopes). During the first half of the pass, a very good similarity of the satellite light curves acquired at two sites distant from each other is observed over a long time span. During the second half of the pass, such a similarity is retained, though there is a marked contrast between the magnitudes of specular flares while the light curves differ in particulars. Figure 8 illustrates portions of two light curves of the Topex/Poseidon satellite acquired from simultaneous observations in Odessa and Lviv on 06 August 2020 at 20:05 (UTC), which have also been superimposed with regard to similar events through a 0.20 sec time-scale shift in one of them.

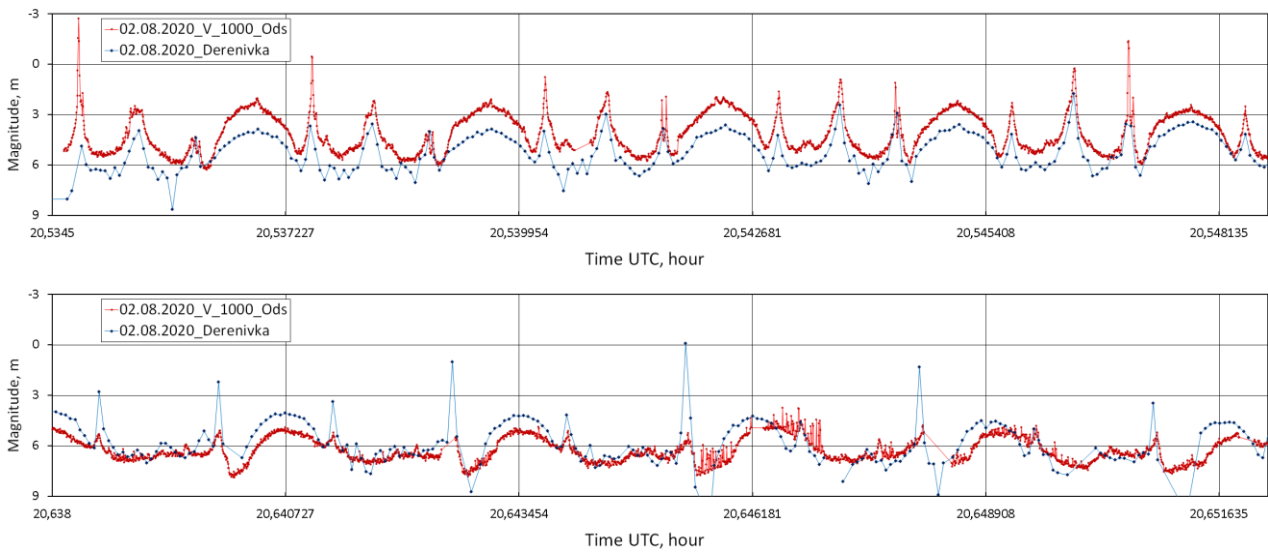


Figure 7: Portions of two light curves of the Topex/Poseidon satellite, synchronously observed in Odessa and Derenevka on 02 August 2020 at 20:32 (UTC), after performing a 0.25 sec time shift in one of the light curves.

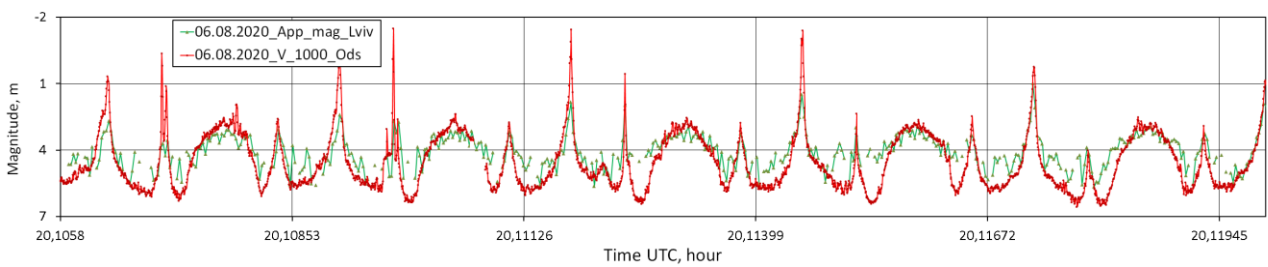


Figure 8: Portions of two light curves of the Topex/Poseidon satellite, synchronously observed in Odessa and Lviv on 06 August 2020 at 20:05 (UTC), after a 0.20 sec time-scale shift in one of the light curves.

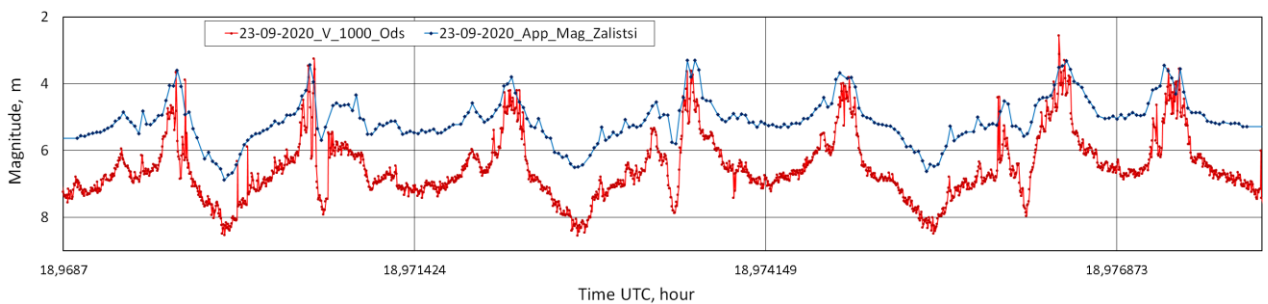


Figure 9: Portions of two light curves of the Topex/Poseidon satellite, synchronously observed in Odessa and Zalistski on 23 September 2020 at 18:58 (UTC).

Despite a considerably higher noise and lower rate of brightness measurements as compared to the photometric data from the KT-50 telescope, the light curve obtained in Lviv is similar, in principle, to that acquired in Odessa. Four major increases in brightness with a distinctive wide “diffuse” maximum and three quasi-specular maxima in between such increases are observed over a single revolution of the satellite. The Topex/Poseidon light curve exhibits such behaviour till the end of this pass.

During another pass, a portion of which is shown in Figure 9, the Topex/Poseidon light curve behaves differently: there are only two major increases in brightness associated with complex quasi-specular reflection of light during that pass of the satellite.

Notably, the interval between adjacent maxima changes rapidly from one revolution to the next, which is usually the case when the light is reflected off of a smooth conical surface. Synodic rotation period is characterised by intervals between minima of the satellite brightness. The light curves presented in Figure 9 were obtained synchronously in Odessa and Zalistski on 23 September 2020 at 18:58 (UTC), but to obtain visual similarity in terms of the shape of the light curves, the time-scale of the Zalistski observations was shifted additionally by four synodic periods. At the end of this pass, both light curves have a typical appearance with four major increases in brightness with a wide “diffuse” maximum and three quasi-specular flashes in between them (same as in Figure 7).

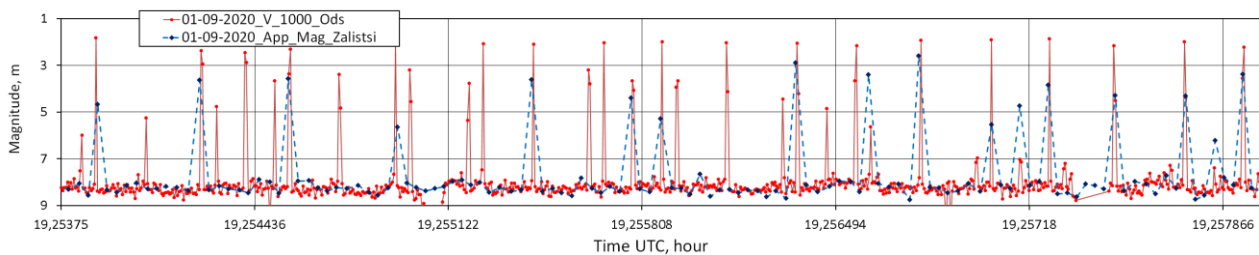


Figure 10: Portions of two light curves of the Ajisai satellite, synchronously observed in Odessa and Zalistsi on 01 September 2020 at 19:15 (UTC).

Synchronous brightness measurements of the geodetic satellite Ajisai were only employed to verify the time-scale displacement (shift) at OSs relative to each other and with respect to Coordinated Universal Time (UTC). It is a feasible procedure as the Ajisai light curve exhibits numerous glints with an ultra-short duration of about 0.01 seconds (Koshkin *et al.*, 2017), and the developed model of this satellite and its rotation makes it possible to calculate precisely a time lag in the occurrence of each glint as observed from different OSs within similar error. An off-nominal delay in the occurrence of the glint at two OSs will indicate a respective error at the zero-point of the time scale at one of the OSs.

Portions of two light curves of the Ajisai satellite, acquired synchronously in Odessa and Zalistsi, are plotted in Figure 10 (for the sake of convenience, one of the light curves is already shifted along the time scale by the computed time lag). As can be seen, a large number of glints occur synchronously, which suggests that there is no noticeable systematic error at the zero-point of the time scale at two OSs. Some glints are missing within the Ajisai light curve obtained in Zalistsi due to insufficient sample rate of brightness measurements at this OS.

The analysis of synchronous measurements of the Topex/Poseidon satellite brightness acquired by the network of observatories is still ongoing. The main challenge is a low sampling frequency of measurements taken at some observatories, which impairs the accuracy of calculating phase and time delays between correlated segments of the satellite light curves. A low signal-to-noise ratio of the brightness measurements for this satellite is also a factor that contributes to reduced accuracy of the resulting estimates of time lags.

4. Conclusions

It is well known that photometry of SO enables the estimation of their spin-axis orientations and spin rates in the most cost-effective manner; however, methods of determinate the spin-axis orientation from photometric data obtained at a single OS require long high-quality time-series of observations.

This paper introduces a new technique for estimating orientation parameters of slowly spinning SOs that relies on simultaneous multi-site photometry with high temporal resolution. Preconditions for effective planning and building a local photometric network of OSs have been

tested via computer simulation. Synchronous photometric observations from three OSs enable us to calculate time lags (phase delays) between correlated light-curve segments and almost instantly solve the problem of the determination of the direction of the SO rotation and its angular spin rate. Repeated measurement of these parameters by this local network or second independent measurements allows the estimation of the spatial orientation of the SO spin axis.

Monitoring the rotation of different SO in LEO requires a distributed local network comprising from five to nine OSs (photometric sensors). Such a local network will allow solving this problem in general, and in particular, it will make it feasible to estimate orientation of slowly rotating SOs that do not produce specular flares with respective peculiarities in their light curves.

References

- Gasdia F., Barjatya A., Bilardi S.: 2017, *Sensors (Basel)*, **17**(6), 1239. doi: [10.3390/s17061239]
- Hall D., Kervin P.: 2014, in: *Proc. of the Advanced Maui Optical and Space Surveillance Technologies Conference*; Maui, HI, USA. 9–12 September 2014.
- Hall D., Calef B., Knox K., Bolden M., Kervin P.: 2007, in: *Proc. of the Advanced Maui Optical and Space Surveillance Technologies Conference*; Maui, HI, USA. 12–15 September 2007.
- Hall D., Africano J., Archambeault D., Birge B., Witte D., Kervin P.: 2006, *The AMOS Technical Conference Proceedings*, Kihei, HI, 2006.
- Kurosaki H., Yanagisawa T., Nakajima A., Kuribayashi T. and Watanabe A.: 2005, *56th International Astronautical Congress of the International Astronautical Federation*, October 2005. <https://doi.org/10.2514/6.IAC-05-B6.1.09>
- Schafer E.: 2017, *Stereoscopic Light Curve Analysis of Space Debris Objects / Geology*. Universität Würzburg. <https://elib.dlr.de/127086/>
- Koshkin N., Shakun L., Korobeinikova E., Melikyants S., Strakhova S., Dragomiretsky V., Ryabov A., Golubovskaya T., Terpan S.: 2018, *Odessa Astron. Publ.*, **31**, 179. DOI: <http://dx.doi.org/10.18524/1810-4215.2018.31.147807>
- Koshkin N., Shakun L., et al.: 2017, *Advances in Space Research*, **60**, 7, 1389. DOI: <https://doi.org/10.1016/j.asr.2017.06.045>

DOI:<http://dx.doi.org/10.18524/1810-4215.2020.33.216434>

UKRAINIAN RADIO METEOR NETWORK — DEVELOPMENT AND FIRST RESULTS

Kulichenko M.O.¹, Kaliuzhnyi M.P.¹, Bushuev F.I.¹, Shulga O.V.¹, Malynovskyi Ye.V.²,
Savchuk S.G.³, Yankiv-Vitkovska L.M.³, Hrudynin B.O.⁴

¹ Research Institute “Mykolaiv Astronomical Observatory”

² Rivne Minor Academy of Sciences

³ Lviv Polytechnic National University

⁴ Oleksandr Dovzhenko Hlukhiv National Pedagogical University

niiko4kulichenko@gmail.com, nikalyuzhny@ukr.net, shulga-av@ukr.net

ABSTRACT. The network of the meteor observation in the radio range consisting of 6 stations located in Mykolaiv (3 stations), Rivne, Lviv and Hlukhiv has been created. The main goal of the network is to expand information about meteor phenomena, including the assessment of the kinematic parameters (velocities, radiants and orbital elements) of meteoroids and their relationship with other small bodies of the Solar system (potentially hazardous asteroids approaching the Earth). The operation of the meteor observing hardware and software complex is based on the continuous receiving of signals from FM radio station reflected from ionized meteor trains that occur in the Earth's atmosphere at altitudes of 80-100 km. SDR technology is used to receive radio signals from over-the-horizon FM broadcast stations reflected by a meteor train, which has allowed to improve the sensitivity and frequency selectivity of radio signals. In 2017–2020 the network registered 1093015 meteors. The observational data are posted on the RMOB website. Diurnal variation of meteor counts and comparison with Perseids meteor stream activity are presented in the work.

Keywords: Meteors, forward scattering, software defined radio (SDR).

АНОТАЦІЯ. Створено мережу спостереження метеорів у радіо діапазоні, яка складається з 6 станцій, що знаходяться в Миколаєві (3 ствнції), Рівному, Львові та Глухові. Основною метою мережі є розширення інформації про метеорні явища, включаючи оцінку кінематичних параметрів (швидкостей, радіантів та елементів орбіт) метеороїдів та виявлення взаємозв'язку з іншими малими тілами Сонячної системи (зокрема потенційно небезпечними астероїдами, що зближуються із Землею). Функціонування метеорного апаратурно-програмного комплексу базується на безперервному, цілодобовому прийомі сигналів радіомовної FM станції, відбитих від іонізованих метеороїдних слідів, що виникають в атмосфері Землі на висотах 80–100 км. Використання SDR технології для прийому радіосигналів загоризонтних FM-станцій, відбитих метеороїдним слідом, дало змогу поліпшити чутливість і частотну вибірковість прийому радіосигналів. За час роботи в 2017-2020 рр. мережею було зареєстровано 1093015

метеорних явищ. Спостережні дані у вигляді текстових таблиць погодинних чисел щомісяця відправляються на сайт RMOB. Для підтвердження достовірності даних спостережень проведено: а) перевірку добових варіацій кількості метеорів, зареєстрованих станціями мережі, на відповідність відомій залежності (спостереження метеорів в апексі та антиапексі); б) порівняння отриманих мережею характеристик для метеорного потоку «Персеїди», що спостерігався в серпні 2020 р., на відповідність очікуванім, як у часі появи, так і в інтенсивності. Для підвищення достовірності реєстрації метеорних явищ пропонується провести додаткові дослідження характеристик радіоперешкод, що діють в місцях дислокації станцій, з метою розробки методів їхнього придушення.

Ключові слова: Метеори, пряме розсіювання, SDR технологія.

1. Introduction

Forward scattering of radio waves off meteor trails is the most common and accessible way of meteors observation in radio band. The advantage of this way is that transmitter which has enough power is located behind the horizon and the observer only manage receiving station which is relatively easy to build. According to RMOB (Radio Meteor Observing Bulletin, <https://www.rmob.org/>) 46 observers of radio meteors from all over the world send their data online. Most of them (Europe) receive the signal from french military radar GRAVES, observers from USA receive the signal from VHF radio beacons, observers from Belgium set their own radar station which has small power but stable signal with known parameters. Radio meteor observers also establish networks in some countries: BRAMS (Belgium) (Calders et al., 2018), Bolidozor (Czech Republic) (Kakona et al., 2016). The main information received by radio meteor observers is the number of detected phenomena per hour, which allows both to estimate the parameters of meteor showers (period and peak of activity, observability function) and to monitor the distribution of meteoroid matter during the diurnal and annual cycles of the Earth motion.

Table 1: Locations of the network receiver stations and their characteristics

Location	Latitude	Longitude	Antenna height, m	Frequency, MHz	Distance between transmitter and receiver, km	Azimuth of antenna direction, deg
Mykolaiv (Ukraine)	46°58'17" N	31°58'22" E	65	88.2	905 (Kielce) 715 (Istanbul)	302 (Kielce) 199 (Istanbul)
Rivne (Ukraine)	50°37'23" N	26°14'55" E	205	94.8	637 (Budapest)	240
Lviv (Ukraine)	49°50'11" N	24°00'52" E	316	91.7	900 (Sonnenberg)	278
Hlukhiv (Ukraine)	33°54'56" N	51°40'43" E	175	88.2	900 (Kielce)	269

Table 2: Locations of transmitters and their characteristics

Location	Latitude	Longitude	Antenna height, m	Power, kW	Frequency, MHz
Kielce (Poland)	50°51'36.29" N	21°02'54.76" E	697	120	88.2
Budapest (Hungary)	47°29'30.17" N	18°58'44.00" E	592	100	94.8
Sonnenberg (Germany)	50°26'48.29" N	11°00'15.78" E	1005	100	91.7
Istanbul (Turkey)	41°00'58.75" N	29°03'56.11" E	384	100	88.2

Our main goal of creating and developing a meteor observations network using the forward scattering of FM radio broadcasting signals is to expand information about meteor phenomena, including the assessment of the kinematic parameters (velocities, radiants, and orbital elements) of meteoroids and their relationship with other small bodies of the Solar system (potentially hazardous asteroids approaching the Earth).

2. Hardware and software

It is possible to observe meteors by forward scattering from FM radio stations which work in frequency band 88-108 MHz. Such experiments were started in Ukraine at Research Institute «Mykolaiv astronomical observatory» (RI «MAO») in 2010 (Vovk et al., 2012). During the ten-year research period, hardware and software were developed to observe, extract and calculate the parameters of meteor phenomena (Vovk et al., 2017). Successful work on observations of meteor phenomena and automatic processing of results allowed expanding the number of stations and creating a network of radio observations of meteors in Ukraine. Herewith three network stations were set in RI «MAO», as well as standard station equipment was set in Rivne (Rivne Minor Academy of Sciences for Student Youth), Lviv (Lviv Polytechnic National University), and Hlukhiv (Olexandr Dovzhenko Hlukhiv National Pedagogical University). The RI «MAO» stations were named as «MAIN», «AMC» and «WAGON». The location of receiver stations

and corresponding transmitters are given in tables 1 and 2 as well as transmitters power and frequency and distances between receiving and broadcasting stations.

Network station hardware consists of:

- 1) 6 or 8-elements Yagi-Uda antenna;
- 2) SDR DVB-T receiver RTL2832U;
- 3) PC with following minimum requirements: the 150 GB hard drive, 2.0 GHz dual-core processor, 2GB RAM, and 32-bit operating system (OS).

The input information for searching for signals reflected from meteor trains is the signal from the output of the receiver quadrature detector or signal that has not been demodulated yet and whose characteristics fully correspond to the signal in the carrier frequency. Due to the use of such a signal, it is possible to determine the amplitude and Doppler shift of the frequency of the signal reflected from the plasma trail as a result of carrier frequency recovery on a known modulation signal, which is impossible for a signal that has been demodulated and analyzed in Bushuev et al., 2010.

The HSDR software, which is freely available, is used to record radio signals. The program allows to save recordings of the amplitudes values from the receiver quadrature channels as wav-files and image files of the amplitude-frequency-time plot (waterfall) for continuous monitoring of meteor activity. The minimum bandwidth is 250 kHz, and the maximum is 3.2 MHz. This is much larger than the spectrum width of the FM signal, which does not exceed 75 kHz, and which is necessary for optimal processing of this signal.

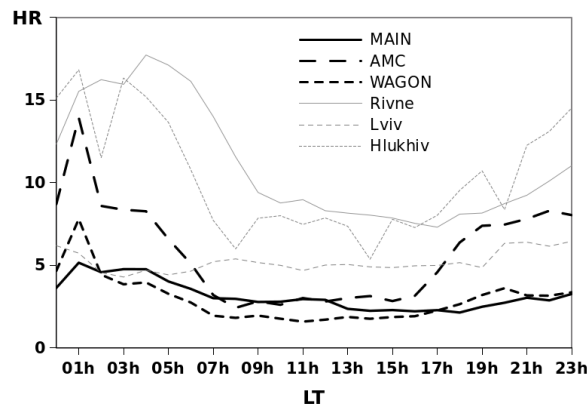


Figure 1: Diurnal variations of meteors HR for each receiving station

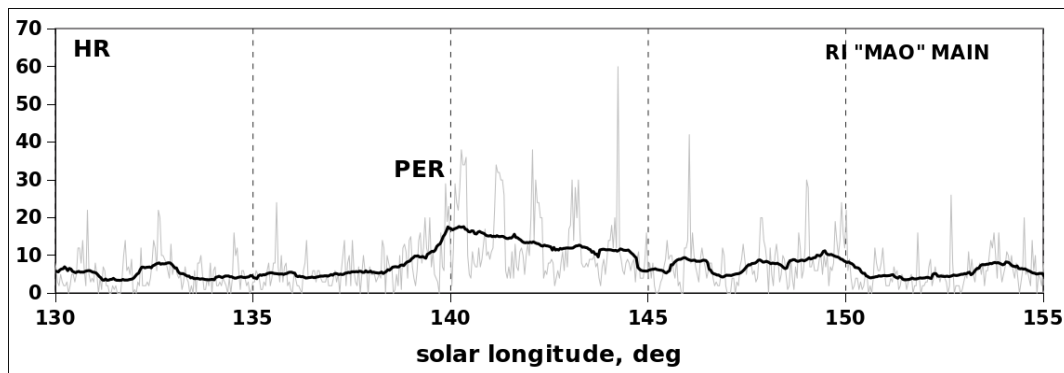


Figure 2: August hourly rate data obtained by RI "MAO" channel MAIN.

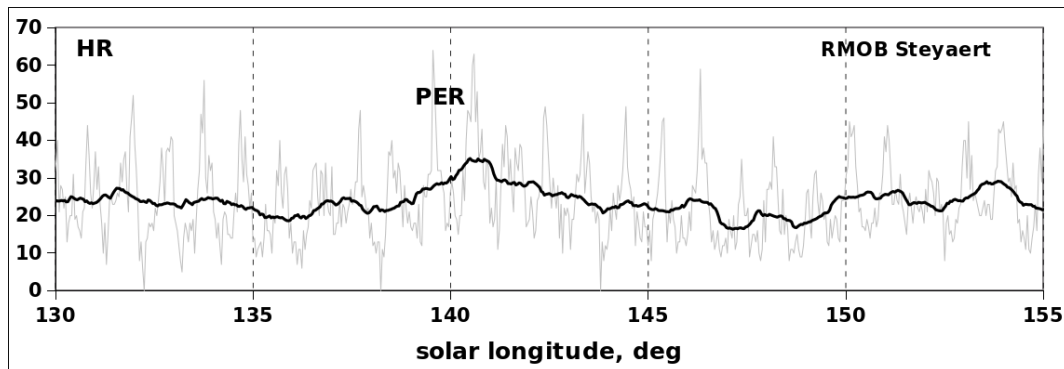


Figure 3: August hourly rate data obtained by RMOB user Chris Steyaert.

Each station provides continuous automatic processing of observational data and automatic e-mailing to users which interested in receiving daily data on space intrusions into the Earth's atmosphere. The method of processing and extracting of meteor phenomena parameters is described in Vovk et al., 2017. Monthly reports are also posted on the RMOB website. The daily amount of processed information per station is about 80 GB.

3. Results

Total amount of events identified as meteors registered by the network in 2017-2020 is 1093015. To confirm

reliability of meteor phenomena identification the diurnal variation of hourly rate was analyzed. From the early radio meteor research campaigns the certain shape of meteor number variation curve during day and night is found: the maximum of hourly rate (HR) is nearly at 6 LT (local time) and corresponds with meteoroids moving from apex source. The minimum of HR variation is at 17 LT caused by meteoroids of antapex source. Diurnal variations of meteors HR averaged for data observed in 2019 for each receiving station of the network are shown on fig. 1.

From the curves shown on fig. 1, it is seen that for stations in Lviv and Mykolaiv (MAIN) that variations of change in time of meteors quantity do not correspond to

expected. These features may be caused by the appearance of significant radio interference near the stations in certain periods during the year. Additional research is needed to solve this problem.

Certain character of diurnal variation of meteors HR typically observed when sporadic meteors only registered. For meteor showers another behavior is typical. On fig. 2 and 3 the comparison of August HR data obtained by RI “MAO” channel MAIN (fig. 2) and RMOB user Chris Steyaert (fig. 3) is shown. Both curves has maximum near solar longitude 140.0° which is corresponding with Perseids meteor shower peak activity. HR values on fig. 2 and 3 (gray line) are smoothed by 24 points moving average trend (black line).

4. Conclusion

The network of observations of the meteor phenomena in a radio range consisting of 6 stations located in Mykolaiv (3 stations), Rivne, Lviv and Hlukhiv is created. In 2017–2020 the network registered 1093015 meteor phenomena. The registration results are posted on the RMOB website. To confirm the reliability of these observations, the following was performed: a) verification

of daily variations in the number of meteors registered by network stations for compliance with the known dependence (meteor observations in the apex and antapex); b) comparison of the characteristics obtained by the network of major meteor showers (Perseids were chosen as an example) for compliance with the expected both at the time of peak activity and intensity. To increase the reliability of registration of meteor phenomena, it is proposed to conduct additional studies of the characteristics of radio interference operating in the locations of stations in order to develop methods for their suppression.

References:

- Bushuev F.I. et al.: 2010, *Cosm. Sci. and Tech.*, **16** (6), 68.
- Calders S. et al.: 2018, The Radio Meteor Zoo: involving citizen scientists in radio meteor research. European Planetary Science Congress EPSC2018-148.
- Kakona J. et al.: 2016, *preprint (arXiv:1606.02052)*.
- Vovk V.S. et al.: 2012, *Astroschool Report*, **8** (2), 166.
- Vovk V.S. et al.: 2017, *Sci. and Inov.*, **13** (1), 70.

DOI:<http://dx.doi.org/10.18524/1810-4215.2020.33.216433>

INVESTIGATION OF THE PHOTOMETRIC SYSTEM OF THE METEOR TV CCD CAMERAS

Kulichenko M.O.¹, Maigurova N.V.², Shulga O.V.³

Research Institute "Mykolaiv Astronomical Observatory", Ukraine

¹niiko4kulichenko@gmail.com, ²nadija@nao.nikolaev.ua, ³shulga-av@ukr.net

ABSTRACT. The study of meteoroids and the phenomena arising from their entry into the Earth's atmosphere is of considerable scientific and practical interest to obtain data on the origin and evolution of the solar system, to study the physics of planetary atmospheres, and to solve the problem of asteroid-cometary-meteoroid hazard. Today the most effective and informative are photometric and spectral studies of meteor phenomena, which provide information on the chemical composition and physical properties (density, combustion temperature, etc.) of meteoroids that allow us to classify these bodies by parental origin and mineralogical structure. This paper presents the results of a study of the photometric system of eight meteor telescopes of the same type with a lens having a wide field of view ($f = 50$ mm, $f/1.2$) and WAT-902H2 cameras. Telescopes equipped with broadband Cokin filters P050 (cyan) and P003 in the blue and red bands are installed in Mykolaiv and Odesa. An original method is used to observe meteors - the method of accumulation of shifted frames for TV cameras, which provide an accumulated image of reference stars in the form of points on a motionless telescope. In this work, simultaneous observations of reference stars in two filters obtained on 2 different observation nights were used. Cross-identification of the observational data with the Gaia DR2 catalog showed that the standard error of the residual coordinate differences (Obs – Gaia DR2) is about 7" for both coordinates in both filters. The bandwidths of our filters are closest to the photometric system Gaia BP/ RP, which was selected as a standard system to which the obtained instrumental stellar magnitudes were transformed. Transformation coefficients for converting instrumental stellar magnitudes into Gaia BP/RP photometric system were obtained by linear regression. Average standard photometric solution errors were 0.2^{mag} and 0.3^{mag} for red¹ and blue band, respectively. The possibility of determining the color index based on the array of common stars from observations in two bands is shown.

Keywords: Meteors, photometry, Gaia BP/RP photometric system, color index.

АНОТАЦІЯ. Вивчення метеороїдів та явищ, що виникають внаслідок їх входження в атмосферу Землі, має значний науковий та практичний інтерес для отримання даних про походження та еволюцію Сонячної системи, вивчення фізики планетних атмосфер, а також для вирішення проблеми астероїдно-

метеороїдної безпеки. Найбільш ефективними й інформативними на сьогоднішній день є фотометричні та спектральні дослідження метеорних явищ, які дозволяють отримати інформацію про хімічний склад і фізичні властивості (щільність, температуру згоряння тощо) метеороїдів, а відповідно і класифікувати ці тіла за походженням батьківських тіл і мінералогічною структурою. Ця робота представляє результати дослідження фотометричної системи восьми метеорних телескопів одного типу з об'єктивом, що має широке поле зору ($f = 50$ мм, $f/1,2$) та камерами WAT-902H2. Телескопи, оснащені широкосмуговими Cokin фільтрами у червоному(P003) та синьому (P050) діапазонах, встановлені у Миколаєві та Одесі. Для спостережень метеорів використовується оригінальний метод – метод накопичення кадрів зі зсувом для ТВ камер, які забезпечують отримання накопиченого зображення опорних зірок у вигляді точок на нерухомому телескопі. У даній роботі були використані одночасні спостереження опорних зірок в двох фільтрах, отримані в 2 різні ночі спостережень. Виконана крос-ідентифікація отриманих даних з каталогом Gaia DR2 показала, що середньоквадратична помилка остаточних різниць координат (Obs – Gaia DR2) становить близько 7" для обох координат в обох фільтрах. Смуги пропускання наших фільтрів найбільш близькі до фотометричної системи Gaia BP/RP, яка була обрана в якості стандартної системи, до якої було переведено отримані інструментальні зоряні величини. Коефіцієнти перетворення для переведення інструментальних значень величин у фотометричну систему Gaia BP/RP отримані методом лінійної регресії. Середні стандартні похибки фотометричного розв'язку склали 0.2^{mag} та 0.3^{mag} відповідно для червоного та синього діапазонів. Показано можливість визначення показника кольору на основі сформованого масиву спільних зірок зі спостережень у двох смугах.

Ключові слова: Метеори, фотометрія, Gaia BP/RP фотометрична система, кольоровий показник.

1. Introduction

Photometric studies can be effective and informative means to obtaining information about the chemical

composition and physical properties of the target bodies. But in order to use and compare the data obtained by different scientists at different times, it is required to measure magnitudes to a standard internationally agreed system with good precision. The most studied and widespread in this respect is the UBVRI Johnson - Cousins system, in which a large amount of astronomical data has been accumulated. Unfortunately, there are a number of difficulties for the mass reproduction of this system, associated both with the availability of filters and with a limited number of standard stars for performing photometric reductions. Gaia DR2 was released in April 2018 and contains a photometric catalogue of more than 1 billion sources over all celestial sphere. This release contains color information in the form of integrated BP and RP photometry in addition to the latest G-band photometry (Riello et al., 2018). This is full-sky survey with the unprecedented spatial resolution, high accuracy could use for the purpose of photometric calibration for wide range of astronomical tasks.

2. Instrumental system

Four pairs of meteor telescopes equipped with TV CCD cameras WAT-902H2 and lens with focal length 50 mm (f/1.2) are located at RI «MAO» (2 pairs), Vitovka (1 pair, 12 km baseline) and Kryzhanivka (1 pair, 100 km baseline). First results obtained with these telescopes are described in Kulichenko et al., 2019. Telescopes equipped with broadband Cokin filters P050 (cyan) and P003 (red) hereinafter referred to as blue and red bands. Observations are provided using track-and-stack technique for obtaining frames with reference stars (Kulichenko et al., 2015). Cameras work in the interlace mode (50 fps) and number of accumulated frames is 500 (10 s).

3. Astrometric Reductions and Accuracy

Processing of obtained observations included next steps:

- 1) Frames filtering using software for processing of the CCD images developed in RI «MAO»;
- 2) Extracting stars and cross-match with catalog Tycho-2 for obtaining reduction coefficients using Astrometry.net software (Lang et al., 2010). Brightness of extracted stars in ADU with subtracted background also saved in result files;
- 3) Obtaining a summary csv-table for all detected stars with measured celestial coordinates and streams from all processed frames using a Python script developed at the Research Institute "MAO". The table also includes coordinates and magnitudes from Tycho-2 catalogs for all stars.

In this study, further results and calculations were obtained on the basis of arrays of simultaneous observations of stars for two evenings (2018/11/08 and 2018/11/09) in P050 (BLUE) and P003 (RED) bands.

The obtained observational arrays were cross matching with Gaia DR2 catalog to estimate positional accuracy. The standard deviations of the residual coordinate differences (Obs - Gaia DR2) in right ascension and declination were used as an estimate of the accuracy of the observations. Cross match procedures was made by TOPCAT software (Taylor M., 2005) with 30" match radius parameters. The results of cross matching are shown in Table 1. (Obs – Gaia DR2)

differences and their standard deviations in right ascension and declination are given in column 3, N – number of stars. Differences in right ascension include cos DE.

As you can see from the table, there are no significant systematic differences between obtained coordinates and Gaia DR2 catalog. The accuracy is almost the same for both coordinates in the blue and red ranges.

Table 1: Results of cross matching between observational arrays and Gaia DR2 catalog

Data	Band	(Obs – Gaia DR2)		N
		RA, arcsec	DE, arcsec	
11/08	Blue	-0.7 ± 6.8	-0.5 ± 6.6	6490
11/08	Red	0.5 ± 6.9	0.0 ± 6.6	1925
11/09	Blue	-0.5 ± 6.9	-0.5 ± 6.7	1647
11/09	Red	-0.2 ± 6.7	0.2 ± 6.7	1530

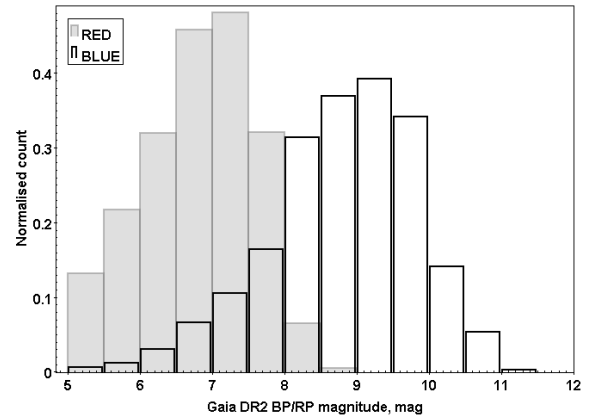


Figure 1: Histogram distribution in BP and RP Gaia DR2 magnitudes.

The histogram of distribution in BP Gaia DR2 magnitude for observational array with blue filter and RP Gaia DR2 magnitude for observational array with red filter is presented in Fig. 1. The difference in penetration for the two bands is associated with the higher sensitivity of WAT-902H2 camera in the blue region.

4. Photometric reductions

The brightness measurements of stars in the CCD images were carried out using built-in source extractor of the Astrometry.net software. The counts from the stars with the subtracted background were converted to the scale of instrumental magnitudes according to the known ratio:

$$M_i = -2.5 \lg(\text{Flux})$$

The brightness correction for the relative change in the air mass in the frame field of view was not made here. Since the Cokin P050 (cyan) and P003 (red) filters have wide bandwidths, Gaia DR2 BP/RP photometric system has been selected as the standard system. The relationship between magnitudes and color index in these systems can be represented in the form (Hardy, 1967):

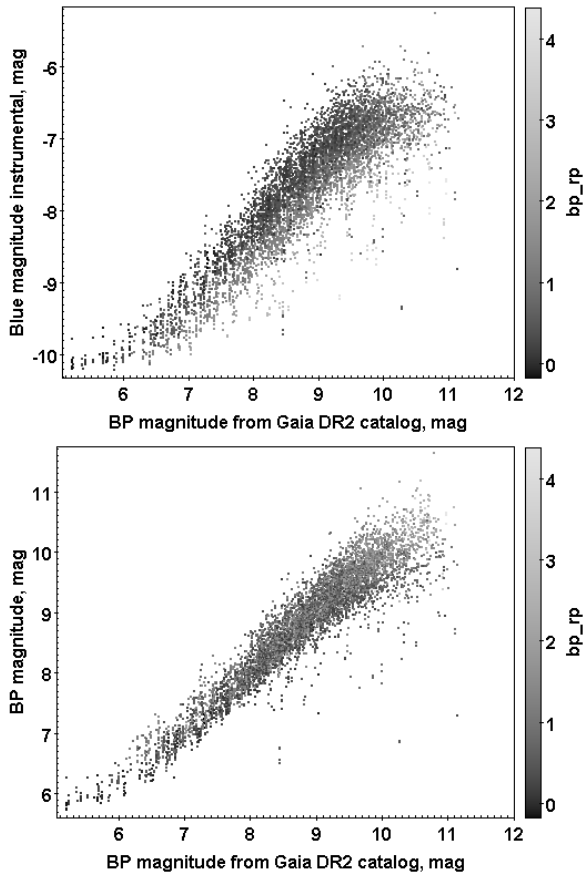


Figure 2: Relation between instrumental and standard magnitudes for observations in blue range, up – before transformation, down – after transformation.

$$Mag_{Gaia}^i = a1 \times Mag_{Instr}^i + a2 \times (BP - RP)_{Gaia}^i + M_0^i,$$

$$(BP - RP)_{Gaia}^i = a3 \times C_{Instr}^i + C_0^i,$$

where $Mag_{Gaia}^i, (BP - RP)_{Gaia}^i$ – catalog values of star magnitude and color index, $Mag_{Instr}^i, C_{Instr}^i$ – observational values of star magnitudes and color indices, $a1, a2, a3$ – transformation coefficients, M_0^i, C_0^i – zero point constant.

The transformation coefficients were found by the least squares method. The solution was carried out by the method of fixed-point iteration using the 3-sigma criterion. The calculated values of transformation star coefficients and their errors are presented in Table 2.

Table 2: Transformation coefficients (star magnitude)

	$a1$	$a2$	M_0	SD	N
B	0.980 ± 0.004	0.504 ± 0.004	15.84 ± 0.03	0.25	7684
R	0.938 ± 0.005	-0.215 ± 0.004	14.08 ± 0.04	0.21	3302

The Fig. 2 presents correlation between instrumental and Gaia DR2 magnitudes before and after recalculation of the instrumental magnitudes.

As could be seen from table 2 the accuracy of link between the two systems is 0.25^{mag} in blue band and 0.21^{mag} in red band.

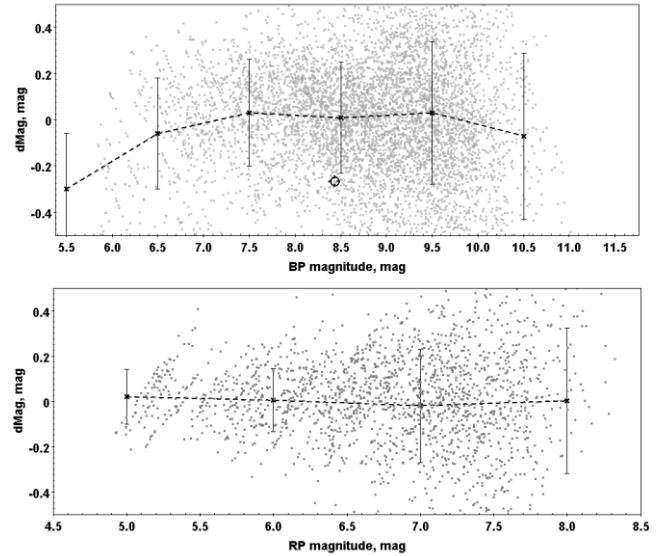


Figure 3: Residual differences between instrumental and standard magnitudes vs standard magnitude from Gaia DR2 catalog.

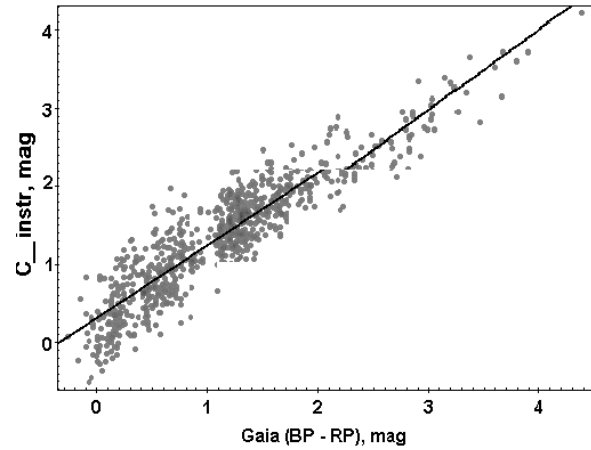


Figure 4: Relation between instrumental and standard (Gaia DR2) color indexes

Relation between residual differences between standard and instrumental magnitudes is presented in Fig. 3. The figure shows the absence of significant systematic differences in magnitudes in the observational range. The random error is determined by the errors of the least squares method solution.

To calculate the color relation, the observational arrays are cross-matched to find common stars in the blue and red bands. The coefficients were found by the least squares method, similar to the scheme for determining the transformation coefficients for the star magnitudes. The most widely used color characteristic of astronomical objects is (B–V). The values (B–V) for our stars were selected from APASS DR9 catalog (Henden et al., 2015). Transformation coefficients between (B–V) color and instrumental color index also has been calculated. The calculated values of transformation color coefficients and their errors are presented in Table 3.

Table 3: Transformation coefficients (color index)

	a_3	C_0^i	SD	N
BP – RP	0.88 ± 0.01	-0.08 ± 0.02	0.28	855
B – V	0.69 ± 0.02	0.06 ± 0.04	0.32	265

The obtained data show the possibility to estimate of the meteors color from the observations at the meteor telescopes equipped filters in two bands.

5. Conclusion

The transformation coefficients to link the instrumental values of magnitudes and color indexes of the meteor complex telescopes to the Gaia BP/RP photometric system were calculated.

The mean standard errors of the photometric solution are 0.25^{mag} and 0.21^{mag} for BP and RP ranges, respectively. The possibility of color index determinations based on reference stars observations with red and blue broadband filters is shown.

Acknowledgements. This research has made use of the VizieR catalogue access tool, CDS, Strasbourg, France.

References:

- Hardy X.: 1967, *Astronomical Techniques ed.by W.A. Hiltner*, 536.
- Henden A. et al.: 2015, *ASS*, **336**, 16.
- Kulichenko N. et al.: 2015, *WGN*, **43**(3), 81.
- Kulichenko M.O. et al.: 2019, *OAP*, 32, 165.
- Lang D. et al.: 2010, *AJ*, **137**, 1782.
- Riello M. et al.: 2018, *A&A*, **616**, A3.
- Taylor M.: 2005, *ASP Conf. Ser.*, **347**, 29.

DOI:<http://dx.doi.org/10.18524/1810-4215.2020.33.216436>

SIGNATURES OF EXOCOMET ACTIVITY AROUND STARS AT DIFFERENT EVOLUTIONARY STAGES

Y. Kuznyetsova, Ya. Pavlenko, I. Kulyk, O. Zakhochay, P. Korsun,
S. Borysenko, V. Krushevska, O. Shubina, M. Andreev

Main astronomical observatory of NAS of Ukraine,
Kyiv, Ukraine, juliana@mao.kiev.ua

ABSTRACT. We discuss the current state of problems associated with the discovery and study of exocomets, i.e. objects of extrasolar systems, that are in many aspects similar to the solar system comets. Thus far, more than 4,300 exoplanetary systems have been discovered, but little is known about the populations of subplanetary bodies in these systems, in particular comets. Existing theories of planet formation suggest that populations of small bodies in the planetary systems should be numerous, especially at the early stages of their formation. Currently, most of the stars observed with the confirmed transit exoplanets and candidate stars with exoplanetary systems have been collected in the Kepler and TESS space mission databases. These databases can be used for a search and study of the exocomet transit signatures in extrasolar systems. So far, the number of observed cases of exocomet transits has been small, only about 20 events. Due to the rapid accumulation of data, new researches aimed to identify the specific transit events and study the physical characteristics of small bodies in the extrasolar systems are of great importance. Worth considering is the concept of “falling evaporating bodies”, massive enough bodies surrounded by mini-atmospheres, which fall on the parent star. The events might produce the variable, short-time red-shifts of some spectral features in their spectra. Alternative evidence of exocomet transits can be obtained by detection of the cometary emissions in CO, C, and O lines in the millimeter region of the spectra of debris disks by the ALMA and APEX telescopes. We discuss the known detection methods based on the analysis of the photometric and spectral series of observational data of space missions and ground-based complexes. Some results of experimental studies of the exocometary transit signatures obtained by other authors are presented and discussed.

Keywords: extrasolar planetary systems, exocomets.

АНОТАЦІЯ. У даній роботі обговорюється сучасний стан проблем, пов'язаних з відкриттям та дослідженням екзокомет — об'єктів позасонячних систем, багато в чому подібних до комет Сонячної

системи. На сьогодні відкрито вже більше 4300 екзопланетних систем, але водночас мало що відомо про популяції субпланетних тіл у цих системах, зокрема комет. Існуючі теорії формування планет передбачають, що популяції малих тіл планетних систем можуть бути багаточисельними, особливо на ранніх стадіях їх формування. Наразі основна кількість спостережень зір із підтвердженими транзитами та ймовірних зір-кандидатів з екзопланетними системами накопичена в базах даних космічних місій Kepler та TESS. Ці бази даних можуть використовуватися і для пошуку та вивчення проявів екзокометної активності в позасонячних системах. На сьогодні чисельність спостережених проявів екзокометної активності є дуже незначною, всього близько 20 подій. Але швидке накопичення даних стимулює активні дослідження, направлені на виявлення та вивчення фізичних характеристик малих тіл у позасонячних системах. У нашій роботі представлено основні методи детектування, які ґрунтуються на аналізі фотометричних та спектральних рядів спостережених даних космічних місій та наземних спостережених комплексів. Наведено та обговорено результати експериментальних досліджень проявів екзокометної активності, отриманих іншими авторами. Наголошується на необхідності більш комплексного аналізу наявних проблем. Вартою розгляду є концепція падіння на зорю маломасивних тіл, оточених мініатмосферами, так званих “falling evaporating bodies”. У спектрах це проявляється появою мінливих, часто короткотривалих, змін зі зміщенням у червону ділянку спектра. Іншим ймовірним свідченням кометної активності є випромінювання в лініях CO, C та O в міліметровій ділянці спектра, що спостерігалися в уламкових дисках телескопами ALMA та APEX.

Ключові слова: позасонячні планетні системи, екзокомети.

1. Introduction

During recent years, the transit method for the study of extrasolar planetary systems has shown its effectiveness. Using this method, the following low-mass bodies have already been discovered:

- **Sub-Earths:** the smallest solid body, moon-size Kepler 37b object, which was detected in 2013 [Barclay et al., 2013].
- **Disintegrating planets:** Ceres-sized objects with short-period orbits (~ 10 hours), which were detected spectroscopically, but detection is possible by the transit photometric method assumed that objects are surrounded by optically thick material (eg, dust). This fact leads to increasing of depths on the transit light curve of the parent star. Examples of such objects are KIC 12557548b, KOI 3794 [Rappaport et al., 2012], KOI 2700b [Rappaport et al., 2014?], K2-22 [Sanchis-Ojeda et al., 2015].
- **Comets in other stellar systems:** 6 asymmetric transits in the system KIC 3542116 (F2V) and one in the system KIC 11084727 (F5V) were detected; their transit light curves have an asymmetric appearance and correspond to that, which could be caused by an object having the cometary coma and tail [Rappaport et al., 2018].

2. Orbital observational complexes

The majority of observations of stars with confirmed transits and probable candidate stars with exoplanetary systems have been accumulated in the Kepler and TESS space mission databases. Kepler Space Telescope was the first mission planned specifically to discover and study exoplanets resembling terrestrial planets located in a habitable zone. Observations were carried out using 0.95 m telescope of Schmidt system with a CCD photometer in the spectral range 420 – 905 nm. During the period from 2009 to 2013, the photometric monitoring of brightness changes of about 170,000 stars within a sky area ~ 115 square degrees was performed. The photometric accuracy for calculating the brightness curves is estimated at 0.002% for a star of 12 magnitude and spectral class G2V when integrated for 6.5 hours [Jenkins et al., 2010].

The main task of the TESS (Transiting Exoplanet Survey Satellite) mission is the search for transits by exoplanets across the nearest and brightest stars. The TESS is located in high satellite orbit in 2:1 resonance with the Moon. It maintains the optimal thermal

regime and necessary geometric conditions for the approximately similar visibility of selected sky area for the observations. The TESS has four wide-angle cameras, each with a field of view $24^\circ \times 24^\circ$, which makes it possible to obtain simultaneously an image of the celestial sphere band $24^\circ \times 96^\circ$ from the ecliptic plane to its pole. A total of 15,000 – 20,000 stars are observed in each band for 27 days. The bandwidth of the cameras cuts the spectral region 600 – 1040 nm. It is expected that the catalog final version will contain the results of monitoring of stars brighter than 13 mag in the camera spectral band, meanwhile a particular attention will be paid to more than 200,000 cool dwarfs of spectral classes F-G-K-M to search for exoplanets with radii between 2.5 and 4.2 of the Earth radius [Stassun et al., 2019].

3. The difference between the light curves of exoplanets and exocomets

Ordinary transit profiles of exoplanets are U-shaped. If a planet passes through the host star disk, the light curve has a symmetrical profile with respect to the center of the transit. The asymmetric shape of the photometric transit profile, as it seen in Fig. 1, can be considered as a manifestation of the presence of an object with the dusty tail. Rappaport et al. (2018) investigated a set of 201,250 photometric light curves from the Kepler database. Several transits were found and interpreted as exocometary ones for stars KIC 3542116 (Fig. 1) and KIC 11084727. These transits have a pronounced asymmetric shape with a steeper drop in starlight at the beginning of the transit event and a slower increase in brightness of the star when leaving the shadow. The similar shape and depth of transits are theoretically predicted in the work of Lecavelier des Etangs et al. (1999) for the case when an extended comet-like object surrounded by a dusty atmosphere passes through the star's disk. The depth of the light curve in Fig. 1 is about 0.1%, the duration of the transit is about 1 day. Opposite to planet transits, photometric profiles of exocometary transits reveal a relatively small amplitude and a fairly long duration, an average of 1.5 days. It is worth to note that the transit profile of a disintegrating planet with the long dusty tail and small fragments could also have a similar shape. However, the researchers ruled out this possibility, because in this case there should be periodicity in transit events, meanwhile an exocomet transits are sporadic ones.

Rappaport et al. (2018) calculated the basic parameters of exocomets. They assumed that the asymmetry of the transit profile is associated with the transit of a comet having the dust tail shifted in the direction opposite to the direction of the comet motion. The calculated orbital velocities are within 35.2

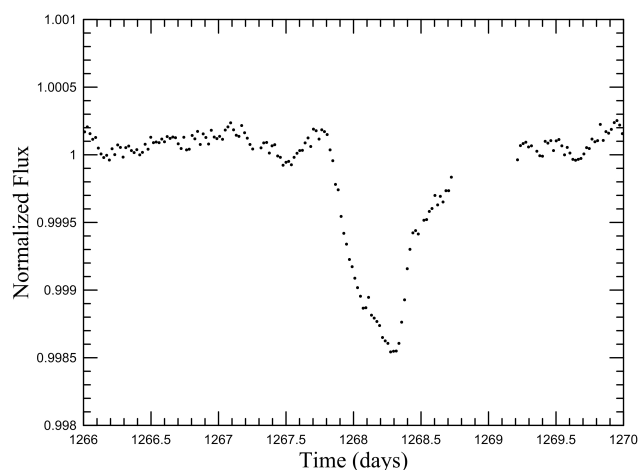


Рис. 1: Asymmetric transit of an exocomet in the system of KIC 3542116 plotted based on the data from MAST archive.

– 89.8 km/s; tail lengths are within the range from 3.1×10^5 to 5.9×10^5 km. The estimated mass of the exocomet $M_c \geq 10^{17}$ g, correlates with the mass of Halley’s comet, i.e. 2.2×10^{17} g [Cevolani et al., 1987].

Another interesting case for exocomet investigation provides the star Beta Pictoris (β Pictoris) located at a distance of 63.4 light years from the Earth. Fig. 2 shows the image of the β Pictoris system made by HST [Mouillet et al., 1997]. The age of the star is estimated as 8 – 10 Myrs. Icy bodies similar to those in the Kuiper belt in our Solar System are likely condensed in dust and gas disc around the star. Fortunately, from the Earth we can see the disk from its edge. Strong dust scattering makes the disk quite bright for the observations .

Zieba et al. (2019) analyzed the TESS observation of star β Pictoris for the period October 19, 2018 – February 1, 2019 and identified several asymmetric transits. These authors estimated the orbital velocity of exocomet to be 19.6 ± 0.1 km/s, and the probable length of the tail of order 2×10^8 km at a distance from the star of $r = 1$ AU.

4. Stars and exocomets

Existing theories of planet formation suggest that populations of small bodies in planetary systems should be large. It is expected that more pronounced signatures of exocometary activity can be detected at the early stages of the stellar evolution, i.e. around the stars of spectral types A – F, surrounded by debris disks of aged from several millions to 0.5 Gyr. It is considered that more massive stars may have massive protoplanetary (primordial) disks. In this case larger bulks of secondary material, like disk fragments, will remain around a star and become a source of cometary and asteroid “material” in the system. Such fragments

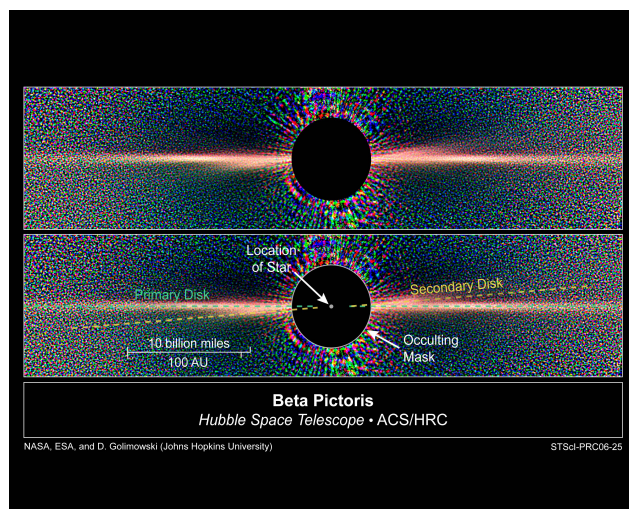


Рис. 2: The disk of β Pictoris formed by the multiple belts of debris material with different inclinations. The size of dust disk is much more than 100 AU [Wahhaj et al., 2003; Okamoto et al., 2004; Quillen et al., 2007]. Credits: ©NASA, ESA, D. Golimowski (Johns Hopkins University), D. Ardila (IPAC), J. Krist (JPL), M. Clampin (GSFC), H. Ford (JHU), and G. Illingworth (UCO/Lick) and the ACS Science Team

can be expected to exhibit CO emissions, as can be seen for HD 181327 [Marino et al., 2016], η -Corvi [Marino et al., 2017], and Fomalhaut [Matrà et al., 2017]. For these systems, circumstellar CO emissions were recorded by radio observations. It was interpreted in favor of the presence of significant populations of small bodies at large orbital distances.

In general, emissions of CO, C and O lines are observed in debris disks by ALMA and APEX telescopes in the millimeter region of the spectrum. The Table 1 presents the list of the young stars where gas has been detected and which may be of interest for finding exocomets or other low-mass bodies.

As it was noted above, the bulk of the photometric observations of transit phenomena is accumulated in the databases of the space telescopes. During the TESS mission, special attention is paid to the observations of close bright dwarfs having radii in the range $\sim 0.1 - 4.0$ solar radius, in order to detect transits caused by small objects of the Earth’s size. Could we expect the evidences of exocometary activity in the systems of these stars? Assuming that the main component of exocomets (like for comets of the Solar system) is the ices of volatile elements, we expect the development of comet-like activity when the object is approaching to the parent star and its surface temperature increases. We calculated the dependence of the equilibrium temperature on the distance from a host star, assuming that the amount of radiation absorbed by the nucleus is equal to the amount of the radiation

Табл. 1: Stars with debris disks in which gas was detected.

Star	Right ascension	Declination	Reference
HD 21997	03 31 54	-25 36 51	Moór et al. 2011
HD 32297	05 02 27	+07 27 40	Redfield 2007
HD 10908 (eta Crvor, 8 Crv)	12 32 04	-16 11 46	Marino et al. 2017
HD 149630 (sig Her, 35 Her)	16 34 06	+42 26 13	Chen & Jura 2003
HD 158643 (c Ophor, 51 Oph)	17 31 25	-23 57 46	Thi et al. 2013
HD 181327	19 22 59	-54 32 17	Marino et al. 2016

emitted. It is shown in Fig 3 together with the sublimation temperatures of pure ices of certain volatile elements (CO, NH₃, CH₃OH, H₂O), which have been found in the solar system comets [Meech and Svoren, 2004]. These estimates are based on the simple equilibrium model and some parameters derived for the solar system comets, such as the surface albedo and roughness, bolometric emissivity, zero thermal inertia as well as on assumption of rapid rotation of the comet's nucleus [Spencer et al., 1989]. Nevertheless, Fig. 3 shows that in the exoplanet systems similar to our Solar system, we can expect the manifestation of cometary activity due to sublimation of water ice at distances of about 3 AU. In the systems of the hosting stars larger than the Sun (1.4 – 4.2 solar radii) the ices of volatile elements, including water ice, are likely to evaporate at distances greater than 20 AU. Comet-like activity at close distances is likely to be caused only by the decay and evaporation of the solid component of the comet's nucleus. Around smaller stars (0.65 – 0.79 solar radii), the comet-like activity can occur at closer distances (~ 1 AU) and only if the cometary nucleus includes a significant part of ice impurities that are more volatile than water ice. Therefore, to search for comet-like activity in the TESS satellite database, it is necessary to select the objects from the list of candidates, which includes the dwarfs of spectral types F0 – K5 with radii in the range of 0.7 – 2.0 of the solar radius. Both the relatively small radii of these stars and the effective temperatures in the range of 4000 – 7500 K increase the probability to detect a transit phenomenon caused by small objects, including exocomets. Indeed, the volatile small bodies in the systems of such stars may develop the comet-like activity in the interval of distances of 1 – 20 astronomical units from the host star.

5. Conclusions

Nowadays, the very fact of the existence of comets in the exoplanetary systems is not in doubt. First robust detections, both spectroscopic and photometric, point out likely the abundance of exocomets in extrasolar stellar systems. We expect that similarly

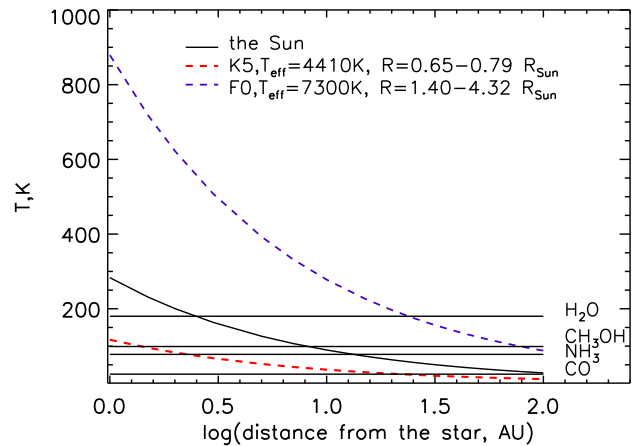


Рис. 3: Equilibrium black-body temperature vs. the distance to a host star. The horizontal lines mark the sublimation temperature of the pure ices of corresponding molecules in vacuum.

to comets in the Solar system, exocomets are bodies of the ages comparable with the age of the planetary system formation. The detection of exocomets can be interpreted as indirect evidence of the existence of exoplanets, as well as the presence of dust in the system might indicate a large number of collisions of small bodies in this system.

According to the modern knowledge, volatile small bodies — remnants of the planet formation — can deliver water and other volatile substances to the planets, which indicate their importance for astrobiology. There is no doubt that the discovery of exocomets by photometric and spectral methods using the ground-based optical observations and space orbital telescopes, provide a better understanding of the evolution of star-planetary systems and the nature of physical processes in the Solar system.

Acknowledgements. This study was funded as part of the routine financing programme for institutes of the National Academy of Sciences of Ukraine. The researches were partially supported by the 1230 program 16.01.2020 № 3/20 of the National Academy of Sciences and grant of the National Research Foundation of Ukraine № 2020.02/228.

References

- Barclay T., Rowe, J.F., Lissauer J.J., et al.: 2013, *Nature*, **494**, issue 7438, 452.
- Cevolani G., Bortolotti G., Hajduk A.: 1987, *Nuovo Cimento C Geophysics Space Physics C*, **10**, 587.
- Chen C.H. and Jura M.: 2003, *Astrophys. J.*, **582**, issue 1, 443.
- Jenkins J.M., Caldwell D.A., Chandrasekaran H. et al.: 2010, *Astrophys. J. Lett.*, **713**, issue 2, L120.
- Lecavelier Des Etangs A., Vidal-Madjar A., Ferlet R.: 1999, *Astron. and Astrophys.*, **343**, 916.
- Marino S., Matrà L., Stark C., et al.: 2016, *MNRAS*, **460**, issue 3, 2933.
- Marino S., Wyatt M.C., Panić O., et al.: 2017, *MNRAS*, **465**, issue 3, 2595.
- Matrà L., MacGregor M.A., Kalas P., et al.: 2017, *Astrophys. J.*, **842**, issue 1, id. 9, 15 pp.
- Meech K.J., Svoren J.: 2004, *Comets II Festou M.C., Keller H.U., and Weaver H.A. (eds.)*, University of Arizona Press, Tucson, 745 pp., 317.
- Moór A., Bbrahám P., Juhász A., et al.: 2011, *Astrophys. J. Lett.*, **740**, issue 1, id. L7, 6 pp.
- Mouillet D., Lagrange A.-M., Beuzit J.-L., Renaud N.: 1997, *A&A*, **324**, 1083.
- Okamoto Y.K., Kataza H., Honda M., et al.: 2004, *Nature*, bf 431, issue 7009, 660.
- Quillen A.C., Morbidelli A., and Moore A.: 2007, *MNRAS*, **380**, issue 4, 1642.
- Rappaport S., Barclay T., DeVore J., et al.: 2014a, *Astrophys. J.*, **784**, issue 1, id. 40, 16 pp.
- Rappaport S., Levine A., Chiang E., et al.: 2012, *Astrophys. J.*, **752**, issue 1, id. 1, 13 pp.
- Rappaport S., Vanderburg A., Jacobs T., et al.: 2018, *MNRAS*, **474**, issue 2, 1453.
- Redfield S.: 2007, *Astrophys. J.*, **656**, issue 2, L97.
- Sanchis-Ojeda R., Rappaport S., Pallè E., et al.: 2015, *Astrophys. J.*, **812**, issue 2, id. 112, 22 pp.
- Spencer J.R., Lebofsky L.A., and Sykes M.V.: 1989, *Icarus*, **78**, 337.
- Stassun K.G., Oelkers R.J., Paegert M., et al.: 2019, *AJ*, **158**, issue 4, id. 138, 21pp.
- Thi W.F., Ménard F., Meeus G., et al.: 2013, *Astron. and Astrophys*, **557**, id. A111, 11 pp.
- Wahhaj Z., Koerner D.W. Ressler M.E., et al.: 2003, *The Astrophysical Journal*, **584**, issue 1, L27, 5pp.
- Zieba S., Zwintz K., Kenworthy M. A., Kennedy G.M.: 2019, *Astron. and Astrophys.*, **625**, id. L13, 7 pp.

DOI:<http://dx.doi.org/10.18524/1810-4215.2020.33.216467>

DEGRADATION OF THE REFLECTANCE PROPERTIES OF SOME GSS IN SPACE, PRELIMINARY RESULTS

P.P.Sukhov¹, K.P.Sukhov²

¹ Astronomical Observatory of the I. Mechnikov Odesa National University, Odesa, Ukraine

² National Space Facilities Control and Testing Centre, Ukraine

ABSTRACT. A spacecraft in near-Earth orbit is exposed to extreme environmental factors, such as high vacuum, zero gravity, collisions with meteors and orbital debris, corpuscular and electromagnetic radiations, etc. These factors result in changing properties of spacecraft surfaces which leads to changes in mechanical, optical, electrical and physical properties of materials and elements of spacecrafts. This paper presents experimental data obtained from ground-based photometric observations of several geostationary satellites (GSS) built on different types of buses, starting from the beginning of their operational lives and during several years after their launches. It has been experimentally proved that spectral reflectance properties of the satellite surface materials undergo gradual degradation with time of the satellite's stay in space. Noticeable changes in spectral reflectance properties of GSS make it possible to detect damages to the satellite external payload. Comparison of changes in the reflective characteristics of different platforms over time can show the level of technical and scientific progress of spacecraft designers.

АНОТАЦІЯ. Космічний апарат, що знаходиться на навколосемній орбіті, піддається впливу цілого комплексу чинників: глибокий вакуум, невагомість, зіткнення з метеоритами і частинками штучного походження, корпускулярне і електромагнітне випромінювання різних видів і т.д. В результаті змінюються властивості поверхні, що призводить до зміни механічних, оптичних і електрофізичних характеристик матеріалів і елементів космічного апарату. У статті представлені експериментальні дані, отримані з наземних фотометричних спостережень декількох геостационарних супутників з різними типами платформ з моменту початку роботи супутника і через кілька років після початку роботи. Експериментально підтверджено, що спектральна відбивна здатність матеріалів поверхні супутника поступово деградує в залежності від часу перебування в космосі. За значної зміни спектральних відбивних характеристик геостационарного супутника можливо визначити пошкодження зовнішньої корисного навантаження супутника. Порівняння змін відбивних характеристик різних платформ з часом може

показати рівень технічного та наукового прогресу конструкторів космічних апаратів.

1. Introduction

Studying the effects of the harsh space environment on the optical properties of materials is a topical and challenging issue of great interest to not only designers and engineers of space-based systems. According to expert data, the space environment effects contribute significantly to breakdowns, failures and malfunctions in spacecraft operations [1].

The following key factors affect a spacecraft's surface in the space environment:

Meteoric dust and solid particles of orbital debris that affect optical properties of the surface;

Temporal effect of ageing (degradation) of the materials covering a spacecraft's surface and solar arrays under high-vacuum conditions;

Different types of radiations affecting photo-voltage of solar arrays, especially when solar flares occur or when the spacecraft travels through the Van Allen radiation belts. Exposure to high-energy electrons results in the breaking and reforming of physical and chemical bonds;

Extreme temperature variations due to continuous transition of the orbiting spacecraft body from excessive cooling in dark portions of its orbit to heating when illuminated by the Sun, and vice versa. It results in destruction of mechanical fasteners used to mount elements of solar arrays, payload and bus (platform), as well as joints between these components.

There have been a huge number of publications and manuscripts on the subject of space materials science [1, 2, 3, etc.]. However, all these papers, with the exception of [4], present theoretical findings or results obtained under laboratory conditions not allowing for the atmospheric effects [5]. The paper by A. Didenko [4] presents experimental data on the spacecraft surface-coating ageing with time for the period of four and a half years for three types of GSS, namely Horizont, Raduga and Intelsat, obtained during ground-based observations through Earth's atmosphere. As is commonly known, Earth's atmosphere distorts the light rays, especially

colour characteristics of light, which change with time of the GSS stay in the space environment.

Availability of the results of long-term ground-based multicolour photometric observations of one and the same GSS makes it feasible to detect variations in the reflectance properties of the satellite. To solve this problem, it is necessary to have a database of photometric ground-based observations that should be expanded and updated for many years. Such a database was created at the Astronomical Observatory of the I. Mechnikov Odessa National University with 2004. It contains more than 2,000 sets of observational data for satellites of many classes operated by different GSS operators throughout the world.

In this paper, we present and discuss variations in the spectral reflectance index over a period of seven years orbiting in the space environment for the following GSS built upon the European bus Eurostar 3000: Astra 2E, and Express AM7. Observations of Sicral 1B on the GeoBus platform (ItaSat-3000), began 2 years later, when the IGSS began its work at the sub-satellite point.

Photometric observations of GSS enable to detect diurnal, seasonal and annual brightness variations. The causes of variations in the satellite brightness are described in detail in the studies [6 and 7]. It is known that spectral optical properties of the satellite surfaces are defined by the spectral reflectance index. In this case, the spectral reflectance index (γ_λ) coincides with geometric albedo.

It is known that the spectral-band brightness of a spacecraft m_λ is defined by formula [4]:

$$m_\lambda = m_\lambda^\ominus - 2,5 \lg \left[\frac{S \gamma_\lambda F(\psi)}{d^2} \right] \quad (1)$$

where m_λ^\ominus is the Sun's brightness in the respective spectral band (B, V, R); (γ_λ) is the spectral reflectance index; ($S\gamma_\lambda$) is the apparent effective reflecting area of the satellite surface; d is the distance to the satellite, which is known for GSS; $F(\varphi)$ is a function of phase which is analytically solved for simple geometric shapes (plate, sphere, cone, etc.).

Constant or calculated values in formula (1) are as follows: the satellite brightness, the Sun's brightness, distance to the satellite, function of phase and size (dimensions) of the satellite (if known).

If the satellite dimensions are not known, as is the case for Sicral 1B, it is possible to set dimensions similar to those typical for a certain class of GSS which can be adopted from different sources. In any case, the pattern of changes in the spectral reflectance indices becomes apparent. Taking into account that the dimensions of an active satellite are invariable over many years of its operation, it must be the spectral reflectance index (γ_λ) to change. A. Didenko in the study [4] suggested calculating relative reflection indices $\Delta\gamma_{(B-V)}$ and $\Delta\gamma_{(V-R)}$. The authors embraced the idea and suggested studying variations in the spectral reflectance indices ($\gamma_b, \gamma_v, \gamma_r$) as a function of time.

2. Results of observational data processing

The figures below depict variations in $\Delta\gamma_{(B-V)}$ and $\Delta\gamma_{(V-R)}$ for the GSS Astra 2E (at the sub-satellite point $28^{\circ}.5$ E),

Express AM7 (at the sub-satellite point $40^{\circ}.0$ E) and the GSS Sicral 1B at the sub-satellite point $11^{\circ}.8$ E.

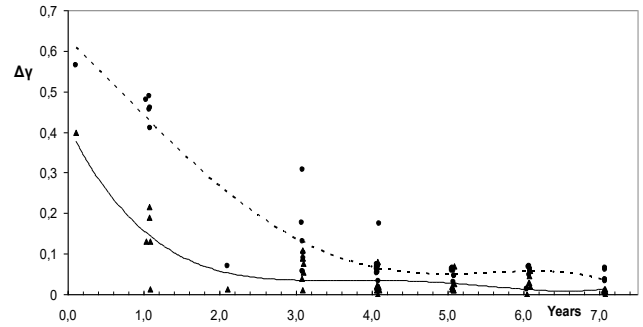


Figure 1: The GSS Astra 2E. Changes $\Delta\gamma_{(B-V)}$ – solid line; $\Delta\gamma_{(V-R)}$ – dotted line. Began observations from the moment the sub-satellite point was reached in 2013.

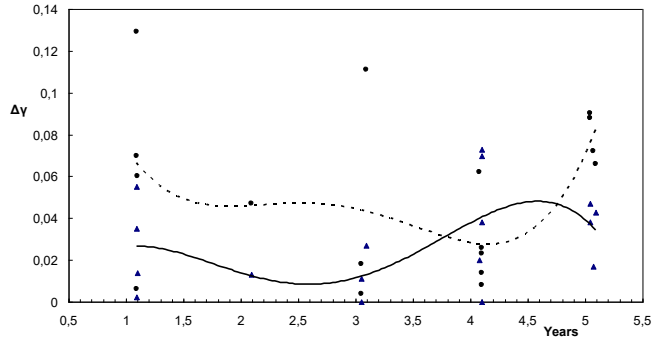


Figure 2: The GSS Express AM7. Changes $\Delta\gamma_{(B-V)}$ – solid line, $\Delta\gamma_{(V-R)}$ – dotted line. Began observations from the moment the sub-satellite point was reached in 2017.

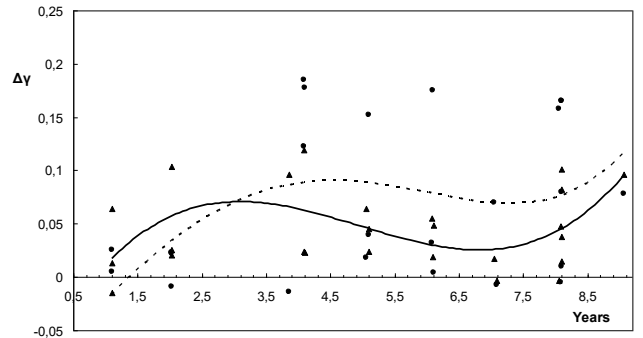


Figure 3: The GSS satellite Sicral 1B. Changes $\Delta\gamma_{(B-V)}$ – solid line, $\Delta\gamma_{(V-R)}$ – dotted line. Was launched on the orbit in 2009. It was monitored began after two years of operation at the sub-satellite point.

3. Conclusions

Geostationary satellites Astra 2E have been observed from the start of their in-orbit operation. For this GSS, variations in $\Delta\gamma_{(B-V)}$ and $\Delta\gamma_{(V-R)}$ were noticeable during the first three years of observations. For GSS Sicral 1B whose observations started two years after launch, such a correlation is practically insignificant. For this GSS, negative quantities are observed $\Delta\gamma$.

The Russian communications satellite Express AM7 showed no significant changes in reflectivity. It probably

has a nice modified platform and solar panels compared to the Astra 2E.

It should be noted that all observed objects do not change their reflective characteristics in the same way.

The obtained relations $\Delta\gamma_{(B-V)}$, $\Delta\gamma_{(V-R)}$ can serve as a medical record describing the medical history, that is, the health of a satellite's surface. Noticeable changes in these characteristics make it possible to detect damages to the GSS external payload. Comparison of changes in the reflective characteristics of different platforms over time can show the level of technical and scientific progress of spacecraft designers. Our database contains sets of observational data for GSS of many classes operated by different states, including Azerbaijan, Bulgaria, Belarus, Greece, China, Turkey, Russia, USA, India, Italy, France, Israel, ESA etc.

References:

1. Novikov L.S.: 2014, *Kosmicheskoye materialovedeniye*, M.: Maks Press.
2. Kulikov V.M., Ladygin Ye.A. et al.: 1980, *Deystviya pronikayushchey radiatsii na izdeliya elektronnoy tekhniki*, M.: Sov. Radio.
3. Kreyinin L.B., Grigor'yeva G.M.: 1979, *Itoги nauki i tekhniki. Issledovaniya kosmicheskogo prostranstva*, **13**, M.: VINITI.
4. Didenko A.V.: 2005, *Vestnik Kazakhskogo natsional'nogo pedagogicheskogo universiteta im. Abaya. Seriya «Fiziko-matematicheskiye nauki»*, № **1(12)**, 81.
5. Engelhart D.P., Cooper R., Cowardin H., Maxwell J., Plis E., Ferguson D., Barton D., Schiefer S., Hoffmann R.: 2019, *The Journal of the Astronautical Sciences*, **66**, 210. DOI: 10.1007/s40295-019-00175-2.
6. Didenko A.V., Usol'tseva L.A.: 1987, *Trudy AFI AN KazSSR*, **48**, 112.
7. Sukhov P.P.: 2014, *Kinematika i fizika nebesnikh tel*, **30**, № 2, 72.

ASTROINFORMATICS

DOI:<http://dx.doi.org/10.18524/1810-4215.2020.33.216403>THE EMISSION-LINE DUSTY OBJECT IRAS 07080+0605,
A LESS-EVOLVED EXAMPLE OF THE RED RECTANGLES.A. Khokhlov^{1,2}, A.S. Miroshnichenko^{2,3,4}, S.V. Zharikov^{5,1}, N. Manset⁶,
O.V. Zakhzhay⁷, I.O. Bilinskyi^{7,8}, K.N. Grankin⁹, A.V. Kusakin⁴, C.T. Omarov⁴,
R.I. Kokumbaeva⁴, I.V. Reva⁴, D. Korčáková¹⁰, I.A. Usenko^{11,12}, A.K. Kuratova¹¹ Physical-Technical Faculty, Al-Farabi Kazakh National University,
Almaty, Kazakhstan, *skhokh88@gmail.com*² Department of Physics and Astronomy, University of North Carolina at Greensboro,
Greensboro, NC, USA, *a_mirosh@uncg.edu*³ Main Astronomical Observatory of the Russian Academy of Sciences, Saint-Petersburg,
Russia⁴ Fesenkov Astrophysical Institute, Almaty, Kazakhstan, *raushan.raushan@mail.ru*⁵ Institute for Astronomy, Universidad Nacional Autónoma de México,
Ensenada, Mexico, *zhar@astro.unam.mx*⁶ Canada-France-Hawaii Corporation, Kamuela, HI, USA, *manset@cfht.hawaii.edu*⁷ Main Astronomical Observatory, National Academy of Sciences of Ukraine, Kyiv 03680,
Ukraine, *zakhzhay.olga@gmail.com*⁸ Department of Astronomical Science, The Graduate University for Advanced Studies,
Tokyo, Japan, *illia.bilinskyi@grad.nao.ac.jp*⁹ Crimean Astrophysical Observatory, Nauchnyj, Crimea, *konstantin.grankin@craocrimea.ru*¹⁰ Astronomical Institute of Charles University, Prague, Czech Republic,
*kor@sirrah.troja.mff.cuni.cz*¹¹ Astronomical Observatory, Odessa National University, Odessa, Ukraine, *igus99@ukr.net*¹² Mykolaiv Astronomical Observatory Research Institute, Mykolaiv, Ukraine

ABSTRACT. The all-sky survey conducted by the InfraRed Astronomical Satellite (IRAS) in the 1980's discovered many objects with infrared excesses whose nature has not been explored until recently. IRAS 07080+0605 is one of those identified in the visual spectral range with an early-type star, which shows the B[e] phenomenon. The object is puzzling, because it exhibits one of the strongest infrared excesses associated with a star of one of the lowest surface temperatures (~ 8500 K) among objects with the B[e] phenomenon, an apparent combination of spectral features of dwarfs and supergiants, and the absence of a surrounding optical nebula. Our photometric and spectroscopic study shows that the object's properties are similar to those of the famous Red Rectangle proto-planetary nebula. In this paper we describe our findings and hypotheses about the nature and evolutionary status of IRAS 07080+0605.

Keywords: Stars: emission-line, Be – Stars: evolution – (Stars:) circumstellar matter – (Stars:) binaries: general

АНОТАЦІЯ. Завдяки огляду всього неба, проведеному супутником IRAS у 80-ті роки, було виявлено багато об'єктів з інфрачервоними надлишками, чия природа не була досліджена до сьогодні. IRAS 07080+0605 – один з цих, що був ідентифікований, у візуальному діапазоні спектру, як зоря раннього спектрального класу, що показує B[e] феномен. Цей об'єкт є загадковим, тому що він демонструє один з найсильніших інфрачервоних надлишків, що асоціюється з зорею з однією з найменших ефективних температур (~ 8500 K) серед об'єктів з B[e] феноменом, очевидною комбінацією спектральних особливостей карликів та надгігантів, та відсутністю навколишньої оптичної туманності. Наші фотометричні та спектральні дослідження показують що властивості об'єкту є подібними до відомої протопланетної туманності "Червоний прямокутник". В цій роботі ми опишемо наші знахідки та гіпотези щодо природи та еволюційного статусу IRAS 07080+0605. IRAS 07080 + 0605 – це перший об'єкт групи FS CMA,

який може представляти ранню стадію подвійних зірок після стадії AGB. Здається, ця подвійна менш розвинена, ніж "Червоний прямокутник", але вона може йти тим самим еволюційним шляхом. Якщо припустити, що супутник типу А показує мало доказів дефіциту вогнетривких елементів, IRAS 07080 + 0605, ймовірно, також менш розвинений, ніж пилові подвійні після стадії AGB. Молодий вік об'єкта не підтверджується енергетичним балансом між спостережуваним болометричним потоком та інтегрованим ГЧ-надлишком, відсутністю сусідньої зореутворюючої області та швидким зменшенням ГЧ-потоків у напрямку довгих хвиль, що виявляє відсутність холодного пилу, типового для зірок до стадії Головної Послідовності.

Ключові слова: Зірки: емісійна лінія, Be – Зірки: еволюція – Зірки: навколосоряна речовина – Зірки: подвійні файли: загальне

1. Introduction

Excess of infrared (IR) radiation in the spectral energy distribution (SED) of a star or stellar system typically manifests the presence of a circumstellar material in the form of gas and/or dust. Various distributions of this material produce different features in the object's spectrum, such as emission lines (both permitted and forbidden) that form in its gaseous part and emission or absorption bands that form in its dusty parts. Examples of these effects in the observational behavior of early-type stars are known as the Be phenomenon and B[e] phenomenon. In particular, the B[e] phenomenon discovered by Allen & Swings (1976) is defined as the presence of line emission (e.g., H I, Fe II, [O I]) and large IR excesses produced by circumstellar dust in the spectra of B-type stars. It has been detected in objects, which belong to five stellar groups: pre-main-sequence stars, symbiotic binaries, compact Proto-Planetary Nebulae, some supergiants, and FS CMa objects. The former four groups were identified by Lamers et al. (1998), while the latter one was proposed by Miroschnichenko (2007) to explain the properties of nearly half (~ 30) of the objects originally found by Allen & Swings (1976) and called unidentified by Lamers et al. (1998).

The group of FS CMa objects exhibits the following observational features: a hot star continuum with emission lines of H I, Fe I, O I, [Fe II], [O I], Ca II; a large IR excess peaking at $\lambda = 10 - 30 \mu\text{m}$ and sharply decreasing at longer wavelengths; location outside of star-forming regions. A hot star in them has a spectral type between O9 and A2 and a luminosity range of $\log L/L_{\odot}$ between ~ 2.0 and ~ 4.5 . Spectra of some FS CMa objects contain absorption lines of neutral metals typical of cool stars (e.g., MWC 623, MWC 728), while several other group members show

evidence for the presence of a very evolved compact or even a degenerate secondary component (e.g., CI Cam, AS 386, 3 Pup). The main hypothesis about the nature of the FS CMa group implies that it comprises mostly intermediate-mass binary systems at an evolutionary stage after mass-transfer between the stellar components (e.g., Miroschnichenko 2007). Mergers of some binaries with remaining circumstellar medium cannot be ruled out as well (e.g., de la Fuente et al. 2015).

This paper is devoted to a study of the IR source IRAS 07080+0605 ($V \sim 12.0$ mag), which has one of the strongest IR excesses among the objects with the B[e] phenomenon. The star associated with IRAS 07080+0605 was detected by Kohoutek & Wehmeyer (1999) in a survey for stars with H α emission and designated as HBHA 717-01. Miroschnichenko et al. (2007) included it in the FS CMa group and suggested a binary nature. However, neither Miroschnichenko et al. (2007) nor a recent study by Condori et al. (2019) found a direct evidence of a companion in their limited observations. Additionally, the latter authors suggested that IRAS 07080+0605 is an A[e] star with an uncertain classification, such as either main-sequence or pre-main-sequence object.

2. Observations

Optical spectroscopic observations of IRAS 07080+0605 were obtained with échelle spectrographs at the following telescopes: 3.6 m Canada-France-Hawaii Telescope (CFHT, USA, spectral resolving power $R = \lambda/\Delta\lambda = 65000$), 2.7 m Harlan J. Smith telescope (McDonald Observatory, USA, $R = 60000$), 2.1 m telescope of the Observatorio Astronómico Nacional San Pedro Martir (OAN SPM, Mexico, $R = 18000$). One spectrum taken with the FEROS spectrograph ($R \sim 40,000$) was retrieved from the ESO archive. Photometric observations were obtained with a 1 m telescope of the Tien-Shan Astronomical Observatory (Kazakhstan) in *BVR* filters in 2014–2016. We have also used a *V*-band light curve from the ASAS SN all-sky survey (Kochanek et al. 2017).

3. The properties of IRAS 07080+0605

The absorption-line spectrum of IRAS 07080+0605 is represented by weak lines of He I, Fe II, Mg I as well as by strong hydrogen lines of the Balmer and Paschen series. Such a content is typical for early A-type stars. We found a good fit of the object's optical spectrum for $T_{\text{eff}} \sim 8500$ K, $\log g = 3-4$, and a projected rotational velocity of $v \sin i \sim 60 \text{ km s}^{-1}$ using the program *SPECTRUM* (Gray & Corbally 1994), which calculates synthetic spectra based on model atmospheres. At the

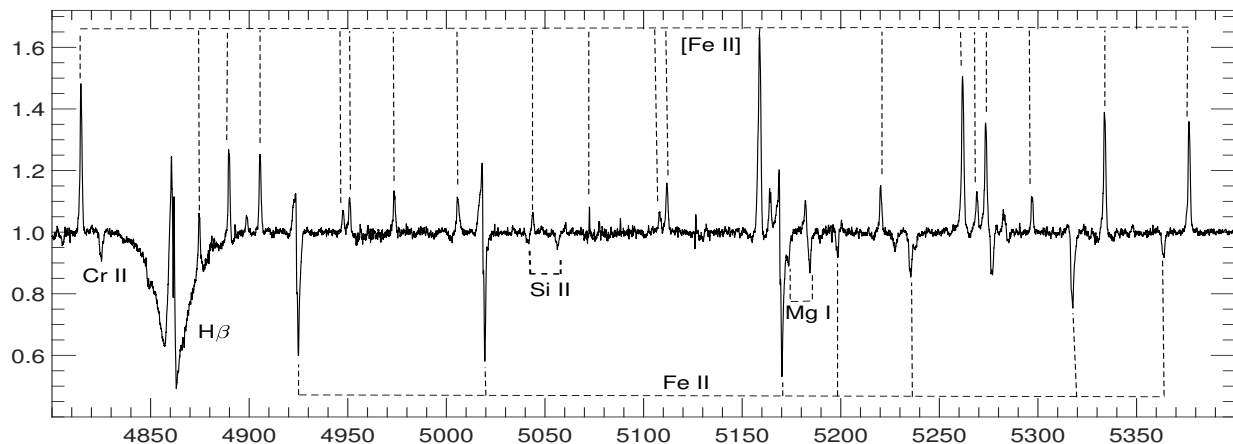


Figure 1: Part of the spectrum of IRAS 07080+0605 taken at CFHT on 2018/11/20. Most identified spectral lines are shown with dashed vertical lines. Intensity is normalized to the local continuum, heliocentric wavelengths are shown in Å.

same time, the O I 7772–7775 Å triplet (equivalent width ~ 3 Å) and Si II 6347 & 6371 Å lines (equivalent widths ~ 0.3 – 0.5 Å), which are weak in the spectra of dwarf stars, are unexpectedly strong and comparable to those of the highest luminosity supergiants. The emission-line spectrum of IRAS 07080+0605 includes emission components of the H α and H β lines and forbidden lines of [O I], [Fe II], [Ca II], and [N II]. A part of the CFHT spectrum taken on 2018 November 20 is shown in Fig. 1.

Most emission lines in the spectrum of IRAS 07080+0605 show variable profiles. In particular, the H α line profile varies from a single-peaked to a triple-peaked (Fig. 2, top panel). Profiles of the forbidden oxygen lines (6300 and 6364 Å) sometimes exhibit a strong central peak on top of a double-peaked structure typical of a circumstellar disk (Fig. 2, bottom panel).

The IR-excess of IRAS 07080+0605 is unusually strong compared to the observed flux in the visual spectral region. Assuming that the object’s brightness is affected by the interstellar extinction only, which is calculated from the color-excess $E(B - V) = 0.1$ mag, and using the effective temperature derived above, the bolometric flux from the star turns out to be ~ 10 times lower than the integrated IR-excess. The low interstellar extinction is supported by the absence of diffuse interstellar bands in the object’s spectrum. This result implies that the star may be attenuated by almost grey circumstellar extinction and/or has a compact companion, which supplies additional energy to the circumstellar dust. The emission features detected in the IR spectrum of IRAS 07080+0605 belong to carbonaceous molecules, which are typically observed in very evolved stars (e.g., planetary nebulae).

The parallax measured by the GAIA mission (GAIA Collaboration 2018) corresponds to a distance of

543 ± 15 pc, which is consistent with the interstellar extinction law in the object’s direction (Fig. 3) and the derived color-excess. Using the average optical brightness of IRAS 07080+0605 ($V \sim 12.0$ mag, see Fig. 4) corrected for the interstellar extinction ($A_V = 3.1 \times E(B - V) = 0.3$ mag) and the GAIA distance result in an absolute visual magnitude of $M_V = 3.1$ mag and a luminosity of $5 L_\odot$, below the main sequence. It is difficult to reconcile some of the object’s spectral features mentioned above (e.g., the oxygen triplet strength) and the strong IR excess with such a low luminosity. The absence of a nearby star forming region and a lack of the far-IR excess compared to that of pre-main-sequence stars contradicts the assumption of the object’s young age made by Condori et al. (2019).

4. Results and Discussion

Positions of both the absorption and emission lines in the optical spectrum of IRAS 07080+0605 are variable. In particular, the Si II absorption lines at 6347 and 6371 Å, which are nevertheless weak and noisy in some spectra, change their radial velocity determined by Gaussian fitting within ± 40 km s $^{-1}$. The strongest Fe II lines (e.g., at 4923, 5018, 5169 Å) exhibit both absorption and emission components at their short-wavelength edge (see Fig. 1). This type of profile (inverse P Cyg) may be interpreted as evidence of the matter infall onto the A-type star.

Even a visual inspection of the light curve of IRAS 07080+0605 composed from the data of the ASAS SN survey (Fig. 4) implies the presence of a cyclic component in the brightness variations. Nevertheless, no stable period has been found in these data. After deleting a long-term trend, the most prominent period in the Fourier power spectrum is found at 127

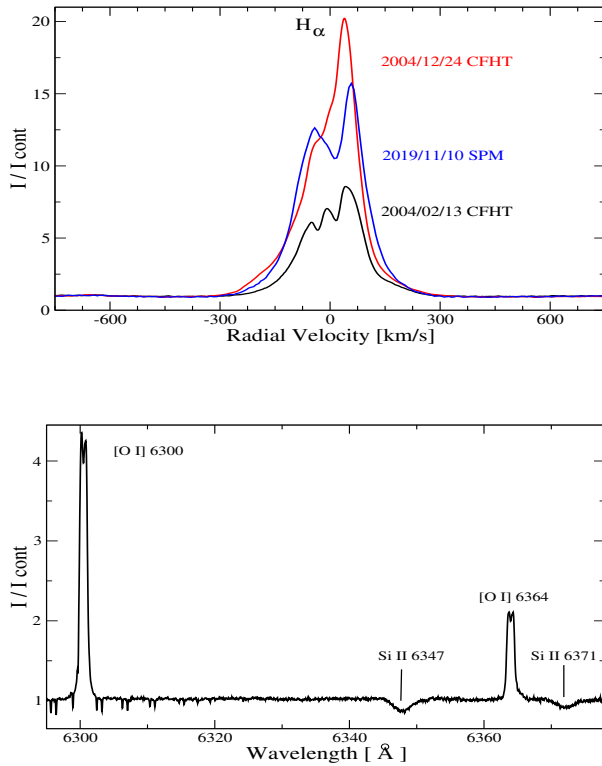


Figure 2: **Top panel.** Comparison of the H α line profiles in the spectrum of IRAS 07080+0605 taken at different times. **Bottom panel.** Part of the spectrum of IRAS 07080+0605 taken at CFHT on 2018/11/20 with [O I] and Si II lines. Intensity and wavelengths are in the same units as in Fig. 1.

days, while the last three observing seasons suggest a period of 190 days. Condori et al. (2019) reported a most probable period of 72 days, although they also found that the highest peak in the Fourier power spectrum corresponds to 248.2 days based on the ASAS-3 survey data (Pojmanski 1997). The ASAS SN data do not show regular variations with these two periods.

The *BVR* photometric data taken at TShAO shows no noticeable variations in the optical color-indices, although this data set is rather small (10 observations). Also, the high-resolution spectra taken near a local brightness maximum (ESO spectrum of 2015/12/06) and near a minimum (CFHT spectrum of 2018/11/20), time of whose taking is shown in Fig. 4) are nearly identical. Therefore, it is reasonable to assume that the cyclic variations are due to a variable circumstellar extinction rather than to eclipses in the system.

Among many objects with IR-excesses, there is one with a number of properties similar to those of IRAS 07080+0605. This is HD 44179, a binary system with a brighter A/F-type post-AGB star and a much fainter hot companion. The system is surrounded by a prominent visual nebula known as Red Rectangle. Both the absorption-line optical spectrum and the IR

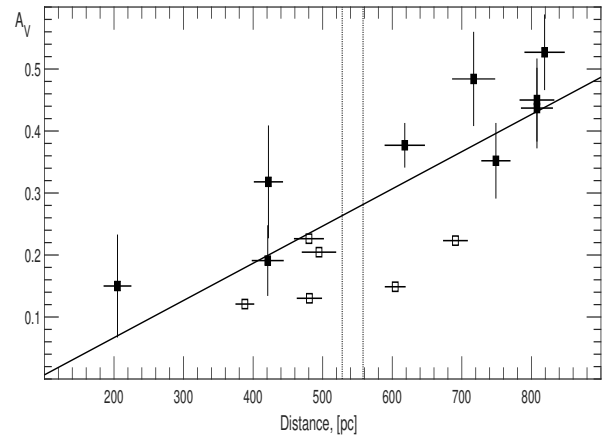


Figure 3: Interstellar extinction law in the direction of IRAS 07080+0605. The thick line shows a linear fit to the star data, while the thin lines show the object's distance uncertainty. Filled and open symbols show data for stars from a 15-arcminute and a 1-degree area around the object, respectively.

spectrum resemble those of IRAS 07080+0605 (Fig. 5).

The integrated flux in the IR excess of Red Rectangle is ~ 18 times larger than the bolometric flux of the bright stellar companion (Oomen et al. 2019). Men'shchikov et al. (2002) modeled the SED of Red Rectangle and found that large carbonaceous grains in the circumstellar disk/torus attenuate the visible system component by a factor of ~ 30 . A similar solution is probably applicable to IRAS 07080+0605.

The largest difference between the two objects is that IRAS 07080+0605 shows no detectable nebula around it, although both are located at about the same distance from the Sun (0.5 kpc for IRAS 07080+0605 and 0.7 kpc for Red Rectangle). Furthermore, IRAS 07080+0605 shows somewhat wider absorption profiles of the Balmer lines (see Fig. 5, top panel), which may imply a higher surface gravity than that of Red Rectangle ($\log g = 1.5$, Men'shchikov et al. 2002). If this is the case, IRAS 07080+0605 is less evolved than Red Rectangle.

Visible components of most of the post-AGB binaries with dusty envelopes are cooler (FGK spectral type) than IRAS 07080+0605 and demonstrate weaker absorption lines compared to those in the spectra of same spectral types with solar abundances. The latter effect has been explained by depletion of refractory elements from the star's atmosphere (Oomen et al. 2019). Although the absorption-line spectrum of IRAS 07080+0605 resembles those of A-type dwarfs, it also contains some lines highly sensitive to the luminosity, such as the Si II 6347 and 6371 Å lines and the O I triplet at 7772–7775 Å mentioned above, whose strengths are closer to those of giants and supergiants. This fact can be due to at least partial

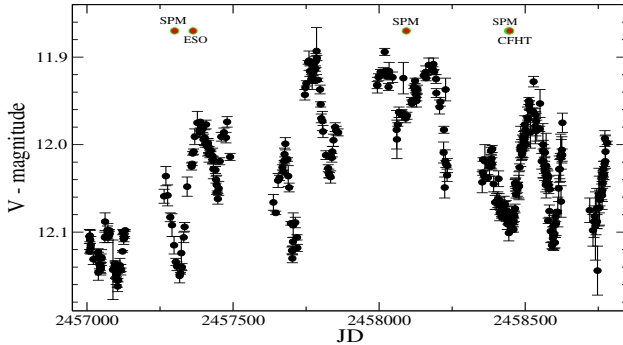


Figure 4: V -band light curve of IRAS 07080+0605 from the ASAS SN survey in 2013–2019 (Kochanek et al. 2017). Dates when some spectra of IRAS 07080+0605 were taken at various observatories are shown above the light curve.

formation of these lines in the circumstellar area.

5. Conclusions

Our spectroscopic and photometric study of the FSCMa object candidate IRAS 07080+0605 shows that in order to explain its observed properties one needs to assume that it is a binary system, in which:

1. the A-type companion's brightness is attenuated by the circumstellar disk-like envelope by a factor of 10 or more in order to explain the large amount of energy in the IR excess as Men'shchikov et al. (2002) did for Red Rectangle;
2. the secondary component is a hot star, which supplies UV photons to ionize the circumstellar gas;
3. some absorption lines, such as the Si II 6347 & 6371 Å and the near-IR oxygen triplet at 7772–7775 Å, partially form in the circumstellar disk.

IRAS 07080+0605 is the first object from the FSCMa group that may represent an early stage of binary post-AGB stars, which has been always studied separately (e.g., Van Winckel et al. 2009). The binary seems to be less evolved than Red Rectangle, but it may follow the same evolutionary path. Assuming that the A-type companion shows little evidence for the refractory element depletion, IRAS 07080+0605 is probably also less evolved than the dusty post-AGB binaries. The young age of the object suggested by Condori et al. (2019) is not supported by the energy balance between the observed bolometric flux and the integrated IR excess, the absence of a nearby star-forming region, and a fast decrease of the mid-IR flux toward longer wavelengths which manifests a lack of the coldest dust typical for pre-main-sequence stars.

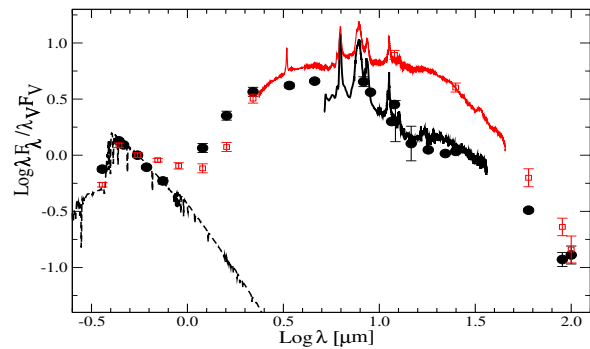
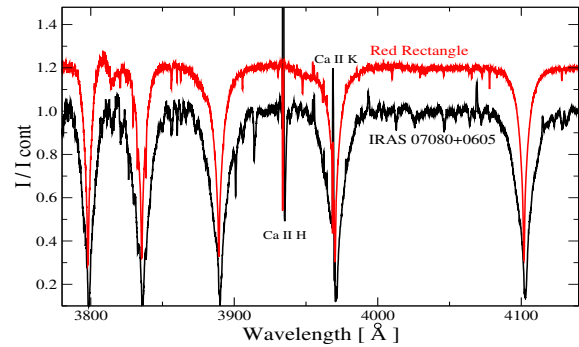


Figure 5: **Top panel.** Comparison of the blue part of the spectra of IRAS 07080+0605 (black line) and Red Rectangle (red line) taken with the ESPaDoNS spectropolarimeter at CFHT. **Bottom panel.** Spectral Energy Distributions of IRAS 07080+0605 (black filled circles – photometric data, black solid line – IR spectrum taken at the Spitzer Space Observatory) and Red Rectangle (red open squares – photometric data, red solid line – IR spectrum taken at the Infrared Space Observatory) corrected for the interstellar reddening. The dashed line shows a theoretical SED for the model atmosphere for $T_{\text{eff}} = 8500$ K, $\log g = 3.0$. The same model atmosphere was chosen to show the IR excess, although the optically brighter component of Red Rectangle was found to be ~ 800 K cooler (Waelkens et al. 1992).

Acknowledgements. A. M. and S. Z. acknowledge support from DGAPA/PAPIIT Project IN102120. The work was carried out within the framework of the Project No BR05236322 "Studies of physical processes in extragalactic and galactic objects and their subsystems" funded by the Ministry of Education and Science of the Republic of Kazakhstan and by the Science Committee of the Ministry of Education and Science of the Republic of Kazakhstan (Grant No AP08856419). The results are partially based on observations obtained at the Canada-France-Hawaii Telescope (CFHT) which is operated by the National Research Council of Canada, the Institut National des Sciences de l'Univers of the Centre National de la Recherche Scientifique de France, and the University of Hawaii. The work of ZOV and BIO was partially conducted in frame of the budgetary program of the NAS of Ukraine "Support for the development of priority fields of scientific research" (CPCEL 6541230).

References

- Allen, D.A., & Swings, J.-P.: 1976, *A&A*, **47**, 293.
Condori, C.A.H., Borges Fernandes, M., Kraus, M., et al.: 2019, *MNRAS*, **488**, 1090.
de la Fuente, D., Najarro, F., Trombley, C., et al.: 2015, *A&A*, **575**, A10.
GAIA Collaboration, Brown, A.G.A., Vallenari, A., et al.: 2018, *A&A* **616**, A1.
Gray, R.O., & Corbally, C.J. 1994, *AJ*, **107**, 742.
Kochanek, C.S., Shappee, B.J., Stanek, K.Z., et al.: 2017, *PASP*, **129**, 104502.
Kohoutek, L., & Wehmeyer, R.: 1999, *A&AS*, **134**, 255.
Lamers, H., Zickgraf, F.-J., de Winter, D., et al.: 1998, *A&A*, **340**, 117.
Men'shchikov, A.B., Schertl, D., Tuthill, P.G., et al.: 2002, *A&A*, **393**, 867.
Miroshnichenko, A.S.: 2007, *ApJ*, **667**, 497.
Miroshnichenko, A.S., Manset, N., Kusakin, A.V., et al.: 2007, *ApJ*, **671**, 828.
Oomen, G.-M., Van Winckel, H., Pols, O., & Nelemans, G.: 2019, *A&A*, **620**, A85.
Pojmanski, G.: 1997, *Acta Astron.*, **52**, 397.
Van Winckel, H., Lloyd Evans, T., Briquet, M., et al.: 2009, *A&A*, **505**, 1221.
Waelkens, C., Van Winckel, H., Trams, N.R., & Waters, L.B.F.M.: 1992, *A&A*, **256**, L15.

DOI:<http://dx.doi.org/10.18524/1810-4215.2020.33.216407>

RE-REDUCTION OF THE OLD PHOTOGRAPHIC OBSERVATIONS OF INTERAMNIA (704) BASED ON GAIA DR2 REFERENCE CATALOGUE

Yu.I. Protsyuk, N.V. Maigurova

Research Institute "Mykolaiv Astronomical Observatory", Ukraine
yuri@nao.nikolaev.ua, nadija@nao.nikolaev.ua

ABSTRACT. A new astrometric reduction of old photographic astroplates benefiting from integration of modern technologies such as the high precision digitizing machines and the high precision Gaia DR2 catalogue could be useful to study the orbital motion of Solar system minor bodies. Based on the newly released Gaia DR2 star catalogue, the scans of the photographic plates containing images of Interamnia (704) taken by the Zonal Astrograph of Mykolaiv Astronomical Observatory (MAO) in 1974–1985 were re-reduced. For our investigation we used 29 plates from the UkrVO archive digitized by commercial EPSON scanner with 1600 dpi resolutions. Besides for 2 of them were digitized by the high precision digitizing machine of Shanghai Astronomical Observatory of the Chinese Academy of Sciences (ShAO) with 2540 dpi resolution. Almost all the plates have 3 exposures with a small shift. Each of 29 plates was scanned 6 times by EPSON scanner in 0° direction. The ShAO digitizing machine scanned 2 plates also 6 times but 3 times in 0° direction and 3 times in 90° direction. Totally, 85 asteroid positions taken from 29 plates were derived. Only 5 asteroid positions were calculated from ShAO scans.

The full identification was conducted and coordinates of all objects were obtained with usage of different options of astrometric reductions. The mean inner accuracy of obtained asteroid positions is $0.03''$ in RA and $0.14''$ in DEC for EPSON scanner and $0.014''$ in RA and $0.013''$ in DEC for the ShAO digitizing machine in 0° direction and $0.010''$ in RA and $0.011''$ in DEC in 90° direction. The comparison of the new topocentric asteroid positions with Horizons ephemeris was made for calculation (O-C) residuals and their RMS. The mean residual differences between the scan obtained positions and JPL calculated positions were $(0.09 \pm 0.16)''$ in RA and $(-0.09 \pm 0.25)''$ in DEC for the MAO digitized plates; the calculated differences for the ShAO scans are close to zero. Comparison of the results obtained with previous reductions of these observations with Tycho2 and UCAC4 reference catalogues showed that the use of the Gaia DR2 reference catalogue does not lead to a significant improvement in the random and systematic component of the residual differences (O-C) for scans with EPSON scanner from the UkrVO archive. The results obtained by processing images with the ShAO digitizing machine suggest that in this case, the re-reduction of all photographic observations based on the Gaia DR2 could

improve the accuracy of old photographic observations to the level of modern ground-based CCD observations.

Keywords: asteroids, photographic observations, ephemeris, reference catalogue.

АНОТАЦІЯ. Нові астрометричні редуції старих фотопластинок із використанням сучасних технологій, таких як високоточні машини для оцифрування, у поєднанні з опорним високоточним каталогом Gaia DR2, можуть бути корисними для вивчення орбітального руху малих тіл Сонячної системи. Для сканів фотопластинок із зображеннями астероїда Інтерамнія (704), що були отримані на Зонному астрографі Миколаївської астрономічної обсерваторії (MAO) у 1974–1985 рр., виконано нові астрометричні редуції. Для нашого дослідження ми використали 29 пластинок з архіву УкрВО, оцифрованих комерційним сканером EPSON з роздільною здатністю 1600 dpi. Крім того, дві з них були оцифровані за допомогою високоточної машини для оцифрування Шанхайської астрономічної обсерваторії (ШАО, КНР) з роздільною здатністю 2540 dpi. Майже всі пластинки мають 3 експозиції з невеликим зсувом. Кожна з 29 пластинок була сканована 6 разів сканером EPSON у напрямку 0° . Оцифрувальна машина ШАО сканувала 2 пластинки також 6 разів, але 3 рази у напрямку 0° та 3 рази у напрямку 90° . Загалом були отримані 85 положень астероїда з 29 пластинок. Зі сканів, отриманих в ШАО, було отримано лише 5 положень астероїдів.

Була проведена повна ідентифікація та отримані екваторіальні координати всіх об'єктів з використанням різних варіантів астрометричних редуцій. Середня внутрішня точність отриманих положень астероїда становить $0.03''$ за прямим піднесенням (RA) і $0.14''$ за схиленням (DEC) для сканера EPSON і $0.014''$ за RA і $0.013''$ за DEC для машини ШАО в напрямку 0° і $0.010''$ за RA і $0.011''$ за DEC в напрямку 90° . Порівняння нових топоцентричних положень астероїду Інтерамнія з ефемеридами Horizons було проведено для розрахунку остаточних різниць (O-C) та їх середньоквадратичних похибок. Середні остаточні різниці між отриманими зі сканів та розрахованими положеннями за ефемеридою JPL становили $(0.09 \pm 0.16)''$ за RA та $(-0.09 \pm 0.25)''$ за DEC для пластинок, що оцифровані сканером EPSON, а для сканувань ШАО значення остаточних різниць несуттєво відрізняються від нуля. Порівняння результатів, отриманих з попередніх астрометричних реду-

цій цих спостережень, що було виконано з опорними каталогами Tycho2 та UCAC4, показало, що використання опорного каталогу Gaia DR2 не призводить до значного поліпшення випадкової та систематичної складової остаточних різниць (O-C) для зображень з архіву УкрВО, що отримано сканером EPSON. Результати, отримані з використанням зображень, що зроблено машиною ШАО, дозволяють припустити, що в цьому випадку повторні астрометричні редуції старих фотографічних спостережень з опорним каталогом Gaia DR2 можуть підвищити точність положень з фотографічних пластинок до рівня сучасних наземних ПЗЗ спостережень.

Ключові слова: Астероїди, фотографічні спостереження, ефемериди, опорні каталоги.

1. Introduction

The studied astroplates were taken with the Mykolaiv Observatory Zone astrograph ($F = 2044\text{mm}$, $D = 120\text{mm}$, $\text{FoV } 5^\circ \times 5^\circ$). The telescope was removed to Mykolaiv from Pulkovo in 1959 with the aim to expand declination zone up to -20° for Solar system minor bodies' observations. The telescope has a four-element lens that has a minimum of aberration. The regular observations of selected asteroids with this telescope were conducted during 36 years (1961–1997). Unfortunately, the low aperture ratio of the instrument did not allow obtaining good quality images for objects fainter than 12^m . In total, 2450 positions of 19 asteroids of the main belt were obtained. All observational data were processed in the international ICRS system with the AC TRC reference catalogue (Gorel et al., 2000). For the first time, the mean accuracy of the positions of a long series of photographic observations turned out to be better than $0.2''$, which makes these observations valuable material for solving a number of problems of ephemeris astronomy.

Since 2007, the work on digitizing glass plates in order to saving and further using the old observations has begun at the Mykolaiv Observatory (Protsyuk et al., 2007, 2014a; Vavilova et al., 2010, 2011). In 2016, we processed images of 4 asteroids with EPSON scans in the UCAC4 catalogue reference system (Zacharias et al., 2013). Reprocessing results of plates with Interamnia observations showed the repeats (O-C) of the system with a slight increase in accuracy (Protsyuk et al., 2016). In this paper, we present the results of astrometric reductions of EPSON scans using the high-precision Gaia DR2 (Gaia Collaboration, 2018) catalogue as a reference catalogue, as well as preliminary results of processing of the some scans obtained by the digitizing machine of the Shanghai Astronomical Observatory (ShAO).

2. Plate Digitization

Digitization of astroplates at the MAO: we used Epson Perfection V750 Pro scanner and each plate was scanned 6 times with 1600 dpi resolution with same methodic (Protsyuk et al., 2014b, 2014c). Digitization of astroplates at the ShAO: a new digitizing machine was used with 2540 dpi resolution and each plate was scanned 3 times in 2 directions (Zhao et al., 2017).

Table 1: Inner accuracy of coordinates (repeatability) for the Interamnia asteroid (in $0^\circ | 90^\circ$ direction).

Cat, method	RA, mas	DE, mas	Scanned
Gaia DR2, Max	121	153	MAO
Gaia DR2, Mid	83	142	MAO
Gaia DR2, No	19	372	MAO
Gaia DR2, Max	74 64	62 86	ShAO
Gaia DR2, Mid	63 77	55 81	ShAO
Gaia DR2, No	14 10	13 11	ShAO

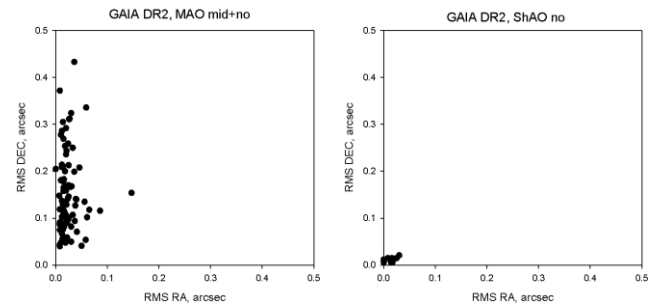


Figure 1: Difference in coordinate repeatability for the Interamnia asteroid with the best methods (bold in Table 1) for the MAO and ShAO scans.

3. Astrometric Reductions and Accuracy

The processing of the digitized images to extract asteroid astrometry exploits methods that are quite similar to those for CCD-based image data. The detailed description of all steps of processing of digitized image of astronegatives from the UkrVO archive is given by Protsyuk et al. (2014c, 2014d), Andruk et al. (2014, 2015), Pakuliak et al. (2020). The scan processing includes such steps as follows: preliminary filtering, choosing PSF (point spread function) objects and scheme of astrometric reductions to calculating the equatorial coordinates and magnitudes in a system of the selected reference catalogues.

In this investigation we used UCAC4 and Gaia DR2 catalogues. The limited magnitude of reference stars were 13^m . Also we check three different model of correction of systematic errors for data from both scanners: “Max” model with 6 iteration, “Mid” model with 4 iterations and “No” model without any correction. For the MAO images we use combined method with 4 iterations for declination and no correction for right ascension (Table 1). Also for the MAO scans we used only 5 from 6 images for all the Interamnia observations with more good inner accuracy. An inner accuracy of reference stars for the reduced MAO images is from less than $0.1''$ for “Max” model to $0.5''$ for “No” model. An inner accuracy for the ShAO images is from $0.01\text{--}0.02''$ for “Max” model to $0.35''$ for “No” model. In other case, we have another picture for accuracy of the Interamnia coordinate repeatability (Table 1).

4. Results

We have made the comparison of obtained topocentric equatorial coordinates (O) with the ephemeris (C) one provided by on-line service HORIZONS and have calculated the residuals differences (O–C) in both coordinates for different modes of processing. The mean differences (O–C) and their standard deviation in both coordinates are presented in Table 2. The last table row shows values of the (O–C) for glass photographic plates reduction from on-line resource AstDys-2 (<https://newton.spacedys.com/astdys/>), where C–ephemeris positions are calculated with OrbFit software.

As can be seen from the Table 2 and Fig. 2, the use of modern reference catalogues with the high spatial resolution (such as UCAC4 and Gaia DR2) for processing the digitized images of photographic plates does not lead to a significant improvement in the accuracy of asteroid positions in comparison with the results obtained from processing glass photographic plates. The expansion of the reference system is mainly due to faint stars, and the accuracy of their measurements is limited by the stability of the EPSON scanner.

Table 2: Differences (O–C) and their standard deviations for the MAO scans of Interamnia asteroid.

Cat, method	RA, mas	DE, mas	N	Year
Gaia DR2, No	-89 ± 158		29	2020
Gaia DR2, Max	19 ± 299	-85 ± 251	28	2020
Gaia DR2, Mid	5 ± 281	-87 ± 257	28	2020
UCAC4, Max	34 ± 236	-131 ± 254	29	2020
UCAC4, Mid	32 ± 244	-144 ± 242	29	2020
UCAC4	-149 ± 178	-17 ± 188	29	2016
Tycho2, Max	77 ± 246	-73 ± 277	28	2020
Tycho2	60 ± 219	-119 ± 312	29	2016
AC TRC (AstDys-2)	-204 ± 165	-87 ± 208	29	1992

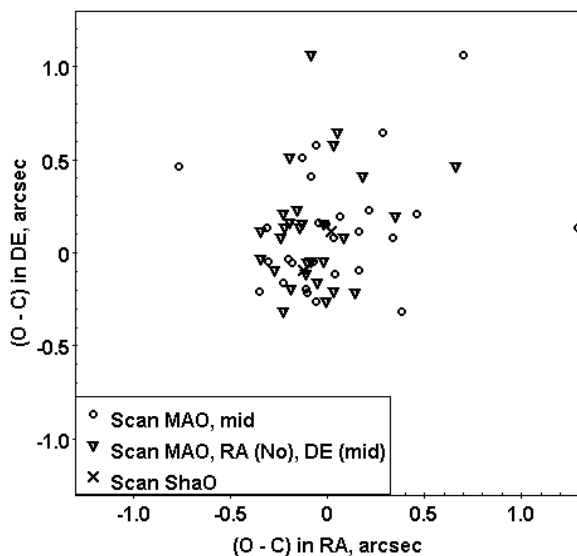


Figure 2: Differences (O–C) for the MAO and ShAO scans of Interamnia asteroid in Gaia DR2 system.

5. Conclusion

Digital scans of 29 photographic plates with images of an asteroid (704) from the UkrVO archive (Vavilova et al. 2010, 2011, 2012a, 2012b, 2014a, 2020; Savanevych et al. 2015, 2018) obtained with the Zonn Astrograph during 1974–1981 were re-reduced in the Gaia DR2 reference catalogue system. The average internal accuracy of the asteroid obtained positions is $0.03''$ in RA and $0.14''$ in DEC for the EPSON scanner; $0.014''$ in RA and $0.013''$ in DEC for scans obtained by the ShAO scanning machine. The mean residual differences between the positions obtained from the scans and the positions calculated by the JPL ephemeris HORIZONS were $(0.09 \pm 0.16)''$ in RA and $(-0.09 \pm 0.25)''$ in DEC for scans from the UkrVO archive; the corresponding differences for the ShAO scans are close to zero. Comparison of the obtained results with previous reductions of these observations with the reference catalogues Tycho2 and UCAC4 showed that the use of the Gaia DR2 catalogue does not significantly improve the random and systematic component of residual differences (O–C) for the EPSON scans from the UkrVO archive. The previous results for repeatability obtained with scans using the ShAO scanning machine allow us to suggest that re-reduction of old photographic observations in the Gaia DR2 reference catalogue system could increase the accuracy of old photographic observations to the level of modern ground-based CCD observations.

References

- Andruk V. et al.: 2014, *Odessa Astron. Publ.*, **27/1**, 53.
 Andruk V. et al.: 2015, *Odessa Astron. Publ.*, **28/2**, 192.
 AstDys-2: 2016, <http://hamilton.dm.unipi.it/astdys/>
 HORIZONS: 2016, <http://ssd.jpl.nasa.gov/?horizons>.
 Gaia Collaboration 2018, *A&A*, **616**, A1.
 Gorel G. K. et al.: 2000, *Kinem. Phys. Cel. Bodies*, **16**, N5, 463.
 Pakuliak L.K., Andruk V.M.: 2020, in: *Knowledge Discovery in Big Data from Astronomy and Earth Observation*. ISBN: 978-0-128-19154-5 (Elsevier), DOI: 10.1016/B978-0-12-819154-5.00029-1, 325.
 Protsyuk Yu. et al.: 2007, *Proc. IAU Symp.*, **248**, 548.
 Protsyuk Yu. et al.: 2014, ISBN: 978-80-7080-918-1, 131.
 Protsyuk Yu. et al.: 2014, *Kinem. Phys. Cel. Bodies*, **30**, N6, 296.
 Protsyuk Yu. et al.: 2014, *Odessa Astron. Publ.*, **27/1**, 63.
 Protsyuk Yu. et al.: 2014, *Odessa Astron. Publ.*, **27/1**, 59.
 Protsyuk Yu. et al.: 2016, *Odessa Astron. Publ.*, **29**, 147.
 Savanevych et al. : 2015, *MNRAS*, **451**, 3287.
 Savanevych et al. : 2018, *Astron. Astrophys.*, **609**, A54.
 Vavilova I.B. et al.: 2010, *Kosm. Nauka Technol.*, **16**, N5, 62.
 Vavilova I.B. et al.: 2011, *Kosm. Nauka technol.*, **17**, N4, 74.
 Vavilova I.B. et al.: 2012, *Kinem. Phys. Cel. Bodies*, **28**, N2, 85.
 Vavilova I.B. et al.: 2012, *Baltic Ast.*, **21**, N3, 356.
 Vavilova I.B. et al.: 2014, *Odessa Astron. Publ.*, **27/1**, 65.
 Vavilova I. et al.: 2014, ISBN: 978-80-7080-918-1, 8.
 Vavilova I. et al.: 2020, in: *Knowledge Discovery in Big Data from Astronomy and Earth Observation*. ISBN: 978-0-128-19154-5 (Elsevier), DOI: 10.1016/B978-0-12-819154-5.00015-1, 57.
 Zacharias N. et al.: 2013, *Astron. J.*, **145**, 44.
 Zhao Yu Y. et. Al: 2017, *Res. Astron. Astroph.*, **17**(3), 28.

DOI:<http://dx.doi.org/10.18524/1810-4215.2020.33.216420>

SOFTWARE FOR SEARCH AND MEASURING OF WDS CATALOG DOUBLE AND MULTIPLE STARS FROM DATABASE OF RESULTS OF CCD OBSERVATION

Yu.I. Protsyuk, N.V. Maigurova

Research Institute “Mykolaiv Astronomical Observatory”, Mykolaiv, Ukraine

<yuri@mao.nikolaev.ua>, <nadija@mao.nikolaev.ua>

ABSTRACT. Double and multiple star systems are the source of unique information for determining the parameters of star formation models and for testing stellar models evolution. Therefore observations and measuring of their mutual configuration parameters is still important.

Observations of double and multiple star systems at the Research Institute “Mykolaiv Astronomical Observatory” (RI MAO) were performed with different telescopes since 2013. In addition, we also have an observational database and proceeding results of the fields in open clusters vicinity, which were performed using the KT-50 telescope (D=500mm, F=3000mm) in 2011–2020. All astrometric processing was carried out by the Astrometrica software using UCAC4 or GAIA DR2 as reference catalogs. The catalogs of stars positions and proper motions in the vicinity of open clusters that contain more than 5.6 million stars were created as results of these observations. There are a lot of double and multiple stars in the fields with open clusters, which, moreover, could be the physical member of clusters. With this aim software for search and measuring of mutual configuration parameters of the double and multiple stars from the WDS was created. Our software uses previous reduction data from Astrometrica software and allows finding stars from double and multiple systems, which are presented in WDS catalog.

We determined separations and position angles for pairs of the found WDS systems and checked observational array over 71 nights of 2019. Data of 9679 CCD images were reduced and 34277 WDS pairs were found in 7232 of them. Total numbers of unique pairs are 1504 in 1091 systems with average number of pair observations near 23. The standard errors of measurements were 0.15" for separations and 0.5° for position angles. The epoch difference between our observations and the last observation in the WDS database is in the range from 2 to 28 years. The comparison with the WDS data has shown that residual differences and their standard errors are $(-0.03 \pm 0.24)''$ in separations and $(-0.07 \pm 0.88)^\circ$ in position angles for close observation periods. The obtained data are of original observations that extend the observation period of stars from double and multiple systems and can be used to construct orbits and to determine the masses of components. The calculated parameters of mutual configuration of the found pairs and estimates of differences in magnitudes of the components will be sent to the WDS database.

Keywords: CCD observations, double and multiple stars, WDS catalog.

АНОТАЦІЯ. Подвійні та кратні зоряні системи є джерелом унікальної інформації для визначення параметрів моделей формування зірок та для тестування еволюції зоряних моделей. Тому спостереження та вимірювання їх взаємних параметрів конфігурації все ще є важливим. Спостереження за подвійними та кратними зоряними системами в НДІ МАО проводяться з використанням різних телескопів з 2013 року. Крім того, ми також маємо базу даних спостережень та результатів обробки зоряних полів поблизу розсіяних скупчень, які проводились за допомогою телескопа КТ-50 (D = 500 мм, F = 3000 мм) у 2011-2020 рр. Вся астрометрична обробка проводилася за допомогою програмного забезпечення Astrometrica з використанням каталогів UCAC4 або GAIA DR2 в якості опорних. За результатами цих спостережень створено каталоги положень та власних рухів зірок в околицях розсіяних скупчень, що містять понад 5,6 млн зірок. В отриманих полях з розсіяними скупченнями є багато подвійних і кратних зірок, які, крім того, можуть бути фізичними членами розсіяних скупчень. Тому було створено програмне забезпечення для пошуку та вимірювання параметрів взаємної конфігурації подвійних та кратних систем з Вашингтонського каталогу подвійних зірок (WDS). Наше програмне забезпечення використовує попередні дані обробки від програмного забезпечення Astrometrica, знаходить там подвійні та кратні зірки, які представлені в каталозі WDS, та визначає їх взаємні відстані й позиційні кути. Перевірено масив спостережень за 71 ніч 2019 року.

Всього було оброблено дані 9679 ПЗЗ-зображень, і в 7232 з них було знайдено 34277 пар подвійних зірок. Загальна кількість унікальних пар становить 1504 в 1091 системах із середньою кількістю спостережень пар ~ 23 . Стандартні похибки вимірювань становили 0.15" для відстаней та 0.5° для позиційних кутів. Різниця епох між нашими спостереженнями та останнім спостереженням у базі даних знаходиться в діапазоні від 2 до 28 років. Порівняння з даними WDS показало, що залишкові різниці та їх стандартні похибки становили $(-0.03 \pm 0.24)''$ у відстанях та $(-0.07 \pm 0.88)^\circ$ в позиційних кутах для близьких періодів спостереження. Отримані дані є оригінальними спостереженнями, які продовжують період спостереження подвійних та кратних зірок і можуть бути використані для побудови орбіт та визначення мас компонентів. Розраховані параметри взаємної конфігурації виявлених пар та оцінки різниць зоряних величин компонентів будуть передані в банк даних WDS.

Ключові слова: ПЗЗ спостереження, подвійні та кратні зірки, WDS каталог.

1. Introduction

The observations of double and multiple systems were conducted at the RI MAO in 2013–2020 with the AMC and KT-50 telescopes (Bodryagin et al., 2014, 2015, 2017). Observational data were matched with the Washington Double Star Catalog (Mason et al. 2001) maintained by the US Naval Observatory. The WDS Catalog contains positions (J2000), discoverer designations, epochs, position angles, separations, magnitudes, spectral types, proper motions, and, when available, other information and notes for the components of 152,352 systems (till August 8, 2020). Not all the catalog objects have proven physical linkages between components. In many cases it is simply the result of close projection onto the celestial sphere of objects at different distances. As a rule, for stars in a gravitationally bound system the term “binary” used. Visual binary and multiple stars are mainly stars in the vicinity of the Sun with a very long orbital period. Due to the long period, the binary’s orbit can be traced only by numerous observations over the course of tens of years. By this reason the orbits were determined only for several thousand stars: for example, the Sixth Catalog of Orbits of Visual Binary Stars as of July 27, 2017 (Hartkopf et al., 2001) included 2,739 orbits of 2,656 systems with sufficient accuracy to obtain estimates of the masses of the components.

Under the old processing scheme, our measurements were performed for each pair separately in manual mode, which made it impossible to process large volumes of observations. The REDUC software was used in this variant. At the same time, a combination of the ground based original observations with accurate astrometric catalogues is available due to the Strasbourg astronomical Data Centre. It allows to obtain new knowledge about nature of linkage between components of the investigated double and multiple systems (Maigurova, 2018), to search for vanishing stars (Villarroel et al., 2020) or probable invisible components inside of multiple stellar systems (Maigurova, 2019).

2. Program of observations and software

Simultaneously with the program of observations of double and multiple systems at the Mykolaiv Observatory, observations were conducted in frame of other programs. We have an observational database and proceeding results of the fields in open clusters vicinity, which were performed using the KT-50 telescope (D=500mm, F=3000mm) in 2011–2020 (Protsyuk et al., 2014, 2019). The observations were carried out in the zone of latitudes $\pm 30^\circ$ from the galactic plane. All astrometric processing was made with the Astrometrica software using UCAC4

(Zacharias et al., 2013) or GAIA DR2 (Gaia Collaboration, 2018) as reference catalogs. As a result of these observations we created the catalogs of stars positions and proper motions in the vicinity of open clusters that contain more than 5.6 million stars (Protsyuk et al., 2014). We supposed that these catalogs should include many double and multiple stars in open cluster fields, which, moreover, could be physical member of clusters.

Firstly, we created software for processing our CCD observations in manual mode (Fig. 1). This software works primarily with images with a small number of reference stars and has more stable results with more convenient manual processing than REDUC software.

Secondly, we created software to search for WDS pairs in the results of the previous processing performed by Astrometrica software.

The new AstroWDS program works in batch mode and uses the downloaded version of WDS catalog. The search is carried out in the WDS catalog sequentially for all stars from the Astrometrica’s cat-file. The cross matching procedure is performing with the following configurable parameters: search radius of the main star for both coordinates is 3”; distance difference (WDS-Astrometrica) in the found pairs is no more than 5”. Pairs with a distance of up to 2” in the WDS catalog or in our processing are to be ignored due to FWHM of stars in our observations. Also, the angular difference (WDS-Astrometrica) in the found pairs is no more than 5 degrees.

The processing time is less than 1 second for one CAT file with few thousands of stars. The results are output in two files: detail one for all pairs and summary one with the most relevant information (Table 1), which can be sent to update the WDS catalog.

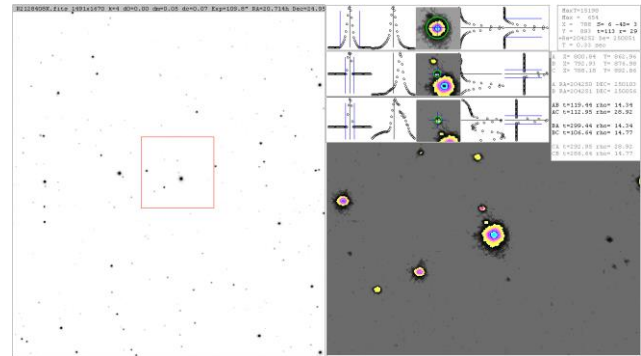


Figure 1: Software for processing CCD observations in manual mode.

Table 1: File format with summary information about the found pairs of stars.

WDS	Comp	ObsDate	pa	sep	mag1	mag2	dmag	pa (O-WDS)	sep (O-WDS)	T (WDS)
00013+6021	AB	2019 09 21	89.35	57.45	8.07	8.47	0.40	0.35	-0.25	2010
00013+6021	AB	2019 09 21	89.35	57.49	8.93	9.86	0.93	0.35	-0.21	2010
00013+6021	AB	2019 09 21	89.51	57.26	8.42	8.74	0.32	0.51	-0.44	2010
00013+6021	AB	2019 10 18	89.26	57.44	8.34	9.32	0.98	0.26	-0.26	2010
00013+6021	AB	2019 10 18	89.31	57.39	8.54	9.48	0.94	0.31	-0.31	2010
00013+6021	AB	2019 11 09	89.09	57.36	8.88	9.90	1.02	0.09	-0.34	2010
00013+6021	AB	2019 11 09	89.44	57.51	8.57	9.68	1.11	0.44	-0.19	2010
00013+6021	AC	2019 09 21	323.61	155.28	8.42	10.75	2.33	-0.39	0.28	2007
00013+6021	AC	2019 09 21	323.77	155.29	8.07	10.43	2.36	-0.23	0.29	2007
00013+6021	AC	2019 09 21	323.81	155.63	8.93	11.29	2.36	-0.19	0.63	2007
00013+6021	AC	2019 10 18	323.72	155.32	8.34	10.75	2.41	-0.28	0.32	2007
00013+6021	AD	2019 09 21	117.84	181.50	8.07	10.46	2.39	-0.16	0.10	2016

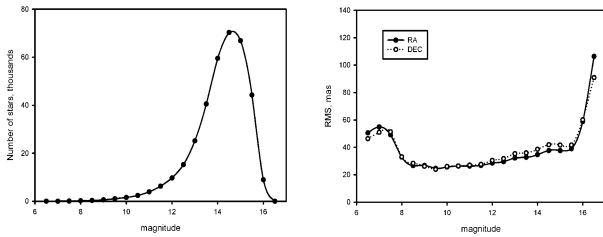


Figure 2: Distribution of stars from the MAO-2019: number of stars (left) and accuracy (right) vs. magnitude

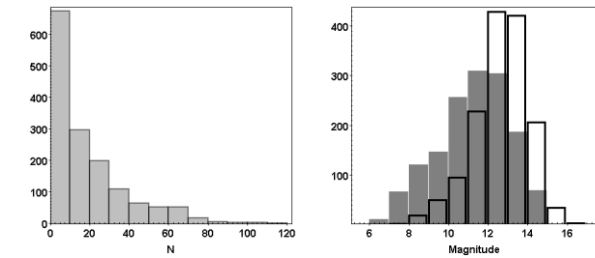


Figure 3: Number of observations of the found WDS pairs (left); distributions of these pairs by stellar magnitude (right): filled – first component, open – second one.

3. Reductions and results

In this article we use the KT-50 array of observations in 2019, which was processed by Astrometrica software. Observations were carried out in fields that include open clusters in the zone of latitudes $\pm 30^\circ$ from the galactic plane. In total, 9679 CCD frames were obtained; 12 million objects were selected of CCD images. On the basis of these observation the MAO-2019 catalog of more than 357 thousand stars ($7 \div 16^m$), which have more than five observations was obtained (Fig. 2).

For our work we used these 9679 CAT files obtained in the process of creating the catalog to find the WDS pairs. As a result we selected 34277 WDS pairs from 7232 CAT-files. Total numbers of unique found pairs are 1504 in 1091 systems with average number of the observations of one pair near 23, a mean magnitude for the first component is 11.5m, for the second is 13m (Fig. 3, 4). The standard errors of measurements were $0.15''$ in separations and 0.5° in position angles (Fig. 5). The epoch difference between our observations and the last observations in the WDS is in the range from 2 to 28 years.

We compared the obtained values of the configuration parameters with data from WDS catalog and determined that residual differences and their standard errors were $(-0.03 \pm 0.24)''$ in separations and $(-0.07 \pm 0.88)^\circ$ in position angles for close observation periods (Fig. 6).

4. Conclusions

New software has been created for the search and subsequent measurement of the parameters of mutual configuration (angular distance between components and position angle) for double and multiple systems from the WDS catalog. This software uses positional files obtained in the process of performing astrometric reductions by Astrometrica software as input files.

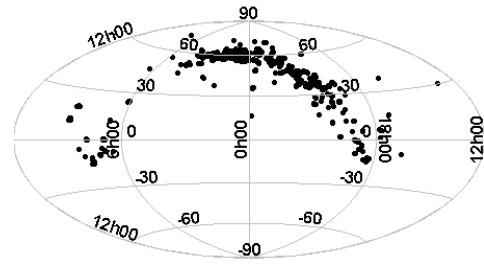


Figure 4: Celestial distribution of the found WDS systems in equatorial coordinates (Aitoff projection).

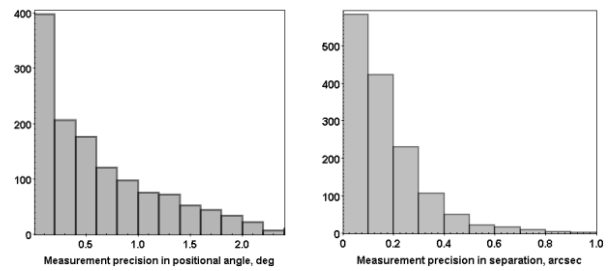


Figure 5: Measurement precision in positional angle (left) and separation (right) for the found WDS pairs.

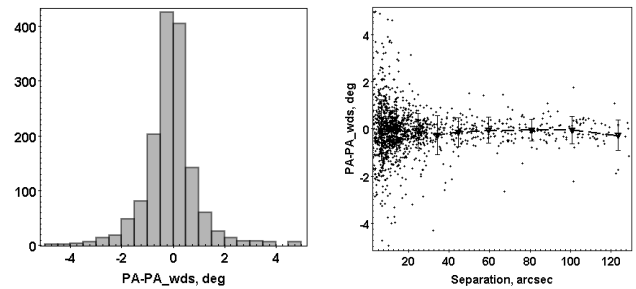


Figure 6: Histogram of positional angle differences between measured and WDS catalog values (left), relation of measurement accuracy of positional angle vs separation parameter (right).

The search and measurement of the parameters of the mutual configuration of the WDS catalog object were carried out on the array of KT-50 telescope observations of fields with open clusters in 2019. Totally we found 1504 pairs from 1091 systems of the WDS catalog for which mutual configuration parameters were measured. The average (median) number of observations of one pair is 15 times. For comparison, only 1019 systems with an average number of observations of about 5 were resulted according to the program of observations of double and multiple systems in 2014–2018. Comparison with the WDS data showed that the values of the differences in measurements of parameters of the mutual configuration and their standard errors are $(-0.03 \pm 0.24)''$ for the angular distance and $(-0.07 \pm 0.88)^\circ$ for the positional angle for close periods of observation.

New software will be included into the UkrVO resources (Vavilova et al., 2017, 2020) to help for anybody to find new objects, likely double and multiple star systems, inspecting the old observational data.

References

- Astromerica, [on-line resource]. Available at:
<http://www.astrometrica.at>
- Bodryagin D. et al.: 2015, *Odessa Astron. Publ.*, **28**, 163.
- Bodryagin D.V. et al.: 2016, *JDSO*, **12**, 320.
- Bodryagin D.V. et al.: 2017, *Sci. Innov.*, **13**, 46.
- Gaia Collaboration 2018, *A&A*, **616**, A1.
- Hartkopf et al.: 2001, *AJ*, **122**, 3472.
- Maigurova N.V. et al.: 2018, *Odessa Astron. Publ.*, **31**, 220.
- Maigurova N.V. et al.: 2019, *Odessa Astron. Publ.*, **32**, 192.
- Mason B.D. et al.: 2001, *Astron. J.*, **122**, 3466.
- Protsyuk Yu.I. et al.: 2014, *KPCB*, **30**, N6, 296.
- Protsyuk Yu.I. et al.: 2019, *Odessa Astron. Publ.*, **32**, 196.
- REDUC software, [on-line resource]. Available at:
<http://www.astrosurf.com/hfosaf/reduc>
- Vavilova I.B. et al.: 2017, *Proc. IAU Symp.*, **325**, 361.
- Vavilova I.B. et al.: 2020, in: *Knowledge Discovery in Big Data from Astronomy and Earth Observation*. DOI: 10.1016/B978-0-12-819154-5.00015-1, 57.
- Villarroel B. et al.: 2020, *Astron. J.*, **159**, 2020.
- Zacharias N. et al.: 2013, *Astron. J.*, **145**, 44.

DOI:<http://dx.doi.org/10.18524/1810-4215.2020.33.216421>

ASTEROID POSITIONS BASED ON THE DUSHANBE PART OF THE FON PROJECT OBSERVATIONS

S.V. Shatokhina¹, H. Relke², A.Sh. Mullo-Abdolov³, O.M. Yizhakevych¹,
Q.X. Yuldoshev⁴, Yu.I. Protsyuk⁵, V.M. Andruk¹

¹ Main Astronomical Observatory of the National Academy of Sciences of Ukraine, Kyiv, Ukraine, svetash@mao.kiev.ua

² Walter Hohmann Observatory, Essen, Germany

³ Institute of Astrophysics of the Academy of Sciences of the Republic of Tajikistan, Dushanbe, Tajikistan

⁴ Ulugh Beg Astronomical Institute of the Uzbekistan Academy of Sciences, Tashkent, Uzbekistan

⁵ Research Institute Mykolaiv Astronomical Observatory, Mykolaiv, Ukraine

ABSTRACT. Asteroid images identification and creation the positional catalogs based on digitized photographic observations of previous years were continued. Namely, the cooperation between Ukrainian Virtual Observatory (UkrVO) and the Institute of Astrophysics of the Academy of Sciences of Tajikistan make it possible to expand this work by involving numerous additional archives of digitized observations and processing services and thus obtaining new original data about the Universe.

The Dushanbe part of the Northern Sky Survey (FON project) is represented by about 1570 photographic plates obtained in 1985-1992 on the Zeiss-400 astrograph at the Hissar Astronomical Observatory of the Institute of Astrophysics of the Academy of Sciences of Tajikistan. At present, their digitization and further scan processing continue until the final product is obtained in the form of a catalog of equatorial coordinates and stellar magnitudes for all registered objects on the plates. The equatorial coordinates α , δ of all objects on the plates were obtained in the Tycho-2 reference system at the epoch of exposure of each plate. Photometry of stars for the plates was carried out based on the principles implemented in the processing of the plates of the FON project using photoelectric measurements of stars to construct the characteristic curves of the plates. Photographic B-magnitudes of objects were calibrated with photoelectric standards.

In parallel with solving the main task of the project to create a catalog of stars and galaxies, we analyzed the results of processing the plates to search for images of asteroids and comets and create a catalog of their coordinates and values.

About 300 positions of asteroids and comets were obtained with visual magnitudes from 7 to 16.5. All positions of the asteroids were compared with the ephemeris. A preliminary analysis of the O-C differences and their comparison with similar results obtained from the digitized observations of the Kyiv and Kitab parts of the FON project are conducted.

Keywords: data archives, digitized observations, catalog, asteroid positions.

АНОТАЦІЯ. На основі оцифрованих фотографічних спостережень попередніх років продовжена робота з ідентифікації зображень астероїдів та створення каталогів їхніх положень і зоряних величин.

Кооперація між Українською віртуальною обсерваторією і Інститутом астрофізики Академії наук Таджикистану дають можливість розширити цю роботу, додаючи нові архіви оцифрованих спостережень і сервіси їх обробки, отримуючи, таким чином, нові оригінальні дані про Всесвіт.

Спостереження третьої частини Фотографічного огляду північного неба (ФОН) в Душанбе представлені приблизно 1570 фотопластинками, отриманими в 1985-1992 рр. на астрографі Zeiss-400 в Гісарській астрономічній обсерваторії Інституту астрофізики Академії наук Таджикистану. Тривають оцифрування фотонегативів та подальша обробка сканів, поки за даними всіх спостережень буде отримано каталог екваторіальних координат та зоряних величин для всіх зареєстрованих об'єктів на пластинках. Екваторіальні координати α , δ усіх об'єктів отримані в системі опорного каталогу Tycho-2 на епоху експонування кожної пластинки. Фотометрія зір проводилась на основі принципів, реалізованих при обробці спостережень проекту ФОН з використанням фотоелектричних вимірювань зір для побудови характеристичних кривих для кожної пластинки. Фотографічні B-величини об'єктів відкалібровані за фотоелектричними стандартами.

Паралельно з вирішенням основного завдання проекту зі створення каталогу зір і галактик ми проаналізували результати обробки пластинок з метою пошуку зображень астероїдів і комет та створення каталогу їх положень і B-величин.

Загалом було ідентифіковано близько 300 положень астероїдів і комет з візуальними зоряними величинами від 7 до 16,5. Всі положення астероїдів були порівняні з ефемеридними. Виконано попередній аналіз різниць O-C та їх порівняння з аналогічними результатами, одержаними з цифрованих спостережень Київської та Kitabської частин проекту ФОН.

Ключові слова: архіви даних, оцифровані спостереження, каталог, положення астероїдів.

1. Introduction

At the end of the 20th century, six observatories took part in the implementation of the Photographic Survey of the Northern Sky (FON project): the Main Astronomical Observatory of Ukraine (Kyiv, Goloseevo), the Zvenigorod Observatory of Russia, the Hissar Observatory of Tajikistan, the Abastumani Observatory of Georgia, the Zelenchuk Observatory of Russia and the Kitab Observatory of Uzbekistan (Pakuliak et al., 2016; Andruk et al., 2017b).

The Kyiv and Kitab parts of the project have been successfully completed. The processing of the digitized observations resulted in a few catalogs of coordinates and B-magnitudes for more than 19 million stars and galaxies from the FON-Kyiv part (Andruk et al., 2016) and more than 13 million stars and galaxies from the FON-Kitab part (Yuldoshev et al., 2017; 2019). Besides, based on these data, two catalogs for more than 5,000 positions and B-magnitudes of asteroids were compiled (Shatokhina et al., 2018a; 2018b). These catalogs are placed on the website of UkrVO (<http://gua.db.ukr-vo.org/starcatalogs.php>) and in Strasbourg astronomical Data Center (<http://cdsweb.u-strasbg.fr>).

The digitizing of astroplates has been performed using Epson™ and Microtek™ commercial scanners with 16-bit gray levels and a resolution of 1200 dpi. Images of all objects registered on plates were processed using the advanced software complex for CCD images processing MIDAS/ROMAFOT in the LINUX environment. Additional software modules developed and implemented in the Main Astronomical Observatory of the NAS of Ukraine and Research Institute “Mykolaiv Astronomical Observatory” provide both the digitized images processing and the final product as a catalog of positions and stellar magnitudes of all registered objects (Andruk et al., 2015; Protsyuk et al., 2016b; 2019b).

The equatorial coordinates α , δ , and stellar B-magnitudes of all objects on the plates were obtained in the reference system of Tycho-2 at the epoch of the exposition of each plate. The photometry of stars was made on the principles implemented in processing the plates of the FON project (Andruk et al., 2017a) using photoelectric measurements of stars to construct the characteristic curves of each plate (Relke et al., 2015). Photographic B-magnitudes of objects were calibrated with photoelectric standards.

Based on these developed methods (Andruk et al., 2016; Pakuliak et al., 2020; Protsyuk et al., 2019a), we currently prepared similar catalogs for the third part of the FON project in cooperation with the Hissar Astronomical Observatory of the Institute of Astrophysics of the Academy of Sciences of the Republic of Tajikistan. Observations were obtained in 1985–1992 with the Zeiss-400 astrograph (Marsden's code 190, D/F=400/2000 mm) at the Hissar Astronomical Observatory near Dushanbe. The plate collection includes about 1570 negatives covering the northern hemisphere from -8° to $+90^\circ$. Plate digitization began in 2017 after the commercial Microtek ScanMaker 1000XL Plus scanner was provided. The first results of this work were published in articles by Mullo-Abdolv et al. (2017, 2018); Rahimi et al. (2018); Yizhakevych et al. (2018).

2. Main results

The results of processing the digitized plates contain coordinates and magnitudes not only for stars, but also for all objects that were fixed on these plates during exposure.

These data were used for a global search for small bodies of the Solar System on these plates (Ivanov et al., 2013; Protsyuk et al., 2015; 2016a; 2017; Shatokhina et al., 2017; 2019).

The asteroid identifications were performed according to the coordinates and stellar magnitudes of asteroids. The diameter and maximum intensity of the central pixel of the asteroid images are also taken into account. Ephemeris support for asteroid identifications and further precise comparison of results was made using the online Internet resources (<https://ssd.jpl.nasa.gov/sbfind>, <https://ssd.jpl.nasa.gov/horizons>).

After such identifications and analysis, the 302 asteroid positions and magnitudes from the processing results of digitized plates of the two zones of the FON-Dushanbe project were compiled into a preliminary catalog. The positions of asteroids that were fixed on photographic plates in the immediate vicinity of stars according to the Gaia DR2 catalog data were excluded from compiled catalog. We considered them to be ambiguous identifications of asteroid or star images.

We analyzed the quantitative and qualitative characteristics of the catalog data. Figure 1 shows the distribution of all the identified asteroids by year. Figure 2 shows the number of asteroid positions obtained from FON-Dushanbe observations for each visual magnitude interval. Asteroids with a visual magnitude of up to 16.5^m have been identified. In comparison to the results of other parts of FON observations, the asteroids with a maximum visual magnitude of 16^m were identified with FON-Kyiv and $17-17.5^m$ with FON-Kitab.

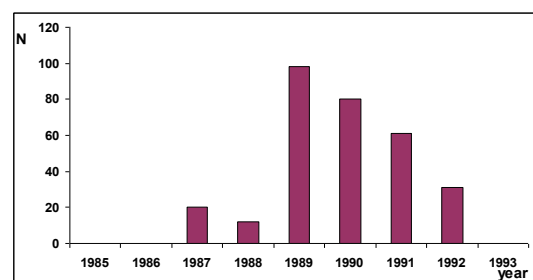


Figure 1: Distribution of identified asteroids by years.

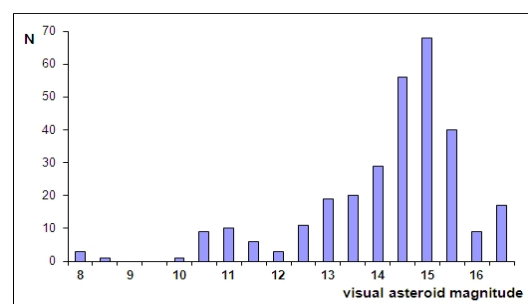


Figure 2: Distribution of identified asteroids by visual magnitudes.

All positions of asteroids were compared with the JPL DE431 ephemeris. The O-C differences in both coordinates for all asteroids are presented in Fig.3. Additionally, this figure also shows similar results for all asteroid positions from the FON-Kyiv and FON-Kitab observations. The scatter of O-C values is greater in both coordinates for the FON-Dushanbe observations than for the FON-Kyiv and FON-Kitab observations. A systematic O-C shift is noticeable in the RA coordinate for all asteroid positions from the two FON-Dushanbe zones. To find the reasons for the appearance of systematic O-C shift at the asteroid positions, they were further analyzed.

Firstly, several plates were selected, where many asteroids identified, their O-C differences have large values, and a clear systematic O-C shift was found. For example, on plate No.1108 with identified seven asteroids, the coordinates of all stars were also analyzed. All stars on this plate were identified and O-C differences were calculated (Fig. 4) between the coordinates of the stars determined on the plate and identified in the Gaia catalog. From the analysis of the coordinate differences, both separately for the magnitude intervals, and as a whole, systematic shifts for the coordinates of stars inherent in the positions of asteroids were not found.

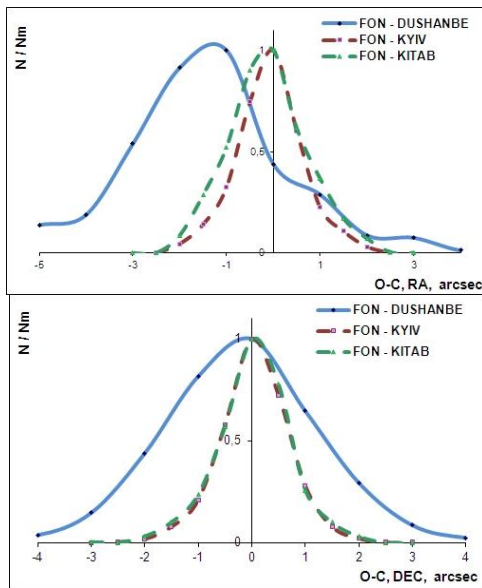


Figure 3: Histograms of distribution of O-C differences on both coordinates for 302 asteroid positions from the FON-Dushanbe observations.

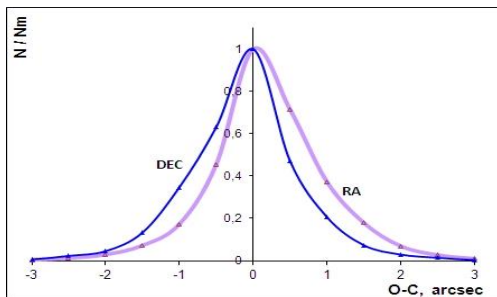


Figure 4: Distribution of O-C differences between the coordinates determined from plate No. 1108 (observations of FON-Dushanbe) and identified from the data of the Gaia DR2 catalog for 14103 stars.

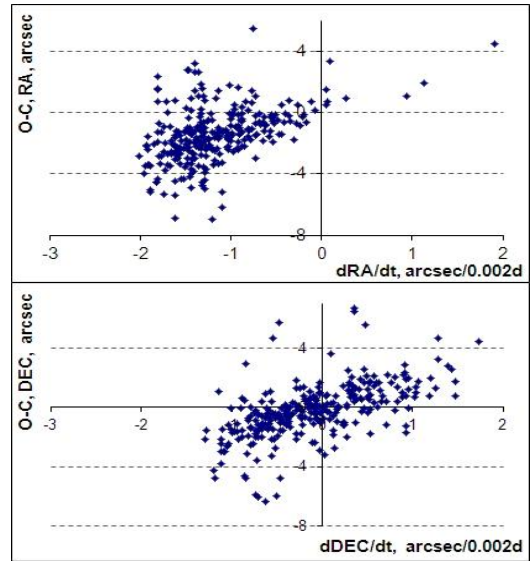


Figure 5: Dependence of the O-C differences on the values of orbital velocities for all asteroid positions.

Secondly, the O-C differences for all asteroid positions were analyzed depending on asteroid orbital velocities near the corresponding observational moments. The results are shown in Fig. 5. A clear correlation of the O-C differences of asteroids with the value of their orbital velocities near the observational moments was found in the right ascension coordinate. For asteroids with a higher orbital velocity, the largest values of the O-C differences and their significant scatter are observed. Therefore, the systematic shift of asteroid O-C differences may be the result of a systemic underestimation of time in the positions of asteroids, as also noted in the article by Yizhakevych et al. (2018). According to the preliminary estimates, its value can reach several minutes. Further analysis of the results is also required using the remaining observations from other FON-Dushanbe zones. As a result, the systematic component of the asteroid positional errors can be analyzed and, if possible, taken into account.

3. Conclusion

According to the results of processing the digitized plates of the third part of the FON project in Dushanbe, more than 300 asteroid positions were obtained.

Precise recording of the time of each exposure on a photographic plate, as is required when observing moving celestial objects, was not a necessary requirement for observing stellar areas in the FON project implementation.

Therefore, using FON observations to determine the precise positions of moving celestial objects may lead to some increase in positional errors for different plates or their groups. However, in most cases, this leads to an increase in the random component of these errors. So, the systematic components of errors should be analyzed and, if possible, taken into account.

We note that the observations of the FON-Kyiv and FON-Kitab parts gave successful results in identifying the positions of asteroids compiling their catalogs and determining their positional accuracy.

The use of new digital technologies for processing observations made it possible to increase the total number of positions of small bodies of the Solar System by searching for images from various digitized archives of observations of previous years as well as to increase their accuracy.

The covering of time intervals with missing data on asteroid positions and their analysis can be useful not only for modern ephemeris calculations but also for studying the evolution of asteroid orbits along time, non-gravitational effects, and others. These missing data can be obtained from the digitized observational archives of the UkrVO (Pakuliak et al., 2013; Vavilova et al., 2016; 2017; 2020), modern processing methods (Savanevych et al., 2015a; 2015b; 2018) and other databases.

The magnitudes of asteroids determined simultaneously with their coordinates can be used to determine the photometric characteristics of asteroids, constructing light curves and phase dependencies.

Note. While the article was being typeset, a previously lost log-book of observations was found. Preliminary analysis of several records showed differences in observational moments. This gives hope for a decrease in the values of the O-C differences for asteroids. The work is continued. The final complete list and positions of asteroids will be received after all observations have been processed.

Acknowledgments. The authors are sincerely grateful to Dr. Vavilova I. B. for support and active participation in the discussion of the results of the work.

References

- Andruk V.M., Pakuliak L.K., Golovnia V.V. et al.: 2015, *Odessa Astron. Publ.*, **28**, 192.
- Andruk V.M., Pakuliak L.K., Golovnia V.V. et al.: 2016, *Kinem. Phys. Cel. Bodies*, **32**, N5, 260.
- Andruk V.M., Pakuliak L.K., Golovnia V.V. et al.: 2017, *Science and Innovation*, **13a**, 17.
- Andruk V., Yuldoshev Q., Eglitis I. et al.: 2017, *Odessa Astron. Publ.*, **30**, 159.
- Ivanov G., Pakuliak L., Shatkhina S. et al.: 2013, *Izvestia of the Main Astronomical Observatory at Pulkovo*, **220**, 501.
- Mullo-Abdolov, A.; Kokhirova, G.; Relke, H.; et al.: 2017, *Odessa Astron. Publ.*, **30**, 186.
- Mullo-Abdolov, A.; Relke, H.; Kokhirova, G.; et al.: 2018, *Odessa Astron. Publ.*, **31**, 224.
- Pakuliak L., Golovnya V., Virun N. et al.: 2013, *Odessa Astron. Publ.*, **26**, 236.
- Pakuliak L.K., Andruk V.M., Golovnia V.V. et al.: 2016, *Odessa Astron. Publ.*, **29**, 132.
- Pakuliak L.K., Andruk V.M.: 2020, Applications of Big Data in Astronomy and Geosciences: Algorithms for Photographic Images Processing and Error Elimination. In: Knowledge Discovery in Big Data from Astronomy and Earth Observation. 1st ed./ eds. P. Skoda, F. Adam. ISBN: 978-0-128-19154-5 (Elsevier), p. 325–330. DOI: 10.1016/B978-0-12-819154-5.00029-1
- Protsyuk Yu., Yizhakevych O., Kovylianska O. et al.: 2015, *Odessa Astron. Publ.*, **28**, 204.
- Protsyuk Yu., Maigurova N., Protsyuk S. et al.: 2016, *Odessa Astron. Publ.*, **29**, 147.
- Protsyuk Yu., Relke E.: 2016, *Odessa Astron. Publ.*, **29**, 144.
- Protsyuk Yu. I., Kovylianska O.E., Protsyuk S.V. et al.: 2017, *Sci. innov.* (ISSN 2409-9066), **13(1)**, 81.
- Protsyuk Yu. I., Kovalchuk O.M., Andruk, V.M.: 2019, *Odessa Astron. Publ.*, **32**, 196.
- Protsyuk, Yu.I.; Andruk, V.N.; Relke, H.: Astroplate 2016, in: Proc. of a conference held in March, 2016 in Prague, Czech Republic. Editor Petr Skala. ISBN: 978-80-01-06566-2, Prague 2019, p. 47.
- Rahimi, F.; Mullo-Abdolov, A.Sh.; Kokhirova, G. et al.: 2018, *Reports of the Academy of Sciences of the Republic of Tajikistan* (ISSN 0002-3469), **61**, Is.2, 144.
- Relke E., Protsyuk Yu.I., Andruk V.M.: 2015, *Odessa Astron. Publ.*, **28**, 211.
- Savanevych V.E., Briukhovetskyi A.B., Ivashchenko Yu.N. et al.: 2015, *Kinemat. Phys. Cel. Bodies*, **31**, 6, 302.
- Savanevych V.E., Briukhovetskyi O.B., Sokovikova N.S. et al.: 2015, *MNRAS*, **451**, Is. 3, 3287.
- Savanevych V.E., Khlamov S.V., Vavilova I.B. et al.: 2018, *Astronomy & Astrophysics*, **609**, id.A54, 11 pp.
- Shatkhina S.V., Kazantseva L.V., Yizhakevych O.M. et al.: 2017, *Odessa Astron. Publ.*, **30**, 198.
- Shatkhina S.V., Kazantseva L.V., Yizhakevych O.M. et al.: 2018, *Kinem. Phys. Cel. Bodies*, **34**, N5, 270.
- Shatkhina S.V., Relke H., Yuldoshev Q.X. et al.: 2018, *Odessa Astron. Publ.*, **31**, 235.
- Shatkhina S.V., Yizhakevych O.M., Protsyuk Yu.I. et al.: 2019, *Odessa Astron. Publ.*, **32**, 203.
- Vavilova I.B.: 2016, *Odessa Astron. Publ.*, **29**, 109.
- Vavilova I.B., Pakuliak L.K., Babyk Iu.V. et al.: 2020, Surveys, Catalogues, Databases, and Archives of Astronomical Data. In: Knowledge Discovery in Big Data from Astronomy and Earth Observation, 1st ed./ eds. P. Skoda, F. Adam, p. 57–102. DOI: 10.1016/B978-0-12-819154-5.00015-1.
- Vavilova I.B., Yatskiv Ya.S., Pakuliak L.K. et al.: 2017, *Proc. IAU Symposium*, **325**, 361.
- Yizhakevych O.M., Mullo-Abdolov A.Sh., Relke H.V. et al.: 2018, *Odessa Astron. Publ.*, **31**, 247.
- Yuldoshev Q.X., Ehgamberdiev Sh.A., Muminov, M.M. et al.: 2017, *Kinem. Phys. Cel. Bodies*, **33**, N5, 250.
- Yuldoshev, Q.; Protsyuk, Y.; Relke, H.; et al.: 2019, *Astronomische Nachrichten*, **340**, 6, 494.

DOI:<http://dx.doi.org/10.18524/1810-4215.2020.33.217122>

UKRVO SPECTRAL PHOTOGRAPHIC ARCHIVE OF VARIABLE STARS

A.V. Zolotukhina, L.K. Pakuliak, I.B. Vavilova, B.M. Kaminsky

Main Astronomical Observatory of the NAS of Ukraine,
27 Akademik Zabolotny St., Kyiv 03143 Ukraine
nasty@mao.kiev.ua

ABSTRACT. The overview of the content of an Archive of the spectral photographic observational data stored at the MAO NAS of Ukraine in 1965–1985 is presented. Being the part of the UkrVO Joint Digitized Archive, this archive contains of 50,000 spectra of mostly variable stars.

The spectral photographic material (glass astroplates) was obtained by the 70-cm reflector AZT-2 (MAO NAS of Ukraine, Kyiv), 60-cm Zeiss telescope at the Mount Terskol (North Caucasus, Russia), and 1-m telescope at the Mount Sanglok (Institute of Astrophysics, Tajikistan) equipped with spectrographs UAGS with a set of gratings to obtain dispersions in the range of 29...167 Å/mm of the wavelengths 3500...6800 Å. There is also data related to the observations by the Double Short Astrograph (MAO NAS of Ukraine) with a pre-objective prism to monitor Nova Cygni 1975 in the initial stage of outburst. Almost all the spectra are calibrated with the 9-step attenuator and comparison spectra for the wavelength scale.

We discuss observational programs (aims, instruments, results), in frame of which this archive was accumulated, as well as key principles for digitizing spectra and their processing by modern tools of virtual observatory software.

Keywords: astroplates, database, variable stars, spectral photographic archive.

АНОТАЦІЯ. У роботі представлено огляд архіву даних спектральних спостережень, отриманих в ГАО НАН України з 1965 року. Цей архів охоплює період часу близько 20 років і містить 50 000 спектрів, головним чином, змінних зір.

Спектральний фотоматеріал (скляні астропластинки) отриманий здебільшого на 70-см рефракторі АЗТ-2 (ГАО НАН України, Київ), а також 60-см телескопі Цейс високорічної обсерваторії на піку Терскол (Північний Кавказ, Росія) та 1-метровому телескопі на горі Санглок (Інститут астрофізики АН Таджикистану), оснащеному спектрографами UAGS з набором ґраток для отримання дисперсії 29...167 Å/мм у діапазоні довжин хвиль 3500–6800 Å. А також дані, отримані на Подвійному широкутному астрографі (ГАО НАН України) з дооб'єктивною призмою для моніторингу Nova Cygni 1975 на початковій стадії спалаху. Майже всі спектри відкалібровані за допомогою 9-ступінчастого аттенюатора та спектрів порівняння для шкали довжин хвиль.

У роботі розглянуто спостережні програми (мета, інструменти, результати), в рамках яких був накопичений цей архів, а також ключові принципи оцифрування

спектрів та їх обробки сучасними інструментами програмного забезпечення віртуальної обсерваторії.

Ключові слова: астропластинки, бази даних, змінні зорі, спектральний фотографічний архів.

1. Introduction

In 2020, the next International Workshop on Stellar Spectral Libraries (IWSSL) was supposed to be held in Beijing. One of the main issues to be considered at the meeting can be defined as the problem of preparation of stellar spectral libraries (SSL) for data sharing, simplification of access to their archives, and the use of VO tools for the solution of the first two challenges (<http://svo2.cab.inta-csic.es/projects/is-sibj/>). The priority of this task is determined by the “*considerable disagreements on the atmospheric parameters and chemical abundances of stars, and on the ages, metallicities of masses of galaxies, persist for decades*” due to different approaches to observations, spectra restoration, and analysis used in every SSL, as it is noted in the objectives of IAU Commission G5 WG Stellar Spectral Libraries (https://www.iau.org/science/scientific_bodies/working_groups/306/). Thus, the systematic uncertainties of SSLs prevent the resulted catalogues from providing the comprehensive coverage of the galactic evolution even if the internal accuracies of the components are extremely high.

David Montes presented the most complete list of SSLs of all types, both existing and future (<https://webs.ucm.es/info/Astrof/invest/actividad/spectra.html>). We note some of the state-of-the-art SSLs.

X-Shooter Library (XSL) contains the collection of 3000–25000 Å medium-resolution (R~10000) stellar spectra obtained with the X-Shooter spectrograph at the VLT in 2009–2010 (pilot program) and 2012–2014 (Large Program).

The second data release (Gonneau et al., 2020) contains 813 observations of 666 stars covered the extended wavelength range, including infrared data and spectral types between O and M. Spectra are available via CDS <http://cdsarc.u-strasbg.fr> (<ftp://130.79.128.5>) or via <http://cdsarc.u-strasbg.fr/viz-bin/cat/J/A+A/634/A133>.

MILES Library contains near 1000 stars spanning a large range in atmospheric parameters. The spectra were obtained at the 2.5m INT telescope and cover the range 3525–7500 Å at 2.5 Å (FWHM) spectral resolution.

The shape of the continuum for the stellar spectra has been carefully calibrated. The current version of the Library presents a high level of homogeneity (Falcón-Barroso et al.,

2011). The complete library is available as single tar files in ASCII and FITS formats at the website of the project as well as a set of WEBTOOLS to retrieve, handle and transform the data (<http://miles.iac.es/pages/stellar-libraries.php>). The VO access to the MILES was developed at Spanish VO (<http://svo2.cab.inta-csic.es/vocats/v2/miles/>).

Gaia Benchmark stars (GBS) is a library of high resolution and high signal to noise ratio stellar spectra. Extremely high-resolution spectra of ~ 40 stars are spanning FGK spectral classes. The stars benefit from interferometric observations and have extremely accurate associated stellar parameters. This library can be used as a set of calibration stars for automatic stellar parameter pipeline developments in on-going spectroscopic surveys. Data are available through <https://www.blancocuaresma.com/s/benchmarkstars> or at the CDS as catalog III/281 (Blanco-Cuaresma et al., 2014).

Among the SSLs with low-resolution the **LAMOST** project (China's Large Sky Area Multi-Object Fiber Spectroscopic Telescope) stands out (Cui et al., 2012). The Empirical SSL from the LAMOST in its last release DR7 contains 14.5 million low (10.6 million) and medium resolution ($R \sim 1800$) flux calibrated spectra of ~ 8 million stars across the Galaxy with a wavelength coverage of the entire optical range. The number of high-quality ($S/N > 10$) spectra reaches 11.4 million. A catalogue, which has provided stellar parameters of 5.34 million stars, was also released in this data set. The DR7 is available at <http://dr7.lamost.org>.

The examples of the design of SSL web-interfaces for data search and presentation of query results are the **ELODIE** online database of 35 000 high-resolution stellar spectra (<http://atlas.obs-hp.fr/elodie/>) and the **DAO** Spectroscopic Plate Archive (<http://www.cadc-ccda.hia-ihp.nrc-cnrc.gc.ca/en/search/?collection=DAOPLATES&noexec=true>).

ELODIE archive preserves data obtained with ELODIE echelle spectrograph at 1.93 m telescope of Observatoire de Haute Provence. The spectra have the nominal resolution $R \sim 42\,000$ and $S/N > 3$. Spectra can be visualized on-screen or are available for download as FITS-files. The re-processing of data is organized on the fly as a pipeline. The present archive is extended with spectra of new instrument SOPHIE, which are available through the same interface.

The **DAO** spectroscopic plate collection consists of 1) over 16 800 high-dispersion spectrograms exposed at the coudé focus of the 1.2-m DAO telescope and McKellar spectrograph between 1962 and 2000, and 2) more than 93 000 spectra obtained at the Cassegrain focus of the DAO 1.8-m telescope and spectrograph between 1918 and 1984. The interface of archive and query builder allow searches by important criteria (object name, date, wavelength) and presents the results of the search in a tabular format.

The **NVO** Virtual Observatory Spectrum Services (<http://voservices.net/spectrum/default.aspx>) proposes the web-interface for the search of objects in SDSS DR6 collection by means of related VO services built using the VO *ConeSearch* standard. The collection of spectra is expandable. The registered users can upload their own spectra and use VO tools for their processing. The site provides several visualization and computational tools (Dobos et al., 2004).

The list of available VO tools and software for processing the spectral data can be accessed through the IVOA web-site <https://www.ivoa.net/astronomers/applications.html>.

So, a vast amount of spectral data with a quality from low to medium resolution is available from releases of the Gaia space mission and its complementary ground-based spectroscopic surveys.

The question is: why, having millionth SSL, we intend to digitize spectral photographic archives with dozens or hundreds of objects? Which science could be done with archival data?

The answer is: a collation of archival and modern observational data is crucial for astronomical objects, which manifest variability of their physical parameters (novae, variable stars, multiple systems) and might display new facts (for example, as ϵ Aurigae) about properties during evolution (Griffin, 2013).

The correct digitization and treatment of the old stellar spectra, regardless of apparent quality, is the main demand for the glass collections of spectral plates to preserve the information which they bear.

2. The UkrVO database of spectral archive

The glass library of the MAO NAS of Ukraine is still a hard-to-reach repository of a huge amount of astronomical data. Searching for information even in a separate glass archive is an almost impossible task due to problems of its orderliness, visibility, the ability to use search algorithms, time consumption, performance, media aging, physical loss of information, etc. Digitized archives are devoid of all these shortcomings and make it possible to obtain information in full on a set of archives and at finite intervals (Vavilova et al., 2011, 2020; Savanevych et al. 2015, 2017).

At the moment, the Ukrainian VO archive contains of 654 digitized spectral astronegatives, mostly of variable stars. Table 1 shows the name and type of stars as well as the number of spectral astronegatives for these objects.

We started the process of digitizing this collection with the photographic spectra, which can be systematized. It aims at creation a database of free access using modern image digitizing technologies. Plate digitizing is conducted using a flatbed scanner Epson Expression 10000XL with 16-bit gray levels, resolution of 4800 dpi. Digitized images are stored in TIFF and FITS formats (<http://ukr-vo.org/spectra/>). The SSL database is described by Pakuliak et al. (2014).

3. Observational and research projects

The spectral photographic material (glass astroplates) was obtained by the 70-cm reflector AZT-2 (MAO NAS of Ukraine, Kyiv), 60-cm Zeiss telescope at the Mount Terskol (North Caucasus, Russia), and 1-m telescope at the Mount Sanglok (Institute of Astrophysics, Tajikistan) equipped with spectrographs UAGS with a set of gratings to obtain dispersions in the range of 29...167 Å/mm in the wavelengths 3500...6800 Å.

Table 1. Description of the UkrVO archive of spectral photographic astroplates with variable stars observed in 1965–1985 and stored at the MAO NAS of Ukraine

No.	Object	Number of spectral astrophotographs	Type (SIMBAD)
1	R And	26	S Star
2	W And	14	S Star
3	EG And	5	Symbiotic Star
4	β And	14	High proper-motion Star
5	α Aql	5	Variable Star of delta Sct type
6	γ Aql	11	Star
7	α Aqr	7	Star
8	R Boo	1	Variable Star of Mira Cet type
9	V Boo	1	Long-period variable star
10	η Boo	6	Spectroscopic binary
11	R Cam	2	S Star
12	T Cam	6	S Star
13	XX Cam	1	Variable Star of R CrB type
14	R Cas	22	Variable Star of Mira Cet type
15	T Cas	4	Variable Star of Mira Cet type
16	V Cas	6	Variable Star of Mira Cet type
17	SU Cas	1	Classical Cepheid (delta Cep type)
18	TU Cas	1	Classical Cepheid (delta Cep type)
19	UV Cas	2	Variable Star of R CrB type
20	β Cas	12	Variable Star of delta Sct type
21	δ Cas	2	Eclipsing binary of Algol type
22	η Cep	15	High proper-motion Star
23	o Cet	2	Variable Star of Mira Cet type
24	τ Cet	6	High proper-motion Star
25	V Cnc	2	S Star
26	S CrB	3	Variable Star of Mira Cet type
27	R Cyg	2	S Star
28	U Cyg	2	Carbon Star
29	CH Cyg	210	Symbiotic Star
30	RT Cyg	6	Variable Star of Mira Cet type
31	RU Cyg	2	Variable Star of Mira Cet type
32	γ Cyg	2	Variable Star
33	δ Cyg	1	High proper-motion Star
34	ζ Cyg	7	Spectroscopic binary
35	ξ Cyg	17	Spectroscopic binary
36	UX Dra	2	Carbon Star
37	β Dra	20	Star
38	χ Dra	5	Spectroscopic binary
39	ϵ Eri	3	Variable of BY Dra type
40	R CMi	4	S Star
41	β Gem	24	High proper-motion Star
42	γ Gem	1	Spectroscopic binary
43	ϵ Gem	7	Variable Star
44	μ Gem	7	Long-period variable star
45	ξ Gem	6	High proper-motion Star
46	ρ Gem	1	High proper-motion Star
47	ν Gem	1	High proper-motion Star
48	α Her	18	Double or multiple star
49	μ Her	17	Double or multiple star
50	ϵ Hya	5	Rotationally variable Star
51	Sp K	3	Unknown star, possibly K-type star for comparison
52	R Leo	6	Variable Star of Mira Cet type
53	ζ Leo	7	Variable Star
54	η Leo	3	Star
55	α Lep	3	Variable Star
56	R Lyr	3	Long-period variable star
57	W Lyr	4	Variable Star of Mira Cet type
58	α Oph	7	Double or multiple star
59	α Ori	10	Red supergiant star
60	β Ori	9	Blue supergiant star
61	π^3 Ori	2	High proper-motion Star
62	ν Peg	4	High proper-motion Star
63	α Per	13	Variable Star
64	γ Per	1	Eclipsing binary of Algol type
65	ν Per	3	Star
66	V Sge	1	Nova-like Star

67	SU Tau	1	Variable Star of R CrB type
68	α Tau	15	Long Period Variable candidate
69	R Tri	4	Variable Star of Mira Cet type
70	R UMa	2	Variable Star of Mira Cet type
71	β UMa	1	High proper-motion Star
72	R Vir	3	Variable Star of Mira Cet type
73	γ Vir	1	Double or multiple star
74	R CVn	1	Variable star of Mira Cet type

The first instrument AZT-2 ($D = 70$ cm) was mounted in 1959 at the MAO NASU (Fig. 1) for astrophysical purposes: photometric, spectral, and polarimetric observations of the Solar System bodies and stars.

The research on stellar spectroscopy have started at the MAO NASU in 1960. They were initiated by Prof. Tsesevich V.P. and conducted later by his post-graduate students and followers (Andronov, 2017; Vavilova, 2017). Among them were I.G. Zhdanova, F.I. Lukatskaya, R.I. Chupryna, and later (the “Odessa landing”) M.Ya. Orlov (research of RCrB type stars with anomalous chemical composition), M.G. Rodrigues (research of stars of late spectral classes), A.F. Pugach (research of physics of non-stationary stars), E.S. Kheilo (variable stars in globular clusters, astronomical instrumentation) and yet later, G.U. Kovalchuk, A.E. Rozenbush, R.M. Goncharova.

Observations were carried out at the AZT-2 in Golosiv (MAO NASU), at large telescopes of the Crimean Astrophysical Observatory (CrAO) and Shemakha Astrophysical Observatory (ShAO). Spectral-photometric archive of the MAO NASU is stored within a large number of observational projects related to the variable stars of different types. The observational data are not fully digitized and systematized due to the absence of observation’s protocols in several cases. We note several programs.

In 1972, under the leadership of M.Ya. Orlov, the complex studies of non-stationary stars of the R Northern Corona type (R CrB) began, which are characterized by anomalous physical composition (significant hydrogen deficiency, carbon excess) and the presence of non-stationary dust shells, sometimes so dense, that the apparent brightness of the star is weakened by several magnitudes.

In 1974, the photoelectric observations of nonstationary stars were conducted by Pugach A.F., Kovalchuk G.U., and Kondratyuk R.R. with AZT-14 at the Terskol Observatory and with MTM-500 television set at the Crimean AO. Then exactly, the spectral and polarimetric observations of UV Cas, a little-studied star of the R CrB type, have begun. Spectral observations of stars of the late spectral types were continued with AZT-2, the Zeiss universal diffraction spectrograph. As a result, 102 spectrograms were obtained (Annual Scientific Report of the MAO NASU, 1974, p. 58);

Catalog of B-V stellar magnitudes of spectra of about 20000 stars has been prepared for printing and the spectra of early stars up to 15^m in the region of the NGC2129 cluster have been recorded (i.e., p. 60); 900 double scans were obtained at the Terskol Observatory (i.e., p. 80).



Figure 1: The 70 cm reflector AZT-2 (MAO NAS of Ukraine, Kyiv)

In 1978, the four-color observations of non-stationary stars with non-periodic brightness attenuation were carried out (RZ Psc, V530 Cyg, BO Cep, XY Per, RCrB) (Annual Scientific Report of the MAO NASU, 1978, p. 60); the energy distribution in the spectrum of η Agl was obtained for the first time by E.A. Depenchuk (i.e., p. 105).

In 1978, under the “Nadir” research program, the images of variable stars were registered with the scanning spectrometer at the observational station “Lisnyky” (Kyiv National University). The AZT-2 telescope in Golosiv allowed obtaining 35 scans with a dispersion of 84 \AA/mm of Cepheids and standard stars of spectral types F-G. A catalog of equivalent absorption line widths in the RR Lyra spectra has been prepared for publication (i.e., p. 106).

In 1985, the debugging and testing of the operability of the interface of the automatic electro-spectrophotometer with the control micro-computer “Electronica DZ-28” (E.A. Depenchuk, A.F. Pereverzentsev) was completed. Trial observations were carried out at the Mayaki astronomical station near Odessa. Then the equipment was delivered to the Terskol Observatory and installed at the AT-80 telescope (Annual Report of the MAO NASU, 1985, p. 105).

The bigger collection of observations of variable stars, which are at the disposal of the Astronomical Observatory of the I.I. Mechnikov National University of Odesa, numbers ~84000 photographic plates obtained with the 7-camera astrograph at the Mayaky station in 1957–1998 (Chochol et al. 1999; Šimon et al. 2002; Andronov et al. 2014). It could be used as the complemented photometric data while studying spectra of individual variable stars. Some description about collection of spectral and photometric observations of stars stored at the CrAO (Shlyapnikov et al. 2019) can be found through web-site of the Crimean Virtual Observatory (<https://sites.google.com/view/cravo-invo/about>).

4. Digital versions of star spectra from photographic astronegatives

Figure 2 shows a digital version of the XX Cam spectrogram from the MAO archive as the example. It includes information about the star's name (XX Cam), date of observation (Oct 15/16, 1978), number in the journal of observations (Z-413) as well as the time of exposure (70 min).

This object (No. 13 in Table 1) has only one spectrogram that make unable to use it for the following study with a spectral archive of the MAO NASU. Object of observation: the star XX Cam [α (J2000) = $04^{\text{h}}08^{\text{m}}38.7^{\text{s}}$, δ (J2000) = $+53^{\circ}21'39.35''$], one of the brightest stars of the R CrB type ($V = 7^{\text{m}}.35$), radial velocity 15.5 km/s, parallaxes 0.6407 ± 0.0355 mas, spectral type F8I C, Gaia DR2 275138564223556608. From the year 1898 till to date, apparently XX Cam has undergone only one visual brightness light minimum in 1939–1940. From inspection of a single low-dispersion spectrogram obtained in 1947, Bidelman (1948) noted abnormal weakness of the hydrogen lines and presence of the lines carbon as well as he marked general similarity of the spectra of XX Cam and R CrB (Orlov & Rodriguez, 1974). The stars of R CrB type were deeply studied in various observational programs of the MAO NASU, see, for example, the monograph by Zhiliaev et al. (1978) and papers by Začs et al. (2007), Yakovina et al. (2013). The R CrB stars as the long-term variables are of particular interest for the modern projects such as the VASCO (Villarroel et al. 2020).

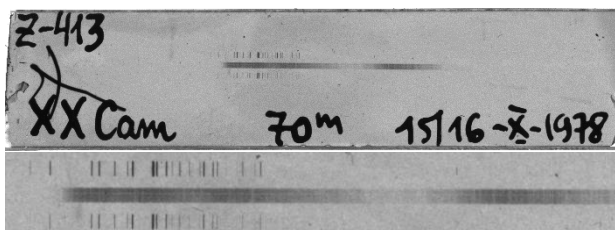


Figure 2: Digital version of the XX Cam spectrogram from the spectral archive of the MAO NASU

One of the interesting objects from a spectral archive is the R And (No. 1 in Table 1, 24 spectral astronegatives, Gaia DR2 379224622732758528). Object of observation (Fig. 3): R And [α (J2000) = $00^{\text{h}}24^{\text{m}}01.95^{\text{s}}$, δ (J2000) = $+38^{\circ}34'37.33''$], S star ($V = 5.8^{\text{m}} - 15.2^{\text{m}}$), parallaxes 4.1281 ± 0.4616 mas, radial velocity -6.40 km/s, spectral type S5-7/4-5e B. It shows periodic variations in brightness approximately every 409 days (Samus et al., 2009).

The spectrum visualization of digitized spectrogram of R And in scale of scan is given in Fig. 4. It obtained with software developed by S.G. Sergeev (Crimean Astrophysical Observatory), which creates a standard FITS file with the required header parameters. That is, the source file will be interpreted by any spectra processing software tools likely IVOA VOSpec (Baines et al., 2009), Aladin, DECH20 (Galazutdinov, 1992) etc. As a result, it will be possible to “breathe new life” in old spectral photographic archives of variable stars from their discovery (for example, Pickering, 1895) to nowadays research: chemical composition and molecular spectra (Lambert 1988), spectral variability (Záčs et

al., 2016), methods of processing (Calderon et al., 2002), VO spectral stellar library (Mickaelian et al., 2017) etc.

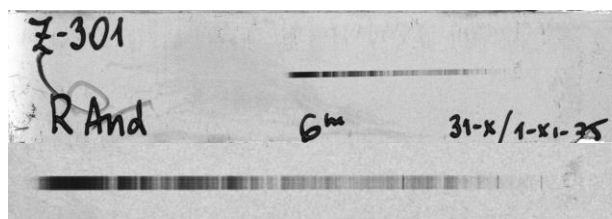


Figure 3: Digital version of the R And spectrogram from the photographic archive of the MAO NASU (observation date: Oct 31 – Nov 1, 1975; exposure: 6 min)

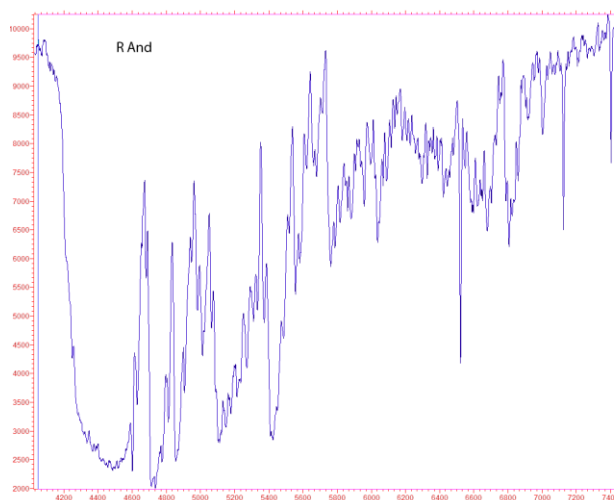


Figure 4: Visualization of R And spectrum from the digitized astronegatives in scale of scan as in Figure 3 (axis X: in pixels of X axis of scan; axis Y: relative flux)

5. Conclusion

We describe the start points of the new UkrVO project related to the development of database of astronegatives with stellar spectra from the archive of the MAO NASU. Now it contains 654 systematized spectra, mostly of variable stars, and covers observational period of 1965–1985 years. We envisage the main stages of the project as follows:

- Systematization of spectra collection (creation of database for the archive of photographic stellar spectrograms).
- Search for any reports on the topic and for annual reports in the archive of the MAO NASU with description of the observational material (instruments, objectives of observational programs, observers, results etc.).
- Search for scientific articles written by observers that describe their results and observational programs, etc.
- Digitization of star's spectra.
- Further reduction of spectra extracted from astronomical negatives, including programs to compute astrometric solution, extract spectra, and apply wavelength and photometric calibration for objects.
- Interactive access and processing of digital versions of spectra.
- Identification of spectral lines.

• Scientific project with archive of Spectral Digital Library of the UkrVO (<http://ukr-vo.org/spectra/>).

The implementation of advanced digital technologies to ensure the interactive use of accumulated data on archive spectra of individual stars is of particular relevance, given the possibility of retrospective analysis of their state at time intervals from decades to days.

Acknowledgements. This research has made use of the SIMBAD database, operated at CDS, Strasbourg, France (Wenger et al. 2000).

References

- Andronov I.L.: 2017, *Odessa Astron. Publ.*, **30**, 252. DOI: 10.18524/1810-4215.2017.30.118686
- Andronov I.L., Marsakova V.I., Kudashkina L.S.: 2014, *Adv. Astron. Space Phys.*, **4**, 3.
- Annual Scientific Report of the MAO NAS of Ukraine: 1974, Kyiv, 88 p.
- Annual Scientific Report of the MAO NAS of Ukraine: 1978, Kyiv, 111 p.
- Annual Scientific Report of the MAO NAS of Ukraine: 1985, Kyiv, 126 p.
- Baines D., P. Osuna, Gonzalez-Núñez J.: 2009, Multi-wave-length Astronomy using VOSpec. Proceedings of the EURO-VO Workshop, held at the ESA, 2008. ESA, p. 99.
- Bidelman W. P.: 1948, *Astrophys. J.*, **107**, 413.
- Blanco-Cuaresma S., Soubiran C., Jofré P., Heiter U.: 2014, *A&A*, **566**, 98. DOI:10.1051/0004-6361/201323153
- Calderón J.H., Villada M., Bustos F.: 2002, *Revista Mexicana de Astronomía y Astrofísica Serie de Conferencias*, **14**, 148.
- Chochol D., Andronov I.L., Arkhipova V.P.: 1999, *Contrib. Astron. Obs. Skalnaté Pleso*, **29**, 1, 31
- Cui X.-Q., Zhao Y.-H., Chu Y.-Q. et al.: 2012, *Research in Astronomy and Astrophysics*, **12**, Is. 9, 1197. DOI:10.1088/1674-4527/12/9/003
- Dobos L., Budavári T., Csabai I., Szalay A.S.: 2004, *Astronomical Data Analysis Software and Systems (ADASS) XIII*, **314**, 185.
- Falcón-Barroso J., Sánchez-Blázquez P., Vazdekis A. et al.: 2011, *Astron. & Astrophys.*, **532**, 95. DOI: 10.1051/0004-6361/201116842
- Galazutdinov G.A.: 1992, Eshelo-spectra processing system DECH-20, Preprint No. 92 (Spec. Astrophys. Observ., Nizhny Arkhyz), 52.
- Gonneau A., Lyubenova M., Lançon A. et al.: 2020, *Astron. & Astrophys.*, **634**, 133. DOI: 10.1051/0004-6361/201936825
- Griffin R.E., Stencel R.E.: 2013, *PASP*, **125**, Is. 929, 775. DOI: 10.1086/671781
- Kashuba S.G., Bazyey N.V., Kashuba V.I., Andrievsky S.M.: 2019, In: *Large surveys with small telescopes: Past, Present, and Future* (AstroplateIII); https://www.plate-archive.org/applause/wp-content/uploads/2019/04/Bazyey_Odessa_Archive.pdf
- Lambert D.L.: 1988, *Publ. Astron. Soc. Pac.*, **100**, 1202.
- Mickaelian A.M., Astsatryan H.V., Knyazyan A.V., Mikayelyan G.A.: 2017, *BAOJ Physics*, **2**, Is. 1, id. 8, 11.
- Orlov M.Ya.: 1975, *Perem. Zvezdy, Byull.*, **19**, 6, 501.
- Orlov M.Ya., Rodriguez M. H.: 1974, *Astron. & Astrophys.*, **31**, 203.
- Pakuliak L., Shlyapnikov A., Rosenbush A. et al.: 2014, International Workshop on Stellar Spectral Libraries ASI Conference Series, **11**, 103 (digital versions).
- Pickering E.C.: 1895, *Astrophys. J.*, **1**, 27.
- Samus N.N., Kazarovets E.V., Durlевич O.V. et al.: 2009, VizieR Online Data Catalog: General Catalogue of Variable Stars (Samus+ 2007–2017): B/gcvs. Originally Published In: 2017AREp...61...80S.
- Savanevych V.E., Briukhovetskyi A.B., Sokovikova N.S. et al.: 2015, *Mon. Not. R. Astron. Soc.*, **451**, 3, 3287. DOI: 10.1093/mnras/stv1124
- Savanevych V.E., Khlamov S.V., Vavilova I.B. et al.: 2018, *Astron. & Astrophys.*, **609**, id. A54, 11 pp. DOI: 10.1051/0004-6361/201630323
- Shlyapnikov A.A., Gorbunov M.A., Gorbachev R.R. et al.: 2019, *Izv. Krymsk. Astrofiz. Observ.*, **115**, 1, 38 (In Russian).
- Šimon V., Hric L., Petřík K.: 2002, *Astron. Astrophys.*, **393**, 921
- Vavilova I.B.: 2016, *Odessa Astron. Publ.*, **29**, 109. DOI: 10.18524/1810-4215.2016.29.85269
- Vavilova I.B.: 2017, *Odessa Astron. Publ.*, **30**, 256. DOI: 10.18524/1810-4215.2017.30.118718
- Vavilova I.B., Pakuliak L.K., Protsyuk Yu.I. et al.: 2011, *Kosm. nauka tehnol.*, **17**, 4, 74.
- Vavilova I., Pakuliak L., Babyk Iu. et al.: 2020, “Surveys, Catalogues, Databases, and Archives of Astronomical Data” in “Knowledge Discovery in Big Data from Astronomy and Earth Observation”, p. 57–102. DOI: 10.1016/B978-0-12-819154-5.00015-1
- Villarroel B., Soodla J., Comeron S. et al.: 2020, *Astron. J.*, **159**, 1, 8. DOI: 10.3847/1538-3881/ab570f
- Wenger et al.: 2000, The SIMBAD astronomical database, *Astron. & Astrophys. Suppl.*, **143**, 9.
- Yakovina L.A., Rosenbush A.E., Pavlenko Ya.V., Kaminsky B.M.: 2013, *Astronomy Reports*, **57**, Is. 10, 734.
- Začs L., Mondal S., Chen W.P. et al.: 2007, *Astron. & Astrophys.*, **472**, Is. 1, 247.
- Začs L., Musaev F., Kaminsky B. et al.: 2016, *Astrophys. J.*, **816**, Is. 1, article id. 3, 14 pp.
- Zhiliaev B.E., Orlov M.Ia., Pugach A.F. et al.: 1978, R Coronae Borealis type stars. Kiev: Nauk. Dumka, 128 p. (in Russian).

Наукове видання

Одеські Астрономічні Публікації

том 33 (2020)

Англійською мовою

Технічний редактор *В. В. Ковтюх*
Комп'ютерна верстка *С. Л. Страхова*

Підписано до друку 19.12.20.
Формат 60x84/8. Папір офсетний. Друк різнограф.
Ум. друк. арк. 24,99. Обл.-вид. арк. 28.0. Тираж 300 екз. Зам. № .

Друкарня ТОВ "ПРОМАРТ"
61023, Харків, вул. Весніна, б. 12, оф. 17
Свідоцтво про внесення до Держреєстру суб'єкта видавничої справи
серія ДК №5748 від 06.11.2017 р.
тел. (057) 717-28-80

